João Oliveira Ventura

Magnetic Nanostructures

FACULDADE DE CIÊNCIAS
UNIVERSIDADE DO PORTO

Department of Physics
Faculty of Sciences of the University of Porto
February 2006

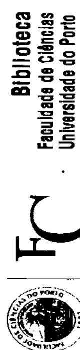

Biblioteca
Faculdade de Ciências
Universidade do Porto
D000109302

QC176.8.N35 VENj M 2006

MC

João Oliveira Ventura

Magnetic Nanostructures

Thesis submitted to the
Faculty of Sciences of the University of Porto
in partial fulfillment of the requirements
for the degree of
Doctor of Philosophy in Physics

Supervisor: Prof. João Bessa Sousa

Department of Physics
Faculty of Sciences of the University of Porto
February 2006

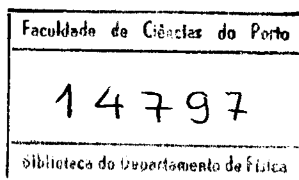
Faculdade de Ciências do Porto
14797
Biblioteca do Departamento de Física

M

Acknowledgments

First and foremost, I would like to thank Prof. João Bessa Sousa for these four wonderful years. Without his constant dedication and motivation this work could never have even been started. Without his knowledge it could not have been completed.

The friendship of fellow researchers at IFIMUP gave me four years to remember. Their help gave me a Ph.D. thesis. They are (in order of appearance) Francisco Carpinteiro, Filipe Correia, Dr. João Pedro Araujo, Jose Miguel Teixeira, Nelson Muga, Rui Silva, Andre Pereira and Rui Fermento.

To other members of IFIMUP, first Prof. Yuri Pogorelov for always being interested in the studies made and for the new ideas brought. The professionalism and constant dedication of Florbela and Isabel Alves.

A special thanks for Prof. Paulo Freitas, director of INESC-MN, for the ever-present collaboration, suggestions, share of knowledge and interest demonstrated in the work performed. To the members of INESC-MN that were so kind as to share part of their hard work with me: R. Ferreira, Dr. Z. Zhang, Dr. Y. Liu, Dr. Susana Freitas and Dr. M. Rickart. Also to Mr. Faustino for the wire bonding work.

I would also like to acknowledge IFIMUP and the Physics Department of the Faculty of Sciences of the University of Porto for the support they gave me. Finally I would like to thank Fundacao para a Ciencia e Tecnologia for their funding of my doctoral years (SFRH/BD/7028/2001) and of research projects and conference attendances.

A special word to those not named here. You know who you are.

Resumo

A recente possibilidade de depositar filmes finos com espessuras da ordem dos Å (10^{-10} m) permitiu o desenvolvimento dos chamados dispositivos nanoestruturados. A sua importância é já enorme, com um mercado potencial estimado nos milhares de milhões de dólares. O trabalho apresentado nesta tese foca dois destes novos dispositivos: Válvulas de spin, correntemente utilizadas em aplicações comerciais (como sensores em cabeças de leitura), e junções de efeito túnel, que são o alvo de uma intensa investigação na demanda de uma memória magnética universal.

Neste trabalho realizámos um estudo comparativo entre válvulas de spin convencionais e especulares (com camadas nano-oxidadas). Observámos que a Magnetoresistência Gigante aumenta consideravelmente com a introdução de camadas nano-oxidadas em válvulas de spin convencionais. A comparação entre as curvas de magnetoresistência [MR(H)] e magnetização [M(H)] de válvulas de spin especulares mostraram uma quebra na correlação habitual entre os dois processos, indicando que a difusão interfacial é extremamente importante neste tipo de estruturas. Inferimos também a existência de um óxido antiferromagnético (AFM) com uma temperatura de blocking $T_B \approx 175$ K, tendo então estudado a sua influência nas curvas de MR(H). Medidas de arrefecimento com campo magnético aplicado permitiram-nos demonstrar que as curvas de magnetoresistência dependiam fortemente do sinal e magnitude do campo de arrefecimento H_0. Esta dependência foi relacionada com o efeito de H_0 no ordenamento AFM das camadas nano-oxidadas. Medidas de arrefecimento com campo magnético aplicado até diferentes temperaturas permitiram-nos concluir a existência de uma larga distribuição de temperaturas de blocking nas camadas nano-oxidadas. Realizámos também medidas de efeito treino para estudar a estrutura de domínios das camadas AFM-nano-oxidadas.

Estudámos em detalhe o efeito de comutação de resistência induzida por uma corrente eléctrica (CIS) em junções de efeito túnel finas (barreira de 7 Å) e de baixa resistência. Este novo efeito foi atribuído a electromigração de iões metálicos em nanoconstrições na barreira isoladora. Seguimos então a evolução do efeito CIS entre dois (ou três) estados resistivos, induzidos por uma corrente eléctrica, com e sem campo magnético (H) aplicado. Esta evolução é controlada por rearranjos nano-estruturais nas interfaces entre os eléctrodos e a barreira e pela comutação magnética da camada fixa quando correntes suficientemente elevadas são aplicadas (para $H \neq 0$). Foi realizado um estudo sistemático na gama de temperaturas 300 – 25 K, tendo sido observado o decréscimo do efeito CIS com o decréscimo da temperatura. Estimámos então duas barreiras de energia para electromigração: Uma baixa (~ 0.13 eV) e uma alta (~ 0.85 eV), associadas com electromigração envolvendo diferentes tipos de sítios/defeitos. Se medirmos ciclos CIS sob um campo magnético aplicado, somos capazes de, com uma corrente eléctrica, modificar o sinal do campo de troca da junção de efeito túnel e o correspondente estado magnético (de antiparalelo para paralelo). Este efeito aparece devido a um excessivo aquecimento local na junção, e permitiu-nos obter um ciclo CIS com três estados resistivos diferentes.

Realizámos então estudos em diferentes séries de junções de efeito túnel com uma camada não-magnética (NM) de Ta depositada abaixo, acima, e abaixo-e-acima da barreira isolador. Em particular, estudámos a influência destas camadas no efeito CIS. Interessantemente, descobrimos que, em junções com uma camada NM depositada abaixo da barreira, a co-

mutação da resistência é induzida por uma corrente de sentido oposto ao de junções com uma camada FM (CoFe) depositada por baixo da barreira. Utilizámos então o modelo balístico de electromigração para demonstrar que a força directa domina a electromigração nas nossas camadas de Ta, enquanto a força "vento" é dominante nas camadas de CoFe. A diferença nos sentidos de comutação é então associada com o domínio de diferentes forças de electromigração (directa ou vento) nos diferentes tipos de junções estudados. Verificou-se que o efeito CIS depende fortemente da corrente máxima aplicada e da temperatura. A temperatura constante, o efeito CIS aumenta com o aumento da corrente máxima aplicada, ate ser atingido um *plateau* constante, relacionado com degradação da barreira. Estudámos também como tal degradação da barreira modifica a dependência térmica da resistência eléctrica. Observámos uma suave transição no processo de transporte eléctrico dominante, de efeito túnel para metálico e relacionámo-la com a formação e crescimento de *pinholes* na barreira. A evolução temporal da resistência eléctrica com diferentes correntes aplicadas foi também estudada, permitindo-nos verificar como se comporta dinamicamente o nosso sistema na fase de electromigração. A baixas temperaturas verificámos uma rápida variação quase contínua da resistência eléctrica com o tempo, passando contudo gradualmente para flutuações descontínuas denotando diferentes processos de electromigração. O aumento da temperatura conduziu a um sinal mais complexo, com muitos flutuadores activos.

Por último, estudámos as propriedades de transporte de junções de efeito túnel magnéticas sub-oxidadas. Mostrámos que o transporte neste sistema é controlado por nano-constrições e defeitos na barreira de AlO_x. De facto, ruptura dieléctrica nestas junções ocorre em regiões localizadas da barreira, provavelmente onde existe uma maior concentração de defeitos (vazios de oxygénio devido à sub-oxidação da barreira). Observámos também fluctuações da resistência eléctrica dependentes do spin, associadas com transporte através de defeitos localizados na barreira. Medidas da resistência eléctrica em função da temperatura em diferentes junções com tempos de oxidação extremamente reduzidos mostraram um conjunto diversificado de comportamentos: metálico ($dR/dT>0$), isolador ($dR/dT<0$) e uma mistura dos dois (metálico para o estado paralelo e isolador para o estado antiparalelo). A origem da elevada magnetoresistência observada em junções cujo transporte eléctrico é predominantemente metálico foi atribuida a transporte dependente do spin através de canais metálicos, provavelmente devido a magnetoresistência balistica.

Summary

The fabrication of smooth films with well controlled thicknesses as low as few Å (10^{-10} m) allowed the development of the so-called nanostructured devices. Their importance, especially in this new information age, is enormous, with an estimated potential market of billion of dollars per year. The work presented in this thesis focus two such devices: Spin valves, that are already used in commercial applications (like read head sensors), and tunnel junctions, that are being intensively researched in the quest for an almost universal memory, Magnetic Random Access Memory.

In our work we performed a comparative study between conventional and specular (with nano-oxide layers) spin valves. The Giant Magnetoresistive ratio was greatly enhanced by the introduction of the nano-oxide layers. A comparison between the magnetoresistance [MR(H)] and magnetization [M(H)] curves of the specular spin valve showed a break in the usual correlation between the two processes, indicating that interfacial scattering is extremely important in this type of nanostructures. We further inferred the existence of an antiferromagnetic (AFM) oxide in the nano-oxide layer, with a blocking temperature $T_B \approx 175$ K, and studied its influence on the MR(H) curves. Field cooling measurements allowed us to show that the shape of the MR(H) curves depend strongly on the sign and value of the cooling field H_0. We related these features to the effects of H_0 on the AFM ordering of the nano-oxide layers (NOLs) below its blocking temperature. Furthermore, field cooling measurements with different cooling temperatures showed the existence of a broad distribution of blocking temperatures in the nano-oxide layer. Training-effect experiments enabled us to study the domain structure of the AFM-NOL and its importance on the residual magnetoresistance observed in the MR(H) curves at large positive fields.

We also studied the Current Induced Resistance Switching (CIS) effect on thin, low resistance (7 Å barrier) CoFe/AlO_x/CoFe tunnel junctions. This new effect was attributed to electromigration (EM) of metallic ions in nanoconstricted regions of the insulating barrier. We traced the evolution of resistance switching in consecutive CIS cycles between two (or three) states, driven by an electrical current, both under zero and applied magnetic field (H). Such evolution is controlled by the nanostructural rearrangements of ions at the electrodes/barrier interfaces (electromigration) and also by magnetic switching in the pinned layer under sufficiently high current pulses (under $H \neq 0$). Current induced resistance switching was observed over the $300 - 25$ K temperature range, decreasing with decreasing temperature. Low (~ 0.13 eV) and high (~ 0.85 eV) electromigration-energy barriers were estimated and associated with EM involving different types of ions sites/defects. If CIS cycles are measured under an external magnetic field, one is able to current-induce a change in the sign of the exchange bias of the tunnel junction, and in the corresponding magnetic state (antiparallel to parallel). This effect arises from excessive local heating in the tunnel junction, and enables us to obtain a CIS cycle with three different electrical resistance states.

We also performed a study on different series of tunnel junctions with a Ta non-magnetic (NM) layer deposited below, above and below-and-above the insulating barrier, investigating the influence of such layers in the Current Induced Switching effect. Interestingly, we found that tunnel junctions with a NM layer deposited below the barrier have opposite R-switching current direction when compared to that of TJs without such NM layer inserted below the barrier. We then used the ballistic model of electromigration to show that the direct force

dominates electromigration in our Ta layers, while the wind contribution is dominant in our FM (CoFe) layers. The different switching directions are then associated with the dominance of different EM forces (direct or wind) in the two types of tunnel junctions. The Current Induced Switching effect was found to be strongly dependent on both maximum applied current ($I_{\max}$) and temperature (T). At constant temperature, the CIS effect increases with increasing $I_{\max}$, until a plateau of constant CIS is observed, related to barrier degradation. On the other hand, the CIS effect decreases with decreasing temperature. We also studied how increasing barrier degradation (irreversible resistance decrease) changed the TJ-$R(T)$ behavior, and we observed a smooth transition from tunnel- to metallic-dominated transport, related to the formation and subsequent increase of pinhole size. A study of the time evolution of the electrical resistance under both low and high electrical currents allowed us to probe the dynamics of our system as electromigration proceeds. At low temperatures we found a fast quasi-continuous R-trend in the early stages of EM. However, as time increases, this trend gradually disappears and the resistance varies by discontinuous steps denoting different EM-processes. The increase of temperature leads to more complex R(t) signals, with many active fluctuators.

Finally, we studied the transport properties of underoxidized magnetic tunnel junctions. We showed that transport in this system is controlled by nanoconstrictions and defects within the AlO_x barrier. In fact, dielectric breakdown in the studied MTJs occurred at different, localized spots of the barrier, likely where a large concentration of defects (oxygen vacancies due to the underoxidation of the barrier) exists. We observed spin dependent resistance fluctuations between two closely separated levels, associated with transport through localized defects in the barrier. Measurements of the electrical resistance as a function of temperature on MTJs with extremely small oxidation times allowed us to observe a wealth of behaviors: Metallic-like ($dR/dT>0$), insulating-like ($dR/dT<0$) and a mixture of the two (metallic for the parallel and insulating for the antiparallel state). The origin of the large MR values obtained even when metallic dominated transport is observed will be attributed to the existence of a metallic spin dependent transport channel, likely associated with ballistic magnetoresistance.

Resumé

La fabrication bien contrôlée de couches minces de matériaux divers, avec des épaisseurs si petites que Å (10^{-10} m), ont permit le développement de dispositifs nano-structurés. Leur importance, particulièrement dans ce nouvel âge de l'information, est énorme, avec un marché potentiel de milliards de dollars par an. Le travail présenté dans ce rapport de thèse de doctorat étudie deux de ces dispositifs : Les valves de spin, couramment employées dans des applications commerciales, comme des sondes de tête de lecture, et des jonctions de tunnel, lesquelles sont intensivement recherchées pour les mémoires magnétiques universelles.

Dans notre travail nous avons réalisé une étude comparatif entre les valves de spin conventionnelles et spéculaires (avec des couches nano-oxydées). Le rapport magnétorésistant géant a été considérablement augmenté par l'introduction des couches nano-oxydées. Une comparaison entre les courbes de magnétorésistance [MR(H)] et de la magnétisation [M(H)] de la valve spéculaire de spin a montré une coupure dans la corrélation habituelle entre les deux processus, indiquant que la diffusion interfaciale est extrêmement importante dans ce type de nanostructures. Nous avons plus loin impliqué l'existence d'un oxyde antiferromagnetic (AFM) dans la couche nano-oxydée, avec une température de blocage $T_B \approx 175$ K, et avons étudié son influence sur les courbes de MR(H). Les mesures de refroidissement sous champ magnétique nous ont permis de prouver que la forme des courbes de MR(H) dépendent fortement du signal et de la valeur du champ de refroidissement H_0. En autre, les mesures de refroidissement dans champ avec différentes températures de refroidissement ont montré l'existence d'une large distribution des températures de blocage dans les couches nano-oxydées. On a aussi effectué plusieurs expériences de façon à d'étudier la structure de domaine de l'AFM et de son importance sur la magnétorésistance résiduelle observée dans les courbes de MR(H) à grands champs positifs.

Nous avons également étudié l'effet commutation de résistance induit par courant (CIS) sur les jonctions de tunnel minces (barrière de 7 Å) de CoFe/AlO$_x$/CoFe de basse résistance. Ce nouvel effet a été attribué à l'électromigration (EM) des ions métalliques dans les nano-constrictions dedans des régions de la barrière isolante. Nous avons étudie l'évolution de la commutation de résistance dans les cycles CIS consécutifs entre deux (ou trois) états, conduits par un courant électrique, en-dessous de zéro et champ magnétique appliqué (H). Une telle évolution est commandée par les remises en ordre nano structural des ions aux interfaces d'électrodes/barrière (électromigration) et également par la commutation magnétique dans la couche goupillée sous des courantes suffisamment élevées (dans $H \neq 0$). On a observé qui la CIS dans un large intervalle de température 300 – 25 K, diminue avec la décente de température. Bas (~ 0.13 eV) et élevées (~ 0.85 eV) barrières d'électromigration ont été estimées et associées à la EM relié à différents types d'ions sites/défets. Si des cycles CIS sont mesurés sous un champ magnétique externe, on peut induire un changement dans le signe de la polarisation d'échange de la jonction de tunnel, et de l'état magnétique correspondant (antiparallèle au parallèle). Cet effet résulte du chauffage local excessif dans la jonction de tunnel, et nous permet d'obtenir un cycle CIS avec trois états électriques différents de résistance.

Nous avons également réalisé une étude sur une série différente de jonctions de tunnel avec une couche non magnétique de Ta (NM) déposée au-dessous, au-dessus et au-dessous-et-au-dessus de la barrière isolante, étudiant l'influence de telles couches dans l'effet CIS. En plus,

c'est intéressant de noter que nous avons constaté que les jonctions de tunnel avec une couche de NM déposée au-dessous de la barrière ont une direction de courante de commutation de la résistance opposé de courante de R-commutation sans la couche NM insérée au-dessous de la barrière. Nous avons utilise le modèle balistique de l'électromigration pour prouver que la force directe domine l'électromigration dans nos couches de Ta, alors que la contribution de vent est dominante dans nos couches avec des électrodes FM (CoFe). Les différentes directions de commutation sont alors associées à la dominance de différentes forces de EM (directe ou de vent) dans les deux types de jonctions de tunnel. L'effet CIS s'est avéré fortement dépendant du courant maximum appliqué (I_{max}) et de la température (T). À température constante, l'effet CIS augmente avec l'augmentation de I_{max}, jusqu'à ce qu'on observe un plateau de CIS constant, lié à la dégradation de barrière. D'autre part, l'effet CIS diminue avec température décroissante. Nous avons également étudié comment la dégradation croissante de la barrière (diminution irréversible de résistance) a changé le comportement $R(T)$, et nous avons observé une transition de transport tunnel pour transport métallique, lié à la formation et à l'augmentation suivante de pinholes. Une étude de l'évolution en temps de la résistance électrique sous de bas et élevés courants électriques nous a permis de sonder la dynamique de notre système pendant que l'électromigration procède. À basses températures nous avons trouvé un comportement rapide de la résistance aux premières parties de EM. Cependant, à mesure que le temps augmente, cette tendance disparaît graduellement et la résistance change par des étapes discontinues dénotant différentes EM-processus. L'augmentation de la température mène à des signaux plus complexes de R(t), avec beaucoup de fluctuations.

Nous avons étudié les propriétés de transport des jonctions magnétiques de tunnel non complètement oxydé. Nous avons prouvé que le transport dans ce système est commandé par des nanoconstrictions et des défauts dans la barrière d'AlO_x. Enfaîte, la panne diélectrique dans les MTJs étudié s'est produite à différentes, endroits de la barrière, probablement où une grande concentration des défauts (vacances de l'oxygène dues à la sous-desoxidation de la barrière) existe. Nous avons observé des fluctuations de résistance dépendantes de spin entre deux niveaux, liées au transport par des défauts localisés dans la barrière. Les mesures de la résistance électrique en fonction de la température sur les MTJs avec l'oxydation extrêmement petite, nous ont permis d'observer une richesse des comportements : Métallique (dR/dT>0), isolant (dR/dT<0) et un mélange des deux (métallique pour l'état parallèle et isolant pour l'état antiparallel). L'origine de la grande valeur de MR obtenu même lorsqu'on observe le transport métallique est attribué à l'existence d'un canal de transport métallique dépendant de spin, probablement liée à la magnétorésistance balistique.

Contents

List of Tables **19**

List of Figures **30**

1 Introduction **33**

1.1 Magnetoresistance . . . 34

1.2 Exchange and coupling fields . . . 35

1.2.1 Exchange field . . . 35

1.2.2 Interlayer coupling field . . . 37

1.3 Applications . . . 40

1.3.1 MRAMs . . . 40

1.3.2 Read head sensors . . . 42

1.3.3 Other applications . . . 43

1.4 This thesis . . . 44

2 Experimental techniques **47**

2.1 Deposition and fabrication of nanostructures . . . 47

2.1.1 Physical Vapor Deposition . . . 47

2.1.2 Ion Beam Deposition . . . 49

2.1.3 Tunnel junction barrier oxidation . . . 50

2.1.4 Tunnel junction fabrication . . . 51

2.1.4.1 Lithography and lift-off . . . 51

2.1.4.2 Fabrication process . . . 52

2.2 Experimental characterization . . . 54

2.2.1 The cryogenic system . . . 54
2.2.2 Transport measurements . . . 56
2.2.2.1 Electrical resistance and magnetoresistance . . . 56
2.2.2.2 Current Induced Switching . . . 58
2.2.2.3 Data acquisition . . . 60
2.2.3 Magnetic characterization . . . 63
2.2.3.1 SQUID magnetometer . . . 63
2.2.3.2 Magneto-Optical Kerr Effect . . . 63

3 Giant Magnetoresistance **65**
3.1 Introduction . . . 65
3.2 Boltzmann semiclassical transport equation . . . 66
3.2.1 The case of thin films . . . 67
3.2.2 The outer surfaces . . . 69
3.3 Semiclassical models of GMR . . . 69
3.3.1 The Model of Camley and Barnas . . . 69
3.3.2 The model of Hood and Falicov . . . 70
3.3.3 Temperature dependence of GMR . . . 71
3.4 Quantum mechanical models . . . 71
3.5 Advanced spin valve structures . . . 72
3.5.1 Specular spin valves . . . 72
3.5.2 Synthetic antiferromagnetic and spin filter spin valves . . . 73

4 Specular spin valves **75**
4.1 Experimental details . . . 76
4.2 Comparative study of NOL SV and CSV . . . 77
4.2.1 Room temperature Magnetoresistance . . . 77
4.2.2 Temperature dependent results . . . 78
4.2.2.1 Magnetoresistance . . . 78
4.2.2.2 Temperature dependence of H_{exch} and H_c . . . 80

4.2.2.3 Magnetization versus Magnetoresistance 81
4.3 Impact of the magnetism of NOL on the GMR 83
4.3.1 Field cooling experiments 83
4.3.2 Distribution of NOL-blocking temperatures 85
4.4 The training effect 88
4.5 Influence of FM_b and FM_a on the MR(H) behavior 94
4.6 Discussion 96
4.7 Conclusions 98

5 Tunnel Magnetoresistance **101**

5.1 Introduction 101
5.2 Spin polarization 102
5.3 TMR models 104
5.3.1 Tunnel Hamiltonian model 104
5.3.2 Free electron model 105
5.3.3 Tight binding model 110
5.4 TMR bias dependence 110
5.5 TMR temperature dependence 113
5.5.1 Spin-polarization temperature dependence 114
5.5.2 Hopping conductance 115
5.5.3 Magnon-assisted tunneling 115
5.5.4 Phonon-assisted tunneling 117
5.5.5 Pinholes 117
5.5.6 Concluding remarks 120
5.6 Dielectric breakdown 121
5.6.1 Intrinsic and extrinsic breakdown 121
5.6.2 Microscopic models 122
5.6.2.1 The E-model 122
5.6.2.2 The $1/E$-model 123
5.7 Current Induced Magnetization Switching 124

5.8 Current Induced Resistance Switching 127
5.8.1 Atomic diffusion 127
5.8.2 Electromigration 130
5.8.2.1 The ballistic model 131
5.8.2.2 Other models 132
5.8.2.3 Electromigration in nanoconstrictions 132

6 CIS in Magnetic Tunnel Junctions 135
6.1 Experimental details 137
6.2 Experimental results 138
6.2.1 Current Induced Switching 138
6.2.2 Temperature dependent measurements 140
6.2.2.1 Electrical Resistance 140
6.2.2.2 CIS effect 140
6.2.3 Time dependent effects 144
6.2.4 Magnetic field effects 146
6.3 Discussion 148
6.3.1 Tunneling versus pinhole conductance 148
6.3.2 CIS behavior under zero magnetic field 149
6.3.3 CIS(H) cycles and current written multi R-states 155
6.3.3.1 Four state resistance 159
6.4 Heating in tunnel junctions 159
6.4.1 Steady-state regime 161
6.4.2 Dynamic regime 162
6.5 Conclusions 162

7 CIS in non-Magnetic Tunnel Junctions 165
7.1 Experimental details 166
7.2 TJs with non-magnetic *pinned* layer (series 834) 167
7.2.1 Room temperature results 168

7.2.1.1 Current Induced Switching 168
7.2.1.2 Discussion 170
7.2.2 Temperature dependent results 175
7.2.2.1 Electrical resistance 175
7.2.2.2 CIS effect 175
7.2.3 Direct ($+I_{\max}$, $-I_{\max}$) Current Induced Switching 182
7.3 TJs with two non-magnetic electrodes (series 835) 183
7.3.1 Current Induced Switching 184
7.3.2 Influence of EM-induced barrier state on the R(T) behavior 184
7.3.2.1 R_B and R_b temperature dependence 184
7.3.2.2 Evolution of R(T) with barrier degradation 186
7.3.2.3 Discussion and conclusions 187
7.3.3 Probing individual EM-driven atomic motion events 190
7.3.3.1 Introduction 190
7.3.3.2 Experimental details 190
7.3.3.3 Experimental results 191
7.4 TJs with non-magnetic *free* layer (series T1) 197
7.4.1 Electrical resistance 197
7.4.2 Current Induced Switching 197
7.4.3 Time dependent effects 199
7.4.4 Discussion 200
7.5 Conclusions 201

8 Underoxidized MTJs **203**
8.1 Experimental details 205
8.2 Experimental results 206
8.2.1 Dielectric Breakdown 206
8.2.2 Spin dependent resistance fluctuations 211
8.2.2.1 Electron trapping and 1/f noise 213
8.2.3 Temperature dependent measurements 214

8.2.3.1 Impact of barrier and constriction parameters on MTJ-electrical resistance and corresponding temperature dependence 216

8.2.3.2 Magnetoresistance origin 218

8.3 Conclusions 219

9 Conclusions and Outlook **221**

Bibliography **227**

List of Tables

1.1 Comparison between different memory technologies. 42

4.1 Conventional and specular spin valves studied in this work. The numbers in subscript are the layer thicknesses in Å. 77

4.2 Transport characteristics of the spin valves studied in this work. Electrical resistivity ρ and $\Delta\rho = \rho_{AP} - \rho_P$ are given in $\mu\Omega$cm. 98

7.1 Tunnel junction series with non-magnetic electrodes studied in this chapter. . 167

7.2 Electrical resistivity, electron transport cross section for scattering and Fermi velocity used to estimate $Z_w(Ta)/Z_w(CoFe)$. 171

7.3 Comparison of relevant CIS-parameters obtained for FM/I/FM (chapter 6) and FM/I/NM (series T1) tunnel junctions. 201

8.1 Series of magnetic tunnel junction studied during this work. Here, SyAFM is a $CoFeB_{40}/Ru_6/CoFeB_{40}$ synthetic antiferromagnetic structure. The numbers in subscript are the layer thickness in Å. 206

8.2 Transport characteristics of the measured tunnel junctions of series TJ1135. . 216

List of Figures

1.1 Exchange bias. Upon cooling under an external magnetic field an exchange interaction is impressed at the FM/AFM interface. The resulting $M(H)$ cycle is shifted away from $H = 0$. In the figure we present the MOKE $M(H)$ cycle of a MnPt(150 Å)/CoFe(50 Å) structure showing $H_{\text{exch}} = 340$ Oe at room temperature. 36

1.2 Magnetization reversal of the free layer of a spin valve under small applied magnetic fields obtained by the MOKE technique. Notice the small shift from zero magnetic field due to the interlayer coupling ($H_{\text{coup}} = 15$ Oe). 38

1.3 a) Correlated interface roughness that causes Néel coupling. b) Simulated Néel and RKYY interlayer coupling as a function of spacer thickness, using $h = 0.04$ Å, $\lambda = 100$ Å, $M_{pl} = M_{fl} = 1$ T, $J_0 = 0.01$ mJ/m^2, $\Lambda = 10$ Å and $\varphi = 1.4\pi$ (see text for discussion). 38

1.4 Single MRAM cell constituted by a magnetic tunnel junction, a transistor and two current carrying lines. (a) Cell sensing scheme: The transistor is in the "on" state so that an electrical current can flow through the MTJ. (b) Cell writing scheme: The transistor is in the "off" state and electrical currents flow through the digit and bit lines, generating a magnetic field large enough to reverse the magnetization of the free layer of the TJ. 41

1.5 MRAM cross point architecture. Each memory cell is in the intersection of a bit and a digit line. An electrical current is sent through one digit and one bit line and, ideally, only the MTJ in their intersection is written. 41

1.6 Read and write head architecture. When a current flows through the coils of the write head, a magnetic field is generated and penetrates into the magnetic media, switching the state of a bit. The MR sensor is then used to detect magnetic flux "escaping" from transition regions between two oppositely magnetized bits. 43

1.7 Detection of: (a) High electrical currents, (b) linear position for robotic control, (c) strain and (d) magnetically tagged biological specimens using magnetoresistive sensors. In the last case, the biomolecule to be detected (target) is immobilized on a magnetic label and passed over probe molecules immobilized over magnetoresistive sensors. 44

2.1 Magnetron sputtering deposition technique. Accelerated Argon (or Xenon) ions bombard the target, whose surface atoms are progressively ejected (sputtered) and deposited on the substrate in front, originating film growth. 48

2.2 Geometry of the Nordiko 3000 Ion Beam Deposition machine installed at INESC-MN. 50

2.3 Schematic of etching process. The material deposited (a) is covered with photoresist which is then partially exposed to a laser light. After removing the exposed areas of the photoresist (b), the unprotected areas of the film are etched away (c) leaving a pattern sample (d). 51

2.4 Schematic of lift-off process. The photoresist (a) is exposed to the laser light and the exposed areas removed (b). A material is then deposited (c) and, after lift-off of the photoresist by a chemical process, the layer is patterned (d). . . 52

2.5 Definition of the bottom electrode area by an etching process. 52

2.6 Junction area definition. A small area of the bottom lead is protected by photoresist. The etching must be stopped before all the bottom electrode is removed. 53

2.7 A SiO_2 layer is deposited to prevent electrical contact between the bottom and top leads (left). The photoresist left during junction area definition is now used to open the top electrode via (right). 53

2.8 Definition and metallization of the top lead and pads and metallization of the bottom pads. Top view of the patterned tunnel junction. 54

2.9 Scheme of a close cycle 10 K cryostat. 55

2.10 Experimental setup available at IFIMUP to measure R(T,H) and MR(H,T) in the 300–4 K and 0–1 T ranges. 57

2.11 Experimental setup for measurements of the electrical transport properties of tunnel junctions. Magnetic field current supply, Hall probe and temperature measurement voltmeter are not included in the scheme. 58

2.12 Tunnel junctions wire bonded to the gold pads of a chip carrier. 59

2.13 Chip carrier placed in a cryostat. Four copper wires are attached to the chip carrier, for current to flow through the tunnel junction and to measure the corresponding voltage drop. 59

2.14 Current Induced Switching on a MnIr (90 Å)/CoFe (80 Å)/AlO_x (7 Å)/CoFe (30 Å)/NiFe (40 Å) sample. (a) Applied electrical current versus time. (b) Remnant resistance (R_m=V/I_m) as a function of time. (c) Remnant resistance (R_m) as a function of the previously applied current pulse I_p; S and F are the start and finish of the CIS experiment. In this example, $\Delta t_m = 3\Delta t_p$. 60

2.15 The Main Form of the data acquisition program. The user can choose between several options, including different experimental measurements, device and file configurations. 61

2.16 The MR(H) Form of the data acquisition program. One can change, among others, the maximum and minimum applied magnetic fields, the applied current and measuring temperature. Experimental data points are displayed in the graph. 62

3.1 Simple two-current model of electron scattering in spin valves for (a) parallel and (b) antiparallel magnetic configurations. 66

3.2 Schematic drawing of a thin film with dimensions $l \times w \times d$, with $(d \ll l, w)$. . 68

3.3 Structure of (a) specular spin valve with two nano oxide layers inserted in the pinned and free layers, (b) synthetic antiferromagnet spin valve and (c) spin filter spin valve. 73

4.1 Magnetoresistance curves obtained at room temperature for (a) conventional and (b) specular spin valves. Notice the enhanced GMR ratio of the NOL SV. 77

4.2 MR(H) curves for the (a) non-specular and (b) specular spin valves at selected temperatures. (c) Temperature dependence of the GMR ratio for the non-specular (hollow triangles) and specular (solid circles) spin valves. Notice that the extrapolation of the MR(T) data to $T > 300$ K gives zero MR at a common $T_C \approx 675$ K. 79

4.3 Temperature dependence of exchange H_{exch} and pinned layer coercive H_c fields of the conventional and specular spin valves. Notice the enhancement of both fields below ~ 175 K for the NOL SV. 81

4.4 Comparative plots of the MR(H) (lines) and M(H) (circles) of the non-specular (left side) and specular (right side) spin valves at three different temperatures. Notice that the M(H) curves display three M-reversal that we associate with the CoFe free, deep NiFe and CoFe pinned layers. 82

4.5 MR(H) curves measured at 15 K for different values of the cooling field H_0 and corresponding dependence of the GMR ratio and exchange field (inset). . 83

4.6 Total exchange field; MnIr and NOL exchange-contributions and GMR (inset) temperature dependencies (lines are guides to the eyes only). 85

4.7 Magnetoresistance and exchange field (inset) obtained at $T = 15$ K after field cooling down to a temperature T_{cool} under different cooling fields H_0. 86

4.8 MR(H) curves measured at $T = 15$ K for different cooling temperatures T_{cool}, under (a) $H_0 = 3000$ Oe and (b) $H_0 = -500$ Oe. 88

4.9 Three MR(H) curves of the specular spin valve measured consecutively (at $T = 15$ K; after FC under $H_0 = +7000$ Oe) and displaying the so called training effect. Upper inset: Enlarged $H \gg 0$ region showing consecutive MR(H) cycles with enhanced electrical resistance and thus poorer $\rightrightarrows$ parallelism. Lower inset: GMR ratio and exchange field dependence on the number of cycles performed. 90

4.10 Experimental exchange field (open circles) as a function of MR(H) cycle number (measured at $T = 15$ K after ZFC) and fits to the different models presented in the text [Eqs. (4.4) (for $n > 1$; blue circles) and (4.5) (red crosses)]. Inset shows the region $1 \leqslant n \leqslant 7$ and also a fit to Eq. (4.4) for $n \geqslant 1$ (green circles). 90

4.11 Dependence of (a) GMR ratio and (b) H_{exch} on the number of MR(H) cycles performed ($n \leq 5$) for several cooling fields. MR(H) cycles obtained at $T = 15$ K after field cooling from 320 K under (c) $H_0 = -500$ Oe and (d) $H_0 = 7000$ Oe. 91

4.12 Dependence of (a) GMR ratio and (b) H_{exch} on the number of MR(H) cycles performed for several temperatures and corresponding training effect [(c) and (d)]. MR(H) measurements were performed after field cooling under $H_0 = 3000$ Oe from 320 K. Inset displays the MR(T) dependence for different number of cycles. 92

4.13 Dependence of (a) GMR ratio and (b) H_{exch} on the number of MR(H) cycles performed for several cooling temperatures and corresponding training effect [(c) and (d)]. MR(H) measurements were performed after field cooling under $H_0 = 3000$ Oe (solid symbols) and $H_0 = -500$ Oe (open symbols) from 320 K. 93

4.14 Schematic representation of a specular spin valve and magnetic interactions between the FM layers (J_{exch} between the AFM and pinned layer, J_{NOL1} between the FM_b and FM_a pinned layer and J_{NM} between the pinned and free layers). 94

4.15 Model simulations of MR(H) curves using different J_{exch}/J_{NOL1} ratios. 95

4.16 Magnetoresistance of NOL SV at low (25 K) and high (300 K) temperature. . 97

5.1 Modeled contributions of s- and d-states to the tunnel current (a) and corresponding spin-polarization (b). Parameters used: $\lambda_d^{-1} = 0.5$ Å, $\lambda_s^{-1} = 0.68$ Å, $i_{d,0} = 0.9$, $i_{s,0} = 0.1$, $P_d = -1$ and $P_s = 0.44$. 103

5.2 Tunnel conductance in a FM/I/FM tunnel junction in the parallel (left) and antiparallel (right) states. 105

5.3 The potential energy eV(z) of a tunnel junction with two non-magnetic electrodes under a bias voltage V_{bias}. 106

5.4 Energy diagram of a ferromagnetic tunnel junction. 109

5.5 (a) Square barrier of height φ, defined as the energy difference between the Fermi level of the FM material and the minimum of the conduction band of the insulator. (b) When a voltage is applied across the barrier, the Fermi levels of the two electrodes become unequal and a current starts to flow. (c) Asymmetric tunnel junction with a barrier asymmetry $\Delta\varphi = \varphi_R - \varphi_L$. 111

5.6 Tunnel current versus applied voltage, calculated using Simmons' model [Eq. (5.30)], (a) for constant barrier thickness and (b) for constant barrier height. 112

5.7 Temperature dependence of tunnel conductance due to Fermi broadening. . . 114

5.8 Sharvin resistance as a function of nanoconstriction radius a for several ρl products. In the inset the resistance is displayed in a logarithmic scale for small constrictions. Notice however, that the Sharvin resistance holds only for a radius larger than an electron wavelength. 118

5.9 $R \times A$ and TMR as a function of pinhole area x. In this case: $A = 0.28$ μm^2, $R \times A_{\text{tunnel}} = 12.7$ $\Omega\mu$m^2, $R \times A_{\text{pinhole}} = 0.8$ $\Omega\mu$m^2 and $TMR_{\text{tunnel}} = 25\%$. . 119

5.10 Temperature dependence of parallel G_P and antiparallel G_{AP} conductance of a magnetic tunnel junction and corresponding difference ΔG. Obtained from magnon- and phonon-assisted tunneling [Equations (5.45), (5.46), (5.49) and (5.50); left graph] and from the P(T) behavior and hopping conductance [Eqs. (5.38) and (5.39); right graph]. 120

5.11 (a) Intrinsic breakdown of a tunnel junction with a well formed oxide barrier. (b) Extrinsic breakdown related with defects/pinholes in the barrier of a magnetic tunnel junction. Notice the different resistance variation associated with the two mechanisms: Abrupt for intrinsic, gradual for extrinsic breakdown (see arrows). 122

5.12 Angular momentum transfer. Electrons flow from the right to the left. A torque is exerted in the magnetization of the left FM layer, trying to align it parallel with that of the right layer. 125

5.13 Angular momentum transfer. Electrons flow from the left to the right. A torque is exerted in the magnetization of the left FM layer, trying to align it antiparallel with that of the right layer. 126

5.14 (a) Diffusion of an atom in the periodic potential created by the lattice. Notice that the energy barrier for diffusion E_b is isotropic. (b) Diffusion of an atom in the presence of an applied force. Notice the different energy barriers for diffusion and jump frequency to the right (E_b^+, Γ^+) and to the left (E_b^-, Γ^-) . 128

6.1 (a) Tunnel Magnetoresistance curve and (b) I(V) characteristic of the studied MnIr (90 Å)/CoFe (80 Å)/AlO$_x$ (3 Å+ 4 Å)/CoFe (30 Å)/NiFe (40 Å) tunnel junction. 138

6.2 Current Induced Switching cycles performed at room temperature in sample A. Resistance switching near $\pm I_{\text{max}}$ is attributed to electromigration of ions from the electrodes into the barrier and back. For $I_{\text{max}} = 46$ mA, we obtained $CIS = 6.9\%$ in the first cycle. Notice the existence of some R-increasing steps during resistance switching to the lower state under negative currents, which can be due to interfacial rearrangements of migrated ions between consecutive current pulses or to the competition between electromigration at the two FM/I interfaces. 139

6.3 Temperature dependence of the electrical resistance of the studied CoFe/AlO$_x$ (7 Å)/CoFe/NiFe TJ (sample A), showing $dR/dT < 0$. This indicates electron tunnelling as the dominant transport mechanism. 141

6.4 Selected CIS cycles performed at constant temperatures in the 280 – 25 K range (sample A). 142

6.5 (a) Temperature dependence of the electrical resistance R(T) measured after performing CIS cycles between RT and $T = 25$ K, in the A-sample. (b) Selected (non-consecutive) CIS cycles obtained at room temperature after electrical transport across the TJ (sample A) is dominated by pinholes. 143

6.6 (a) Half CIS cycle (A–B) and subsequent relaxation processes (B–C–D). (b) Time evolution of the electrical resistance (B–C–D branch). (c) Slow relaxation processes after subtracting $R(\infty) + \Delta R_2 e^{-t/\tau_2}$. Fitting to Equation (6.4) gives $\tau_1 \approx 11.7$ min and $\tau_2 \approx 174$ min. 145

6.7 Complete CIS cycle and subsequent relaxation effects. Using Equation (6.4), one obtains $\tau_1 \approx 2.5$ min and $\tau_2 \approx 125$ min. 146

6.8 Consecutive MR(H) and CIS(I_{p}) cycles performed under an external magnetic field. The thicker (thinner) arrows refer to the magnetization of the pinned (free) layer. 147

6.9 Temperature dependence of the conductance of sample A (hollow circles; 300 – 25 K) and corresponding fit using Eq. (6.5) (line). 149

6.10 (a) Current Induced Switching cycle performed at room temperature in sample A. (b) Electromigration-driven barrier thickness decrease (t→t'), due to the use of a sufficiently high electrical current density across a thin TJ. 150

6.11 Asymmetric CIS R-switching. If a CIS cycle is started with increasingly positive current pulses, no R-switching occurs (full circles). When the tunnel junction is in the low R-branch, only positive current pulses lead to R-recovery (hollow circles). 151

6.12 Current Induced Switching half cycle of (a) sample A and (b) sample B. (c) Time dependent measurements of the electrical resistance of a tunnel junction (sample D) after negative current pulses have been applied. The fit to Eq. (6.4) reveals the existence of two relaxation times, $\tau_1 = 35$ min and $\tau_2 = 770$ min, both associated with *increasing* R. 153

6.13 Quasi-linear temperature dependence of the critical switching current. 154

6.14 Temperature dependence of the resistance increase observed after switching (ΔR_p; left scale) and of the dR/dI_p slope near zero current pulse in the low-R branch (scale on the right); both processes are attributed to relaxation phenomena. 156

6.15 Exchange bias reversal when CIS cycles are performed under an external magnetic field. (1) The TJ is in its antiparallel state due to the applied negative magnetic field. (2) High current densities lead to intense heating above the blocking temperature of the AFM layer. The pinned layer magnetization then reverses and the TJ is in its parallel state. Electromigration of ions from the bottom electrode into the barrier further reduces the electrical resistance of the TJ below R_P. (3) Under lower current densities the TJ is cooled below T_B and a new exchange bias direction is impressed in the AFM layer. (4) High temperatures above T_B again occur, but leading to no magnetic-state changes, since the TJ is already aligned with the applied magnetic field. Electromigration of ions from the barrier into the bottom electrode increases R. (5) When I_p is again reduced, the exchange bias direction is "permanently" impressed, opposite to the initial one. 158

6.16 Envisaged four resistance states in thin tunnel junctions using both CIS and MR effects; R_B (R_b) stand for thick (thin) barrier and R_P (R_{AP}) for parallel (antiparallel) magnetic states. 160

6.17 Simulation of heating processes inside the studied tunnel junctions, under different electrical current densities (1 MA= 10^6 A). Inset: Temperature increase as a function of current density passing through the junction. The results shown in the figure (inset) were obtained disregarding (taking into consideration) the top and bottom leads. 161

6.18 (a) Simulation of dynamical heating processes for j = 112.5 MA/cm^2. (b) Cooling under zero applied current. Inset: Maximum temperature inside the tunnel junction as a function of time during heating and cooling. All simulations were performed disregarding the top and bottom leads. 162

7.1 (a) Current Induced Switching cycle for $I_{\text{max}} = 30$ mA and (b) corresponding V(I_{p}) characteristic (hollow circles). The dashed line is a V(I) characteristic calculated using Simmons' model ($\varphi = 1$ eV; $t = 9$ Å). 168

7.2 Selected CIS cycles performed with I_{max} up to 80 mA. Notice the enhanced R-switching occurring under increasing I_{max}. 170

7.3 (a) Current Induced Switching coefficient and δ-shift as a function of maximum applied current. The CIS coefficient is enhanced with I_{max} but large negative δ-shift values occur for $I_{\text{max}} > 60$ mA, indicating progressive barrier degradation. (b) Maximum applied current pulse dependence of characteristic tunnel junction resistances in a CIS cycle. 171

7.4 Different resistance switching directions in a CIS experiment for tunnel junctions with (a) AFM/FM/NM/I/FM (MnIr/CoFe/Ta/AlO$_x$/CoFe/NiFe) and (b) AFM/FM/I/FM (MnIr/CoFe/AlO$_x$/CoFe/NiFe; see also chapter 6). . . . 172

7.5 CIS cycle and corresponding V(I_{p}) characteristic for $I_{\text{max}} = 80$ mA. Notice the decrease of $|V|$ near $\pm I_{\text{max}}$. The dashed line depicts a V(I) curve calculated using Simmons' model. 172

7.6 Schematic electromigration of Ta ions into and out of the insulating AlO_x barrier. Notice that some Ta ions may remain in the barrier when the electrical current is reversed. 173

7.7 Dependence of the barrier thickness decrease (δt) on the maximum applied current pulse, as obtained from the CIS(I_{max}) curve (Fig. 7.3) and Eq. (7.5) (for $\varphi = 1$ eV). Inset: Energy barrier for migration from Ta into the barrier (E_b^+) and vice-versa (E_b^-), in the first (left) and last (right) CIS cycles. 174

7.8 (a) Half and (b) complete CIS cycles performed at $T = 300$ K, and subsequent R(t) measurements. (c) Enlarged view of R(t) measurements performed after a complete CIS cycle. 176

7.9 Experimental temperature dependence of the electrical resistance and corresponding fit (red line; series 834). 177

7.10 CIS cycles performed at (a) $T = 200$ K and (b) $T = 25$ K. 178

7.11 CIS coefficient as a function of I_{max} over the 300–25 K temperature range for two different samples of the same series (a) and (b). 179

7.12 (a) R_{initial}, R_{half} and R_{final} as a function of I_{max} over the 300–25 K temperature range and (b) CIS coefficient as a function of temperature (300–25 K) for the 30–80 mA I_{max} range. 179

7.13 CIS coefficient and δ-shift as a function of I_{max} (first and second set of measurements) at $T = 300$ K and 250 K. 181

7.14 CIS coefficient as a function of the cycle number using $I_{\text{p}} = \pm 50$ mA and room temperature measurements. 182

7.15 CIS coefficient as a function of the cycle number, for $I_{\text{p}} = \pm 80$ mA at room temperature. 183

7.16 (a) Selected CIS cycles performed at RT. (b) CIS coefficient as a function of temperature for several selected I_{max}. 185

7.17 (a) Temperature dependence of the electrical resistance in the low (R_b; thin barrier) and high (R_B; thick barrier) CIS states. (b) Half CIS cycle performed with $I_{\text{max}} = 50$ mA (open circles) that enabled us to change from the thick to the thin barrier state. 186

7.18 (a) The relative resistance change from 300 K to 20 K (α) as a function of the $R \times A$ product (lower scale; for TJ1 and TJ2) or R_{300K} (upper scale; TJ2 only) as changed by EM-induced barrier degradation (TJ1, open squares and TJ2, open circles). The numbers in the Figure are the number of CIS cycles measured up to the considered R(T) run. (b) Selected normalized R(T) curves in the 300–20 K range (TJ1). 187

7.19 (a) Pinhole radius as a function of the tunnel junction electrical resistance [TJ1 using $R_t = 3.8\ \Omega$ (open squares) and $R_t = 5\ \Omega$ (squares with crosses) and TJ2 using $R_t = 22\ \Omega$ (open circles) and $R_t = 8\ \Omega$ (circles with crosses); see discussion for details]. (b) Corresponding metallic resistance R_m, as calculated from Eq. (7.8). 189

7.20 Time-evolution of the electrical resistance of the studied tunnel junction for $T = 25$ K and several applied electrical currents: (a) $I = 10$ mA, (b) $I = 40$ mA, (c) $I = 60$ mA, (d) $I = -10$ mA, (e) $I = -40$ mA and (f) $I = -60$ mA. . . . 192

7.21 Selected sets of 10 s of the R(t) evolution for (a) $I = 50$ mA and (b) $I = 60$ mA, obtained at $T = 25$ K. The times in the figure correspond to the time approximately passed since the current was applied. 193

7.22 Time-evolution of the electrical resistance of the studied TJ for several applied electrical currents: (a) $I = 10$ mA, (b) $I = 40$ mA, (c) $I = -10$ mA and (d) $I = -40$ mA. 195

7.23 Time-evolution of the electrical resistance of the studied tunnel junction for $I = 40$ mA for several periods of 1024 data points acquired every 10 ms; (a) In the beginning of the data acquisition and (b) at the end. 196

7.24 Time-evolution of the electrical resistance of the studied tunnel junction for $I = -40$ mA for several periods of 1024 data points acquired every 10 ms; the top three in the beginning of the data acquisition and the bottom one at the end. 196

7.25 Selected Current Induced Switching cycles obtained in a sample of series T1, at representative temperatures. 198

7.26 CIS coefficient and resistance shift δ as a function of I_{max} at selected temperatures for a sample of series T1. 199

7.27 CIS cycles performed at room temperature and relaxation phenomena (inset). 200

8.1 Tunnel magnetoresistance versus $R \times A$ for magnetic tunnel junctions with different oxidation times. 204

8.2 Schematic representation of the oxidation process used to fabricate the here studied tunnel junctions. 205

8.3 (a) Electrical resistance versus bias current of a MTJ with (30″)+(30″)+5″ oxidation time (series TJ1001; $A = 1 \times 1\ \mu\text{m}^2$), under both I (black curves) and I_0 (red curves) and for both parallel (P) and antiparallel (AP) states. (b) Tunnel magnetoresistance versus bias current [TMR(I); solid squares]. Open circles display the TMR ratio obtained under a low bias current $I_0 \approx 0.1$ mA after I is applied. (c) V(I) characteristics in the P and AP states. Notice the abrupt decrease in the measured electrical resistance and TMR observed at $|I| \approx 32$ mA, denoting the intrinsic breakdown of the barrier. 207

8.4 (a) Electrical resistance versus bias current of a MTJ with (30″)+(30″)+5″ oxidation time (series TJ1001; $A = 2 \times 3\ \mu m^2$), under both I (black curves) and I_0 (red curves) and for P and AP states. (b) TMR(I) (solid squares) and TMR obtained under a low bias current $I_0 \approx 0.1$ mA after I is applied (open circles). (c) V(I) characteristics in the parallel and antiparallel states. Notice the gradual R- and TMR-decrease observed at and/or just after the breakdown of the barrier. 208

8.5 Tunnel magnetoresistance measured under I (full squares) and I_0 (open circles) for MTJs of series TJ1043 [(30″)+(30″)+5″] with different areas. Notice the gradual TMR-decreases observed for MTJs with (a) $A = 3 \times 6\ \mu m^2$ and (c) $A = 1 \times 4\ \mu m^2$, contrasting with the sharp ones for MTJs with (b) $A = 2 \times 3\ \mu m^2$ and (d) $A = 1 \times 3\ \mu m^2$. 209

8.6 $R \times A$ product (for the parallel and antiparallel states) versus applied current of MTJs of series (a) TJ1022 [(30″)+(30″)+4″] and (b) TJ1018 [(30″)+(30″)]; (c) and (d) display the corresponding TMR bias dependence. 210

8.7 (a) Tunnel magnetoresistance versus bias current [TMR(I)] of a MTJ with (25″) oxidation time. (b) V(I) characteristics in the parallel and antiparallel states. Inset: Corresponding electrical resistance (V/I). 211

8.8 Electrical resistance of the antiparallel (AP) and parallel (P) states and corresponding TMR values (inset) of a MTJ with (30″)+(30″)+5″ oxidation time (series TJ1043; measured under I_0). Notice the two R-levels existent in both R_P and R_{AP}. 212

8.9 Electrical resistance of the antiparallel and parallel states (column 1), corresponding TMR values (column 2) and enlarged low current region (column 3) for MTJs with different oxidation times. 213

8.10 Temperature dependence of the electrical resistance and magnetoresistance (insets) of four different tunnel junctions of the same series, with (25″)+(00″)+00″ oxidation time. 215

8.11 Effects of small variations of (a) t and (b) a in the overall tunnel junction resistance. 217

List of abbreviations

- A, Area
- AFM, Antiferromagnetic
- AP, Antiparallel state
- CIMS, Current induced magnetization switching
- CIS, Current induced switching
- CSV, Conventional spin valve
- e, Electron charge
- E, Electrical field *or* Energy
- E_b, Energy barrier
- EM, Electromigration
- fl, Free layer
- FM, Ferromagnetic
- GMR, Giant magnetoresistance
- H, Magnetic field
- H_0, Magnetic cooling field
- H_{exch}, Exchange field
- I, Electrical current *or* Insulator
- I_c, Critical switching electrical current
- $I_{\max}$, Maximum applied electrical current
- I_p, Electrical current pulse
- IBD, Ion beam deposition
- j, Electrical current density
- ℓ, Electron mean free path
- M, Magnetization
- MR, Magnetoresistance
- MRAM, Magnetic random access memory
- MTJ, Magnetic tunnel junction
- NM, Non-magnetic
- NOL-SV, Nano-oxide layered spin valve
- P, Parallel state
- pl, Pinned layer
- R, Electrical resistance
- R_{AP}, Electrical resistance of the antiparallel state
- R_b, Thin-barrier electrical resistance state
- R_B, Thick-barrier electrical resistance state
- R_P, Electrical resistance of the parallel state
- RT, Room temperature
- SV, Spin valve
- t, Barrier thickness *or* time
- T, Temperature
- T_C, Curie Temperature
- T_N, Néel Temperature
- TE, Training effect
- TJ, Tunnel junction
- TLF, Two level fluctuations
- TMR, Tunnel magnetoresistance
- V, Voltage
- δ-shift, Electrical resistance shift
- ϕ, Barrier height
- ρ, Electrical resistivity

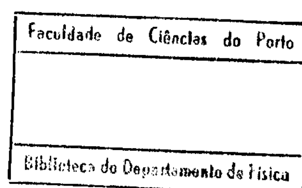
Faculdade de Ciências do Porto
Biblioteca do Departamento de Física

Chapter 1

Introduction

The recent developments in thin film deposition techniques, down to the nanometer scale, opened a huge new field both for technological applications and fundamental research. It is now possible to deposit smooth films with thicknesses as low as a few Å (10^{-10} m), and the accurate and reproducible fabrication of the so-called nanostructures: Multilayers, spin valves, tunnel junctions and granular films among others. A great variety of applications based on such nanostructures are already commercially available, while others are in accelerated development.

Multilayers are made of thin layers ($\sim$ 30 Å) of two different materials (*e. g.* Co, Fe, Cr, Ru, Re, Cu) stacked alternatively. When one of the materials is ferromagnetic (FM) and the other non-magnetic (NM), interesting physical phenomena appear, like interlayer coupling and the giant magnetoresistance (GMR) effect. Grünberg *et al.* [1] observed in 1986 that the magnetizations of two Fe layers separated by a thin Cr spacer were spontaneously antiparallel aligned (antiferromagnetic interlayer coupling). Four years later, Parkin *et al.* [2] showed that in Fe/Cr multilayers, the magnetic coupling between the Fe layers depended on the thickness of the Cr spacer, oscillating between ferromagnetic (parallel Fe magnetizations) and antiferromagnetic (antiparallel Fe magnetizations). This oscillatory coupling was later found in several multilayered systems like Co/Ru [3] and Co/Re [4]. In 1988, Baibich *et al.* [5] and Binasch *et al.* [6] observed that the electrical resistance of Fe/Cr multilayers changed by about 50% (at 4.2 K) when a sufficiently high magnetic field was applied ($\sim$ 10 kOe). This effect was then called Giant Magnetoresistance and it was shown that the electrical resistance of the multilayer stack depended on the relative orientation of the magnetizations of the Fe layers. The antiparallel alignment of the magnetizations at zero magnetic field exhibits much larger resistance than the parallel alignment, due to spin dependent electron scattering. Several other multilayered systems were then investigated and GMR values as large as 50% at room temperature were obtained. However, the high magnetic fields necessary for switch between the two resistance states limited the implementation of multilayers in technological applications.

In 1991 Dieny *et al.* [7] developed simple try-layered structures made of two ferromagnetic materials (NiFe) separated by a non-magnetic spacer (Cu). One of the FM layers (the so called pinned layer) was deposited just adjacent to an antiferromagnetic (AFM) material. Its magnetization was then fixed by a strong exchange interaction at the AFM/FM interface

(see section 1.2.1). The other FM layer (free layer) stayed magnetically loose from the pinned layer due to the Cu spacer, and so its magnetization could be easily reversed under a small applied magnetic field of a few Oe. Although this new structure had a lower GMR than multilayers (5% at room temperature), the switching field from the parallel to the antiparallel configuration was greatly reduced ($\approx$ 10 Oe). Thus, this new structure, named spin valve (SV), is currently used in the read heads of hard drives.

In 1995 Moodera *et al.* [8] and Miyazaki and Tezuka [9] were the first to fabricate magnetic tunnel junctions (MTJs) with large Tunnel Magnetoresistance (TMR) at room temperature (TMR$\approx$ 12%). The structure of a tunnel junction is very similar to that of a spin valve. The difference is that the metallic non-magnetic spacer of the SV is replaced by an insulating layer (I; usually Al_2O_3 or, more recently, MgO). Due to spin dependent tunneling, the electrical resistance of the MTJ also depends on the relative orientation of the two FM layers and TMR ratios exceeding 200% are now obtained [10] (compare with the maximum GMR obtained in spin valves of $\approx$ 20% [11]). Another important difference between these two structures is the direction in which the electrical current flows. While in magnetic tunnel junctions the current has to flow perpendicularly to the film plane (CPP geometry), in spin valves it can flow either in the CPP geometry or in the plane of the film (CIP geometry).

1.1 Magnetoresistance

Magnetoresistance (MR) is the change of the electrical resistance (R) of a material when an external magnetic field (H) is applied, and its magnitude is usually written as:

$$MR(H) = \frac{\rho(H) - \rho(0)}{\rho(0)} \times 100(\%), \tag{1.1}$$

where $\rho(H)$ [$\rho(0)$] is the resistivity in a magnetic field H (zero magnetic field). The reasons for such resistance variation can, however, be multiple. In fact, a material does not even have to be magnetic for its resistance to be change by the application of a magnetic field. Every metal exhibits what is called the *Normal Magnetoresistance* [12], arising from the effect of the Lorentz force on the electron's trajectory, $e\mathbf{v} \times \mathbf{B}$ (e the electron charge, $\mathbf{v}$ the velocity of the electron and $\mathbf{B}$ the internal magnetic induction). This effect is, however, negligible in thin films, because of the inherent small electron mean free path.

Another magnetoresistive effect is the *Anisotropic Magnetoresistance* (AMR). In transition ferromagnetic materials (and their alloys), the electrical resistance is a function of the angle between the magnetization and the direction of the current flowing through it. The resistance is usually maximum when the magnetization and the current are parallel and minimum when they are perpendicular, and values as high as $\sim$ 5% at room temperature can be obtained. The physical origin of the AMR effect is the spin-orbit coupling, reflecting the interaction between the spin of the electron and the lattice [13].

The *Colossal Magnetoresistance* (CMR) is observed in doped manganate perovskites [14]. The electrical resistance of these materials can change by several orders of magnitude as a result of a magnetic driven metal-insulator transition at the corresponding magnetic ordering temperature. CMR is then only observed near the Curie temperature of these materials and requires very high applied magnetic fields.

Giant Magnetoresistance (GMR) is related to the change in the electrical resistance of multilayers or spin valves when the angle between the magnetizations of ferromagnetic layers separated by thin metallic non-magnetic spacers is altered [15, 7]. In this case the resistance is usually maximum when the magnetizations of the magnetic layers are antiparallel and minimum when they are parallel. The microscopic origin of the GMR effect is electron spin dependent scattering within the FM layers and at their interfaces. When a SV is in the parallel configuration, majority (spin) electrons flow through both magnetic layers suffering little scattering. On the other hand, minority electrons scatter often. When the SV is in the antiparallel configuration, majority electrons in one FM layer are minority in the other and vice-versa. Both spin electrons will then suffer multiple scattering events and the resistance of the spin valve is increased when compared to the parallel situation (as long as the spacer thickness is smaller than the electron mean free path).

Before the discovery of the GMR effect, it was already known that the electrical resistance of magnetic tunnel junctions depended on the relative orientation of the magnetization of the FM layers, much in the same way as observed for GMR. This effect, called *Tunnel Magnetoresistance*, was found several decades ago [16] but only recently were large TMR ratios observed at room temperature [8, 9]. Currently, TMR ratios of over 70% in tunnel junctions with Al_2O_3 barriers [17] and over 200% in MgO tunnel junctions [10] are achieved, making MTJs promising candidates for numerous applications. The TMR effect has a different physical origin of the GMR effect. In tunnel junctions it is the (non-diffusive) spin-dependent tunneling probability that causes the electrical resistance to depend on the relative orientation of the pinned/free layer magnetizations. In the GMR effect this dependence is a consequence of (diffusive) spin-dependent scattering.

Nevertheless, both TMR and GMR ratios are similarly given by:

$$MR = \frac{R_{AP} - R_P}{R_P} \times 100(\%), \tag{1.2}$$

where R_{P} (R_{AP}) is the electrical resistance in the parallel (antiparallel) configuration. This definition will be used throughout this thesis.

1.2 Exchange and coupling fields

1.2.1 Exchange field

In tunnel junction and spin valve magnetoresistive devices, one can obtain two distinct resistance states if an external magnetic field H is used. This is possible because the two FM layers constituting the device invert the orientation of their magnetization (M) at different H values. For this to occur, one can either use FM layers with different coercivities (different FM materials and/or of different thicknesses) or, as first introduced by Dieny *et al.* [7], one can deposit an antiferromagnetic (AFM) layer just adjacent to one of the FM layers, fixing its magnetization.

In fact, when an AFM material adjacent to a FM material is cooled below its Néel temperature (T_N) under an applied magnetic field ($\mathbf{H}_0$; its direction is taken as positive), the interfacial AFM spins will align (usually ferromagnetically) with the FM spins as long as $T_N < T_C$ (T_C

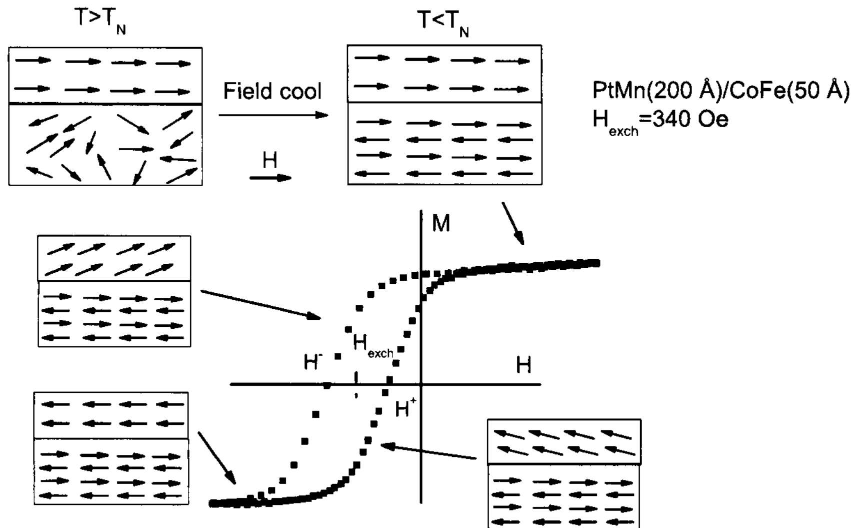

Figure 1.1: Exchange bias. Upon cooling under an external magnetic field an exchange interaction is impressed at the FM/AFM interface. The resulting $M(H)$ cycle is shifted away from $H = 0$. In the figure we present the MOKE $M(H)$ cycle of a MnPt(150 Å)/CoFe(50 Å) structure showing $H_{\text{exch}} = 340$ Oe at room temperature.

being the Curie temperature of the FM layer) [18, 19]. The other (underlying) spin planes in the AFM layer will follow the corresponding antiferromagnetic alignment, as illustrated in Fig. 1.1. Below T_N an exchange interaction (equivalent to an unidirectional anisotropy) is then induced between the interfacial AFM and FM spins. If a $M(H)$ hysteretic cycle is then initiated (Fig. 1.1; sample starts with a positive magnetization in the free layer), under a decreasing H, the FM magnetization (M_{FM}) will only reverse its direction when a sufficiently large (negative) magnetic field (H^-) is applied, so that $M_{FM} = 0$ at $H = H^-$. The strong exchange interactions continuously try to align ferromagnetically the FM moments with the AFM spins at the interface. These AFM interfacial spins are, in turn, strongly coupled to the AFM lattice and will therefore (ideally) experience no misalignment. In the M(H) ascending branch, the FM moments will rotate at a magnetic field higher than H^- due to the coercivity (so that $M_{FM} = 0$ at $H = H^+$; see Fig. 1.1). The M(H) hysteretic cycle will then be shifted in the direction opposite to that of $\mathbf{H}_0$. The exchange field H_{exch} is then defined by the simple expression (Fig. 1.1):

$$H_{\text{exch}} = \left| \frac{H^+ + H^-}{2} \right| . \tag{1.3}$$

In magnetoresistive devices the FM layer in contact with the AFM layer is called the pinned layer because its magnetization is fixed. The magnetization of the other FM layer, called the free layer, readily follows a small magnetic field as it is applied. Antiferromagnetic materials studied for applications include FeMn [20], NiO [21], Fe_2O_3 [22], MnIr [23] and PtMn [24] (see Reference [25] for a detailed analysis of Mn alloys exhibiting exchange bias), and exchange fields as high as 850 Oe have been obtained [26].

Several theories exist which try to explain the exchange bias effect but none was able to fully account for the variety of associated phenomena, like the existence of a blocking

temperature, the training and memory effects, positive exchange bias and enhanced coercivity [27]. The simplest model [28] assumes coherent rotation of the magnetizations of the FM (at temperature T) and AFM layers. The energy per unit area E can then be approximated by:

$$E = -\mu_0 H M_{FM} t_{FM} cos(\theta - \beta) + K_{AFM} t_{AFM} sin^2(\alpha) - J_{FM/AFM} cos(\beta - \alpha), \qquad (1.4)$$

where μ_0 is the magnetic permeability of vacuum, M_{FM} is the saturation magnetization of the FM layer and t_{FM} (t_{AFM}) is the thickness of the FM (AFM) layer. K_{AFM} is the anisotropy of the AFM layer and $J_{FM/AFM}$ is the interfacial exchange constant between the FM and AFM layers. θ is the angle between the applied magnetic field and the FM anisotropy axis, β is the angle between the FM magnetization and the FM anisotropy axis and α is the angle between the AFM magnetization and the AFM anisotropy axis. Minimizing the energy with respect to α and β one can obtain the hysteresis loop shift [28]:

$$H_{\text{exch}} = \frac{J_{FM/AFM}}{\mu_0 M_{FM} t_{FM}}. \qquad (1.5)$$

However, theoretical estimations based on Eq. (1.5) give values of H_{exch} much larger than those obtained experimentally. Malozemoff [29] then considered a random-field model arising from features such as roughness and defects. These create sites of unidirectional interfacial energy due to the coupling of uncompensated moments in the AFM layer with the FM spins. Such model was able to predict the correct order of magnitude of H_{exch}. More recently, the domain model [30, 31] explained the exchange bias effect by considering the magnetization of the AFM layer divided in multidomains, giving rise to a net surface magnetization at the AFM/FM interface that controls the exchange bias.

1.2.2 Interlayer coupling field

We stated in section 1.2.1 that the magnetization of the free layer rotates readily when a small external magnetic field is applied. This is not entirely correct. In fact, one needs to take into account that a (usually and desirably) small interlayer magnetic coupling exists between the pinned and free FM layers which can have important consequences for technological applications [32]. This coupling is responsible for a small shift of the free layer hysteresis loop away from zero magnetic field (Fig. 1.2) and can be phenomenologically described by

$$E = -J_{\text{coup}} cos(\theta), \qquad (1.6)$$

where E is the coupling energy, J_{coup} is the interlayer coupling parameter and θ is the angle between the magnetizations of the two FM layers. The coupling field H_{coup} is then given by:

$$H_{\text{coup}} = \frac{J_{\text{coup}}}{\mu_0 M_{fl} t_{fl}}, \qquad (1.7)$$

where M_{fl} (t_{fl}) is the saturation magnetization (thickness) of the free layer.

The interlayer coupling was found to have three physical origins: magnetostatic (Néel) coupling [33], RKKY-like exchange coupling [34] and pinhole coupling [20].

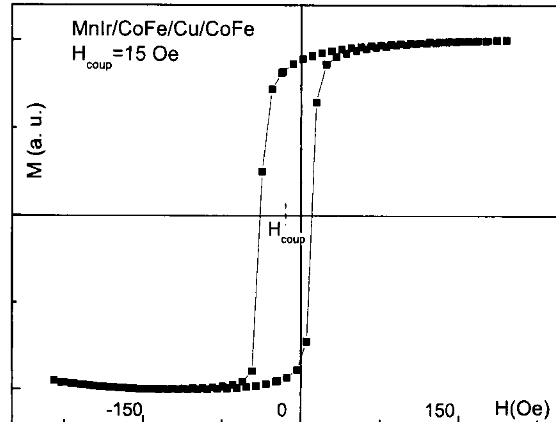

Figure 1.2: Magnetization reversal of the free layer of a spin valve under small applied magnetic fields obtained by the MOKE technique. Notice the small shift from zero magnetic field due to the interlayer coupling ($H_{\text{coup}} = 15$ Oe).

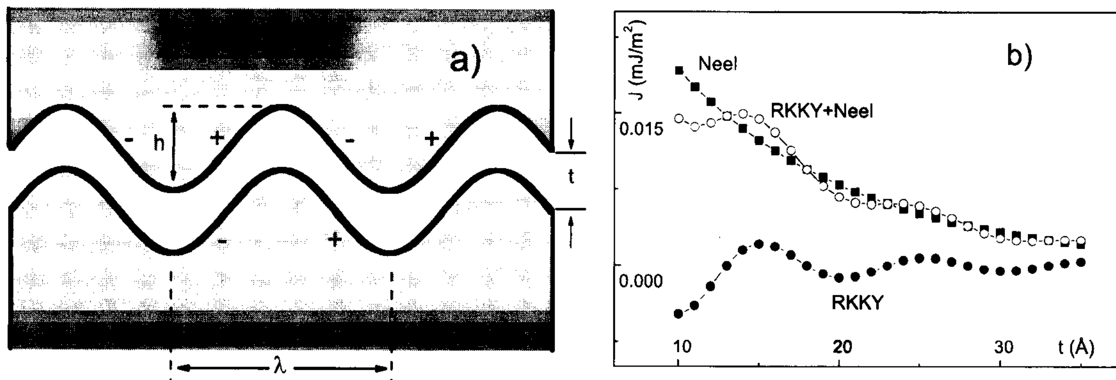

Figure 1.3: a) Correlated interface roughness that causes Néel coupling. b) Simulated Néel and RKYY interlayer coupling as a function of spacer thickness, using $h = 0.04$ Å, $\lambda = 100$ Å, $M_{pl} = M_{fl} = 1$ T, $J_0 = 0.01$ mJ/m^2, $\Lambda = 10$ Å and $\varphi = 1.4\pi$ (see text for discussion).

Néel coupling. This coupling has a magnetostatic origin induced by correlated interface roughness. In this model one considers two ferromagnetic layers separated by a non-magnetic spacer. If the pinned layer/spacer and spacer/free layer interfaces have correlated roughness [Fig. 1.3(a)], described by two-dimensional sinusoidal waviness of amplitude h and wavelength λ (usually associated with the average grain size), the magnetostatic coupling J_{Neel} is given by [33]:

$$J_{\text{Neel}} = \frac{\pi^2}{\sqrt{2}} \frac{h^2}{\lambda} \left(\mu_0 M_{pl} M_{fl}\right) e^{-\frac{2\pi\sqrt{2}t}{\lambda}}, \tag{1.8}$$

where the FM layers are assumed to have infinite thickness with saturation magnetizations M_{pl} (pinned layer) and M_{fl} (free layer), and t is the spacer layer thickness. Under this model, the Néel coupling is always positive (favoring parallel alignment) and decreases exponentially with spacer thickness [Fig. 1.3(b)].

This model can be readily extended to account for both the effect of the finite thickness of the FM layers [33] and of non-conformal roughness [35].

RKKY coupling. Another coupling mechanism is the oscillatory RKKY-like coupling, first observed in Co/Ru and Fe/Cr multilayers [36]. The coupling oscillates as a function of the thickness of the non-magnetic spacer, with a period that depends on its Fermi surface [37].

An exchange interaction between the spins of the conduction electrons in one FM layer and the corresponding ionic magnetic moments, induces a spin polarization in the conduction electrons. This polarization is then propagated to the other FM layer, resulting in an indirect interaction with the magnetic moments of the second FM layer. This gives rise to an exchange coupling J_{RKKY} between the two FM layers that oscillates with the thickness of the spacer t as [38]:

$$J_{\text{RKKY}} = \frac{J_0}{t^2} sin\left(\frac{2\pi t}{\Lambda} + \varphi\right), \tag{1.9}$$

where J_0 is the coupling strength, Λ and φ are the period and phase of the oscillation [39]. As can be seen in Fig. 1.3(b) (parameters taken from Ref. [40]), the RKKY-like coupling is, in spin valves, often masked by the Néel coupling due to roughness. It is, however, possible to observe in high-quality smooth spin valves [41].

The interlayer exchange coupling was, in magnetic tunnel junctions, predicted to exhibit a non-oscillatory behavior with spacer thickness [42, 37] and both its intensity and sign can be changed by an applied bias voltage. However, as long as the system is in equilibrium, the coupling across an insulating spacer should be much smaller than across a metallic one [43] and depend on the intrinsic parameters of the insulating barrier and band structure of the tunnel junction system [42]. Such dependence was experimentally confirmed in epitaxially grown Fe/MgO/Fe/Co tunnel junctions [44].

Pinhole coupling. As one decreases the thickness of the non-magnetic spacer (metallic in spin valves, insulator in tunnel junctions), undesired direct paths between the two FM layers start to appear. Direct exchange coupling then becomes the dominant contribution to the total interlayer coupling [20]. To achieve a pinhole-free nanostructure, the spacer must be deposited on a very smooth surface and under well controled deposition conditions [20].

1.3 Applications

Magnetic nanostructures show enormous potential for a multiplicity of applications such as read head [45, 46, 47], strain [48], current, position and speed [49] sensors. Other applications include field programmable spin-logic gates [50] and the detection of magnetically tagged biological specimens [51, 52]. However, probably the most sought after application is high performance, low cost, non-volatile magnetic random access memories (MRAMs) [53, 54, 55, 56].

1.3.1 MRAMs

As we have seen, in magnetoresistive devices the magnetization of the free layer reverses almost freely when a small magnetic field is applied. One can then obtain two distinct resistance (R) states, associated with the magnetizations of the pinned and free layers being parallel (low R) or antiparallel (high R). This makes magnetoresistive devices suitable for technological applications as non-volatile magnetic random-access memories (MRAMs) [53, 54, 55, 56]. In particular, tunnel junctions are much more attractive for actual device implementation than giant magnetoresistive (Current In Plane; CIP) spin valves [57]. The reason for this is that, to achieve high memory density, several (N) GMR spin valves have to be connected in series, resulting in a reduced reading signal (GMR/N). On the contrary, in (Current Perpendicular to the Plane; CPP) tunnel junctions, the electrical current passes through a single MTJ, giving a reading signal equal to TMR.

A MRAM cell based on magnetic tunnel junctions is constituted by a single TJ stack, a single transistor and several current carrying lines (Fig. 1.4). The tunnel junction stack usually includes several other layers in addition to the simple AFM/FM/I/FM structure. A few selected buffer layers are deposited below the AFM to provide adequate growth conditions for the actual device. Also, the (single) pinned layer is usually substituted by a tri-layered structure called synthetic antiferromagnet (SyAFM or SAF) of composition FM/Ru/FM. The Ru layer of adequate thickness provides very strong antiferromagnetic coupling between the two FM layers, with the further advantage of improving device thermal stability.

The digit line (Fig. 1.4) is unconnected to the tunnel junction and is used to create a (unidirectional) magnetic field in the TJ hard axis direction (created by shape anisotropy). The bit line is used both as a top electrode and to create a (bidirectional) magnetic field along the easy axis [Fig. 1.4(b)]. To write a bit in a selected tunnel junction, current is passed through the corresponding digit and bit lines, producing a large enough magnetic field in the crossing region to reverse the magnetization of the MTJ-free layer. The magnetic state of the tunnel junction is written as "0" or "1" depending on the direction of the current passing in the bit line. In the cross point architecture (Fig. 1.5), each memory cell is in the intersection of a bit and a digit line. Thus, if a current is passed through two such lines, only the tunnel junction in the corresponding intersection senses the magnetic fields along the easy and hard axis. All other cells are exposed to the magnetic field created by a single line (and are thus called half-selected bits), or to none, and their magnetizations are, in principle, not programmed.

Read operations [Fig. 1.4(a)] are performed passing an electrical current through the tunnel

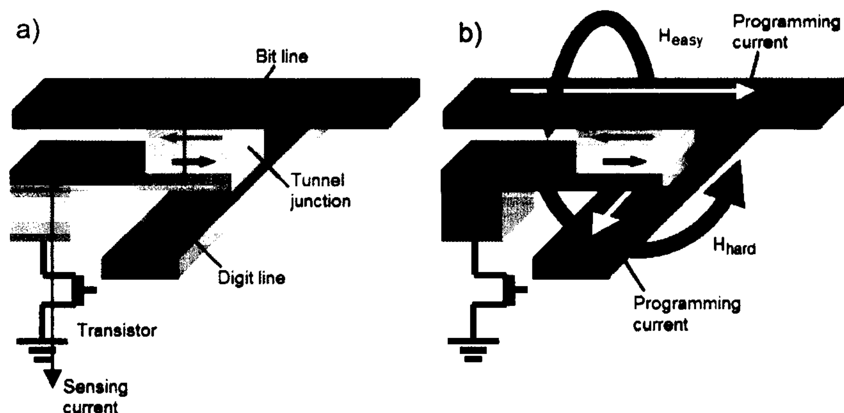

Figure 1.4: Single MRAM cell constituted by a magnetic tunnel junction, a transistor and two current carrying lines. (a) Cell sensing scheme: The transistor is in the "on" state so that an electrical current can flow through the MTJ. (b) Cell writing scheme: The transistor is in the "off" state and electrical currents flow through the digit and bit lines, generating a magnetic field large enough to reverse the magnetization of the free layer of the TJ.

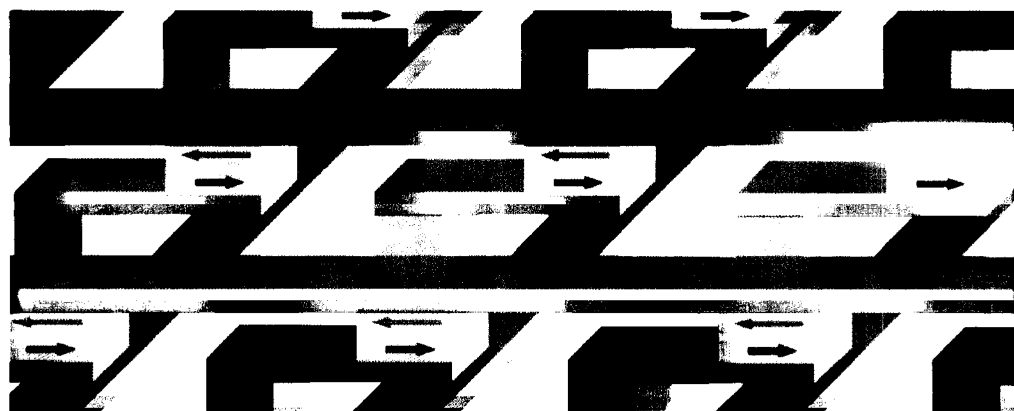

Figure 1.5: MRAM cross point architecture. Each memory cell is in the intersection of a bit and a digit line. An electrical current is sent through one digit and one bit line and, ideally, only the MTJ in their intersection is written.

	MRAM	SRAM	DRAM	FLASH
Read	Moderate-Fast	Fast	Moderate	Fast
Write	Moderate-Fast	Fast	Moderate	Slow
Non-volatility	Yes	No	No	Yes
Endurance	Unlimited	Unlimited	Unlimited	Limited (10^5 - 10^6)
Cell size	Small	Large	Small	Small
Low voltage	Yes	Yes	Limited	No

Table 1.1: Comparison between different memory technologies.

junction, while the isolation transistor is in the "on" state, and measuring the corresponding voltage drop.

Nevertheless, there are still some unsolved problems for commercial MRAMs. Due to the exponential thickness dependence of the MTJ-resistance (see section 5.4), small variations in the insulating barrier thickness result in large variations in the resistance. This puts great challenges to produce wafers with uniform tunnel junction resistance. In addition, not only the resistance but also the TMR ratio has to be as uniform as possible. Tunnel junction non-uniformities can also lead to a distribution of free layer switching magnetic fields. The current passing through the bit and digit lines has then to be large enough to assure that one can switch the magnetization of the free layer of all tunnel junctions, but small enough not to disturb half-selected bits. The operating window is then limited and needs to be maximized.

A comparison [53, 54, 55, 56] between different features of several commercial memory technologies with MRAMs is given in Table 1.1. Notice that each technology has its own advantages and disadvantages, making each suitable for different applications. However, MRAMs show acceptable read/write speed, non-volatility, endurance, high density and low power consumption, making them attractive for a wide range of memory applications. The major non-volatile memory in use today is FLASH. Major drawbacks limiting FLASH expansion are the high voltage needed for operation and their slow write time, low scaling possibilities and limited endurance ($\sim 10^5 - 10^6$ cycles before failure).

1.3.2 Read head sensors

CIP spin valves are currently being used as sensors in commercial read heads [45, 46]. However, and although the GMR ratio of spin valves has been continuously improved over the years, its performance seems to be reaching a limit. Alternatives for the next generation of read head sensors include CPP spin valves [58] and tunnel junctions [59, 47].

Magnetic recording uses a write and read head to record and retrieve information from a magnetic media (Fig. 1.6). The data (bits) are stored as a regular succession of (equal size) differently magnetized regions in the magnetic storage media. The write head consists of a series of coils winded around high permeability magnetic poles. When an electrical current flows through the coils the write head provides an in-plane magnetic field near the write gap (penetrating into the magnetized region), enabling the switching of the magnetic state of a bit. The read head will then be used to detect the magnetic flux "escaping" from the

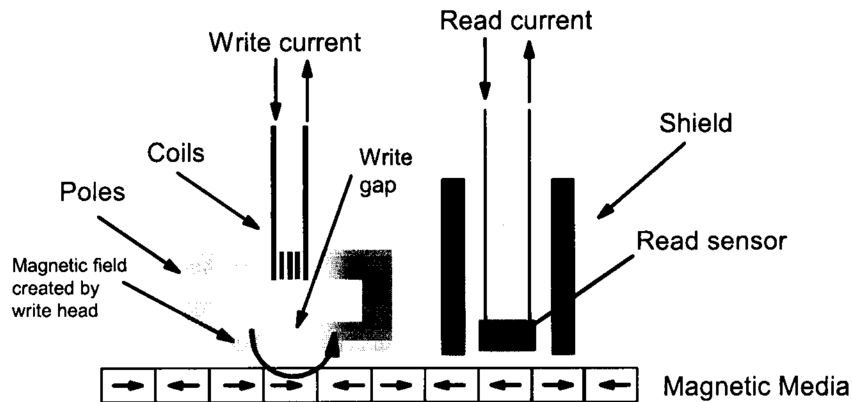

Figure 1.6: Read and write head architecture. When a current flows through the coils of the write head, a magnetic field is generated and penetrates into the magnetic media, switching the state of a bit. The MR sensor is then used to detect magnetic flux "escaping" from transition regions between two oppositely magnetized bits.

transition regions between two oppositely magnetized bits. When we have two successive bits oriented in the same direction, no significant magnetic flux comes out in the transition region. Such absence of signal in the read head is then identified with one definite logical symbol.

The magnetic media stacked in one or more hard disks rotates at speeds as high as 15000 rpm [57]. The head is suspended just above the surface of the magnetic media and is moved across the magnetic media by an actuator. However, a few miliseconds are needed to access the first magnetic bit, due to the need to rotate the media to the head. Complex electronics is then used to process the necessary write and read signals.

1.3.3 Other applications

Besides being used in read heads, the highly sensitive magnetoresistive detectors can be used whenever a magnetic field can be generated to monitor some other physical quantity. For example, successful applications include electrical current, position and speed sensing and control [49].

A bridge configuration, with four magnetoresistive elements, is usually used in sensor applications [60]. This enables thermal variations in resistance to be minimized and zero output in the absence of an external magnetic field. Two of the elements are usually shielded, while the other two are incorporated in flux guides to enhance sensitivity. Also, the easy axis of the pinned and free layer are set perpendicular to each other. The resistance will then change linearly with the applied external magnetic field.

The magnetic field generated by a high electrical currents (*e. g.* in power lines) can be monitored by a bridge sensor [Fig. 1.7(a)]. The changes in such electrical currents can be sensed as a variation in the resistance of the magnetoresistive element. Linear position sensors consisting simply of a bridge sensor and a small ferrite attached to a moving object

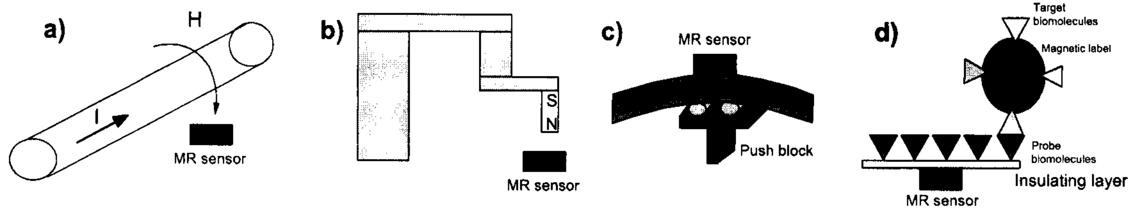

Figure 1.7: Detection of: (a) High electrical currents, (b) linear position for robotic control, (c) strain and (d) magnetically tagged biological specimens using magnetoresistive sensors. In the last case, the biomolecule to be detected (target) is immobilized on a magnetic label and passed over probe molecules immobilized over magnetoresistive sensors.

can be used in, e.g. robotics applications [Fig. 1.7(b)]. To monitor the engine speed in automobiles a sensor is placed in the proximity of a ferrous gear, which, in turn, disturbs the magnetic field of a close permanent magnet. Combining the high sensitivity of MR devices (to changes in the relative orientation between the magnetizations of the pinned and free layer) with enhanced magnetostrictive properties of selected materials for the FM layers allows the development of highly sensitive strain sensors [48] [Fig. 1.7(c)].

Magnetoresistive devices can also be used to detect magnetically tagged biological specimens, using either DNA-DNA hybridization to detect genetic diseases or antibody-antigen interaction to detect micro-organisms [51, 52, 61] [Fig. 1.7(d)]. The actual detection chip contains an array of immobilized probes to which the biomolecules to be detected (target biomolecules having a complementary DNA strand to that of the probe) will bind to. Magnetic microbeads (labels) will then bind to biotin present in the target biomolecules. The magnetic field of the marker will then be detected by the magnetoresistive sensor, enabling the concentration of target biomolecules to be determined.

1.4 This thesis

In the following chapters we will present the main results of the work performed in the last four years, focusing on our studies on transport and magneto-transport properties of specular spin valves and magnetic tunnel junctions.

In Chapter 2 we briefly summarize the main experimental techniques used in this thesis. We start with the deposition tools and nanostructure-fabrication techniques available and used at INESC-MN to develop and finally fabricate the SVs and MTJs studied in this work. We then present in some detail the techniques available at IFIMUP to measure the transport properties of thin films, and also the cryogenic system used in our measurements down to 15 K.

In chapter 3 we revise the current knowledge on giant magnetoresistance and spin valves. We start with the use of the semiclassical Boltzmann transport equation to calculate the conductivity of a thin film and its extension to the case of a spin valve. Quantum mechanical models are also considered. Finally, we refer some advanced spin valves recently developed with improved characteristics, namely higher GMR ratio and exchange bias, better thermal

stability and bias point control. We describe the specular spin valve formed by the partial nano-oxidation of the FM-pinned and free layers (exhibiting an improved GMR ratio due to specular reflection at the nano-oxide/FM interfaces), as well as the synthetic AFM and spin filter spin valves.

The next chapter focus on the experimental results obtained in *specular* spin valves having nano-oxide layers (NOLs) incorporated. We present a comparative study between conventional and specular spin valves, showing that the latest have more than twice the GMR value of the first. Comparison of MR(H) and M(H) cycles shows an unusual separation between transport and magnetic processes in the case of the specular SV, which is attributed to the enhanced role of specular scattering at the NOL interfaces. We will further show that the NOL is an AFM oxide with an average blocking temperature $T_B \approx 175$ K. However, we demonstrate the existence of a broad distribution of local blocking temperatures in the nano-oxide layer, extending from just below RT down to 25 K and having a maximum at ≈ 175 K (from dominant-size domain regions). The here observed training effect in specular spin valves will be related to rearrangements in the domain structure of the AFM nano-oxide layer.

Chapter 5 provides an overview of several topics on tunnel junctions. We first introduce some simple theoretical models that are usually used to explain the tunnel magnetoresistance effect: The model proposed by Juliere based on the tunnel Hamiltonian method and that of Slonczewski that treats FM-electrodes and barrier as one single quantum mechanical system. We will then briefly describe Simmons' model that allows us to obtain information on the insulating barrier characteristics from experimental current-voltage curves. We then present and discuss several existing models that explain the temperature dependence of the electrical resistance R(T) of tunnel junctions. The effects of pinholes (metallic paths between the two FM layers through the insulating barrier) in R(T) will also be discussed. We briefly present the spin-torque effect, enabling a sufficiently high spin polarized electrical current to reverse the magnetization of a FM layer. Such large electrical currents can, however, also lead to electromigration (EM), *i. e.,* to a net flux of ions. Due to its relevance to the experimental results presented in this thesis, we give a fairly complete description of the electromigration phenomenon. We refer the usual separation of the electromigration force into two components: The direct force arising from the interaction of the electrical field with the direct valence of the ion, and the wind force that results from momentum exchange between accelerated electrons and the migrating ions. The ballistic model of electromigration will also be presented.

In chapter 6 we will introduce the Current Induced Switching effect (CIS), resulting from electromigration of metallic ions (Co, Fe) from the bottom electrode into the barrier, induced by an electrical current. The effective barrier thickness of the tunnel junction is then reduced and consequently its electrical resistance as well. If the current sense is reversed, electromigration in the opposite direction occurs and metallic ions previously displaced into the barrier return into the electrode. We present a study on the Current Induced Switching effect on a series of extremely thin (7 Å Al_2O_3), low resistance *magnetic* tunnel junctions (FM/I/FM). We will discuss the CIS effect in terms of heating, relaxation processes and temperature dependence. The CIS effect is thermally assisted and we show the existence of a low (~ 0.13 eV) and a high (~ 0.85 eV) energy barrier for electromigration. Time dependent measurements enabled us to observe two distinct relaxation times, associated with opposite resistance changes, suggesting the involvement of ions from the two FM/I

interfaces. Nevertheless, we conclude that the majority of migrating ions arise from the bottom electrode/barrier interface and relate this to the asymmetry in the MTJ-deposition procedure. CIS cycles measured under an external magnetic field allowed us to conclude on the existence of excessive local heating in the tunnel junction and to demonstrate a CIS cycle with three different electrical resistance states.

Studies on Current Induced Switching in different series of *non-magnetic* tunnel junctions will be presented in chapter 7. We observe that tunnel junctions with a Ta-NM layer deposited just below the barrier show an opposite current switching direction when compared to that observed in FM/I/FM and FM/I/NM tunnel junctions. We show that this difference results from the competition between the direct and wind forces causing electromigration. Furthermore, relaxation phenomena are only observed in tunnel junctions without a Ta layer deposited *below* the insulating barrier, indicating that Ta ions remain stably inside the barrier. We found that the Current Induced Switching effect is strongly dependent on both maximum applied electrical current ($I_{\max}$) and temperature. At constant temperature, the CIS effect increases with increasing $I_{\max}$, until a plateau of constant CIS is observed, related to barrier degradation. Furthermore, with decreasing temperature the CIS effect is seen to decrease for the same maximum applied current. We further study how such electromigration of ions into the barrier influences the R(T) behavior of the tunnel junction: With decreasing TJ resistance (due to the presence of metallic ions in the barrier) we find that R decreases less with decreasing temperature. In particular, we show that the dominant transport mechanism in TJs can be changed from tunnel to metallic, by electromigration. We also probed the existence of individual EM-events down to the 10 ms scale. We will show that as temperature increases, more ions become active in electromigration and the dynamics of the system becomes complex. However, at low temperatures a fairly detailed and neat study was possible and several EM-driven resistance fluctuation events were revealed and studied.

In chapter 8 we study the transport properties of *underoxidized* magnetic tunnel junctions. We show that transport in this system is controlled by nanoconstrictions and defects within the AlO_x barrier. In fact, dielectric breakdown in such MTJs occurs at different, localized spots of the barrier, likely where a large concentration of defects (oxygen vacancies due to the underoxidation of the barrier) exists. We further observed spin dependent resistance fluctuations between two closely separated levels, associated with transport through localized defects in the barrier. Measurements of the electrical resistance as a function of temperature of different MTJs with extremely small oxidation times allowed us to observe a wealth of dependencies: Metallic-like ($dR/dT>0$), insulating-like ($dR/dT<0$) and a mixture of the two (metallic for the parallel and insulating for the antiparallel states). We then studied the influence of unoxidized Al nanobridges on the magneto-transport of such tunnel junctions. We conclude that transport through such metallic channels is spin dependent, which results in the fairly large MR values observed for extremely underoxidized tunnel junctions. This effect will be discussed in terms of ballistic magnetoresistance through non-magnetic nanoconstrictions.

Chapter 2

Experimental techniques

In this chapter we give an overview of the experimental techniques used in this work. First we present the deposition, oxidation and lithography techniques used to fabricate the nanostructures studied in this thesis, including the Ion Beam Deposition (IBD) and Physical Vapor Deposition (PVD) methods, available at the Research Group INESC-MN lead by Prof. P. Freitas. We then shortly describe the cryogenic systems available at IFIMUP, providing temperatures down to 3.7 K, and the experimental methods used to characterize the samples studied: Transport and magneto-transport measurements (resistance, magnetoresistance, current-voltage characteristics), SQUID and MOKE magnetometries. References to previous works where these techniques are fully explained will be given. Due to its very recent observation, a detailed description of the experimental method developed to measured the Current Induced Switching (CIS) [62] effect will be given here.

2.1 Deposition and fabrication of nanostructures (INESC-MN)

Since the samples studied during this work were deposited at INESC-MN within collaborative research projects with local researchers, only a brief description of deposition tools and tunnel junction fabrication methods will be given. Detailed descriptions on these subjects can be found in Refs. [63, 64, 65] that were followed in the subsequent sections.

2.1.1 Physical Vapor Deposition

INESC-MN has a fully automated magnetron sputtering Physical Vapor Deposition (PVD) machine, Nordiko 2000 [64, 65]. This system is used for the deposition of spin-dependent tunnel junctions (pinned and free layers and insulating barrier) and for plasma and natural oxidation of thin films.

In a sputtering deposition method, the target material is bombarded by energetic particles (usually Ar or Xe ions) and is then deposited in a substrate (Fig. 2.1). The target is held at negative bias voltage with respect to the earth, while the shield and chamber are grounded, which results in the ionization of the inert gas (Ar, Xe) present in the chamber. These ions

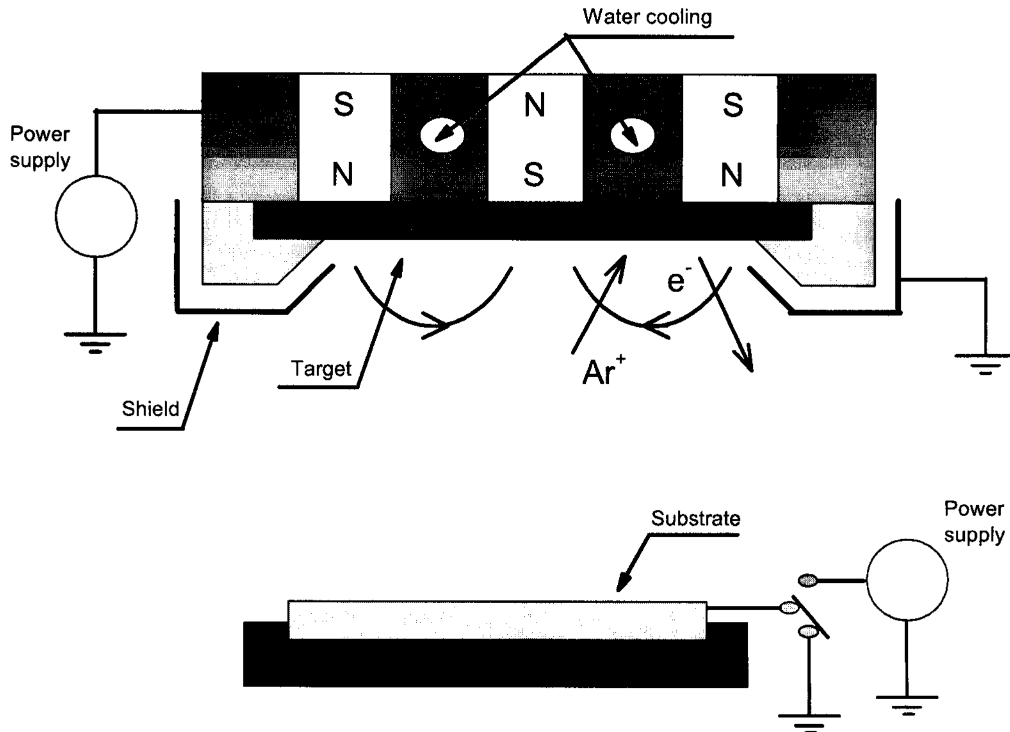

Figure 2.1: Magnetron sputtering deposition technique. Accelerated Argon (or Xenon) ions bombard the target, whose surface atoms are progressively ejected (sputtered) and deposited on the substrate in front, originating film growth.

are accelerated in the direction of the target, while electrons move in the opposite direction, ionizing more atoms of the inert gas. In magnetron sputtering the ion plasma is confined near the target (and away from the substrate) by a static magnetic field created by an array of permanent magnets. Electrons will then spiral as they travel around the magnetic field lines, increasing the probability of gas ionization. The target and the magnet array are water cooled due to the incidence of the energetic ions.

The target can be biased by a DC or RF power supply, depending on the material being deposited. In the case of insulating materials, the RF power supply must be used, because the charge of the ions hitting the target is not neutralized.

The substrate can also be grounded or biased by a RF power supply. In the last case, a ionized plasma is created close to the substrate, much the same way as near the target. When ions hit the substrate, they remove part of the previously deposited material, resulting in a decrease of the effective deposition rate. The use of substrate biasing during deposition is known to reduce surface roughness [66]. This process can also be used after deposition, to remove material from the sample or to clean metallic surfaces with oxide residues.

The magnetron sputtering-based Nordiko 2000 system is fully automated with six water cooled 4 inch diameter magnetrons (3 inch diameter targets), all with two 2.5 kW DC power supplies. Two magnetrons are also equipped with a 550 W RF power supply. The substrates are inserted in the deposition chamber through a loadlock into a substrate table with 12

deposition stations. The table rotates, and places the station used for deposition under the desired target. A shutter stops the target ejected material from reaching the substrate until the desired station is in place. The substrate table is water cooled, except for one quadrant (3 stations) that is electrically isolated from the rest of the table for substrate biasing. One of the stations is equipped with a magnet array providing a 30 Oe magnetic field to induce an easy magnetic axis in the films under deposition. The working base pressure in the Nordiko machine is $\sim 8 \times 10^{-8}$ Torr.

INESC-MN also has an Alcatel SCM450 commercial sputtering system with one deposition chamber and fully manual control. The absence of a load-lock requires the (adverse) venting of the chamber for substrates loading and unloading. The Alcatel SCM450 has three magnetrons with 4 inch diameter targets and a substrate table with four stations (three water cooled). Substrate biasing during deposition is provided by an external power supply. The working base pressure of $\approx 2 \times 10^{-7}$ Torr is achieved in 24 hours with a turbomolecular pump. The main use of this machine is for deposition and oxidation of insulating barriers used in spin-dependent tunnel junctions.

For the electrical contact between the fabricated microscopic devices and transport property measuring probes, one usually uses Al films. In INESC-MN the metal used for tunnel junction leads and pads is deposited by an automated metallization cluster tool, Nordiko 7000. It consists of four process chamber modules (base pressure 5×10^{-9} Torr) served by a load-lock (5×10^{-6} Torr) and a central dealer (2×10^{-8} Torr). After cleaning the sample using soft sputter etch, the metallization is achieved by depositing $Al_{98.5}Si_{1.0}Cu_{0.5}$ and $Ti_{12.5}W_{50}(N_{37.5})$. The soft sputter etch is a modified sputter etching process that uses two RF power supplies. The first biases the substrate, accelerating the Ar^+ ions towards it, while the second keeps the plasma stable through a continuous ionization of the Ar gas. The AlSiCu layer is deposited by a sputter process with a DC power supply. TiW(N) is deposited from a TiW target in an Ar and N_2 gas atmosphere.

A complete description of these systems and deposition parameters can be found in References [64, 65].

2.1.2 Ion Beam Deposition

INESC-MN has a fully automated Nordiko 3000 Ion Beam Deposition (IBD) machine [63] that is used for film deposition (metallic films, Al_2O_3 oxide films, granular multilayers), plasma and natural oxidation of thin films.

This IBD system has a 6 targets holder (water cooled) coplanar with two RF ion sources (deposition and assist guns) in a typical Z configuration (Fig. 2.2). After reaching a working base pressure of 7×10^{-8} Torr (with a turbomolecular and a cryogenic pump), a Ar (or Xe) plasma is created through a discharge in the deposition gun. With this method a low pressure in the deposition chamber (10^{-4} Torr) is maintained during deposition. The ions are accelerated by a three grid self-aligned system, producing a collimated ion beam and avoiding sample contamination during deposition. The typical acceleration voltage adopted is ~ 1450 V. To avoid arching and deflection, the ion beam is neutralized after it exits the deposition (or assist) gun. Deposition rates as low as ~ 0.1–0.5 Å/s can be reached. This offers the possibility to precisely control the thickness of the thin films being deposited. The

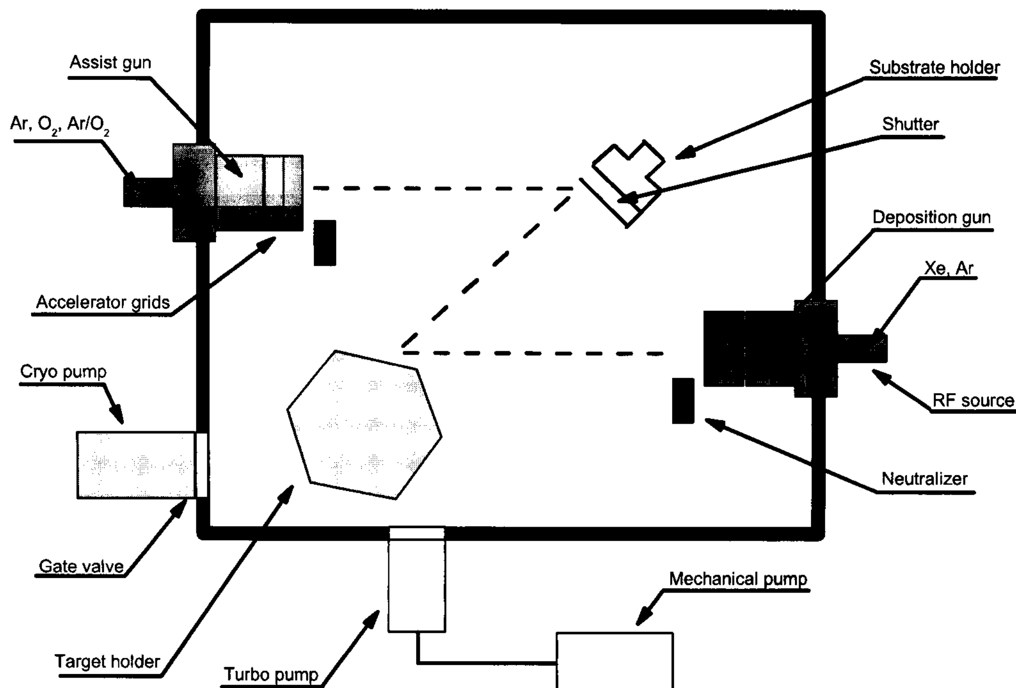

Figure 2.2: Geometry of the Nordiko 3000 Ion Beam Deposition machine installed at INESC-MN.

angle between the incident beam and the target holder can be controlled but it is usually set at 80°. The substrate holder rotates at $\sim$ 15 rpm to ensure maximum uniformity regarding film thickness and resistivity. A permanent magnet array ($\sim$ 40 Oe) is mounted around the substrate holder to induce an anisotropy-axis in the films. The assist gun is directed to the substrate holder, for barrier oxidation and ion milling processes. A complete description of this system and characteristic sets of deposition parameters can be found in References [63, 64, 65].

2.1.3 Tunnel junction barrier oxidation

A crucial step in the deposition process of a tunnel junction is the barrier oxidation, either natural or by remote plasma. Oxidation must be correctly performed, since both over-oxidation (partial oxidation of the bottom electrode) and under-oxidation of the barrier (leaving sub-stoichiometric AlO_x clusters or even metallic, non-oxidized, Al inside the barrier) usually lead to lower tunnel magnetoresistance.

Natural oxidation is, at INESC-MN, performed in the load-lock of the Nordiko 2000 (PVD) and 3000 (IBD) systems. The load-lock is filled with pure oxygen until the require oxygen pressure is obtained. An insulating barrier is achieved in the first minutes of oxidation. Oxidation pressures between 0.5 and 100 Torr and oxidation times between 5 minutes and 4 hours are used for barrier fabrication.

Plasma oxidation can also be performed in the Nordiko 2000 system. After depositing the

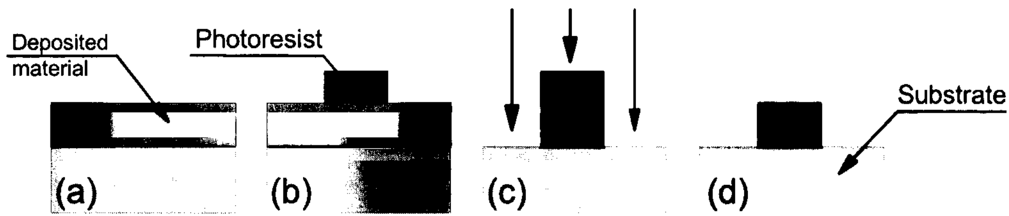

Figure 2.3: Schematic of etching process. The material deposited (a) is covered with photoresist which is then partially exposed to a laser light. After removing the exposed areas of the photoresist (b), the unprotected areas of the film are etched away (c) leaving a pattern sample (d).

bottom electrode and barrier material, an oxygen plasma is directed into the sample, in the substrate bias mode. Oxygen pressure of 3 mTorr at 50 sccm (standard cubic centimeters per minute) is used.

2.1.4 Tunnel junction fabrication

In tunnel junctions the electrical current flows perpendicularly to the plane (CPP geometry). To probe their transport properties, one then needs an electrical contact to the bottom and top electrodes. For this, after the tunnel junction stack is deposited, a microlithographic processing technique is used. We give here a quick review on tunnel junction fabrication, including definition of the junction area, bottom and top electrodes. For a complete run sheet of tunnel junctions fabrication at INESC-MN see References [63, 64, 65].

2.1.4.1 Lithography and lift-off

An optical lithography system (DWL 2.0 by Heidelberg) is used to pattern micron-sized tunnel junctions. After being deposited, the sample is coated with a photosensitive polymer (photoresist; $\sim$ 1.5 μm thick). When the photoresist is exposed to a light of the right wavelength (440 nm HeCd laser), the chemical bonds of the polymer are broken and a developer removes the exposed areas of the photoresist (positive photoresist). The pattern transferred to the photoresist was previously defined using a computer mask made with a computer-aided design (CAD) program and then loaded into the lithographic system. The laser scan is thus software controlled and masks can be easily changed. The photoresist will either protect the covered areas from an etching process (Fig. 2.3) or pattern new layers being deposited (lift-off; Fig. 2.4). In the end, the photoresist can be removed using a wet chemical process (solvent at $\sim 70°$ C). The layers deposited on top of the photoresist are also removed during lift-off. When transferred to the lithographic system, the masks can be set as inverted or non-inverted. In inverted masks all the wafer except the mask is exposed to the laser beam and they are thus used in etching processes. In non-inverted masks, only the mask area is exposed to the laser beam and they are used for lift-off processes. The resolution of the system is 0.8 μm and the alignment precision is $\sim$ 0.25 μm. Higher level masks have to be aligned to previous patterns and reference alignment marks must be provided for in

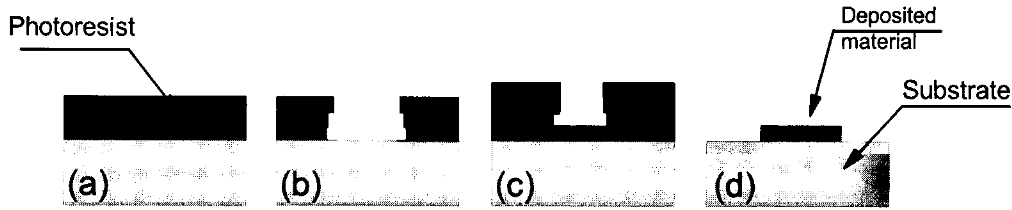

Figure 2.4: Schematic of lift-off process. The photoresist (a) is exposed to the laser light and the exposed areas removed (b). A material is then deposited (c) and, after lift-off of the photoresist by a chemical process, the layer is patterned (d).

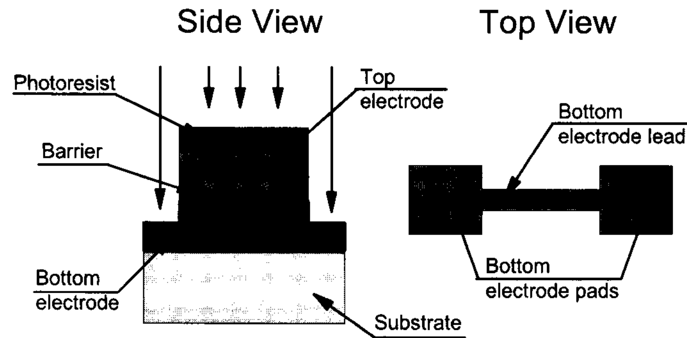

Figure 2.5: Definition of the bottom electrode area by an etching process.

the first pattern.

2.1.4.2 Fabrication process

In order to fabricate tunnel junctions with small junction area INESC-MN uses a microlithographic process [26]. As will be seen, this process has four main steps: The definition of the bottom lead and pads, the definition of the junction area, the electrical isolation between bottom and top electrodes around the junction area and finally the definition of the top lead and pads.

After the tunnel junction stack is deposited, the fabrication process begins and the geometry of the tunnel junction is defined. One starts by the definition of the bottom electrode lead and contact areas (Fig. 2.5). In this step the material not covered by the photoresist pattern is etched away by sputter etching or ion beam miling. Figure 2.5 shows the area protected by the photoresist (side view) and the defined bottom electrode lead and pads (top view). The pads (large squares) will allow direct electrical contact (current supply and voltage measurement) to the bottom electrode. The narrower section (lead) is the path for the electrical current to flow through the bottom electrode of the junction.

The next step is a crucial one when fabricating a tunnel junction: The definition of its area and shape (Fig. 2.6). Again photoresist is patterned, now to protect a small area of the bottom lead and the bottom contact pads. The material not covered by the photoresist is

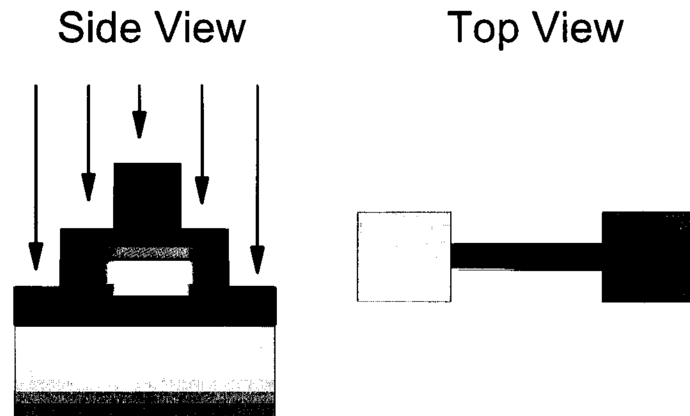

Figure 2.6: Junction area definition. A small area of the bottom lead is protected by photoresist. The etching must be stopped before all the bottom electrode is removed.

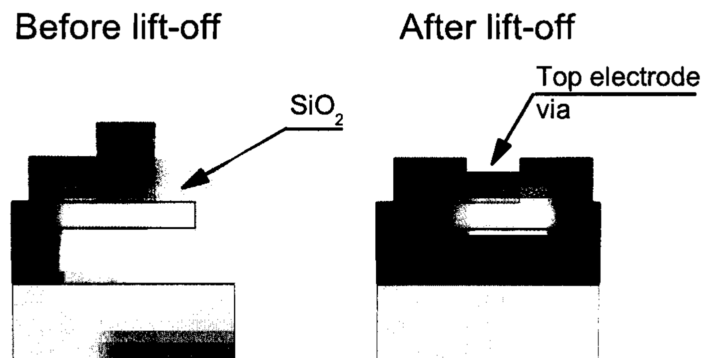

Figure 2.7: A SiO_2 layer is deposited to prevent electrical contact between the bottom and top leads (left). The photoresist left during junction area definition is now used to open the top electrode via (right).

again removed by sputter etch or ion milling. The etch must be stopped *after* the barrier material has been removed, but *before* all the bottom electrode disappears. This is achieved using a previously deposited control sample with similar structure to that being removed during etching. The etch is temporarily stopped several times until the material on the control sample is completely removed.

Before removing the photoresist, an Al_2O_3 or SiO_2 insulating layer ($\sim$ 400 Å) is deposited (Fig. 2.7). This layer will isolate electrically the top and bottom electrodes around the area of the junction. The photoresist covering the junction area will be used as a lift-off mask to open a top electrode via on the insulator. The same mask is thus used to define the area of the junction and the (self-aligned) via in the insulator.

The via connecting the junction area and the bottom pads is now opened. The final step is the metallization of the top lead and respective contact pads and the metallization of the bottom pads. This sequence is performed in the Nordiko 7000 metallization cluster tool and

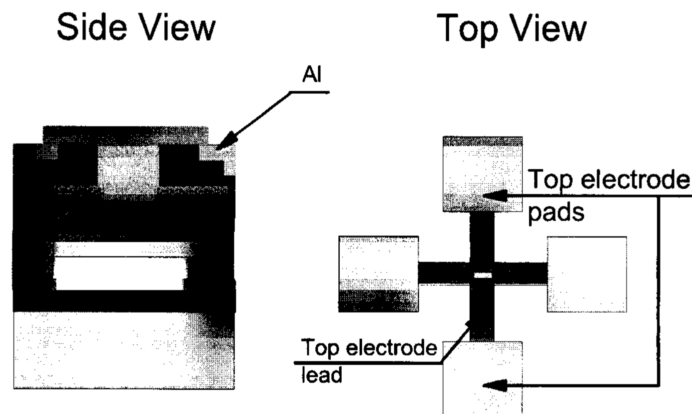

Figure 2.8: Definition and metallization of the top lead and pads and metallization of the bottom pads. Top view of the patterned tunnel junction.

consists on depositing 3000 Å of $Al_{98.5}Si_{1.0}Cu_{0.5}$ and 150 Å of $Ti_{12.5}W_{50}(N_{37.5})$. The TiW(N) layer protects the AlSiCu layer from oxidation during the lift-off of the photoresist. The final step in the tunnel junction fabrication and the view of the fabricated sample are shown in Fig. 2.8.

2.2 Experimental characterization

After the fabrication of nanostructures, one has to characterize their properties. The temperature dependence (300–20 K) of the electrical resistance (R), magnetoresistance (MR), current-voltage characteristic I(V), Current Induced Switching (CIS; observed in tunnel junctions) of the studied samples were measured using the cryogenic systems available at IFIMUP. These experiments give valuable information on transport mechanisms, including spin-dependent scattering (R, MR), exchange, coupling and coercive fields (MR), tunnel junction barrier parameters [I(V)], switching currents (CIS). Magnetic characterization was performed using SQUID and MOKE magnetometries. Detailed descriptions on these subjects can be found in References [67, 68, 69, 70, 71].

2.2.1 The cryogenic system

Temperature dependent electrical transport measurements were performed in the close cycle He cryostats (Gifford-McMahon type) available at IFIMUP. This system (Fig. 2.9) is based in He expansion/compression cycles [72, 73] and temperatures as low as 10 K can be reached (3.7 K when a Joule-Thompson valve is added). Inside these cryostats is a moving displacer whose volumes above and below vary, remaining their sum constant. These volumes are connected to a He fueling system (compressor) through a high (in) and a low (out) valve. The opening/closing of these valves is synchronized with the movement of the displacer. A heat regenerator connects both volumes above and below the displacer. This type of cryostats usually has two stages of cooling to reduce power consume.

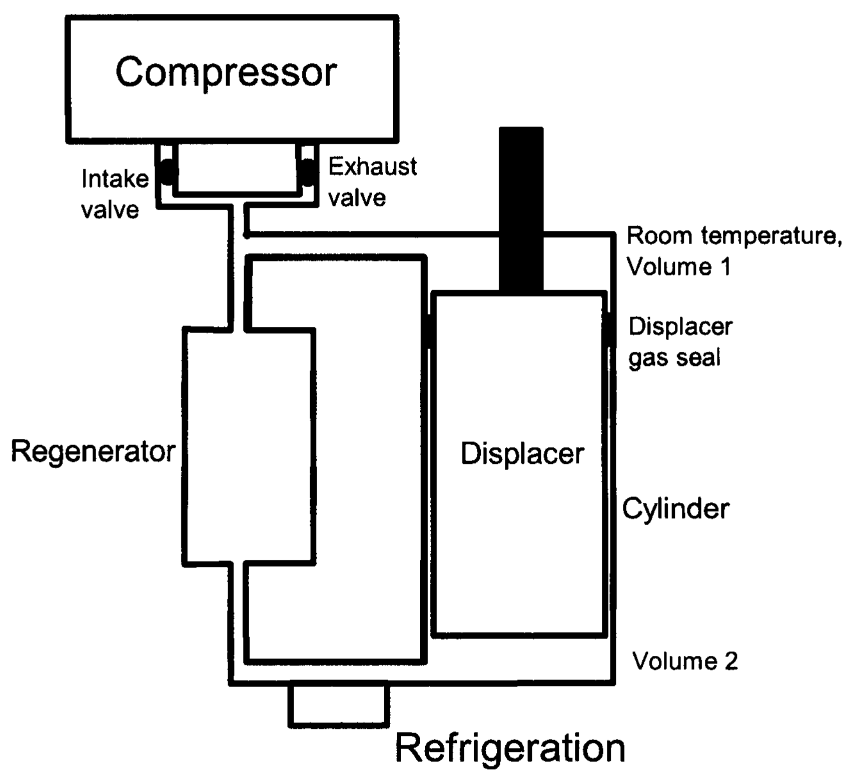

Figure 2.9: Scheme of a close cycle 10 K cryostat.

During an expansion/compression cycle, He gas at room temperature and high pressure is admitted in volume V_1 and passes to volume V_2 due to the movement of the displacer. Then, the closing of the admission valve and opening of the exit valve makes the gas expand in the regenerator, cooling the gas and thus the cryostat. For an ideal gas, the heat Q removed in a cycle is simply given by $Q = (P - P_0)V$, if P and P_0 are the admission (high) and exit (low) pressures and V the empty volume of the cylinder (V_1 or V_2).

The research line (A) of IFIMUP has three 10 K cryostats and one equipped with a Joule-Thompson valve that reaches 3.7 K. In this last type of cryostats, He flows through a narrow constriction causing the further cooling of the gas due to the Joule-Kelvin effect [74]. Detailed analysis of these techniques were already presented and can be consulted [67, 68, 69, 70, 71].

2.2.2 Transport measurements

2.2.2.1 Electrical resistance and magnetoresistance

Thin films. For high-resolution electrical resistance (R) and magnetoresistance (MR) measurements, the setups available at IFIMUP were used to study and characterize thin film samples, in the 300–10 K temperature and 0–1 T magnetic field ranges.

For temperature dependent measurements the samples were glued to a copper sample-holder with a special varnish (GE-varnish), providing electrical insulation and a good thermal contact between the two. To minimize contact and wire resistance, the standard-four-contacts-in-line were used [75]. The electrical contacts were made with silver paste spots, directly connected to 70 μm diameter copper wires. The sample-holder was then mounted in a closed cycle cryostat, allowing measurements ranging from 4 to 300 K. The copper wires are rolled around in different parts of the cryostat providing thermal anchors to minimize thermo-electrical effects in the measured voltages. The temperature in the sample-holder (assumed the same as that of the sample) is measured by a calibrated AuFe0.07%-Cr thermocouple with a Keithley 2001 multimeter (10 nV resolution).

The R(T) data was obtained by continuously changing the temperature with rates typically of 0.5 K/min. This allowed us to obtain a considerable number of experimental V(T) data and thus its temperature derivative with very good precision. The slow variation of temperature in time also allowed us to minimize thermo-electrical signals (through differential thermal lag effects across the samples and wires) and differences between real and measured temperature. Constant DC current is provided to the sample using a Time Electronics 9818 current source (currents from 1 μA to 1 A with $\Delta I/I = 1/10^6$). The electrical current used in each run, although dependent on the electrical resistance of the studied sample, was typically of the order of mA. The voltage drop in the sample was measured by a Keithley nanovoltmeter (181 or 182 models) with 1 nV resolution.

Magnetoresistance measurements (Fig. 2.10) were performed at constant temperature. An APD-K temperature controller ensures temperature stabilization better than 0.1 K in the 300–10 K temperature range. The electromagnet used in magnetoresistance measurements [or R(T,H)] was a GMW-Magnet System (Iron core nucleus), powered by a Danfysik 5000 current source up to 60 A. The magnetic field is measured using a Hall probe locally calibrated (10^{-4} T sensitivity) in a HP 3457A voltmeter. The maximum obtainable magnetic field

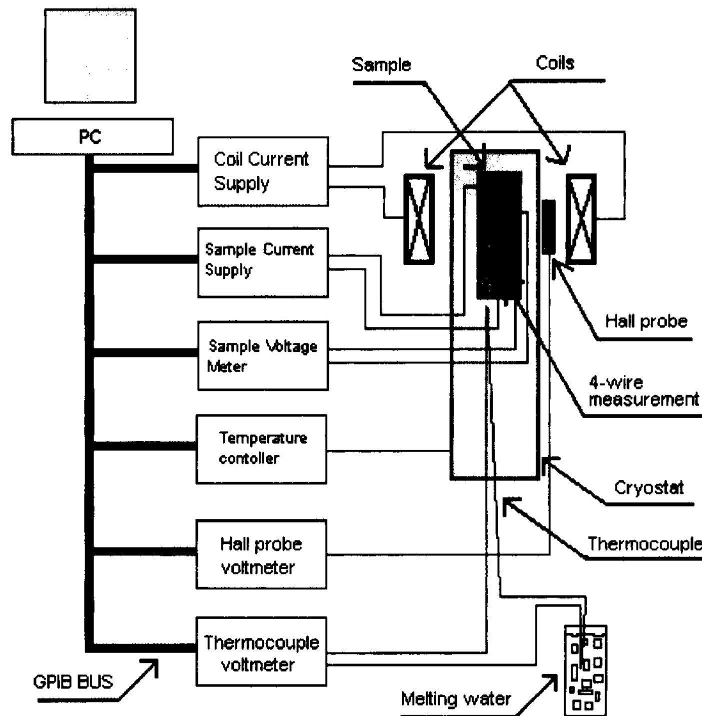

Figure 2.10: Experimental setup available at IFIMUP to measure R(T,H) and MR(H,T) in the 300–4 K and 0–1 T ranges.

was about ~ 1 T for the situation of minimum gap (~ 6 cm). All measurements are fully computer-automated. A detailed description of these experimental apparatus can be found in several references [67, 68, 71].

Tunnel junctions. Measurements of the transport properties of tunnel junctions as a function of temperature were performed in a slightly different setup than that described above. Because tunnel junctions have thin insulating layers, high electrical fields occur across the barrier, which may lead to dielectric breakdown (see section 5.6).

The implemented setup is shown in Fig. 2.11. Four lead measurements were always performed due to the low resistance of the tunnel junctions studied. The current supply (Time Electronics 9818), the nanovoltemeter (Keithley 182), the temperature controller (APD-K) and the magnet current supply (Kepco bipolar) are connected to a computer via a GPIB (IEEE-488) bus. The magnetic field is calculated from the voltage provided by a calibrated Hall probe (measured by a HP 3457A voltmeter) and a maximum field of ~ 250 Oe can be obtained. Two switches short the tunnel junction before it is connected to the circuit, for protection against ElectroStatic Discharge (ESD) damage.

Temperature dependent measurements of electrical resistance, magnetoresistance and Current Induced Switching (see below) were performed in the close cycle cryostat system previously described (section 2.2.1). Due to the micron-metric dimensions of the pads, we had to place all measured samples in a small *chip carrier*. The pads of the TJ were then *wire*

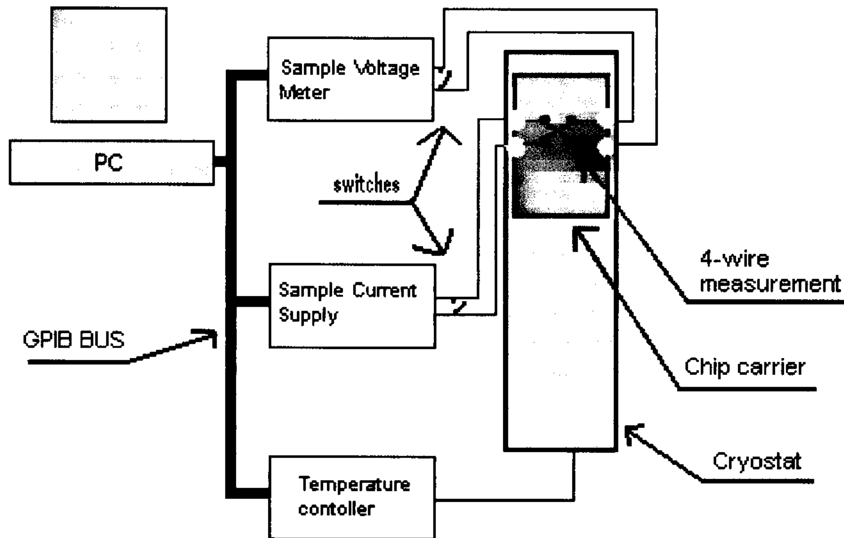

Figure 2.11: Experimental setup for measurements of the electrical transport properties of tunnel junctions. Magnetic field current supply, Hall probe and temperature measurement voltmeter are not included in the scheme.

bounded to the chip carrier gold pads using 0.5 μm Al wires (Fig. 2.12). Only then were we able to connect these gold pads to our external setup using silver paint (Fig. 2.13).

2.2.2.2 Current Induced Switching

Current Induced Switching (CIS) was only recently observed by Liu *et al.* [62, 76] in thin, low resistance magnetic tunnel junctions, while measuring I(V) characteristics. This effect consists of switching between two resistance states (similarly to the common GMR or TMR effects) applying a continuous or pulsed ($I_{\rm p}$) electrical current larger than a characteristic threshold current $I_{\rm c}$. This phenomena was deeply investigated in the course of this thesis and its experimental implementation will thus be explained here in some detail. Initially the CIS effect was studied by simply measuring I(V) characteristics. However, the non-linear I(V) contributions made the CIS effect less visible and more difficult to study. For this reason, another experimental method was developed, the so called *current pulse method* [76].

In this method, current pulses ($I_{\rm p}$) are used to induce resistance switching. One first applies a small pulse ($I_p = -\Delta I_p$ in Fig. 2.14) during a time Δt_p. The pulse is then removed, and the voltage across the tunnel junction is measured under a low measuring current I_m, applied for a period Δt_m. (Both Δt_p and Δt_m remain constant throughout the measurement.) We then measure the TJ-*remnant resistance* (R_m), characteristic of the initial linear part of the corresponding I(V) characteristic. The magnitude of the current pulses is sequentially increased ($I_{\rm p}$ becomes more negative under $-\Delta I_p$ steps; after each step the current is always set at I_m to measure R_m) until a maximum current is reached, $I_{\rm p} = -I_{\rm max}$ (see Fig. 2.14). At this stage, $I_{\rm p}$ is increased, at the $+\Delta I_p$ rate, passing through $I_p = 0$ and up to $I_p = +I_{\rm max}$. As before, R_m is always measured after subjecting the sample to a particular current pulse. To obtain a complete $R_m(I_p)$ cycle, the current pulses are finally decreased to zero. Typical

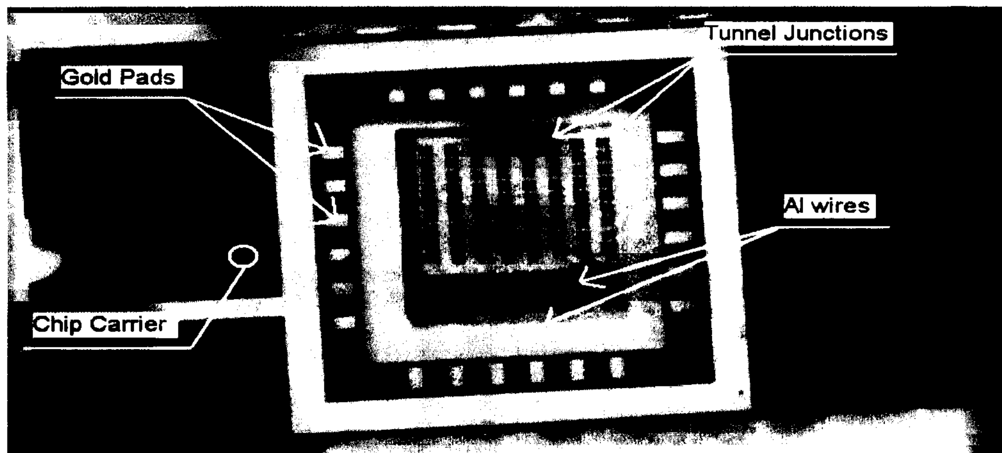

Figure 2.12: Tunnel junctions wire bonded to the gold pads of a chip carrier.

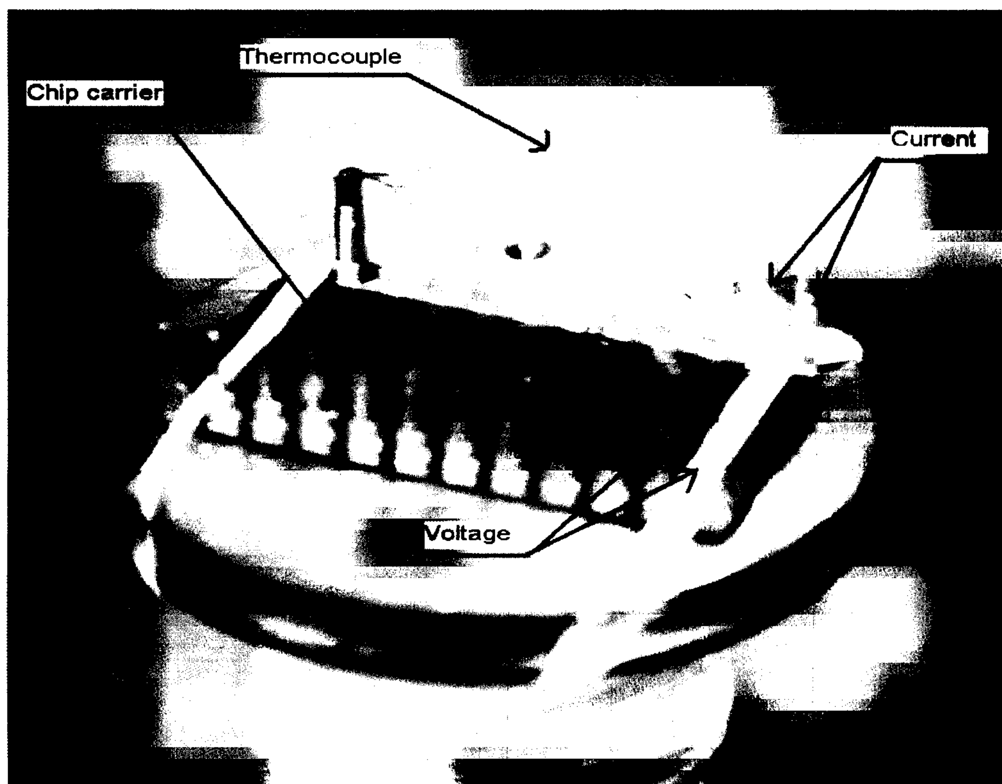

Figure 2.13: Chip carrier placed in a cryostat. Four copper wires are attached to the chip carrier, for current to flow through the tunnel junction and to measure the corresponding voltage drop.

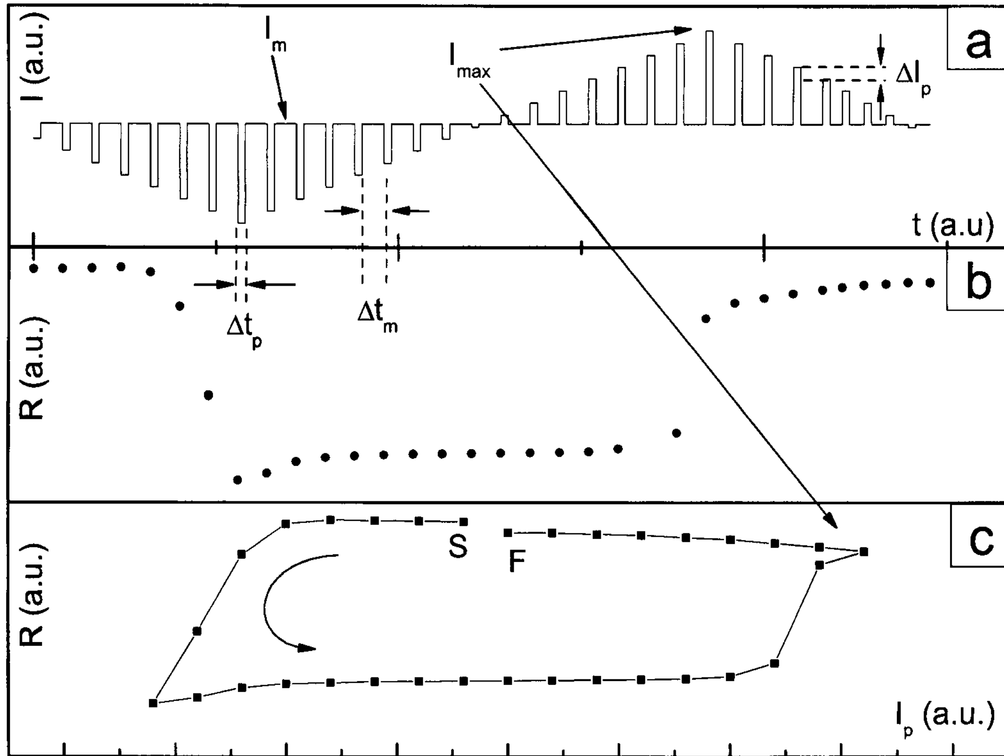

Figure 2.14: Current Induced Switching on a MnIr (90 Å)/CoFe (80 Å)/AlO_x (7 Å)/CoFe (30 Å)/NiFe (40 Å) sample. (a) Applied electrical current versus time. (b) Remnant resistance (R_m=V/I_m) as a function of time. (c) Remnant resistance (R_m) as a function of the previously applied current pulse I_p; S and F are the start and finish of the CIS experiment. In this example, $\Delta t_m = 3\Delta t_p$.

values used throughout this work are: $\Delta I_p \approx$ 2–5 mA, $\Delta t_p \sim$ 1 s, $\Delta t_m \sim$ 5 s, $I_m \sim$ 1 mA and $I_{\max} \sim$ 30–80 mA. Pulse and measuring times were mainly limited by the electrical current source available. Positive current is defined as flowing from the bottom to the top lead.

Figure 2.14(a) shows the applied current as a function of time in an experimental CIS cycle. We can observe the sequence of current pulses/measuring current and the measured remnant resistance as a function of time [Fig. 2.14(b)]. One notices a sharp resistance drop (increase) near $-I_{\max}$ ($+I_{\max}$) - the Current Induced Switching effect. One can also plot the resistance as a function of current pulse $R(I_{\mathrm{p}})$ graph, obtaining a *hysteretic cycle*, the so-called Current Induced Switching cycle [Fig. 2.14(c)].

2.2.2.3 Data acquisition

A new and improved data acquisition program was developed during this thesis, taking advantage of the features offered by Visual Basic 6.0 [77] and Measurement Studio [78] from Microsoft and National Instruments, respectively. This program allows us to measure R(T), CIS(I), I(V), MR(H) and MR(T) in a fully automated and intuitive manner (Fig. 2.15).

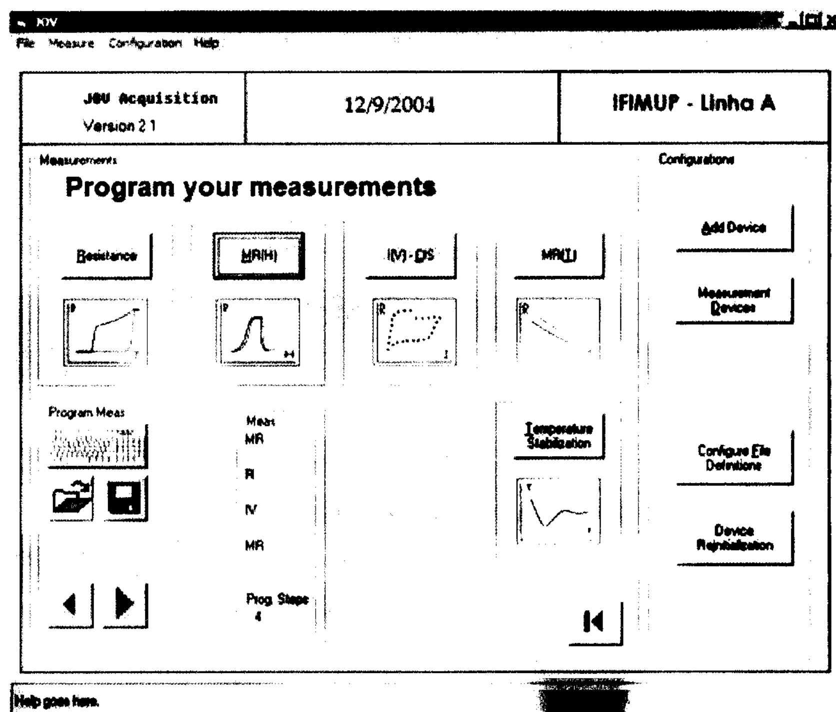

Figure 2.15: The Main Form of the data acquisition program. The user can choose between several options, including different experimental measurements, device and file configurations.

Besides performing individual measurements, the user has now the possibility to program a set of up to 200 consecutive different experiments. For example, one can program MR(H) measurements at $T = 200$ K, followed by another one at $T = 100$ K, followed by a CIS cycle at $T = 50$ K, followed by a R(T) measurement between $T = 20$ K and $T = 300$ K, and so on. All measurements will then be performed automatically by the order they were introduced, without being necessary any further intervention from the user. This greatly minimizes the measuring time of each sample. Furthermore, the user can stop the programmed set of measurements at any time, and each experiment individual data file can be accessed either locally or remotely by a local network without disturbing the measurement system. In fact, the user can, not only remotely monitor the measurements being performed, but also remotely control all functions of the data acquisition program.

In this program each type of measurement has its own Form, that allows the user to choose the desired experimental parameters and observe the graph with the acquired experimental data points. In the case of a MR(H) measurement (Fig. 2.16), the user can select, among others, the maximum and minimum applied magnetic field and the corresponding magnetic field step, the applied electrical current, the temperature at which the measurement is to take place and the magnetic field applied until such temperature is reached (for field cooling experiments). The program is prepared to measure up to two samples at the same time.

To improve the program usefulness and portability, and because each cryostat available at IFIMUP has a different set of measuring devices (voltmeters, current sources, temperature

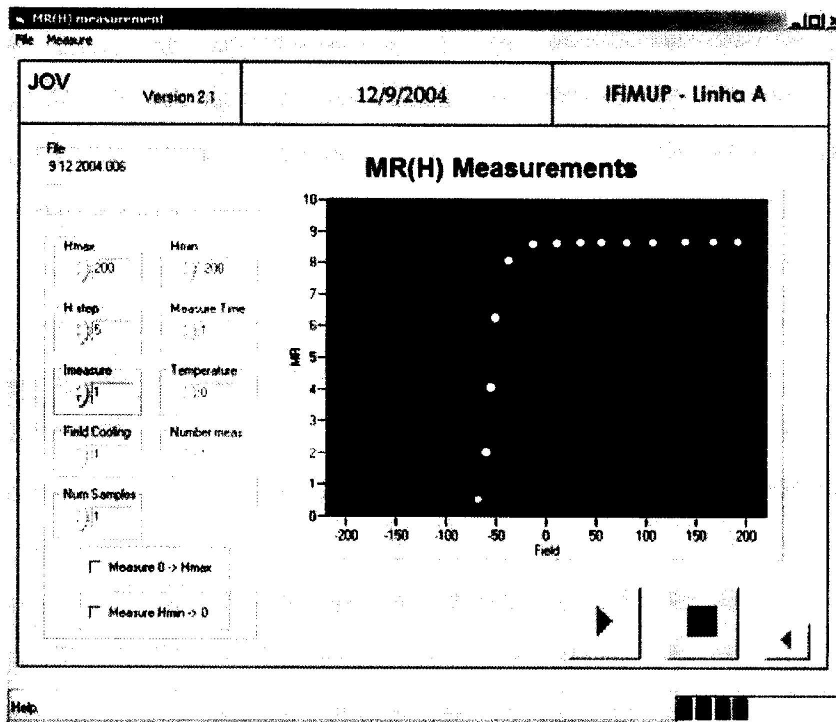

Figure 2.16: The MR(H) Form of the data acquisition program. One can change, among others, the maximum and minimum applied magnetic fields, the applied current and measuring temperature. Experimental data points are displayed in the graph.

controllers), we added a feature that allows the user to choose the devices present in each setup. For this, we included an Add Device Form where a new device can be added or an old one edited. The type of device (current source, voltmeter, temperature controller) has to be defined and the corresponding set of parameters (initialization and read/write messages, number of channels, etc.) can then be accordingly altered.

The measuring temperature (applied magnetic field) is obtained using a calibrated thermocouple (Hall probe). Both calibrations can be edited in the program.

2.2.3 Magnetic characterization

2.2.3.1 SQUID magnetometer

A SQUID (Superconducting Quantum Interference Device) magnetometer from Quantum Design (resolution 10^{-7} emu) installed at IFIMUP and equipped with a 5 T superconducting coil was used (340–4 K temperature range) to perform isothermal magnetization curves as a function of the applied field, M(H). The samples were mounted in plastic straws, glued with a special kapton low temperature scotch. Thin films were measured with in-plane applied field. Details on the measurement scheme and experimental apparatus can be found in Refs. [69, 70].

2.2.3.2 Magneto-Optical Kerr Effect

Magnetization hysteretic cycles M(H) were also measured using a locally developed Magneto-Optical Kerr Effect (MOKE) magnetometer (see Ref. [79] for a detailed description). In fact, when a polarized laser beam is reflected by a magnetic material, its polarization axis is rotated. This rotation is proportional to the local magnetization of the material where the (small) laser beam incides. However, the magnetic moment of the studied sample cannot be quantitatively known and the information obtained is limited to the penetration depth of the laser beam.

Using different MOKE geometries one can measure both the in-plane (longitudinal and transverse geometries) and out-of-plane (polar geometry) moments. When the incident laser beam makes an angle of $\sim 60°$ with the film plane, both the longitudinal or transverse in-plane magnetization can be probed. On the other hand, if the incident beam is almost perpendicular to the film surface the Kerr effect is proportional to the out-of-plane magnetic moment.

Chapter 3

Giant Magnetoresistance: A brief overview

3.1 Introduction

Giant magnetoresistance in spin valves (FM/NM/FM structure) and multilayers [$(\mathrm{FM}/\mathrm{NM})_{\times n}$ structure; n the number of bilayers] arises from spin dependent electron scattering. Since in FM materials conduction electrons with their spin parallel to the local magnetization (M) direction suffer less scattering than those with spin antiparallel to M, the electrical resistance of these nanostructure is changed when their magnetic configuration changes from parallel to antiparallel. This is schematically depicted in Fig. 3.1, where we represent multiple scattering events for up and down spins in both parallel and antiparallel configurations. In Fig. 3.1(a), the magnetizations of the two FM layers of the spin valve are parallel and spin up electrons are less scattered than spin down electrons. The electrical resistivity of the structure will then be mainly determine by the scattering experienced by spin up electrons. In Fig. 3.1(b), the magnetizations of the two FM layers are antiparallel. Spin up electrons in one layer are spin down in the other and vice versa. Thus, both spin up and spin down electrons will suffer the same amount of scattering. Considering that the electrical resistance of the spin up (down) channel is $R^{\uparrow}$ ($R^{\downarrow}$; with $R^{\uparrow} < R^{\downarrow}$), we can model the above description and obtain, in the case of parallel alignment:

$$R_P = \frac{R^{\uparrow} R^{\downarrow}}{R^{\uparrow} + R^{\downarrow}}, \tag{3.1}$$

while, for antiparallel alignment:

$$R_{AP} = \frac{R^{\uparrow} + R^{\downarrow}}{4}. \tag{3.2}$$

The magnetoresistance can now be calculated and gives:

$$MR = \frac{R_{AP} - R_P}{R_P} = \frac{\left(R^{\uparrow} - R^{\downarrow}\right)^2}{4R^{\uparrow} R^{\downarrow}} = \frac{(\alpha - 1)^2}{4\alpha}, \tag{3.3}$$

where $\alpha = \frac{R^{\uparrow}}{R^{\downarrow}}$ is a spin asymmetry parameter.

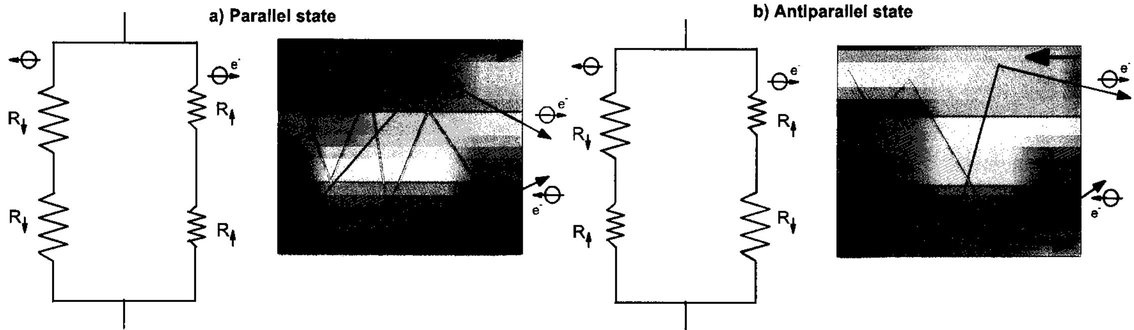

Figure 3.1: Simple two-current model of electron scattering in spin valves for (a) parallel and (b) antiparallel magnetic configurations.

3.2 Boltzmann semiclassical transport equation

The Boltzmann transport equation can be used to calculate the electron distribution function $f(\mathbf{k}, \mathbf{r}, t)$ of a system of electrons in non-equilibrium, so that $fd\mathbf{k}d\mathbf{r}$ represents the probability of finding an electron with wave vector within a volume $d\mathbf{k}$ around $\mathbf{k}$ and position within $d\mathbf{r}$ around $\mathbf{r}$ at a time t. The knowledge of the distribution function then enables us to calculate the electrical current density.

Under the influence of an external electric field $\mathbf{E}$ the distribution function is changed due to the changes in the $\hbar\mathbf{k}$ momentum and position $\mathbf{r}$. In fact, electrons that at time t are in the $d\mathbf{k}d\mathbf{r}$ volume, can leave $d\mathbf{r}$ due to the velocity $d\mathbf{r}/dt$ or $d\mathbf{k}$ due to the acceleration $d\mathbf{k}/dt$. We then have in first approximation:

$$\left(\frac{\partial f}{\partial t}\right)_{\text{field}} = -\frac{d\mathbf{k}}{dt}.\nabla_k f - \frac{d\mathbf{r}}{dt}.\nabla_r f, \tag{3.4}$$

where $d\mathbf{k}/dt$ is given by the semi-classical relation $d\mathbf{k}/dt = \frac{1}{\hbar}e\mathbf{E}$, ($\hbar$ is the reduced Planck constat). Due to electron scattering, a steady state occurs after a given time, and is characterized by:

$$\frac{df}{dt} = \left(\frac{\partial f}{\partial t}\right)_{\text{field}} + \left(\frac{\partial f}{\partial t}\right)_{\text{scat}} = 0. \tag{3.5}$$

This equation is then equivalent to:

$$\frac{df}{dt} = -\frac{d\mathbf{k}}{dt} \cdot \nabla_k f - \frac{d\mathbf{r}}{dt} \cdot \nabla_r f + \left(\frac{\partial f}{\partial t}\right)_{\text{scat}} = 0, \tag{3.6}$$

which is know as the Boltzmann transport equation.

The electrical current density $\mathbf{J}$ is given by the integral of the corresponding contributions for all occupied $\mathbf{k}$ states:

$$\mathbf{J}(\mathbf{r}) = \frac{e}{4\pi^3} \int \frac{d\mathbf{r}}{dt} f(\mathbf{k}, \mathbf{r}) d\mathbf{k}. \tag{3.7}$$

An important and often used approximation is the relaxation time approximation. When the electric field is removed, any distribution function $f(\mathbf{k}, \mathbf{r})$ must return to the equilibrium

distribution f_0. The relaxation time approximation says that the return of $f(\mathbf{k},\mathbf{r})$ to f_0 is exponential in time, with a characteristic relaxation time τ (defined as the mean time between scattering events):

$$\left(\frac{\partial f}{\partial t}\right)_{\text{scat}} = -\frac{f - f_0}{\tau} = -\frac{g}{\tau}, \tag{3.8}$$

where $f = f_0 + g$, with $g \ll f_0$.

The electron equilibrium distribution f_0 is simply given by the Fermi-Dirac distribution:

$$f_0 = \frac{1}{e^{(E-E_F)/k_BT} + 1}, \tag{3.9}$$

where $E = mv^2/2$ is the kinetic energy (free electron approximation), E_F is the Fermi energy and k_B the Boltzmann constant.

3.2.1 The case of thin films

The calculation of the electrical conductivity of thin films using the Boltzmann equation was first performed by Fuchs in 1938 [80] and (in 1952) further developed by Sondheimer [81]. Let us now follow their derivation by considering a thin film parallel to the xy plane, of dimensions $l \times w \times d$, and with thickness $d \ll l, w$ (Fig. 3.2). Let us further consider that an electrical field is applied along the x axis ($\mathbf{E} = E\hat{\mathbf{i}}$). We then have that $\nabla_r f$ is zero in all directions except $\hat{\mathbf{z}}$, as the film dimensions can be considered infinite in the film plane. The Boltzmann equation [Eq. (3.6)] can then be rewritten as:

$$\frac{\partial g}{\partial z} + \frac{g}{\tau v_z} = -\frac{eE_x}{mv_z}\frac{\partial f_0}{\partial v_x}. \tag{3.10}$$

This differential equation can be solved and the non-equilibrium distribution function is obtained:

$$g(\mathbf{v}, z) = -\frac{eE_x\tau}{m}\frac{\partial f_0}{\partial v_x}\left[1 + F(\mathbf{v})e^{-\frac{z}{\tau v_z}}\right], \tag{3.11}$$

where $F(\mathbf{v})$ is an integration constant that can depend on the velocity and must be determined using appropriated boundary conditions.

Assuming completely diffuse scattering at the outer boundaries of the film, the distribution function of electrons leaving the surface must be independent from their velocity directions. From Eq. (3.11) we see that this condition is only satisfied if $g(\mathbf{v}, z) = 0$ at the $z = 0$ and $z = d$ boundaries. Now, it is usual to separate the solutions of electrons moving away from the $z = 0$ surface (positive direction) and those moving in the opposite direction, away from $z = d$ (negative direction). The solutions of Eq. 3.10 are then:

$$g^+(\mathbf{v}, z) = -\frac{eE_x\tau}{m}\frac{\partial f_0}{\partial v_x}\left[1 - e^{-\frac{z}{\tau v_z}}\right], \tag{3.12}$$

and:

$$g^-(\mathbf{v}, z) = -\frac{eE_x\tau}{m}\frac{\partial f_0}{\partial v_x}\left[1 - e^{\frac{d-z}{\tau v_z}}\right], \tag{3.13}$$

where the superscript + (−) refer to electrons with $v_z > 0$ ($v_z < 0$).

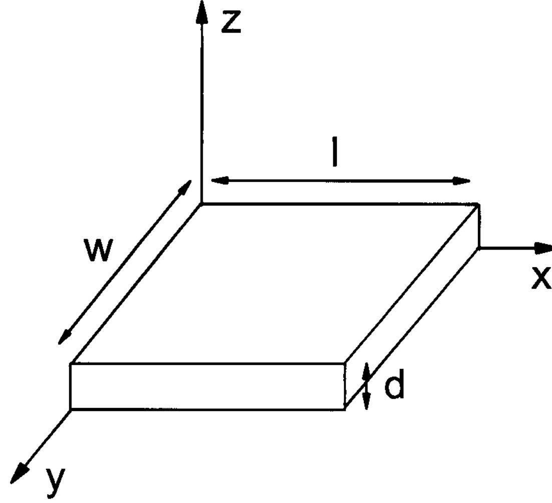

Figure 3.2: Schematic drawing of a thin film with dimensions $l \times w \times d$, with $(d \ll l, w)$.

We can now calculate the current density J. In the case we have been considering, the current density depends only on z due to the diffuse scattering at the outer surfaces of the film, allowing us to write:

$$J(z) = \frac{e}{4\pi}\left(\frac{m}{\hbar}\right)^3 \int v_x \left(g^+(\mathbf{v}, z) + g^-(\mathbf{v}, z)\right) d\mathbf{v}. \tag{3.14}$$

Notice that if the thickness of the film d is large $(d \to \infty)$, one recovers the Drude expression for the (bulk) electrical conductivity σ_0:

$$\sigma_0 = \frac{ne^2\tau}{m}. \tag{3.15}$$

From Equation (3.14) we can obtain, after some calculations, expressions for the limiting cases of thick ($k = d/l \gg 1$; $\ell \equiv$mean free path) and thin ($k = d/l \ll 1$) films [81]:

$$\frac{\sigma_0}{\sigma} = 1 + \frac{3}{8k}, \qquad (k \gg 1) \tag{3.16}$$

and

$$\frac{\sigma_0}{\sigma} = \frac{4}{3k\log(\frac{1}{k})}, \qquad (k \ll 1) \tag{3.17}$$

where the conductivities are normalized with respect to that of a bulk metal σ_0.

In the $d/l \longrightarrow \infty$ limit, Eq. (3.16) becomes $\sigma = \sigma_0$. Then, far from the surface, the bulk value of the conductivity is obtained. However, in a superficial region of characteristic length τv_z (smaller than the electron mean free path, ℓ), the conductivity is reduced from its bulk value [see exponential term in Eqs. (3.12) and (3.13)].

3.2.2 The outer surfaces

The theory developed by Sondheimer also takes into consideration the case where specular reflection occurs. He considered that the probability of an electron being specularly reflected is given by a reflection coefficient p that varies between $p = 0$ for purely diffuse scattering and $p = 1$ for fully specular scattering. In the last case, the electron velocity in the direction of the applied electric field is not altered upon reflection at the outer boundaries and the electrical conductivity will be the same as in the bulk situation.

Equations (3.12) and (3.13) are then written as [81]:

$$g^{+}(\vec{v},z) = -\frac{eE_x\tau}{m}\frac{\partial f_0}{\partial v_x}\left[1 - \frac{1-p}{1-p\,\exp(-\frac{d}{\tau v_z})}\exp(-\frac{z}{\tau v_z})\right], \tag{3.18}$$

and

$$g^{-}(\vec{v},z) = -\frac{eE_x\tau}{m}\frac{\partial f_0}{\partial v_x}\left[1 - \frac{1-p}{1-p\,\exp(\frac{d}{\tau v_z})}\exp(\frac{d-z}{\tau v_z})\right]. \tag{3.19}$$

The limits of thick and thin film (Eqs. 3.16 and 3.17) are now given by:

$$\frac{\sigma_0}{\sigma} = 1 + \frac{3}{8k}(1-p), \qquad (k \gg 1) \tag{3.20}$$

and

$$\frac{\sigma_0}{\sigma} = \frac{4}{3}\frac{1-p}{1+p}\frac{1}{k\log(\frac{1}{k})}. \qquad (k \ll 1) \tag{3.21}$$

This description is the simpler possible and several other more complex approaches were later developed. Ziman [82] calculated the reflection of plane waves on rough surfaces, giving rise to an angular dependent reflection coefficient $p(\theta)$, where θ is the incidence angle. Assuming that the roughness $\zeta(x,y)$ follows a normal distribution and defining the quantity $\eta = \sqrt{\langle\zeta(x,y)^2\rangle}$, Soffer [83] obtained the specular reflection coefficient:

$$p(cos\theta) = \exp\left[-(\frac{4\pi\eta}{\ell})^2 cos^2\theta\right]. \tag{3.22}$$

3.3 Semiclassical models of GMR

3.3.1 The Model of Camley and Barnas

In 1989, Camley and Barnas [84, 85] extended the Fuchs-Sondheimer theory to calculate the conductivity of a FM/NM/FM spin valve. In this case, the solutions to the Boltzmann equation [similar to Eqs. (3.12) and (3.13)] have to be found for each layer, and spin-dependent scattering must also be included. Thus, one must consider a spin-dependent electron mean free path, $\ell^{\sigma} = \tau^{\sigma} v_F$ (with the spin $\sigma =\uparrow,\downarrow$). The resulting four solutions ($g_{\uparrow}^{+}$, $g_{\uparrow}^{-}$, $g_{\downarrow}^{+}$ and $g_{\downarrow}^{-}$) for each layer are then treated with appropriate boundary conditions. Notice that the separation between the two conduction channels, up and down spins, is only valid at low temperatures, where spin-flip magnon scattering can be neglected [86].

In the Camley-Barnas model, fully diffuse scattering at the outer boundaries was initially assumed ($p = 0$). In the inner interfaces, electrons can be (spin-dependent) coherently transmitted (with a transmission coefficient T^σ), reflected (with a reflection coefficient R^σ) or diffusely scattered ($D^\sigma = 1 - T^\sigma - R^\sigma$). The perturbation functions g of layer i and $i+1$ are then related by:

$$g^+_{\sigma,i+1} = T^\sigma g^+_{\sigma,i} + R^\sigma g^-_{\sigma,i+1}. \tag{3.23}$$

The parameters T^σ, R^σ and D^σ are adjustable and independent of the incidence angle. $R^\sigma = 0$ at the inner interfaces is usually assumed.

The current density of the layer i is then calculated:

$$J_i(z) = \frac{e}{4\pi}\left(\frac{m}{\hbar}\right)^3 \int \sum_{\uparrow,\downarrow} \sum_{+,-} v_x g^\pm_{\sigma,i}(\mathbf{v}, z) d\mathbf{v}, \tag{3.24}$$

which allows us to calculate the total conductivity.

To calculate the Giant Magnetoresistance ratio of the spin valve, the above calculations must be performed for both parallel and antiparallel alignment of the FM magnetizations. The GMR ratio then depends on the existence of some degree of spin-dependent asymmetry. One source of asymmetry arises from the interfacial transmissivity between the FM and NM layer, since T^σ can depend on the electron spin. An asymmetry parameter β corresponding to interfacial spin-dependent scattering is then defined:

$$\beta = \frac{T^\uparrow}{T^\downarrow}. \tag{3.25}$$

On the other hand, spin-dependent scattering in the *bulk* of the FM layers gives rise to a difference in the mean free paths ℓ_i^σ and a corresponding asymmetry parameter α:

$$\alpha = \frac{\ell_i^\uparrow}{\ell_i^\downarrow}. \tag{3.26}$$

The importance of each mechanism (bulk or interfacial spin dependent scattering) depends on the FM materials and FM/NM interfaces present in each spin valve.

3.3.2 The model of Hood and Falicov

Hood and Falicov [87], arguing that interfacial spin-dependent scattering can play an important role in the GMR effect [5, 88], and that in the Camley-Barnas model the interfacial parameters T, R and D appeared in a purely phenomenological way, introduced a constant inner potential V_i^σ within each layer (naturally spin dependent in the FM layers). Assuming then that scattering is purely elastic and coherent, they calculated the transmission and reflection coefficients. As a consequence of spin dependent potentials, electrons incident at grazing angles can be totally reflected. In the parallel state, these fully reflected electrons are confined in one layer and experience only bulk scattering in that layer.

However, the model of Hood and Falicov still contains a phenomenological parameter S ($0 \leq S \leq 1$), to account for defects and impurities in the interfaces. The parameter S denotes the degree of specular scattering ($S = 1 - D$) and can be a crucial parameter to the GMR ratio. Also notice that in the model of Hood and Falicov the number of adjustable parameters is larger than in the Camley-Barnas model.

3.3.3 Temperature dependence of GMR

It is well known that the magnetoresistive ratio decreases with increasing temperature [89] and that several mechanisms can contribute to such thermal decrease [90]: Scattering by magnons in the ferromagnetic layer; phonon scattering in the non-magnetic spacer and possible temperature dependent interfacial scattering. Using the formalism developed above based on the Boltzmann equation, it is possible to include spin-intermixing between spin up and spin down channels to calculate the temperature dependence of the GMR ratio of a spin valve.

Fert and Campbell [86] found that when spin-flip scattering is present in a FM material, its electrical resistivity ρ is given by:

$$\rho = \frac{\rho^{\uparrow}\rho^{\downarrow} + \rho^{\uparrow\downarrow}\left(\rho^{\uparrow} + \rho^{\downarrow}\right)}{\rho^{\uparrow} + \rho^{\downarrow} + 4\rho^{\uparrow\downarrow}}, \tag{3.27}$$

where $\rho^{\uparrow}$ ($\rho^{\downarrow}$) is the electrical resistivity experienced by spin up (down) electrons and $\rho^{\uparrow\downarrow}$ is the resistivity arising from spin flip collisions. Dieny *et al.* [90] were then able to calculate the temperature dependence of the GMR ratio and to analyze the relative importance of different contributions to the observed experimental results. They concluded that spin intermixing due to magnon scattering is most important to the observed decrease of GMR with increasing temperature. Also, phonon scattering (interfacial scattering) plays a small role in (does not influences) the GMR(T) behavior.

3.4 Quantum mechanical models

When the layer thickness becomes sufficiently thin, the semiclassical models are no longer valid and one needs a quantum mechanical (QM) treatment. This occurs when the quantization of the electron momentum in the z direction (k_z) can no longer be neglected due to the finite size of the sample along z. The quantization then becomes important when the mean free path ℓ is much larger than the layer thickness d.

In the fifties, Kubo developed a method to calculate the response of a quantum system to an external potential and, particularly, of an electrical current to an electric field. Quantic models based on the Kubo formalism were developed by Vedyayev [91, 92], Camblong and Levy [93, 94], and Levy, Zhang and Fert [95, 96] to calculate the electrical resistance and magnetoresistance of magnetic multilayers and spin valves.

Levy, Zhang and Fert treated the case of a NM/FM multilayer to obtain the giant magnetoresistance in the CIP geometry. The local conductivity σ depends only on the z axis perpendicular to the plane of the multilayer and electrons are treated as wave packets, with spin dependent scattering probabilities in the interfaces and in the bulk of the FM layers. They found that both interfacial and bulk scattering affect equally the electron mean free path, a result that differs from those obtained in the semiclassical Boltzmann formalism. Furthermore, QM models predict a finite conductivity even for thin films without bulk scattering. On the other hand, semiclassical theory predicts, in this case, that the conductivity goes to infinite, even in the presence of scattering due to superficial roughness.

The QM model of Camblong and Levy included spin-dependent interfacial scattering and treated scattering in the bulk and at the interface in an unified way. Although this model is based on the Kubo formalism, some approximations are made, limiting its application to the semiclassical limit. Thus, the final results are also semiclassical and agree with those obtained from the Boltzmann transport equation.

Finally, Zhang and Butler [97] solved numerically the Kubo equation for the case of free electrons with random point scatters in a multilayer. They then compared the obtained results with those of both semiclassical and quantum mechanical models. They showed that the semiclassical theory only fails in the very thin layer limit. Furthermore, the model presented by Levy, Zhang and Fert [95, 96] only gives correct results in the very thin and very thick films. From all the above, the semiclassical model is usually preferred over a quantum one.

3.5 Advanced spin valve structures

To increase the areal density of hard drives (section 1.3.2), the industry always seeks new ways to increase the Giant Magnetoresistance ratio of spin valves (SVs), currently reaching values close to 20%. Many other important device characteristics are also continuously researched, like thermal stability, exchange bias and bias point control. To achieve these goals, improved versions of the simple try-layered structure of a common spin valve were developed, among which specular, synthetic and spin filter spin valves.

3.5.1 Specular spin valves

Oxygen was initially used as a surfactant during deposition, to obtain smooth interfaces [98]. Also, the deposition of thin layers of noble metals (4 Å of Au or Ag) on the top of the spin valve structure resulted in an increase of the GMR from 13.5% to 15% [99]. Spin valves with oxide AFM layers (NiO [100, 101, 102] or Fe_2O_3 [103]) showed GMR ratios of over 15%. This enhancement was attributed to specular reflection at the AFM/FM interface leading to increased spin-dependent electron scattering. However, these AFM oxides exhibit several undesirable characteristics for applications: NiO has a low blocking temperature ($\sim$ 500 K) and Fe_2O_3 has small exchange fields. On the other hand, metallic antiferromagnets have high blocking temperature and provide large exchange fields but are (spin-independent) shunting paths for the electrical current. Consequently, spin valves with a metallic AFM layer usually show smaller GMR than those with an oxide AFM.

To overcome this limitation, the so called specular spin valve was proposed [104]. In this structure, electrons are confined in the active FM/NM/FM try-layer by thin nano-oxide layers [NOLs; Fig. 3.3(a)] inserted in both the pinned and free FM-layers. The large electron potential difference at the corresponding NOL/FM interfaces [105] then lead to specular scattering, *i. e.*, both the electron wave vector parallel to the interface and its spin are conserved. Usually the NOLs are formed by the partial oxidation of the FM pinned and free layers. A setback of this design is the necessity for a discontinuous NOL in the pinned layer to still obtain large exchange bias, leading to a smaller than possible GMR. In fact, GMR ratios of only $\sim$ 15% are commonly observed in NOL specular spin valves [106, 107], indicating that

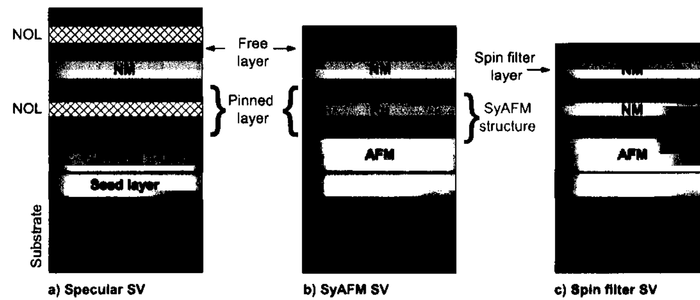

Figure 3.3: Structure of (a) specular spin valve with two nano oxide layers inserted in the pinned and free layers, (b) synthetic antiferromagnet spin valve and (c) spin filter spin valve.

the specularity at the NOL/FM interfaces is much smaller than one. Notice that, in theory, the GMR of a specular spin valve should approach that of multilayered structures. However, for spin valves one currently obtains GMR$\sim$ 20% [11], while for multilayers GMR$>$ 50% [15]. Besides increasing GMR, the fabrication of the NOL also has the desirable effect of decreasing the interlayer coupling due to the decrease of interfacial roughness [107]. Current research focus on the enhancement of GMR using different oxide layers (CoFe, Co, Fe, NiFe, Cu, Ta,...), and shows that nano-oxide layers formed by the oxidation of CoFe lead to the higher GMR ratios [108]. The effect of the NOL position in the spin valve [109], Cu spacer [110] and free layer [111] thicknesses, oxidation method [104, 106] and its duration [104, 112], and annealing temperature [109] were also studied. Semi-classic treatments of the electrical resistivity of specular spin valves using the Boltzmann formalism and assuming specular reflection at the NOL/FM interfaces were also developed [113], including the effect of NOL insertion in different positions of the spin valve stack.

3.5.2 Synthetic antiferromagnetic and spin filter spin valves

One way to increase the exchange field of a spin valve is to replace the FM pinned layer by what is called a synthetic antiferromagnet (SyAFM or SAF) pinned layer-structure [114, 115, 116] [Fig. 3.3(b)]. This SAF structure is made by two FM layers separated by a thin non-magnetic metallic layer (usually Ru). For a Ru thickness of $\approx$5–7 Å, a very strong (negative) RKKY-like exchange interaction between the two FM layers occurs, leading to the antiparallel alignment of their magnetizations. Usually one of the FM layers is still pinned by a biasing AFM layer. The magnetic fields needed to reverse the magnetization of the other FM layer can reach several thousands of Oersteds and these spin valves show enhanced thermal stability [117]. Furthermore, the magnetostatic stray field created by the pinned layer on the free layer is reduced due to the antiparallel alignment of the SAF structure. This, allows an easier control of the bias point of a spin valve sensor [118].

To increase magnetic recording densities, the thickness of the pinned layer must decrease [119]. However, the GMR ratio decreases strongly for free layer thicknesses below $\sim$ 50 Å, due to diffuse scattering at the interface between the free and capping layers, which prevents majority electrons from experiencing their full mean free path in the free layer. To overcome this limitation, a so called spin filter layer can be added to the FM/NM/FM spin valve

structure [Fig. 3.3(c)]. In this new structure, a high conductive non-magnetic layer (usually Cu; enhancing electron mean free path) is deposited just above a very thin FM free layer [120]. Large magnetoresistance ratios and small free layer thicknesses (~ 25 Å) can then be made compatible [121]. Also, the magnetic field generated by the electrical current passing through the two NM (spacer and spin filter) layers will mostly cancel at the free layer, again helping to control the bias point of a SV sensor [122, 123].

Chapter 4

Specular spin valves

Summary

A spin valve (SV) [7] is a nanostructure with two ferromagnetic (FM) layers separated by a non-magnetic (NM) spacer. An antiferromagnetic (AFM) material fixes the magnetization of the adjacent FM layer, the so called pinned layer. The other FM layer, called the free layer, is only weakly coupled to the pinned layer by a small magnetic interaction. Giant magnetoresistance (GMR) in a spin valve nanostructure arises from the difference in scattering of spin-up and spin-down electrons at the internal and outer interfaces and in the bulk of the FM layers. When the free layer magnetization reverses with respect to that of the pinned layer by the application of a small external magnetic field, the electrical resistance of the SV is altered.

The first semi-classical treatments of the GMR effect only considered diffuse scattering [84, 124] but when a spin valve is between two insulating smooth layers (producing a high potential barrier) electrons can be specularly scattered at the corresponding interfaces, as shown on a Co/Cu/Co structure bounded by a NiO surface [99]. Recent reports on spin valves with the pinned and/or free layer partially oxidized [104, 125, 103] under air or O_2 exposure, showed great MR enhancement when compared to that of conventional (non-oxidized) spin valves (CSV). Electrons are believed to reflect specularly at the nano-oxide layer (NOL)/FM interfaces, thus yielding higher MR ratios in this type of SVs. The simultaneous knowledge of the temperature dependence of the MR ratio, absolute ΔR and R(T) for zero and applied magnetic field, is important to understand the different roles played by magnetic/non-magnetic electron scattering processes, and the specific effects arising from the nano-oxide layers.

We present here a comparative study of a non-specular MnIr/CoFe/Cu/CoFe spin valve and the corresponding specular SV version obtained by controlled nano-oxidation of the CoFe layers. The introduction of the NOLs more than doubled the GMR value of the specular SV compared to that of the non-specular. However, the MR(T) dependence is quasi-linear in both cases, extrapolating to zero MR practically at the same temperature. Also, below T$\sim$ 175 K the MR(H) curves of the specular spin valve displays two anomalous bumps not seen in the non-specular curves. A model based on the total energy [126] of a NOL SV

was developed, to describe the orientation of the magnetizations of the FM layers under an external magnetic field and the resulting MR(H) behavior. The model accounts well for the observed anomalous MR(H) bumps, relating them to the complex M-reversal in the pinned layer.

Extended experimental measurements on MR(H;T) from 300 to 20 K, enabled us to extract the temperature dependence of the exchange bias (H_{exch}) and the pinned layer coercive fields (H_c). We will relate the observed anomalous enhancement of these fields at low temperatures to the presence of an AFM oxide in the NOLs, having a blocking temperature $T_B \approx 175$ K.

We also performed SQUID magnetization (M) measurements (300–20 K) both for the specular and non-specular SV, revealing the magnetization changes in the free and pinned CoFe layers. Direct comparison of MR(H) and M(H), including their temperature dependencies, shows a drastic departure from the usual connection between transport and magnetic processes (in the case of the specular SV), indicative of the importance of interfacial scattering in the NOL SV.

A detailed study on the existence of training effects in specular spin valves (using different experimental procedures) was performed in the 320–15 K range. Such effects were only observed in the specular spin valve below $T \approx 150$ K, and will be related to rearrangements in the domain structure of the AFM nano-oxide layer.

4.1 Experimental details

Specular SV structures were fabricated using a standard SV inserted between two nano-oxide layers of CoFe (Table 4.1). A NOL-SV with the structure Ta (67 Å)/ NiFe (42 Å)/MnIr (90 Å)/CoFe (15 Å)/oxidation (NOL1)/CoFe (15 Å)/Cu (22 Å)/CoFe (40 Å)/oxidation (NOL2)/Ta (30 Å) was grown on a glass substrate using Ion Beam Deposition. The samples were post-annealed in vacuum (10^{-6} Torr) at 270° C for 10 minutes, and then cooled in a 3 kOe applied field. CoFe stands for $Co_{90}Fe_{10}$, NiFe for $Ni_{81}Fe_{19}$ and MnIr for $Mn_{83}Ir_{17}$. The CoFe oxidation was done using the remote plasma method, for 3 min. To compare results, a standard (non-specular) spin valve was also fabricated, with the same composition, nominal thickness and growth conditions, except for the missing NOL (Table 4.1).

The first FM deposited layer (CoFe on top of MnIr) will be called here the *below-NOL1* FM-pinned layer (FM_b) since its upper part is oxidized over an adequate thickness to form the NOL1 layer. The FM layer deposited after this oxidation will be called the *above-NOL1* FM-pinned layer (FM_a). The pinned layer thus consists of both FM_b and FM_a sub-layers, separated by the NOL1 oxide layer (see Fig. 4.14, page 94).

The electrical resistivity and magnetoresistance of the studied samples were measured with a standard four-point d.c. method, with a current stable to $1:10^6$ and applied magnetic fields up to 7 kOe. An automatic data acquisition system provided R(T) values every 80 mK. SQUID magnetization was measured at several temperatures between room temperature (RT) and 25 K, for which independent MR(H) measurements were also done.

Series	Spin valve	Structure
Ex3651	CSV	$Ta_{67}/NiFe_{42}/MnIr_{90}/CoFe_{30}/Cu_{22}/CoFe_{40}/Ta_{30}$
Ex3652	NOL SV	$Ta_{67}/NiFe_{42}/MnIr_{90}/$...
		...$CoFe_{15}/NOL1/CoFe_{15}/Cu_{22}/CoFe_{40}/NOL2/Ta_{30}$

Table 4.1: Conventional and specular spin valves studied in this work. The numbers in subscript are the layer thicknesses in Å.

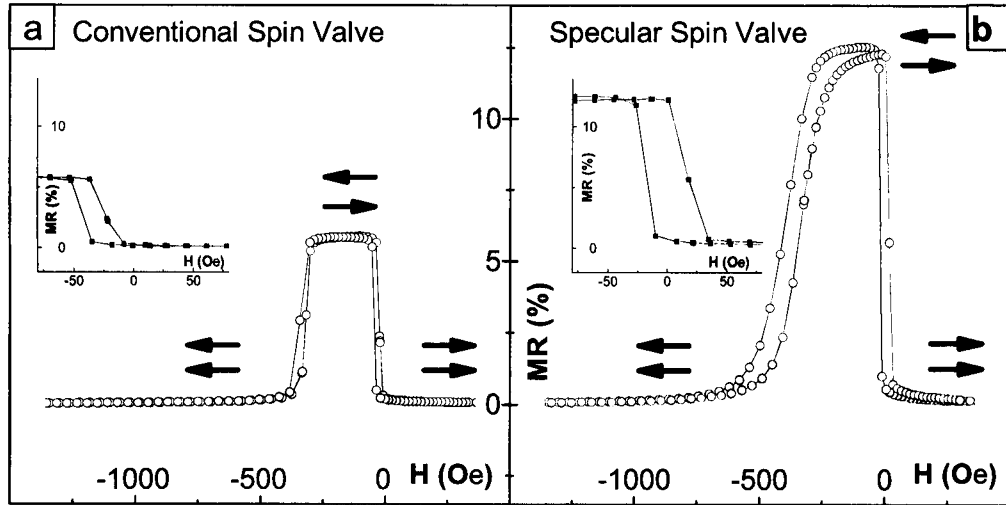

Figure 4.1: Magnetoresistance curves obtained at room temperature for (a) conventional and (b) specular spin valves. Notice the enhanced GMR ratio of the NOL SV.

4.2 Comparative study of nano-oxide and conventional spin valves

4.2.1 Room temperature Magnetoresistance

The room temperature MR(H) curve of the Conventional Spin Valve (CSV) exhibits the usual SV behavior [Fig. 4.1(a)]: In a positive field both pinned and free layers are parallel aligned ($\rightrightarrows$; low resistance R_P), but the magnetization of the free layer abruptly reverses in a small negative field (antiparallel alignment results, $\leftrightarrows$), leading to a high resistance R_{AP}-state which persists over a finite ΔH-range. Parallel alignment in the opposite sense ($\leftleftarrows$) ultimately occurs when the negative field is large enough to overcome the exchange bias between the AFM and FM pinned layer, leading again to the low resistance parallel state (R_P). Defining the Giant Magnetoresistance ratio as:

$$GMR = \frac{R_{AP} - R_P}{R_P}, \tag{4.1}$$

one obtains GMR = 5.9% for the conventional SV.

The MR(H) cycle of the NOL SV [Fig. 4.1(b)] is quite similar to that of the conventional spin

valve, displaying the usual two R-states associated with parallel and antiparallel magnetizations of the pinned and free layers. However, the incorporation of the two nano-oxide layers greatly enhances the MR ratio over that observed in the nonspecular SV, from 5.9% to 12.5% at room temperature. The large MR value is associated with electron-specular reflection at the NOL/FM interfaces.

The exchange field of the specular spin valve ($H_{\text{exch}} = 380$ Oe) is larger than that of the non-specular one ($H_{\text{exch}} = 330$ Oe). This is likely related to the smaller thickness of the pinned layer (t_{pl}) of the NOL SV due to the partial oxidation of the FM_b layer ($H_{\text{exch}} \alpha \frac{1}{t_{pl}}$; [19]). Using our experimental data, we estimate a FM_b+FM_a pinned layer thickness $t_{pl} \approx 26$ Å. Thus, about 4 Å of the FM_b layer were oxidized and the thickness of the NOL is ~ 8 Å (assuming that the incorporation of oxygen results in an expanded oxide layer relatively to the metal one by a factor of ~ 2 [125]).

The reversal loop of the free layer of the NOL SV at RT [inset of Fig. 4.1(b)] shows a small interlayer coupling field H_{coup} (only 3 Oe when compared to 50 Oe in the CSV), while retaining soft magnetic properties (free layer coercive field 16 Oe for the NOL SV and 10 Oe for the CSV). The almost suppression of H_{coup} results from the reduction of roughness in the NOL SV [104, 107] (thus reducing the Néel orange peel coupling contribution), and from the enhancement of the RKKY-type coupling contribution due to specular reflection at the NOL/FM interfaces [127, 107].

4.2.2 Temperature dependent results

4.2.2.1 Magnetoresistance

We also performed MR(H) measurements for both the non-specular and specular SVs below RT (Fig. 4.2). The measurements always started with the sample saturated at positive fields, where the CoFe FM-layers (free and pinned) are spin aligned ($\rightrightarrows$), providing the low resistance state. Striking differences are observed between the MR(H) curves of the two spin valves as temperature decreases. For the non-specular spin valve [Fig. 4.2(a)], we always observe the same features: MR abruptly rises near $H = 0^-$ (at a negative field of a few tens of Oe) when the free layer magnetization suddenly reverses ($\leftrightarrows$ alignment). This is followed by a ΔH-region (plateau) of maximum resistance due to the persistence of the antiparallel alignment in the active FM layers. Finally, an abrupt decrease in the resistance occurs when the magnetization of the pinned FM layer reverses ($\leftleftarrows$ alignment). These usual features occur over the whole temperature range.

In contrast, the NOL spin valve [Fig. 4.2(b)] exhibits only an incipient ΔH-region of maximum resistance near $H = 0$, and then MR gradually decreases towards zero at high negative fields. These features rapidly grow below $\sim$175 K, when two anomalous bumps also emerge in MR(H), one at each side of the curve. Since these effects are absent in the non-specular SV [Fig. 4.2(a)], they are due to the presence of the NOL. A peculiar MR(H) asymmetry also arises in the NOL-SV below $\sim$175 K: Whereas at moderate negative field we always reach zero MR, indicating perfect $\leftleftarrows$ alignment, under positive H we are unable to achieve full $\rightrightarrows$ alignment in fields up to 7 kOe. This effect will be discussed in more detail below (section 4.6).

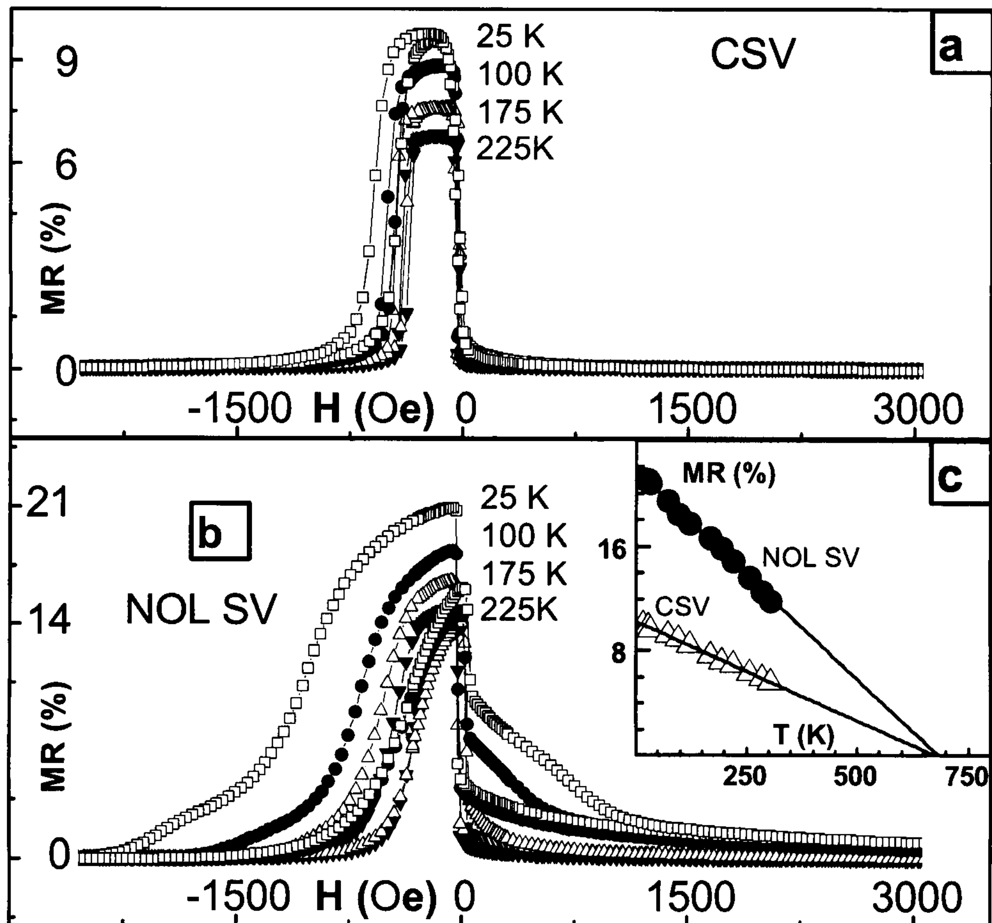

Figure 4.2: MR(H) curves for the (a) non-specular and (b) specular spin valves at selected temperatures. (c) Temperature dependence of the GMR ratio for the non-specular (hollow triangles) and specular (solid circles) spin valves. Notice that the extrapolation of the MR(T) data to $T > 300$ K gives zero MR at a common $T_C \approx 675$ K.

Figure 4.2(c) shows the temperature dependence of the GMR ratio for the studied spin valves. For the non-specular SV (lower curve), the maximum MR is 5.9% at RT and rises quasi-linearly with decreasing temperature, reaching 10% at 20 K. A similar behavior was observed in others non-specular SVs [116] and attributed to electron-spin wave scattering in the FM layers [128]. For the specular SV (upper curve), the GMR ratio is also linear in T, rising from 12.5% at RT to 21.1% at 20 K. The MR(T) extrapolation to high temperature for both spin valves (CSV and NOL SV), gives zero at a common $T_C \sim 675$ K [Fig. 4.2(c)], the effective Curie temperature of the FM layers. This value is much lower than that of bulk CoFe ($T_C \approx 980$ K). Dieny et al [89] showed that T_C in SVs depends essentially on the FM materials and on the nature of the FM/NM and NM/FM interfaces. Our work shows that the nature of the SV outer boundaries (metallic or nano-oxide) has no significant effect on T_C.

4.2.2.2 Temperature dependence of H_{exch} and H_c

Important information can be obtained from the temperature dependence of the exchange ($\mathrm{H_{exch}}$) and pinned layer coercive ($\mathrm{H_c}$) fields (Fig. 4.3). Comparing the $H_{\mathrm{exch}}(T)$ dependence of both SVs, as extracted from the MR(H;T) curves, one finds $\mathrm{H_{exch}}$ always larger in the NOL SV, but growing with decreasing temperature at a slower pace than in the CSV until $T \sim 175$ K, where both are almost equal. Below this temperature, $\mathrm{H_{exch}}$ of the NOL SV grows much faster. On the other hand, $\mathrm{H_c}$ of the NOL SV is also higher than that of the CSV over the entire temperature range, exhibiting much stronger temperature dependence with an abrupt rise below ~ 175 K. We relate these features with the presence of an AFM oxide with $T_B \sim 175$ K, which contributes with extra pinning in the NOL SV.

In fact, several oxides are thought to be present in the (non-uniform) NOL1, formed by the partial oxidation of the pinned layer [129]. The NOL1 is usually discontinuous, with some regions of direct contact between the FM_b and FM_a pinned layers (only so can large exchange fields be obtained). Also, a mixture of CoO, FeO and Fe_2O_3 is found in the nano-oxide layer. Furthermore, the preferential oxidation of Fe over Co is always observed [125, 130, 131, 132]. Notice that the formation energies of CoO, FeO and Fe_2O_3 are, respectively, -216, -245 and -742 kJ/mol [133], and thus Fe-oxides are more stable than Co-oxides. The evidence on the presence of different oxides was obtained using both High Resolution Transmission Electron Microscopy and X-ray Photoelectron Spectroscopy [129, 133, 132]. Furthermore, the blocking temperature of the oxides present in the NOL was observed to strongly increase with increasing concentration of Fe in spin valves with $Co_{1-x}Fe_x$ FM layers, being above room temperature for $x = 0.26$ [134]. Since the blocking temperature of FeO is only $T_B \sim 100$ K [19], and that of Fe_2O_3 is $T_B \sim 450 - 620$ K [19], one concludes that the AFM oxide responsible for the observed enhancement of $\mathrm{H_{exch}}$ is likely Fe_2O_3. Finally, notice that T_B usually decreases with decreasing layer thickness [135], explaining the lower value observed in our NOL SV ($T_B \sim 175$ K).

The coupling field between the pinned and free layer and the coercive field of the free layer do not show a similar significant rise as temperature decreases (not shown). If the NOL2 had a composition similar to that of NOL1, with an AFM oxide with $T_B \sim 175$ K, one would expect H_{coup} to significantly change below T_B. The absence of such enhancement is likely due to the formation of Ta_2O_5 through the solid state reaction $CoFeO_x$+Ta$\rightarrow$ CoFe+Ta_2O_5

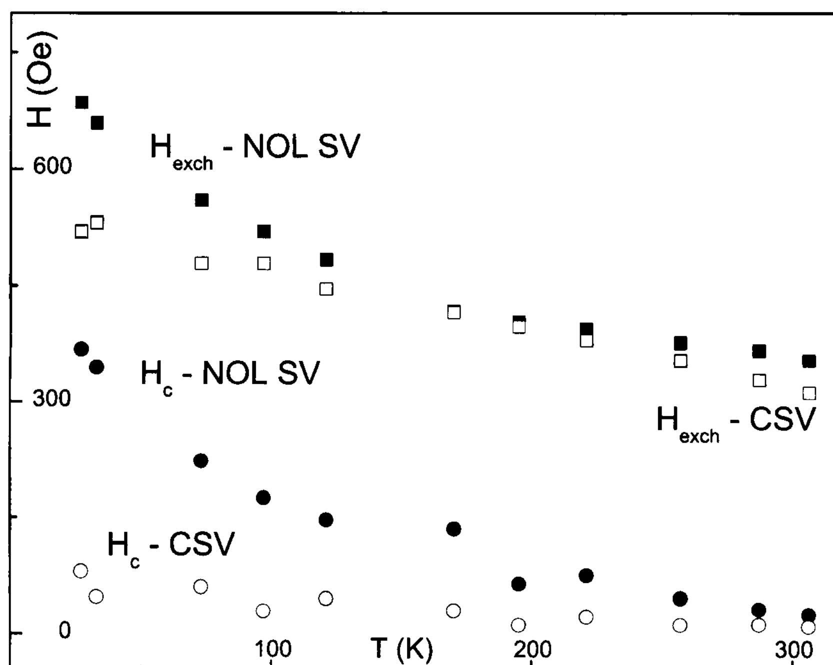

Figure 4.3: Temperature dependence of exchange H_{exch} and pinned layer coercive H_c fields of the conventional and specular spin valves. Notice the enhancement of both fields below ~ 175 K for the NOL SV.

[129]. This reaction is expected because the electronegativities (in the Pauling scale) of O, Co, Fe and Ta are 3.44, 1.88, 1.83 and 1.5, respectively. Thus, ionic bonds between O and Ta are more likely than with Co or Fe [129].

4.2.2.3 Magnetization versus Magnetoresistance

Figure 4.4 compares the MR(H) and M(H) behaviors at different temperatures (225–25 K), both for the non-specular (left curves) and specular (right curves) spin valves. The hysteretic loops can be analyzed in terms of magnetization-changes in the free and pinned CoFe layers.

For the non-specular SV one observes the usual good correlation between M(H) and MR(H) curves at all temperatures. However the NOL spin valve behaves quite differently, with MR(H) still fairly large when the magnetization enters its saturation regime. This effect is more pronounced under negative applied field and greatly increases with reducing temperature. Therefore, important resistive mechanisms are still operative at (long range) magnetic saturation in the NOL spin valve, associated with the persistence of short-range disorder.

We may assume that a complex domain structure is formed in the FM_a CoFe layer, through the competition of several magnetic interactions: Exchange coupling between the MnIr and CoFe pinned-layers, coupling across the NOL and exchange coupling between the AFM oxide and the CoFe layer. Thus, one envisages that local magnetic disorder, though contributing little to the total magnetic moment of the specular SV, plays a non negligible role in electron

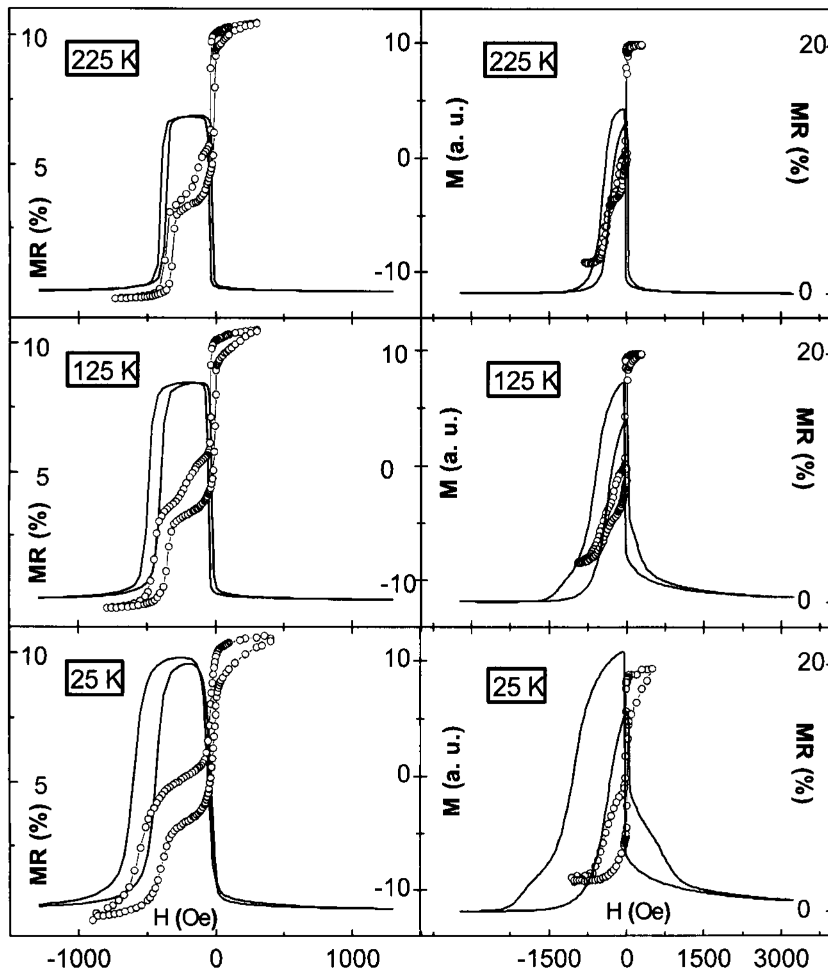

Figure 4.4: Comparative plots of the MR(H) (lines) and M(H) (circles) of the non-specular (left side) and specular (right side) spin valves at three different temperatures. Notice that the M(H) curves display three M-reversal that we associate with the CoFe free, deep NiFe and CoFe pinned layers.

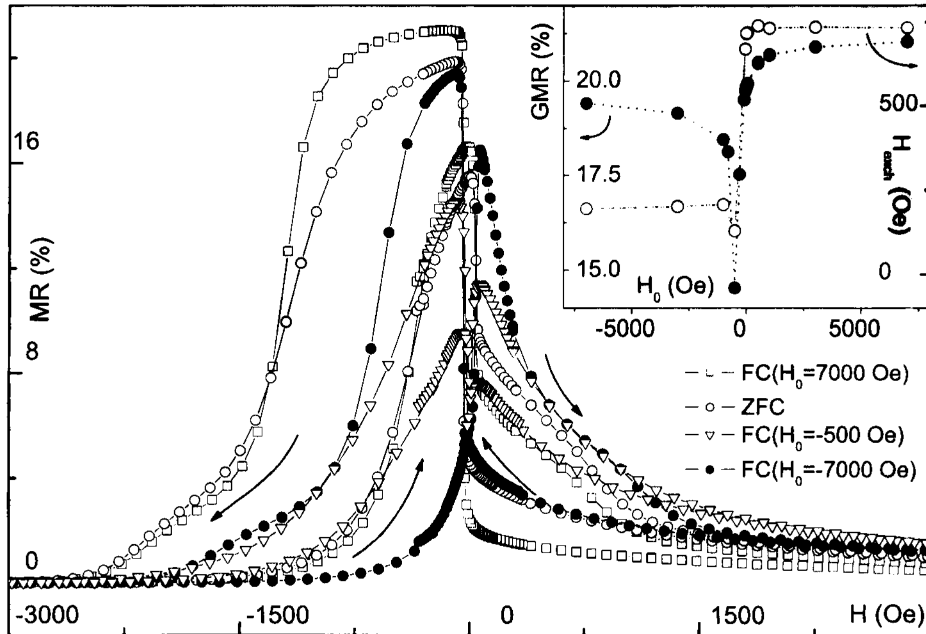

Figure 4.5: MR(H) curves measured at 15 K for different values of the cooling field H_0 and corresponding dependence of the GMR ratio and exchange field (inset).

scattering. These results will be discussed in more detail in section 4.6, but clearly show the importance of disorder at the NOL/FM interfaces on the transport properties of specular spin valves.

4.3 Impact of the magnetism of nano oxide layers on the GMR in specular spin valves

4.3.1 Field cooling experiments

To further study the effects of the NOL on the magneto-transport of specular SVs we measured MR(H) cycles at different constant temperatures (15–300 K), after zero (ZFC) or field cooling (FC) under different applied fields H_0 ($|H_0| \leq 7000$ Oe; always applied along the easy axis of the NOL SV). At low temperatures (15 K) we found a sharp minimum in the value of the GMR ratio after FC under $H_0 = -500$ Oe. The field-cooled GMR curves depart from the ZFC below $T \sim 175$ K, where the exchange field is also observed to start depending on H_0. In fact, the shape of the MR(H) curves is critically dependent on the sign and value of H_0. These features are related to the effects of H_0 on the pinned layer magnetization and consequently on the AFM ordering of the NOL below its blocking temperature.

Figure 4.5 displays MR(H) curves obtained at 15 K after ZFC and FC runs under selected H_0. The inset displays the GMR ratio and exchange field obtained at 15 K as a function of H_0, exhibiting a very sharp minimum for H_0=-500 Oe.

Starting with ZFC and positive H (Fig. 4.5) one first sees the free layer M-switch when $H \sim 0$, producing a large ΔR/R step. When negative H exceeds the exchange + coercive fields ($-H_{\text{exch}} - H_c$) of the pinned layer, its magnetization reverses producing a large MR decrease. In the MR(H) branch corresponding to increasing H, the pinned layer magnetization reverses when $H = -H_{\text{exch}} + H_c$ and when $H \sim 0$ one sees the free layer M-switch, producing a large (negative) $\Delta R/R$ step.

After FC under different H_0, the observed high-resistance plateau ($\leftrightarrows$ SV state) in MR(H) at 15 K becomes wider and flatter for positive H_0 than for $H_0<0$ (and ZFC). The curve obtained after $H_0 \gg 0$ cooling also shows much lower MR values at large positive H (better $\rightrightarrows$ alignment). After large $H_0<0$ cooling (Fig. 4.5; increasing H-branch) the pinned layer starts its M-reversal at negative H but only at high positive H is it complete, much later than the free layer M-reversal (sharp positive $\Delta R/R$ step at $H \sim 0$). In the decreasing H-branch the pinned layer reverses its magnetization at a negative field much smaller than under $H_0 > 0$ (see corresponding lower H_{exch} in the inset). In the MR(H) curve for H_0=-500 Oe one has $\Delta R/R$ at switching (in both branches), far below the corresponding values obtained with other H_0 values, indicating poor antiparallelism.

We then performed MR(H) measurements at other temperatures after FC(H_0) runs from 320 K, enabling us to determine H_{exch}(T) and GMR(T) as shown in Fig. 4.6 and inset. Generally GMR(T; $H_0 \neq 0$) slightly departs from the ZFC curve just below T ~175 K, except for the H_0=-500 Oe curve which shows a very large departure. H_{exch} also exhibits an unusual rise (fall) below the same temperature when H_0>0 (<0). FC runs with large $|H_0|$ enabled us to separate the MnIr and NOL contributions to H_{exch}(T); for this we assumed that the MnIr contribution is unaffected by cooling under H_0 (below 320 K). One can then use:

$$H_{\text{exch}}(H_0 = +3000 \text{ Oe}) = \frac{H_{\text{exch}}^{\text{MnIr}} + H_{\text{exch}}^{\text{NOL}}}{2}, \tag{4.2}$$

and

$$H_{\text{exch}}(H_0 = -3000 \text{ Oe}) = \frac{H_{\text{exch}}^{\text{MnIr}} - H_{\text{exch}}^{\text{NOL}}}{2}, \tag{4.3}$$

to calculate the contributions of MnIr ($H_{\text{exch}}^{\text{MnIr}}$) and NOL ($H_{\text{exch}}^{\text{NOL}}$) to the exchange field experimentally obtained. The MnIr contribution to H_{exch} is large and rises slightly when T decreases, while the NOL contribution is only residual until T ~175 K but rapidly rises below this temperature (Fig. 4.6).

These results can be explained as follows. Large positive H_0 well saturates the magnetization of the pinned layer (positive direction; $\rightarrow$) and, due to the interaction with the NOL, gives a better spin arrangement in the AFM oxide layer below the corresponding T_B [19]. This leads to a higher exchange coupling between CoFe and NOL (enhanced pinning), confirmed by the increase of H_{exch} below T_B. Under low positive H_0 the CoFe magnetization is less homogeneous and induces some degree of unfavored structure in the NOL spins below T_B, weakening the coupling to CoFe. This adverse effect is enhanced under small negative H_0. In particular, for H_0 ~-500 Oe the magnetization of the pinned layer (M_{pl}) starts to switch (from $\rightarrow$ to $\leftarrow$) at a temperature between 320 K and 15 K and thus M_{pl} will not be lying along the easy axis of the NOL SV when crossing T_B. This naturally increases magnetic disorder in the pinned layer. When cooling through T_B of the NOL, the oxide layers spins order in a direction out of the easy axis, preventing $\leftrightarrows$ alignment at SV switching when a MR(H) cycle is performed. (Notice that a distribution of blocking temperatures exists in

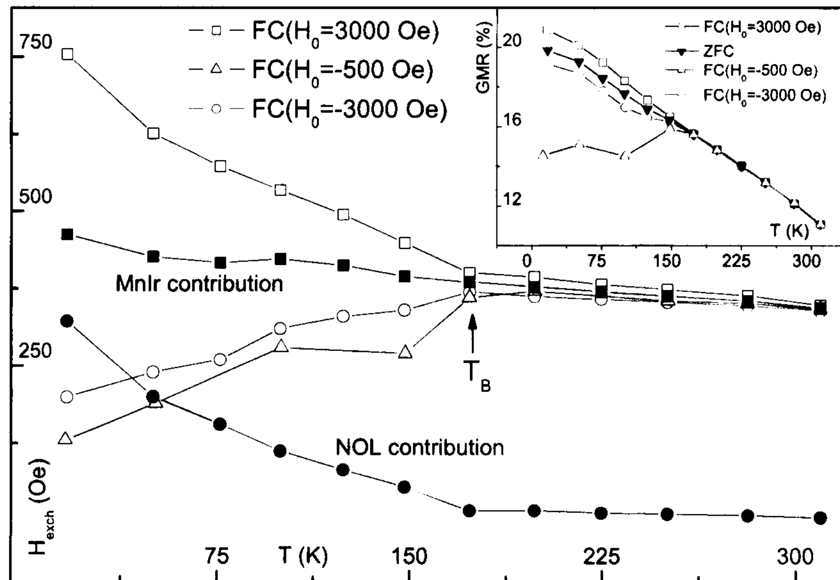

Figure 4.6: Total exchange field; MnIr and NOL exchange-contributions and GMR (inset) temperature dependencies (lines are guides to the eyes only).

the NOL, so that the changes in the direction of M_{pl} with temperature, when cooling under $H_0 = -500$ Oe, give rise to AFM regions with differently induced anisotropy directions and thus to enhanced magnetic disorder; see below.) Higher negative H_0 again saturates the pinned layer magnetization (in the negative direction; $\leftarrow$), improving the spin arrangement (domain structure; see below and sections 4.4 and 4.6) in the NOL below T_B.

4.3.2 Distribution of NOL-blocking temperatures

We also performed magnetoresistance measurements at $T = 15$ K, after field cooling under different H_0 from 320 K down to a temperature T_{cool}. From T_{cool} to the (fixed) measuring temperature $T = 15$ K, cooling was performed under zero applied magnetic field. Figure 4.7 shows the obtained MR(T_{cool}) and H_{exch}(T_{cool}) dependencies (inset). The main results of these experiments confirm those presented above. In fact, while the cooling field is applied only above $\sim$ 200 K, no significant change in MR and H_{exch} is observed. However, $T_{cool} < 200$ K leads to a clear change of both the MR ratio and H_{exch} with H_0. Although these changes occur mainly between $T_{cool} = 200$ K and 150 K (and are more visible for $H_0 = -500$ Oe), the application of the magnetic cooling field below 150 K still leads to changes in the measured MR(H) cycles: Decrease (increase) of MR and H_{exch} for $H_0 = -500$ Oe ($H_0 > 0$). Remember that these measurements were all performed at $T = 15$ K. Thus, these results indicate the existence of a broad distribution of blocking temperatures in the NOL, which may arise from different oxide-grain sizes [136] (on which the exchange field and blocking temperature are known to depend [137]). Further support for the existence of a distribution of blocking temperatures arises from the linear H_{exch}(T)-dependence observed in Fig. 4.6. Such dependence is usually attributed to the presence of exchange contributions arising from local regions with different AFM ordering temperatures [135, 138, 139, 140].

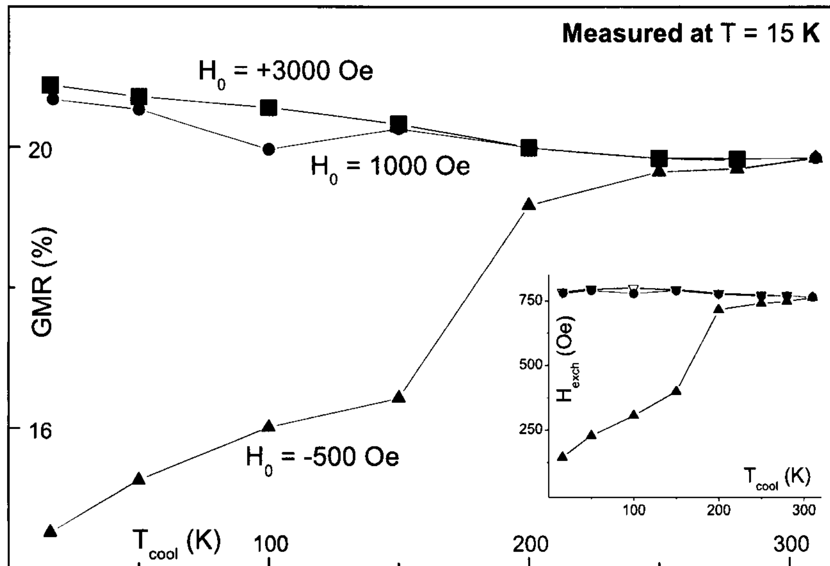

Figure 4.7: Magnetoresistance and exchange field (inset) obtained at $T = 15$ K after field cooling down to a temperature T_{cool} under different cooling fields H_0.

In the measurements performed with $T_{cool} \geqslant 250$ K, MR and H_{exch} are practically the same and similar to the ZFC situation (Fig. 4.7). However, for $T_{cool} = 200$ K one sees a slight change in MR and H_{exch} (increase for $H_0 > 0$, decrease for $H_0 = -500$ Oe), indicating that already some regions of the NOL have ordered antiferromagnetically, inducing an enhanced (reduced) exchange interaction with the FM moments for $H_0 > 0$ ($H_0 = -500$ Oe). Notice that at T_{cool} the magnetic cooling field is switched to zero and the magnetization of the FM pinned layer is in the positive sense ($\rightarrow$). Thus, AFM-regions with $T_B \geqslant T_{cool}$ will be aligned in the direction of M_{pl} (dependent of H_0), while those with $T_B < T_{cool}$ are only affected by the positive magnetization of the pinned layer and are independent of H_0.

Lowering T_{cool} to 150 K again changes the measured MR ratio and exchange field, in a coherent manner to what occurred with $T_{cool} = 200$ K. If all the AFM regions had a well defined, equal blocking temperature, applying a cooling field below this temperature would not lead to changes in the MR(H) cycles and thus on the magnitude of H_{exch} and MR (because for $T_{cool} = 200$ K changes had already occurred). Since both these quantities change with T_{cool}, even between $T_{cool} = 50$ K and $T_{cool} = 15$ K, we conclude that the NOL has a large range of local blocking temperatures T_{B_i}. Regions within the NOL have different blocking temperatures and, as field cooling runs are performed with decreasing T_{cool}, more NOL regions become AFM-ordered in the (H_0-dependent) direction of the pinned layer FM-moments, and their contribution to the measured H_{exch} appear. For $H_0 > 0$ the slight increase of MR and H_{exch} with T_{cool} is related to a more homogeneous M_{pl}, inducing a better spin arrangement in the AFM oxide layer.

Let us focus on the $H_0 = -500$ Oe data. When T decreases below the local T_{B_i} of a given region of the NOL, the AFM spins will be arranged according to M_{pl} at T_{B_i}. For $H_0 = -500$ Oe, the pinned layer reverses its magnetization from $\leftarrow$ to $\rightarrow$ in the 300–15 K range (see Fig. 4.2; page 79). The existence of a distribution of blocking temperatures implies

that each NOL-region starts to contribute to exchange bias at different temperatures. Because the FM magnetization is changed during cooling, different regions of the NOL will contribute to exchange bias in different directions and the AFM spins will have different orientations depending on the local T_{B_i}. Below T_{cool} the magnetic field is turned to zero (FM pinned-layer moments become aligned in the positive direction) and exchange contributions from regions of the NOL with $T_{B_i} < T_{cool}$ will give rise to exchange bias in the positive ($\rightarrow$) direction. One then expects a complex multidomain structure in the AFM nano-oxide layer when FC under $H_0 = -500$ Oe. This domain structure should become more complex with decreasing T_{cool}, due to the T-dependence of the M_{pl} direction. One anticipates the existence of a correlation between the non-zero MR at high positive magnetic fields of a MR(H) cycle and the domain structure of the AFM oxide layer (as will be discussed in section 4.4). Figure 4.8(b) shows the MR(H) curves obtained with $H_0 = -500$ Oe and different T_{cool}. Notice that increasing T_{cool} (increasing the number of domains in the NOL in the positive directions) decreases this *residual* MR.

Finally we comment on the distribution of blocking temperatures within the NOL. From the $H_0 = -500$ Oe curves of Fig. 4.7 we observe that the largest H_{exch} decrease occurs between 200 and 150 K. This marks the maximum of the distribution of blocking temperatures T_B^{max} (see also Fig. 4.6 where T_B^{max} is denoted as T_B). Furthermore, the fact that MR and H_{exch} depend on T_{cool} down to 15 K shows that this distribution is very broad, particularly below T_B^{max}, but from our data we can also infer that a small number of regions with local blocking temperatures slightly above T_B^{max} (up to $\sim$ 250 K) do exist.

Figure 4.8(a) displays the MR(H) measurements performed at $T = 15$ K, after field cooling under an applied magnetic field $H_0 = 3000$ Oe, down to T_{cool} =15, 50, 150 and 250 K. The zero field MR(H) curve is also displayed for comparison. One immediately observes that the plateau of maximum MR is continuously enhanced by field cooling down to decreasing T_{cool}. Notice also that the ZFC and $T_{cool} = 250$ K curves are equal, indicating the absence of significant NOL-regions with $T_{B_i} > 250$ K. However, the MR(H) curve for $T_{cool} = 150$ K already denotes a different shape with increasing MR and H_{exch}. This effect is further enhanced by decreasing T_{cool}. Again, the change of the MR(H) shape, even between $T_{cool} = 50$ K and $T_{cool} = 15$ K, indicates that NOL-regions with local blocking temperatures as low as 15 K indeed exist (as discussed above). Decreasing T_{cool} leads to an enhanced AFM ordering of regions of the NOL with lower T_{B_i}, and thus to the change of the MR(H) curves. Thus, the spin arrangement in the AFM-NOL/FM pinned layer interface is preferentially in the positive direction ($\rightarrow$). The *residual* MR at large positive magnetic fields is seen to increase with increasing T_{cool} [inset of Fig. 4.8(a)], again hinting the influence of the domain structure of the AFM nano-oxide layer on this residual MR. As in the $H_0 = -500$ Oe case, inducing a more homogeneous AFM domain structure in the positive direction leads to the decrease of MR at $H \gg 0$.

The MR(H) curves obtained under $H_0 = -500$ Oe for different cooling temperatures T_{cool} are displayed in Fig. 4.8(b). Again, the MR(H) curve after $T_{cool} = 250$ K is quite similar to the ZFC one, but a marked change is visible after $T_{cool} = 150$ K. These MR(H) changes occur when cooling under $H_0 = -500$ Oe even down to $T_{cool} = 15$ K. As stated above, as T_{cool} decreases, AFM-regions with lower T_{B_i} will have an induced anisotropy in the direction of M_{pl} at T_{B_i}. Thus, with decreasing T_{cool} more domains of the AFM-NOL become aligned out of the easy axis direction, as concluded by the decrease of the exchange field.

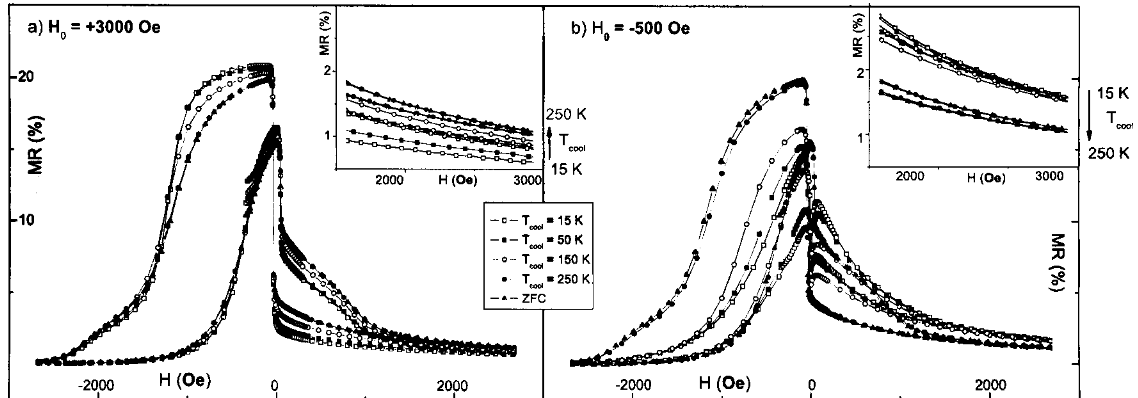

Figure 4.8: MR(H) curves measured at $T = 15$ K for different cooling temperatures T_{cool}, under (a) $H_0 = 3000$ Oe and (b) $H_0 = -500$ Oe.

4.4 The training effect

As noted previously, the AFM/FM exchange interaction shifts the hysteresis loop of the FM layer from zero field by an amount known as the exchange field H_{exch} when the sample is cooled below the blocking temperature of the AFM layer under an applied magnetic field. This interactions also gives rise to enhanced FM-coercive field H_c. Current theoretical models [29, 30, 31] explain the exchange bias effect by considering the magnetization of the AFM layer divided in multidomains, giving rise to a net surface magnetization at the AFM/FM interface that controls the exchange bias. The exchange field and the enhanced coercivity are then attributed to AFM domains that, due to the high local AFM anisotropy, do not flip and to those that (having weaker local anisotropy) reverse with the switching of the FM magnetization.

Another effect that sometimes arises from the AFM/FM exchange interaction is the so called training effect (TE). This effect consists in the change of both the descending and ascending switching fields of a M(H) hysteresis loop with the number of cycles performed (n), resulting in a decrease of exchange and coercive fields. The hysteresis loop shape is also altered due to a change in the reversal mechanism with n [141, 142]. This effect is explained by the domain state model [30, 31] as the rearrangement of the (metastable) domain structure of the AFM layer with each reversal of the magnetization of the FM layer. This leads to a partial loss of its (AFM layer) net magnetization and thus in a reduction of the exchange bias field. Such M-loss with cycling was recently shown to occur in exchange biased NiO/Fe bilayers [143].

The exchange field after the n-th cycle ($n > 1$) is given by the empirical expression [143, 144]:

$$H^{n}_{\text{exch}} - H^{\infty}_{\text{exch}} = \frac{\kappa}{\sqrt{n}}, \tag{4.4}$$

where H^{n}_{exch} (H^{∞}_{exch}) is the exchange field at the n-th cycle (in the limit of an infinite number of cycles) and κ is a system dependent constant. The power law behavior of Eq. (4.4) does not hold for $n = 1$, a fact that is usually attributed to the difference in the dominant FM layer reversal mechanisms for $n = 1$ and $n \geqslant 2$: Domain wall movement and coherent

magnetization rotation, respectively. A more elaborated and solid theoretical basis for Eq. (4.4) was given by Bineck [144] who, based on free energy considerations, arrived at the recursive equation:

$$H_{\text{exch}}^{n+1} - H_{\text{exch}}^{n} = -\gamma \left(H_{\text{exch}}^{n} - H_{\text{exch}}^{\infty}\right)^{3}. \tag{4.5}$$

This relation goes into Eq. (4.4) in the $n \gg 1$ limit, when the parameters κ and γ can also be related [144].

We present here a detailed study on the training effect in specular spin valves, using MR(H) measurements and different experimental procedures. The training effect was never observed in the non-specular spin valve throughout the 300–15 K temperature range. Also, such effect does not occur at room temperature in the specular spin valve (consecutive MR(H) measurements displayed equal exchange and pinned layer coercive fields and GMR ratio), but only for $T < 200$ K. We thus relate the observed training effect to the AFM ordering and AFM domain structure of the NOL layer.

Figure 4.9 depicts the first three MR(H) cycles measured at $T = 15$ K, after field cooling under $H_0 = +7000$ Oe. One observes that the measurements evolve with n, showing a decrease in the pinned layer switching field (particularly of the descending H-branch) and, consequently, of the exchange and pinned-layer coercive fields. This decrease is more pronounced from the first to the second MR(H) cycle. Subsequent MR(H) cycles show much more attenuated differences, as observed between the $n = 2$ and $n = 3$ curves. This is confirmed in the lower inset of Fig. 4.9, that displays the MR ratio (left) and H_{exch} (right) evolution with cycling. In particular, TE leads not only to a reduction of H_{exch}, but also of the GMR due to a *smaller* antiparallelism between the magnetizations of the pinned and free layers.

As stated already, training is related to domain rearrangements in the AFM layer. With cycling the net AFM magnetization is progressively reduced and consequently, so is the exchange field. Thus, cycling increases the number of domains in the negative ($\leftarrow$) direction, while reducing the number of those in the positive ($\rightarrow$) direction. We now turn to the upper inset of Fig. 4.9, were we observe that the residual MR at $H \gg 0$ depends on cycling, increasing with increasing n. This leads us to attribute the observed residual MR in the NOL SV to domains in the negative direction ($\leftarrow$) in the AFM-NOL (see section 4.6).

Figure 4.10 shows the dependence of the exchange field on the number of cycles (open circles). The corresponding curves were measured at $T = 15$ K after ZFC. After 40 cycles the exchange field decreases to $\sim 80\%$ of its initial value. We also show fittings to the theoretical models presented above, *i.e.* Eq. (4.4) for $n > 1$ (blue circles) and Eq. (4.5) (red crosses). It is clear that the fit to the recursive formulation Eq. (4.5) gives a good correlation with the experimental results for all n values, which does not occur for Eq. (4.4) (see inset of Fig. 4.10; green circles). On the other hand, the magnetoresistance dependence on n does not follow the same power law as H_{exch} and H_c.

Notice that the MR(H) cycles presented in section 4.3 were obtained just after cooling below 320 K (and thus represent the $n = 1$ curve). However, such MR(H) measurements were repeated (at least five times) before the sample was heated again to 320 K. We can thus construct a very detailed picture of the training effect in our specular spin valve, in particular, its dependence on temperature, cooling field and cooling temperature.

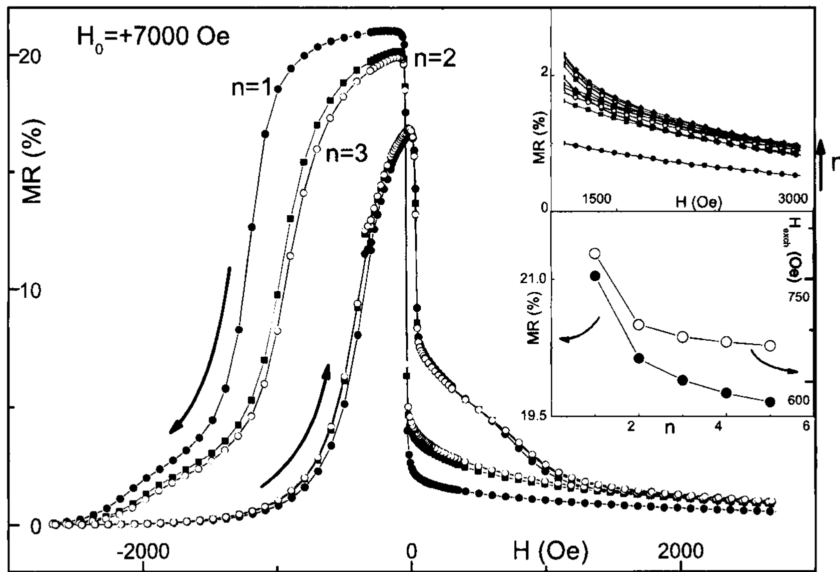

Figure 4.9: Three MR(H) curves of the specular spin valve measured consecutively (at $T = 15$ K; after FC under $H_0 = +7000$ Oe) and displaying the so called training effect. Upper inset: Enlarged $H \gg 0$ region showing consecutive MR(H) cycles with enhanced electrical resistance and thus poorer $\rightrightarrows$ parallelism. Lower inset: GMR ratio and exchange field dependence on the number of cycles performed.

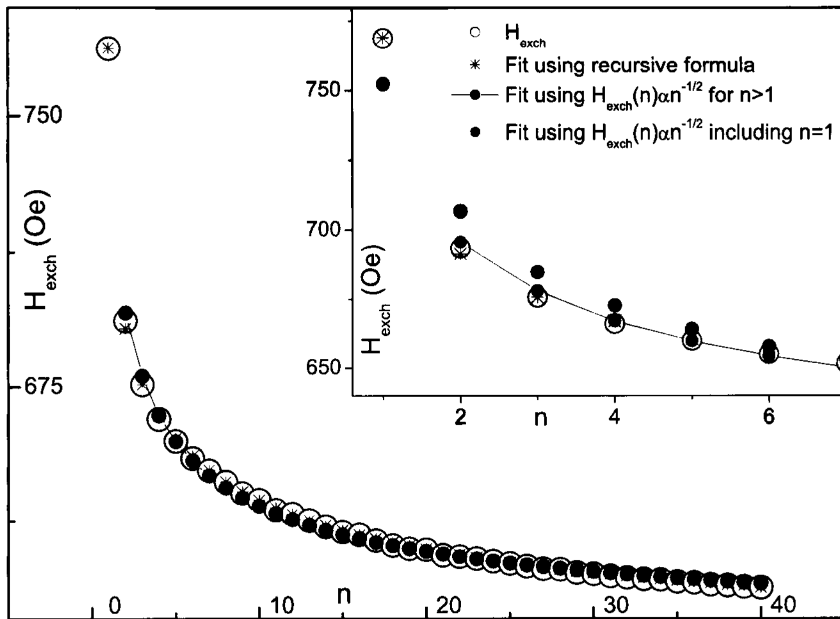

Figure 4.10: Experimental exchange field (open circles) as a function of MR(H) cycle number (measured at $T = 15$ K after ZFC) and fits to the different models presented in the text [Eqs. (4.4) (for $n > 1$; blue circles) and (4.5) (red crosses)]. Inset shows the region $1 \leqslant n \leqslant 7$ and also a fit to Eq. (4.4) for $n \geqslant 1$ (green circles).

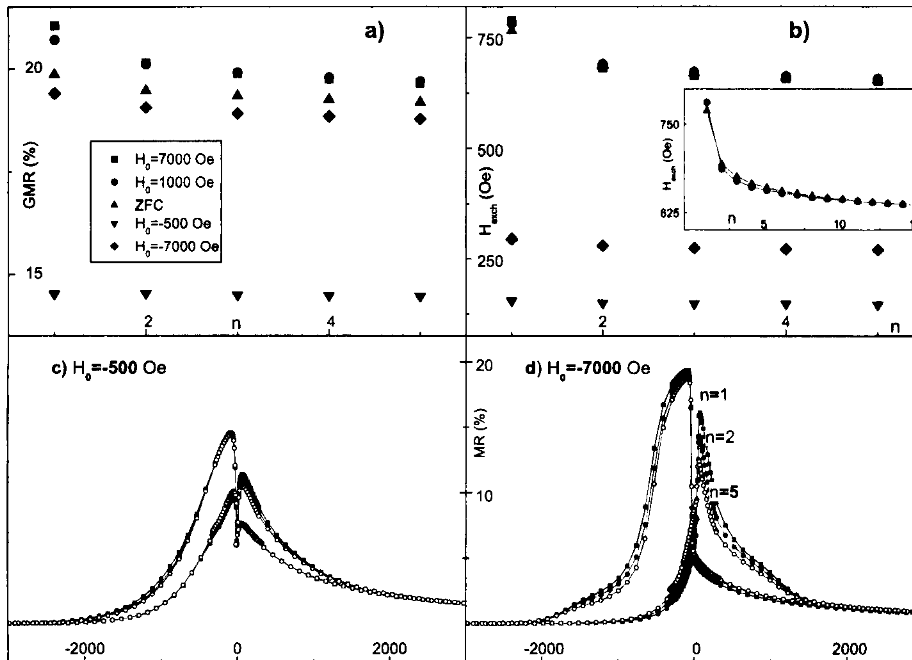

Figure 4.11: Dependence of (a) GMR ratio and (b) H_{exch} on the number of MR(H) cycles performed ($n \leq 5$) for several cooling fields. MR(H) cycles obtained at $T = 15$ K after field cooling from 320 K under (c) $H_0 = -500$ Oe and (d) $H_0 = 7000$ Oe.

We start by defining the training effect TE_n of the exchange field as the relative decrease of H_{exch} from the first to the n-th cycle:

$$TE_n = \left(1 - \frac{H^1_{exch} - H^n_{exch}}{H^1_{exch}}\right) \times 100 \ (\%), \tag{4.6}$$

and the same procedure is used to define the TE for the MR ratio.

The training effect clearly depends on the cooling field as depicted in Fig. 4.11. The GMR ratio decreases with cycling ($n \leq 5$) for all cooling fields, except for $H_0 = -500$ Oe [Fig. 4.11(a) and (c)] for which a practically constant GMR = 14.5% is obtained. The same occurs for the exchange field [Fig. 4.11(b)]: Although a fairly large TE ($\sim$ 80%) is observed for positive H_0, much smaller TE occurs for both $H_0 = -500$ Oe and $H_0 = -7000$ Oe [$\sim$ 95% and $\sim$ 93%, respectively; see also Fig. 4.11(c) and (d)]. Furthermore, H_{exch} extrapolates to the same value in the limit of large number of cycles for all $H_0 \geq 0$ (see inset of Fig. 4.11(b); notice $n \leq 15$). However, the same does not occur for negative H_0, for which H_{exch} tends to different values. Thus, the domain structure of the AFM-NOL has several stable configurations, that depend on the magnetic history of the sample. This reveals that such domain structure of the NOL has a spin glass-like nature [145, 146, 147], with multiple stable configurations. The very small TE observed for negative H_0 (especially for $H_0 = -500$ Oe) indicates that the number of domains in the AFM pointing in the negative direction ($\leftarrow$) is a crucial parameter governing the training effect.

In Fig. 4.12(a) and (b) we observe the GMR ratio and H_{exch} versus n for several temperatures

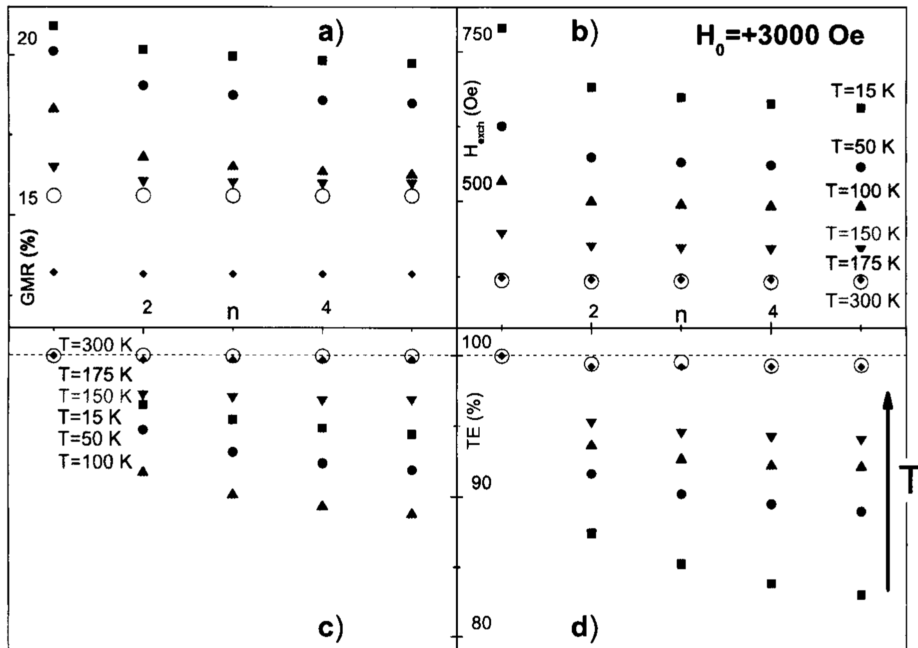

Figure 4.12: Dependence of (a) GMR ratio and (b) H_{exch} on the number of MR(H) cycles performed for several temperatures and corresponding training effect [(c) and (d)]. MR(H) measurements were performed after field cooling under $H_0 = 3000$ Oe from 320 K. Inset displays the MR(T) dependence for different number of cycles.

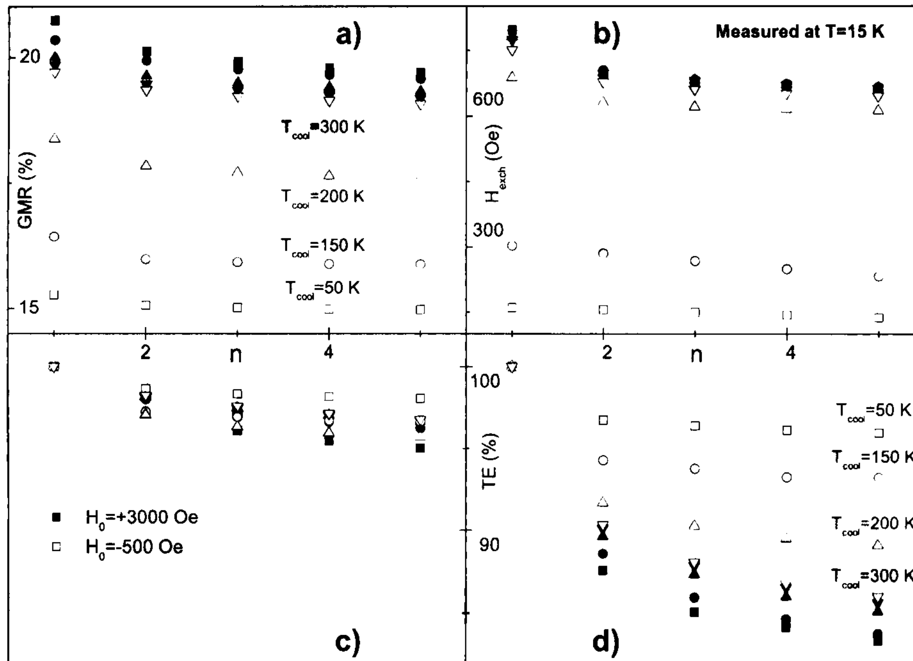

Figure 4.13: Dependence of (a) GMR ratio and (b) H_{exch} on the number of MR(H) cycles performed for several cooling temperatures and corresponding training effect [(c) and (d)]. MR(H) measurements were performed after field cooling under $H_0 = 3000$ Oe (solid symbols) and $H_0 = -500$ Oe (open symbols) from 320 K.

from 300 to 15 K. As shown earlier, the MR ratio and H_{exch} increase with decreasing temperature and one also notices the absence of TE down to $T = 175$ K. Both MR and H_{exch} retain their initial $n = 1$ value with cycling [see dashed line in Fig. 4.12(c) and (d), representing the 100% level]. However, for $T = 150$ K, the value of H_{exch} is reduced to $\sim$ 95% of its initial value for $n = 5$. In fact, the relative change of the exchange bias with cycling increases with decreasing temperature. For $T = 15$ K and after five cycles, the exchange field is only $\sim$ 83% of the initial value. This fact may be related to the above discussed distribution of blocking temperatures: As temperature decreases, localized regions in the NOL with lower T_{B_i} become AFM-ordered. These regions are also expected to have smaller anisotropy (due to the smaller grain size) favoring their magnetization reversal with cycling since TE increases with decreasing layer thickness [141]. On the other hand, TE starts appearing in the GMR ratio also below 175 K, but in this case a maximum occurs in TE at $T = 100$ K [Fig. 4.12(a) and (c)].

Figure 4.13 shows the obtained results concerning training effect versus cooling temperature for $H_0 = 3000$ Oe (solid symbols) and $H_0 = -500$ Oe (open symbols). For $H_0 = +3000$ Oe, TE of the exchange bias slightly increases with decreasing T_{cool} [Fig. 4.13(d)]. Since cooling with decreasing T_{cool} in a large positive field favors domains in the positive direction ($\rightarrow$) in the AFM NOL, the observed increase of TE shows that the (preferentially positive) domain structure is not stable, and the AFM NOL tends to reverse part of the positive domains to lower its energy. On the other hand, TE decreases with decreasing T_{cool} for $H_0 = -500$ Oe [Fig. 4.13(d)]. Experiments performed with higher T_{cool} have more domains in the AFM-

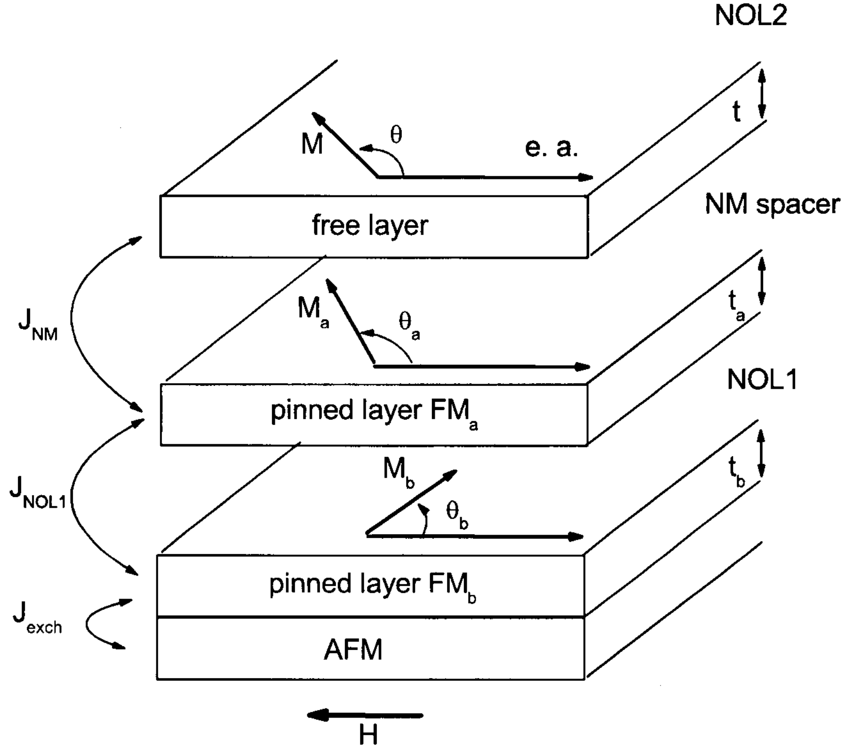

Figure 4.14: Schematic representation of a specular spin valve and magnetic interactions between the FM layers (J_{exch} between the AFM and pinned layer, J_{NOL1} between the FM_b and FM_a pinned layer and J_{NM} between the pinned and free layers).

NOL in the positive direction and its reversal is again the cause of the enhanced training effect. Further notice that different cooling temperatures lead to different exchange fields in the $n \gg 1$ limit [Fig. 4.13(b)]. This again indicates different stable configurations in the AFM domain structure with similar energies, proper of a spin glass-like system.

4.5 Influence of FM_b and FM_a on the MR(H) behavior

We extend the simple model describing the total energy of a Conventional SV [126] to the more complex structure of NOL SVs, explicitly introducing the pinned layer partition into the FM_b and FM_a sub-layers separated by NOL1 (Fig. 4.14). The exchange coupling between the FM_b and AFM layers fixes the magnetization easy axis in the FM_b layer and also (as consequence of coupling interactions) in the FM_a and free layers. To simplify the treatment, and since we are mainly interested on the effect of the FM_b layer on the M(H) and MR(H) curves, no anisotropy terms are included. The total energy per unit area (E) of a NOL SV (H along the easy axis) is thus written as the sum of Zeeman, E_{Zeeman}:

$$E_{\text{Zeeman}} = -\mu_0 M_b t_b H \cos\theta_b - \mu_0 M_a t_a H \cos\theta_a - \mu_0 M t H \cos\theta, \tag{4.7}$$

coupling, E_{coup}:

$$E_{\text{coup}} = -J_{NOL1}\cos(\theta_b - \theta_a) - J_{NM}\cos(\theta_a - \theta), \tag{4.8}$$

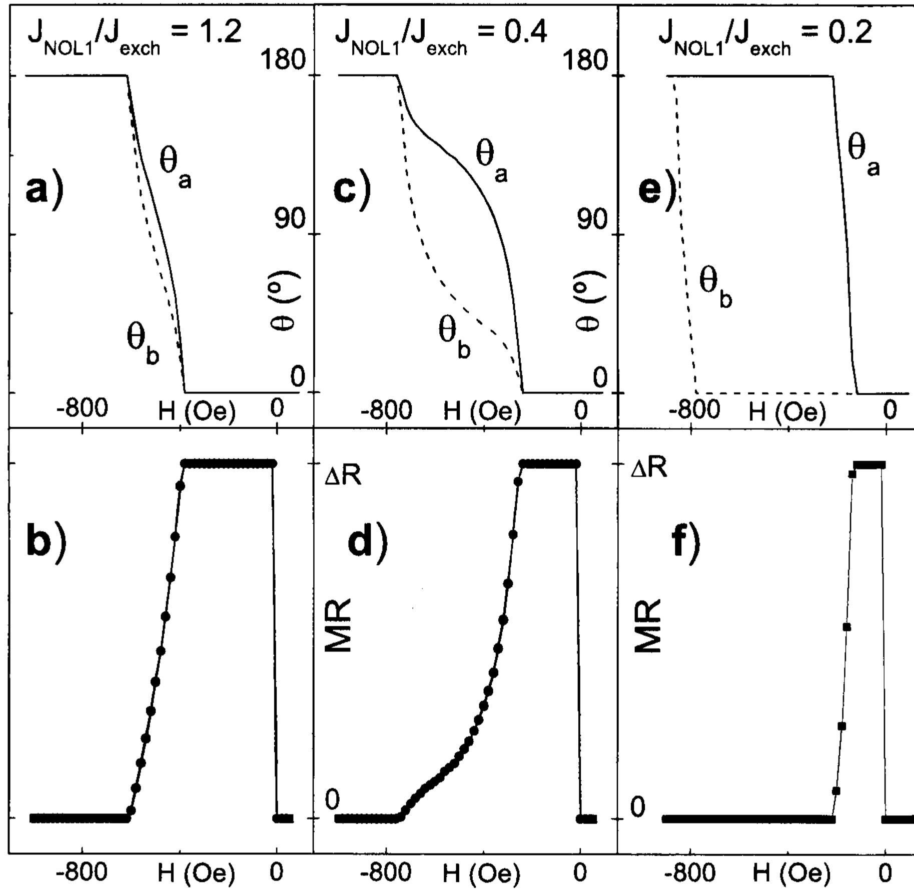

Figure 4.15: Model simulations of MR(H) curves using different $J_{\text{exch}}/J_{\text{NOL1}}$ ratios.

and exchange (E_{exch}) energies:

$$E_{\text{exch}} = -J_{\text{exch}} \cos\theta_b. \tag{4.9}$$

In the above M_b (θ_b), M_a (θ_a) and M (θ) are the saturation magnetizations (at corresponding angles with the easy axis) in the FM_b, FM_a and free layers, respectively. J_{NOL1} (J_{NM}) is the ferromagnetic exchange coupling energy per unit area between the FM_b and FM_a (FM_a and free FM) layers and J_{exch} is the exchange bias energy per unit area between the AFM and FM_b layers. The thicknesses t_b, t_a and t correspond to the FM_b, FM_a (assumed equal) and free layer (thicker than the previous) respectively.

We numerically obtained the θ_b, θ_a and θ angles which minimize E for each value of H and then calculated the total magnetic moment per unit area m of the NOL SV appearing along the easy axis:

$$m(H) = M_b t_b \cos(\theta_b(H)) + M_a t_a \cos(\theta_a(H)) + Mt \cos(\theta(H)). \tag{4.10}$$

Dieny *et al.* [116] showed that in a CoFe/Cu/SyAP/MnPt spin valve (with a synthetic AFM [148] pinned layer SAF, of CoFe/Ru/CoFe), the magnetoresistance associated with the two

CoFe sub-layers separated by the Ru spacer is only a small fraction of total MR. As a first approximation we then assume that MR is only due to the difference between the orientation of the magnetization in the FM_a and free layer:

$$MR(H) = \Delta R \left(\frac{1 - \cos\left[\theta_a(H) - \theta(H)\right]}{2} \right), \tag{4.11}$$

where ΔR is a characteristic amplitude. As expected for very small J_{NM} (across the spacer) the almost uncoupled free layer always rotates at very low negative values of H, but the model predicts three regimes for the rotation of the pinned layer at higher fields, depending on the J_{NOL1}/J_{exch} ratio:

(i) $J_{NOL1} > J_{\text{exch}}$ [Fig. 4.15(a)]: The magnetization of both FM_b and FM_a rotate together ($0 \to \pi$) in a narrow field interval and always with approximately the same angle. This occurs because the large magnetic coupling between FM_b and FM_a (compared to J_{exch}) forces the two layers to behave as a (single) intra-pinned layer. Figure 4.15(b) shows the predicted MR(H) curve, displaying an abrupt MR drop when the magnetizations of FM_b and FM_a rotate.

(ii) $J_{NOL1} \leq J_{\text{exch}}$ [Fig. 4.15(c)]: Both FM_b and FM_a layers reverse in the same field interval, but the corresponding range increases with decreasing J_{NOL1} and a considerable dephasing occurs between θ_b and θ_a at intermediate fields. Such increase in (θ_b - θ_a) leads to broadening in the MR(H) curves. Figure 4.15(d) illustrates, for $J_{NOL1} = 0.4 J_{\text{exch}}$, the predicted bump in the MR(H) curve at sufficiently negative fields.

(iii) $J_{NOL1} \ll J_{\text{exch}}$: The magnetizations of FM_b and FM_a now reverse almost individually and over distinct narrow field ranges; a small disturbance in the others magnetization angle occurs in such ranges, producing also a disturbance in MR (not shown). If J_{NOL1} is further decreased, both M_b and M_a reversals become truly independent, i.e. no change in the angle of the magnetization of one layer is visible when the other rotates [Figs. 4.15(e) and (f)]. This produces three steps in the M(H) curve, corresponding to the magnetization reversal in the FM_b, FM_a and free FM layers. No variation occurs in MR due to the FM_b magnetization reversal [Eq. (4.11)].

4.6 Discussion

We can now give a complete description of our results and, particularly, of the anomalous MR(H) curves obtained in the specular spin valve at low temperatures ($T = 25$ K; Fig. 4.16). Increasing the applied field from $-H_{\text{max}} = -8000$ Oe, where complete $\leftleftarrows$ parallelism occurs, initiates the M-reversal of the pinned layer (exchange coupling with MnIr favors positive magnetization) producing a gradual MR increase. However, when the field reaches small positive values (point B in Fig. 4.16) the free layer suddenly reverses its magnetization, producing a small discontinuous MR step (to point C). One notices that the reversal of the pinned layer is still not complete since MR does not reach zero (full $\rightrightarrows$ parallelism). To confirm that the rotation of the pinned layer continues under positive fields, we ploted the difference between the maximum MR for decreasing and increasing fields (points A and B in Fig. 4.16) and the difference between after-free-layer-reversal in increasing and before-free-layer-reversal in decreasing fields (points C and D in the same figure) as a function of

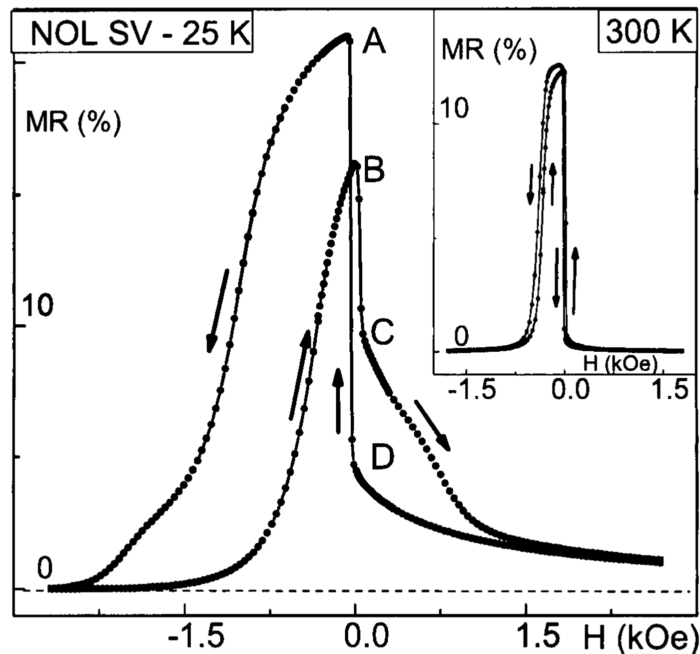

Figure 4.16: Magnetoresistance of NOL SV at low (25 K) and high (300 K) temperature.

temperature (not shown). These differences are indeed similar, showing that the anomalous MR bump in positive fields is due to the incomplete reversal of the pinned layer.

The further increase of H leads to a gradual decrease of MR but we were unable to achieve zero MR even at positive H_{max} =8 kOe. We believe that domains in the negative ($\leftarrow$) direction, originating in the AFM-NOL, strongly interact with interfacial FM pinned layer moments so that, even for large applied positive magnetic fields, they are not fully aligned with H, but only gradually do so as H increases [141]. This prevents full $\rightrightarrows$ parallelism between the pinned and free layers magnetic moments.In fact, domains at the AFM/FM interface were recently observed in such systems [142]. The FM spins in these interfacial domains are strongly coupled by the AFM moments and do not align easily along the applied magnetic field, even for large H [142].

The training effect measurements clearly show that the magnetoresistance at maximum field is influenced by the number of cycles performed, especially for positive cooling fields (Fig. 4.9). Since TE is attributed to the reversal of positive domains in the AFM-NOL (thus decreasing the exchange field) when the magnetization of the FM pinned layer is reversed, the increase of the residual MR with increasing number of cycles (thus with the increase of negative domains in the AFM) shows that these domains are the cause for the observed residual MR.

As shown in section 4.3, when field cooling experiments are performed with decreasing T_{cool} (H_0 = 3000 Oe; favoring domains in the positive direction and thus increasing H_{exch}), the residual MR also decreases [Fig. 4.13(a)]. Again this shows that the domain structure of the AFM nano-oxide layer is crucial to the value of the residual MR at high H. In particular, its increase with decreasing exchange field (increasing T_{cool}) indicates that it is likely caused

SV	300 K			20 K		
	ρ	$\Delta\rho$	MR	ρ	$\Delta\rho$	MR
CSV	57.1	3.4	5.9	44.3	4.4	10.0
NOL SV	53.5	6.7	12.5	37.9	8.0	21.1

Table 4.2: Transport characteristics of the spin valves studied in this work. Electrical resistivity ρ and $\Delta\rho = \rho_{AP} - \rho_P$ are given in $\mu\Omega$cm.

by domains in the AFM-NOL in the negative direction ($\leftarrow$). The same can be concluded from the $H_0 = -500$ Oe experiments [Fig. 4.13(b)].

For decreasing fields from H_{max}, the free layer magnetization suddenly reverses at a small negative field (point D in Fig. 4.16) but maximum MR (full magnetic antiparallelism FM_a/free layer) cannot be achieved due to the previous partial reversal in the pinned layer (notice that MR> 0 at D); no ΔH plateau of maximum MR then occurs. Further field decrease keeps the ongoing reversal of the pinned layer and produces a broad decrease of the MR ratio due to the FM_b/FM_a coupling (as modeled in section 4.5). When the field value reaches the bump in the left side of the MR(H) curve, the reversal of the FM_a magnetization is almost complete, but FM_b is still far from complete reversal [Fig. 4.15(c) and (d)], due to the higher exchange pinning with the MnIr underlayer. Complete parallel alignment is only obtained at a higher (negative) field. The model presented in section 4.5 describes well important characteristics of this descending branch of the MR(H) curve (broadening and MR bump) for $J_{\mathrm{NOL1}} \approx 0.4 J_{\mathrm{exch}}$.

4.7 Conclusions

We presented a comparative study between conventional (non-oxidized) and specular (oxidized) spin valves. The introduction of two nano-oxide layers formed by the partial oxidation of the pinned and free layers greatly enhanced the obtained MR ratio (see Table 4.2).

Temperature dependent MR(H) measurements (300–15 K) revealed a large increase of the exchange bias and pinned layer coercive fields below T$\sim$ 175 K, here associated with the presence of an AFM oxide in NOL1, with $T_B \approx 175$ K (likely Fe_2O_3). In fact, the nano-oxide layers in our specular spin valves strongly influenced the MR(H) curves below the (oxide) blocking temperature. Field cooling measurements allowed us to obtain the contribution of MnIr and AFM-NOL to the exchange bias as a function of temperature. The measured MR(H) curves were found to depend strongly on the sign and value of the cooling field H_0, and the MR(H_0) dependence (measured at $T = 15$ K) showed a sharp minimum for $H_0 = -500$ Oe. Also, the MR(T,H_0) curves departed from the ZFC situation below $T \approx 175$ K. We related all these features to the effects of H_0 on the AFM ordering of the NOL below its blocking temperature. Field cooling measurements with different cooling temperatures T_{cool} allowed us to infer the existence of a broad distribution of blocking temperatures in the nano-oxide layer.

A comparison between the MR(H) and M(H) curves of the specular spin valve obtained at low temperatures showed a break in the usual correlation between the two processes, indicating

that interfacial scattering in the NOL SV is extremely important. Training effect experiments enabled us to study the domain structure of the AFM-NOL. We showed the importance of the domain structure of the NOL on the residual magnetoresistance observed at large positive fields. In fact, the model we extended based on the total energy of a NOL SV gave a fair description of the anomalous bump present in the MR(H) curve at negative fields, correlating it with the presence of the FM_b layer in the NOL SV. However, the nonsaturation of MR at positive fields was not accounted for in our model, and had to be explained in terms of irreversible processes, *i.e.* stable domains in the FM pinned layer due to the domain structure of the AFM-NOL. This explanation was supported by the fact that onset of non-saturation appeared only below $\sim$175 K, suggesting its direct connection to the magnetic order in the NOL1 layer.

Chapter 5

Tunnel Magnetoresistance: An overview

5.1 Introduction

A tunnel junction (TJ) [9, 8] is a nanostructure based on two metallic ferromagnetic (FM) layers separated by a thin (~nm or less) insulator. When a voltage is applied across the insulator, a current starts to flow by tunneling of electrons across the classically forbidden insulating barrier. Due to spin polarized tunneling [149, 150, 151] between the two FM electrodes [16], one is able to switch between two distinct resistance (R) states, when the magnetizations of the FM layers are parallel (R_P; low R) or antiparallel (R_{AP}; high R). These nanostructures thus exhibit large tunnel magnetoresistance (TMR), of over 70% at room temperature in CoFeB/AlO_x/CoFeB tunnel junctions [17] and over 150% in epitaxial [152] and sputtered [153] MgO-based TJs. The potential applications of these nanostructures are enormous, including non-volatile magnetic random access memories (MRAMs) [154, 155] and the next generation of magnetic sensors in read heads for hard drives [156, 157, 47].

However, and although TMR was first observed more than 30 years ago [16], tunnel junctions did not attract much attention for a long period, due to the low TMR values observed (and only) at low temperatures and to the demanding fabrication processes. Only recently have large TMR ratios been observed at room temperature by Miyazaki and Tezuka [9] and Moodera *et al.* [8], triggering increasingly paced research in this field.

Several theoretical models were developed to explain electron transport and the TMR effect in tunnel junctions. In particular, the spin-polarization of the tunnel current is attributed to *free electron-like* d-electrons at the Fermi surface [158, 159]. Since the probability of an electron to tunnel from one electrode into the other depends on its spin-dependent wavevector at the Fermi level, the corresponding tunneling probability will then depend on the electron spin.

5.2 Spin polarization

The density of states of the spin-up and spin-down electrons of a ferromagnetic material (Co, Fe, Ni) are exchange-shifted and the corresponding magnetic moment is determined by the different occupation of the spin-up and spin-down bands. In the case of Co, the d-band for spin-up electrons is completely full, while that for spin-down electrons is only partially filled. Thus electrical conductance should only be carried by spin-down electrons since they are the only ones with final accessible final states. If one assumes that the spin conductance is proportional to the density of states of the majority ($\rho^{\uparrow}$) and minority ($\rho^{\downarrow}$) spin electrons, we can define the spin polarization of a material as:

$$P = \frac{\rho^{\uparrow} - \rho^{\downarrow}}{\rho^{\uparrow} + \rho^{\downarrow}}. \tag{5.1}$$

The larger density of states at the Fermi level of minority d-electrons (at least in Co and Ni) should then lead to negative spin-polarization. However, Meservey and Tedrow, using a technique based on superconductor/insulator/ferromagnetic tunnel junctions measured the spin-polarization of $3d$ FM metals [149, 150, 151], and obtained positive polarization values for all of them. It was then concluded that majority electrons dominate tunnel processes. This contradiction between theoretical expectations and experimental results was justified by Stearns [158], who took into account the complete electronic band structure of the ferromagnetic materials. In $3d$ FM metals the dispersive s-band is partially hybridized with the localized d-band that crosses the Fermi surface over a much larger k-region. The free electron like s-d hybridized bands, through exchange interactions, have low effective mass and thus provide essentially all the tunnel current and give small, positive spin polarizations [160]. The density of states of such free electron like bands is proportional to the corresponding Fermi wavevector $k_F^{\uparrow,\downarrow}$, allowing us to rewrite Equation (5.1) as:

$$P = \frac{k_F^{\uparrow} - k_F^{\downarrow}}{k_F^{\uparrow} + k_F^{\downarrow}}. \tag{5.2}$$

Recently, Munzenberg and Moodera [160] were able to separate the tunneling current into two components: A positive spin-polarized tunneling current due to s (in fact, hybridized s-d) electrons and a negative polarized current due to d electrons. They considered the *interfacial* current $i_{j,0}$ ($j = s$, d) to account for bonding at the interfaces [161, 162, 163] (see below). The tunnel current across the barrier i_j is written as:

$$i_j = i_{j,0} e^{-\lambda_j t}, \tag{5.3}$$

where t is the thickness of the barrier, and, more important, λ_j^{-1} is the characteristic decay length for each j band [164]. Because the d-electrons are more localized than the s-electrons, only s states contribute to the current in the thick barrier limit. Using Equation (5.3), the total polarization can now be written as:

$$P = \frac{P_s i_{s,0} e^{-\lambda_s t} + P_d i_{d,0} e^{-\lambda_d t}}{i_{s,0} e^{-\lambda_s t} + i_{d,0} e^{-\lambda_d t}}, \tag{5.4}$$

where P_s and P_d are the polarization of the s and d states, respectively.

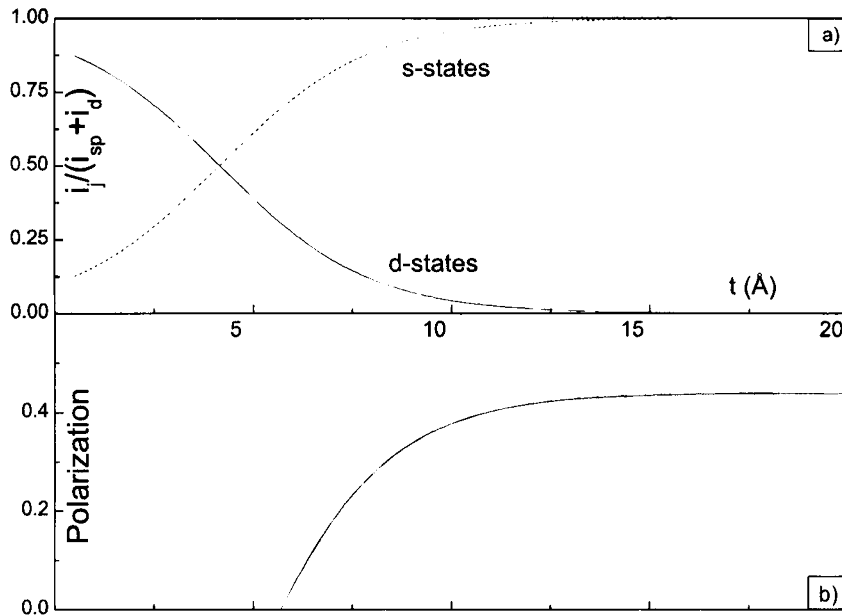

Figure 5.1: Modeled contributions of s- and d-states to the tunnel current (a) and corresponding spin-polarization (b). Parameters used: $\lambda_d^{-1} = 0.5$ Å, $\lambda_s^{-1} = 0.68$ Å, $i_{d,0} = 0.9$, $i_{s,0} = 0.1$, $P_d = -1$ and $P_s = 0.44$.

In Fig. 5.1(a) one sees the normalized tunnel current for s and d electrons as a function of barrier thickness, using $\lambda_d^{-1} = 0.5$ Å, $\lambda_s^{-1} = 0.68$ Å, $i_{d,0} = 0.9$ and $i_{s,0} = 0.1$. For $t \gtrsim 10$ Å [160] the current is totally dominated by s-like tunnel electrons, but as t decreases a larger contribution from d-states is visible. This effect is reflected on the modeled spin polarization [Fig.5.1(b); $P_d = -1$ and $P_s = 0.44$]. The polarization starts decreasing below $t \sim 10$ Å, due to the larger contribution of d electrons to the total current. This decrease was experimentally confirmed [160] and shows that the tunnel magnetoresistance naturally decreases with decreasing barrier thickness.

First principle calculations [161, 165] confirms that tunneling is dominated by s-d electrons. It further showed that the chemical bonding at the ferromagnet/barrier interface can affect the sign of the spin polarization of tunnel junctions. In the case of s-s bonding the spin polarization is positive due to s-d hybridization within the ferromagnet. Interface bonding was also used to explain the TMR behavior of Co/$SrTiO_3$/$La_{0.7}Sr_{0.3}MnO_3$ tunnel junctions. de Teresa *et al.* [162] observed that the spin polarization and the corresponding sign depended on the insulating barrier used. They found that Co/Al_2O_3/$La_{0.7}Sr_{0.3}MnO_3$ tunnel junctions showed, as expected, positive TMR for all bias values. However, Co/$SrTiO_3$/$La_{0.7}Sr_{0.3}MnO_3$ tunnel junctions had negative spin-polarization for bias below ~0.8 V, and this effect was attributed to d-d bonding between Co and Ti or Si at the interface. Furthermore, experiments with TJs with Ta_2O_5/Al_2O_3 insulating barriers [163], showed that the contributions of s- and d-electrons to the tunneling current depends on the ferromagnet/barrier interfaces because of the corresponding different bonding characteristics.

5.3 TMR models

The earliest TMR models [16] are based on the tunnel Hamiltonian theory, in which the left and right electrodes are treated as separated and uncorrelated sub-systems. In this model it is assumed that the spin is conserved during tunneling and that the tunnel conductance is proportional to the product of the density of states at the Fermi level for each spin (up and down) and in each electrode. Although this model explains fairly well the dependence of the conductance on the relative orientation of the magnetizations of the two FM layers, the FM electrodes are treated as completely isolated entities. In fact, the overlap of the electron wave function in both electrodes mandates treating electrodes and barrier as one single system.

Such approach is achieved using the solution of the Schrödinger equation for a rectangular potential barrier (free electron model) [42]. In this model one considers free electron spin dependent wave functions with real (in the electrodes) and imaginary (in the barrier) wavevectors. The wave functions are matched at the interfaces using appropriate continuity relations. The electrodes and barrier are thus treated as a single quantum-mechanical system. One can then obtain a spin-dependent tunneling probability, which is then used to calculate the electron current and the tunnel magnetoresistance behavior. The tunnel magnetoresistance is found not only dependent on the spin polarization of the FM electrodes, but also on the height of the tunnel barrier. In this model the electronic structure of the electrodes is assumed to be that of the bulk metal, discarding interfacial effects. Also, the tunnel conductance depends strongly on the poorly known barrier potential [166], so that approximations used can lead to deviations from the true tunnel junction behavior.

More realistic results are obtained using the tight-binding lattice method [167]. In this model, electrons hop from one atom to the other, and the electronic structure at the electrodes/barrier interfaces and at the bulk of the electrodes and barrier can be differentiated. The resulting conductance reduces to that of the classical tunnel Hamiltonian theory of tunneling when hopping between the two electrodes is weak.

5.3.1 Tunnel Hamiltonian model

A simple model based on the tunnel Hamiltonian method [168, 169] was proposed by Juliere [16] to explain the tunnel magnetoresistance effect by him observed at low temperatures in Co/Ge/Fe tunnel junctions. In this model the left and right electrodes are treated as completely independent, separated systems and it is assumed that spin is conserved in the tunneling process (*i.e.*, that the current flows through two independent spin channels). Thus, electrons with one spin state in one particular FM electrode tunnel to an unfilled state *of the same spin* in the other FM electrode (Fig. 5.2). If the FM electrodes are magnetically parallel (P) aligned, majority (minority) spins tunnel to majority (minority) states. On the other hand, if the FM electrodes are magnetically antiparallel (AP) aligned, majority (minority) spins from one electrode tunnel to the minority (majority) states of the other electrode. Assuming that the tunnel current density is proportional to the product of the density of states in the right (R) and left (L) electrodes, one can write:

$$J_P \propto \rho_L^{\uparrow}\rho_R^{\uparrow} + \rho_L^{\downarrow}\rho_R^{\downarrow}, \tag{5.5}$$

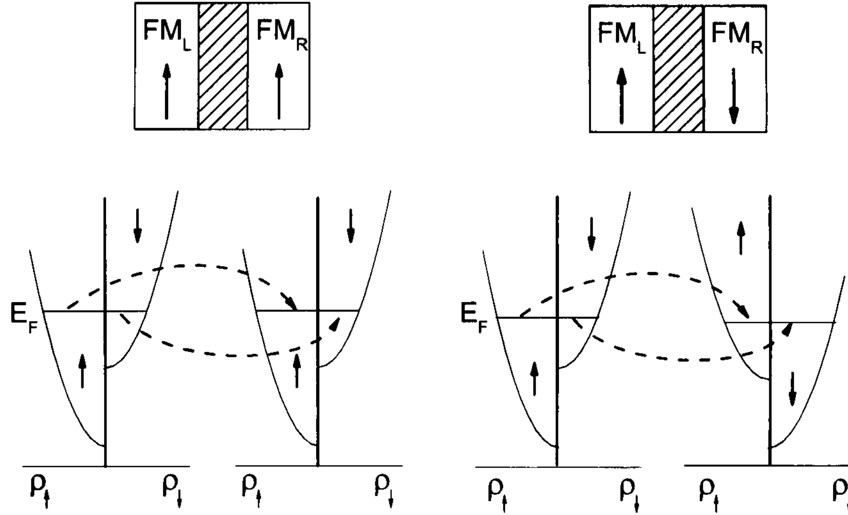

Figure 5.2: Tunnel conductance in a FM/I/FM tunnel junction in the parallel (left) and antiparallel (right) states.

for the parallel state, and

$$J_{AP} \propto \rho_L^{\uparrow}\rho_R^{\downarrow} + \rho_L^{\downarrow}\rho_R^{\uparrow}, \tag{5.6}$$

for the antiparallel state. Defining now the tunnel magnetoresistance (TMR) ratio as:

$$TMR = \frac{J_P - J_{AP}}{J_{AP}} = \frac{R_{AP} - R_P}{R_P}, \tag{5.7}$$

one easily obtains:

$$TMR = \frac{2P_L P_R}{1 - P_L P_R}, \tag{5.8}$$

where we defined the polarization of the i (R, L) electrode as in Equation (5.1).

Thus, in Juliere's model the TMR ratio depends only on the fraction between the majority and minority density of states and not on any property of the barrier. However, as stated previously, the electrodes and barrier need to be treated as a single quantum-mechanical system for a more realistic description of tunnel conductance and magnetoresistance. Nevertheless, disorder in the barrier may lead to tunneling conductance proportional to the product of the density of states and, in the limit of strong disorder, the Juliere's formula [Eq. (5.8)] is recovered [170, 171].

5.3.2 Free electron model

Nonmagnetic tunnel junctions. From quantum-mechanics [172], one knows that an electron with energy E has a certain probability of overcoming a potential barrier of height $\varphi > E$ and width t. In the case of a tunnel junction, the electron wave function on the left and right electrodes overlaps in the barrier and has therefore to be matched at the interfaces of the complete structure using appropriated continuity relations. Assuming that momentum

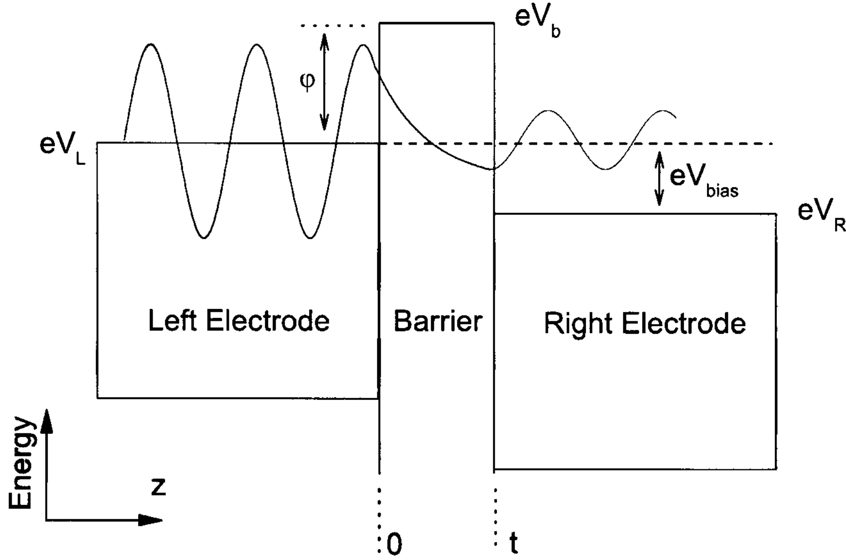

Figure 5.3: The potential energy eV(z) of a tunnel junction with two non-magnetic electrodes under a bias voltage V_{bias}.

parallel to the barrier surface, $\mathbf{k}_{\parallel} = (k_x, k_y)$, is conserved during tunneling and that there is no electron-electron or electron-lattice interactions, one can describe electrons by one-electron wave functions $\Psi(x, y, z)$ with wavevector $\mathbf{k} = (k_x, k_y, k_z)$ and energy E:

$$E = \frac{\hbar^2}{2m}|\mathbf{k}|^2 = \frac{\hbar^2}{2m}(\mathbf{k}_{\parallel}^2 + k_z^2), \tag{5.9}$$

where m is the electron mass and $\hbar = h/2\pi$ (h, Planck's constant).

The parabolic energy band is filled with electrons up to the Fermi level. The density of states is then equal to [12]:

$$\rho(E) = \frac{1}{2\pi}\left(\frac{2m}{\hbar^2}\right)^{3/2} E^{1/2}, \tag{5.10}$$

where $\rho(E)dE$ is the number of electrons with energy between E and $E + dE$.

To describe the electron states in a tunnel junction with two non-magnetic (NM) electrodes, let us consider a free electron moving in a potential which only depends on z [$V(z)$; Fig. 5.3]. This potential takes specific values in the following three regions: Left electrode (L), barrier (b) and right electrode (R). The zero potential energy in the right and left electrode corresponds to the respective bottom of the conductance bands. The barrier potential can vary as a function of z but is always higher than the Fermi level of the electrons in both electrodes.

One can thus write the time independent Schrödinger equation as:

$$\left[-\frac{\hbar}{2m}\nabla^2 + eV(z)\right]\Psi(r_{\parallel}, z) = E\Psi(\mathbf{r}_{\parallel}, z), \tag{5.11}$$

where $\mathbf{r}_{\parallel} = (x, y)$.

Because the potential only depends on the z coordinate, the wave function $\Psi(r_{\|}, z)$ is the product of one-dimensional solutions, $\Psi(r_{\|}, z) = \Psi_{r_{\|}}\Psi_z$. Since the $\Psi_{r_{\|}}$ solution is trivial [166], one focus on those in the z-direction. In the left electrode ($z < 0$) one has:

$$\begin{aligned} \Psi_z^L(z) &= a_L\phi_L^+ + b_L\phi_L^- = \\ &= a_L e^{ik_L z} + b_L e^{-ik_L z}. \end{aligned} \tag{5.12}$$

In the right electrode ($z > t$) one has:

$$\begin{aligned} \Psi_z^R(z) &= a_R\phi_R^+ + b_R\phi_R^- = \\ &= a_R e^{ik_R z} + b_R e^{-ik_R z}. \end{aligned} \tag{5.13}$$

The z component of the wave vectors are defined as:

$$k_L = \sqrt{2m(E - eV_L)/\hbar^2 - k_{\|}^2} \tag{5.14}$$

in the left electrode, and

$$k_R = \sqrt{2m(E - eV_R)/\hbar^2 - k_{\|}^2} \tag{5.15}$$

in the right electrode.

In the region of the barrier (b) the wave function satisfies the equation:

$$\frac{\hbar^2}{2m}\frac{\partial^2\Psi_z^b(z)}{\partial z^2} = \left[E - \frac{\hbar^2 k_{\|}^2}{2m} - eV(z)\right]\Psi_z^b(z). \tag{5.16}$$

Notice that the wave function $\Psi_z^b(z)$ depends on the chosen barrier potential $V(z)$ [166]. If one considers a square potential barrier with a constant potential φ (Fig. 5.3), the solution takes the form

$$\begin{aligned} \Psi_z^b(z) &= a_b\phi_b^+ + b_b\phi_b^- = \\ &= a_b e^{-k_b z} + b_b e^{k_b z}, \end{aligned} \tag{5.17}$$

with $k_b = \sqrt{k_{\|}^2 - 2m(E - eV_b)/\hbar^2}$.

In order to write the tunnel current, one needs to determine the transmission probability, which is obtained by matching wavefunctions and corresponding derivatives at $z = 0$ ($\Psi_{z=0}^L = \Psi_{z=0}^b$ and $\frac{\partial\Psi_z^L}{\partial z}|_{z=0} = \frac{\partial\Psi_z^b}{\partial z}|_{z=0}$) and at $z = t$ ($\Psi_{z=t}^b = \Psi_{z=t}^R$ and $\frac{\partial\Psi_z^b}{\partial z}|_{z=t} = \frac{\partial\Psi_z^R}{\partial z}|_{z=d}$). This system of equations can be represented in matrix form [173]:

$$\begin{aligned} \begin{pmatrix} a_L \\ b_L \end{pmatrix} &= M_L^{-1}|_{z=0} M_b|_{z=0} M_b^{-1}|_{z=t} M_R|_{z=t} \begin{pmatrix} a_R \\ b_R \end{pmatrix}, \\ &= S\begin{pmatrix} a_R \\ b_R \end{pmatrix} \end{aligned} \tag{5.18}$$

where the matrix

$$M_n = \left.\begin{pmatrix} \phi_n^+ & \phi_n^- \\ \frac{\partial\phi_n^+}{\partial z} & \frac{\partial\phi_n^-}{\partial z} \end{pmatrix}\right|_{z=z_n}, \tag{5.19}$$

contains the solutions of the Schrödinger equation and corresponding derivatives in the n-th region, at the position z_n ($n = L$, b, R).

The transmission probability T is defined as the ratio between the flux of incident electrons from the left electrode and the flux of transmitted electrons in the right electrode:

$$T = \frac{k_R}{k_L}\frac{|a_R|^2}{|a_L|^2} = \frac{k_R}{k_L}\frac{1}{|S_{11}|^2}. \tag{5.20}$$

In the weak transmitting limit, $T \ll 1$ one obtains [57]:

$$T \simeq \frac{16 k_L k_b^2 k_R}{(k_L^2 + k_b^2)(k_R^2 + k_b^2)} e^{-2k_b t}. \tag{5.21}$$

The transmission probability is then proportional to $k_L k_R$, which in turn is proportional to the product of the density of states of tunneling electrons of both electrodes.

One can now obtain the current flowing from the left to the right electrode, when a bias voltage V_{bias} is applied. The voltage lowers the Fermi level of the right electrode by eV_{bias} (e the charge of the electron), with respect to that of the left electrode (Fig. 5.3). Electrons thus flow from the left to the right electrode, producing a current density J^+ given by [174]:

$$J^+ = -\frac{2e}{(2\pi)^3\hbar}\int_{-\infty}^{\infty}\int_{-\infty}^{\infty}\int_{-\infty}^{\infty} T f(E)[1 - f(E + eV_{bias})]\frac{\partial E}{\partial k_z} dk_x dk_y dk_z, \tag{5.22}$$

where $(1/\hbar)\partial E/\partial k_z$ is the electron velocity, T the tunnel probability and $f(E) = \frac{1}{1+e^{\left(E-E_f\right)/k_B T}}$ the Fermi-Dirac function (E_F is the Fermi energy and k_B the Boltzmann constant). Subtracting the electron current flowing from the right to the left electrode [similar to Equation (5.22)], one obtains the total current density ($J = J^+ - J^-$) across the barrier:

$$J = \frac{2e}{(2\pi)^3\hbar}\int_{-\infty}^{\infty}\int_{-\infty}^{\infty}\int_{-\infty}^{\infty} T[f(E) - f(E + eV_{\text{bias}})]\frac{\partial E}{\partial k_z} dk_x dk_y dk_z, \tag{5.23}$$

which can be evaluated numerically. Analytical results can be obtained in the thick barrier approximation [42, 57], where only electrons with incidence normal to the barrier ($k_{\parallel} = 0$) contribute to the tunneling current. In this case one has:

$$J = 2\frac{e^2}{\hbar}\frac{4k_b}{\pi t}\frac{k_L k_b^2 k_R}{(k_L^2 + k_b^2)(k_R^2 + k_b^2)} e^{-2k_b t}. \tag{5.24}$$

One notices that a voltage applied across the insulating barrier changes the potential of the barrier from the here used $V(z) = \varphi$ to the linear form $V(z) = V_b - \frac{eV_{\text{bias}}}{t} z$ [Fig. 5.5(b)]. The solutions of the Schrödinger equation in the barrier [Equation (5.16)] are then different from those presented here and are given by Airy functions $Ai(\vartheta)$ and $Bi(\vartheta)$ [175], with the argument $\vartheta = \left(\frac{2meV_{\text{bias}}}{t\hbar^2}\right)^{1/3}\left(t\frac{V_b - E}{eV_{\text{bias}}} + z\right)$.

Ferromagnetic tunnel junctions. In the case of a tunnel junction with ferromagnetic electrodes the tunnel conductance is spin-dependent. Due to the molecular field $\mathbf{h}$, the spin-up and spin-down energy bands and density of states are displaced by $\Delta = 2h_0$ with respect to each other (with $|\mathbf{h}| = h_0$; Fig. 5.4). Thus, energy bands filled up to the Fermi level, have more electrons with a certain spin (majority electrons), than with the other spin direction (minority electrons). If one assumes that the spin of an electron is conserved during tunneling,

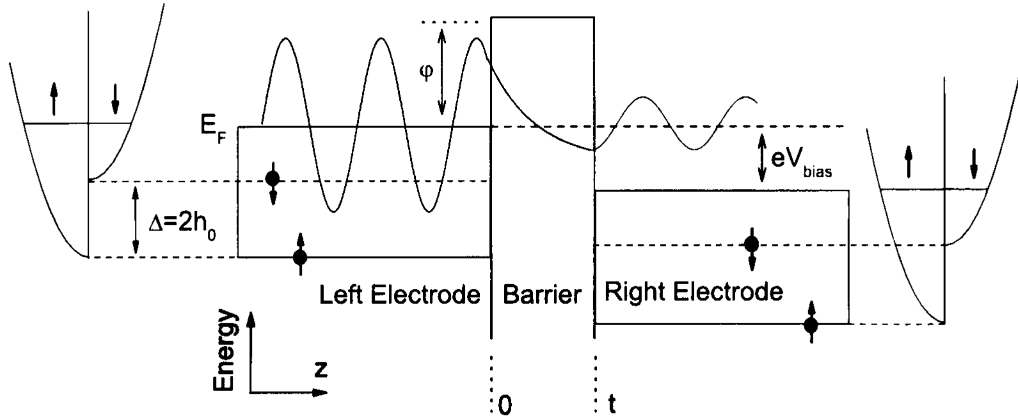

Figure 5.4: Energy diagram of a ferromagnetic tunnel junction.

one has two independent spin-channels, one for each spin. The conductance now depends on the relative orientation of the magnetizations of both electrodes. When the tunnel junction is in the parallel magnetization state, electrons from the majority (minority) spin tunnel to the majority (minority) spin band. On the contrary, when the tunnel junction is in the antiparallel magnetization state, electrons from the majority (minority) spin tunnel to the minority (majority) spin band (Fig. 5.2).

One can calculate the conductance in both cases, using the result obtained previously [Eq. (5.24)], and the wave number of electrons in the majority, $k_\uparrow = \sqrt{2m(E - h_0)/\hbar^2 - k_\parallel^2}$, and minority, $k_\downarrow = \sqrt{2m(E + h_0)/\hbar^2 - k_\parallel^2}$, bands. For equal FM electrodes, one obtains for the parallel state:

$$J_P = J_P^\uparrow + J_P^\downarrow = \frac{e^2}{\hbar}\frac{4k_b^3}{\pi t}\left(\frac{k_\downarrow^2}{(k_\downarrow^2 + k_b^2)^2} + \frac{k_\uparrow^2}{(k_\uparrow^2 + k_b^2)^2}\right)e^{-2k_b t}, \tag{5.25}$$

and for the antiparallel state:

$$J_{AP} = J_{AP}^\uparrow + J_{AP}^\downarrow = \frac{e^2}{\hbar}\frac{4k_b^3}{\pi t}\frac{2k_\downarrow k_\uparrow}{(k_\downarrow^2 + k_b^2)(k_\uparrow^2 + k_b^2)}e^{-2k_b t}. \tag{5.26}$$

The magnetoresistance is then given by:

$$TMR = \frac{2P_{eff}^2}{1 - P_{eff}^2}, \tag{5.27}$$

where P_{eff} is the effective spin-polarization:

$$P_{\text{eff}} = \left(\frac{k_\uparrow - k_\downarrow}{k_\uparrow + k_\downarrow}\right)\left(\frac{k_b^2 - k_\uparrow k_\downarrow}{k_b^2 + k_\uparrow k_\downarrow}\right). \tag{5.28}$$

The first factor is just the polarization as defined by Juliere [Eq. (5.1)], while the second depends on the barrier height (k_b), greatly decreasing the effective polarization when $k_b \sim k_\uparrow k_\downarrow$ [176]. For high enough barriers, Eq.(5.27) reduces to that obtained by Juliere [Equation (5.8)], but the free electron model always gives a better approximation for the conductance of free electrons tunneling through an insulating barrier [177, 178].

5.3.3 Tight binding model

A more accurate description of tunneling is given by the tight binding model [166, 167, 171, 179]. This model takes into account the local, multiband description of the electronic structure, allowing the study of the effects of disorder and roughness of the barrier in tunneling. The tunnel magnetoresistance is related to the electronic structure of isolated electrodes and to a hopping matrix element between the electrodes and the barrier. For perfect tunnel junctions, MacLaren *et al.* [180] found different decay rates associated with different electronic bands within a ZnSe barrier. These decay rates are slower (more rapid) for bands with s (d) character.

If disorder is introduced, one observes that the conductance of the minority spins increases, while that of majority spins remains practically constant. This leads to a decrease of polarization and thus of tunnel magnetoresistance. It was found that in highly disordered tunnel junctions the current flows mainly through highly conductive paths [171]. Remarkably, in such systems and for weak hopping, the magnetoresistance is related to the bulk density of states of the electrodes [166] and one recovers Juliere's formula. The effect of interface roughness was also addressed [166], and it was found that fluctuations in the barrier thickness lead to a reduction of its nominal thickness as obtained by the Simmon's model (see section 5.4).

5.4 Conductance and Magnetoresistance bias dependence

Tunnel current versus voltage. Information on both the barrier height φ and barrier thickness t of a tunnel junction can be obtained by measuring the corresponding current-voltage I(V) characteristic. Simmons [181] used the Wentzel-Kramers-Brillouin (WKB) [169] approximation for slow varying potentials to calculate such relation. This approximation gives simple, widely used, expressions of I(V) characteristics and is based on a simple barrier model. Let us again consider a square barrier [Fig. 5.5(a)] with height φ, defined as the energy difference between the ferromagnetic material Fermi level and the minimum of the conduction band of the insulator. When a voltage is applied across the barrier, the Fermi levels of the two electrodes become unequal and an electron current starts to flow [Fig. 5.5(b)]. As the voltage increases, the potential of an electrode decreases, increasing the energy range of incoming electrons that contribute to the tunnel current from the left to the right [see Eq. (5.23)]. For small applied bias voltage the tunnel current is then proportional to the voltage (see below). However, for larger bias voltage the tunnel current becomes non-linear.

The probability T that an electron can penetrate the potential barrier φ is, in the WKB approximation, for $\varphi \gg k_B T$ and intermediate applied bias voltage $eV_{\text{bias}} < \varphi$ [181]:

$$T = \frac{k_1}{k_2} e^{-2\int_0^t \sqrt{\frac{2m}{\hbar^2}(E-V(x))}dx} . \qquad (5.29)$$

Inserting Equation (5.29) into (5.23), Simmons obtained a simple expression for the current-voltage characteristic:

$$I = \frac{e^2}{2\pi h} \frac{A}{t^2} \left[(\varphi - eV/2)\, e^{-\alpha t\sqrt{\varphi - eV/2}} - (\varphi + eV/2)\, e^{-\alpha t\sqrt{\varphi + eV/2}} \right] , \qquad (5.30)$$

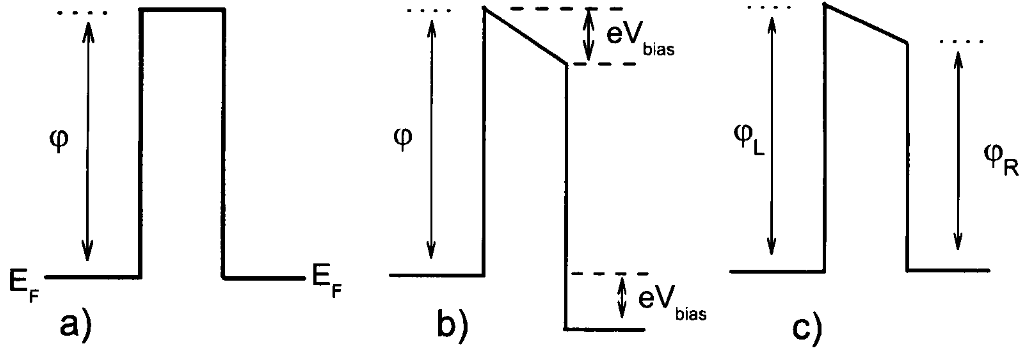

Figure 5.5: (a) Square barrier of height φ, defined as the energy difference between the Fermi level of the FM material and the minimum of the conduction band of the insulator. (b) When a voltage is applied across the barrier, the Fermi levels of the two electrodes become unequal and a current starts to flow. (c) Asymmetric tunnel junction with a barrier asymmetry $\Delta\varphi = \varphi_R - \varphi_L$.

with $\alpha = \frac{4\pi}{h}\sqrt{2me}$. A is the junction area, t the barrier thickness, e and m are the charge and mass of the electron, respectively. This equation is widely used to fit experimental I(V) data of tunnel junctions, providing values for the barrier height and thickness [182].

I(V) characteristics as calculated from Simmons' model can be observed in Fig. 5.6. One sees that the decrease of both the barrier height [Fig. 5.6(a)] and barrier thickness [Fig. 5.6(b)] cause an overall increase of the tunnel current. One also observes the predicted linear I(V) and exponential regimes for small and high bias voltage, respectively.

The low voltage electrical current was also calculated by Simmons [181]:

$$I = 3\frac{e^2}{2\pi h}\frac{AV\sqrt{\varphi}}{2t}\alpha e^{-\alpha t\sqrt{\varphi}}. \tag{5.31}$$

Two important consequences can be taken from this result. First, for low bias voltage, the I(V) characteristic is linear. Second, the tunnel resistance R depends exponentially on the barrier thickness and the square root of the barrier height, $R \propto \frac{t}{\sqrt{\varphi}}e^{\alpha t\sqrt{\varphi}}$.

However, the experimental observation of an exponential barrier thickness dependence of the junction resistance is not a sufficient condition to exclude the presence of pinholes across the TJ barrier (*i. e.* metallic paths connecting both electrodes) and it has been reported that the same $R(t)$ exponential-behavior can be ascribed to pinhole density variation with barrier thickness [183]. Furthermore, good fittings of I(V) curves to tunnel theories do not exclude the presence of pinholes in tunnel junctions [184] and need to be followed by the use of other criteria [185, 186].

The bias dependence for asymmetric tunnel junctions (arising either from different electrodes or from different electrode/barrier interfaces), was first treated by Brinkman *et al.* [187]. They introduced an average barrier height $\overline{\varphi}$ and a barrier asymmetry $\Delta\varphi = \varphi_R - \varphi_L$ to account for a tilted barrier potential [Fig. 5.5(c)]. The barrier parameters $\overline{\varphi}$, $\Delta\varphi$ and d are

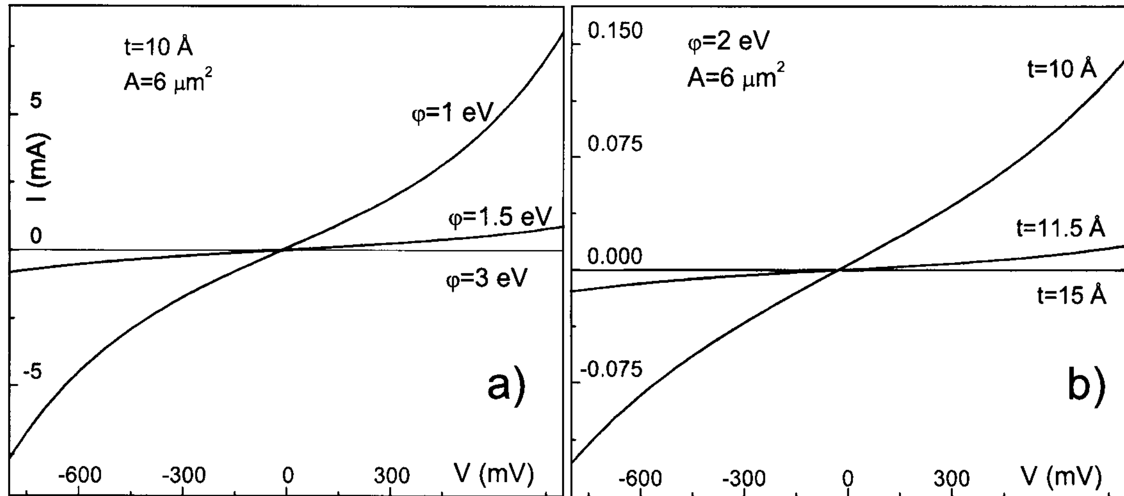

Figure 5.6: Tunnel current versus applied voltage, calculated using Simmons' model [Eq. (5.30)], (a) for constant barrier thickness and (b) for constant barrier height.

obtained [188] using experimental conductance $G(V) = \frac{dI}{dV}(V)$ curves and the relation:

$$\frac{dI}{dV}(V) = G(0)\left[1 - \left(\frac{\sqrt{2me}}{24\hbar}\frac{t\Delta\varphi}{\overline{\varphi}^{3/2}}\right)eV + \left(\frac{2me^2}{24\hbar^2}\frac{t^2}{\overline{\varphi}}\right)(eV)^2\right], \quad (5.32)$$

where $G(0)$ is the zero bias voltage conductance.

Inelastic electron tunneling processes can also be observed in dI/dV and d^2I/dV^2 versus V spectra [57]. Such processes include magnon [189, 190] and phonon [191] assisted electron tunneling and give rise to peaks at low voltages ($V \lesssim 100$ mV) in the measured spectra, which are related to the corresponding excitation density of states [57].

Both Simmons' and Brinkman's models are based on the WKB approximation that accurately describes the tunnel current flowing through thick and high barriers. However, using this approximation and a one band model leads to the cancelation of the density of states from the tunneling current [166]. Thus, the tunnel magnetoresistance effect cannot be accounted for in these models. Also, when considering thin barriers the WKB approximation is not so accurate [192].

Tunnel magnetoresistance versus voltage. It is known that the tunnel magnetoresistance decreases when the bias voltage is increased. The bias voltage for which $TMR(V) = TMR(0)/2$ is denoted by $V_{1/2}$ and is normally used to attest the quality of a tunnel junction. The value of $V_{1/2}$ has been improved from ~ 0.3 mV observed by Juliere [16] to ~ 200 mV later observed by Moodera [193] and currently to ~ 1300 mV for double magnetic tunnel junctions [194]. This enhancement is thought to have been achieved because of the improvement of oxidation processes and barrier quality.

However, the decrease of TMR with bias voltage is also related to intrinsic mechanisms operating in the tunnel junction. One such mechanism, proposed by Zhang *et al.* [189], is inelastic

scattering by magnons at the ferromagnet/insulator interface. At non-zero bias, electrons with energy above the Fermi level (hot electrons) may emit a magnon upon tunneling, thus reversing their spin. As voltage increases, more magnons can be emitted and consequently TMR decreases. However, as pointed out by Cabrera and collaborators [195, 196], this magnon inelastic scattering process should only account for the TMR behavior near zero bias, where inelastic scattering is known to take place [190, 191]. As referred, peaks associated with magnon spectra were observed at voltages below ~100 mV and this effect was shown to be too small to account for all the TMR(V) decrease up to ~500 mV. They then explained the dependence of TMR with voltage bias as a combined effect of several factors: Magnon-assisted tunneling with maximum magnon energy of ~100 meV; lowering of the barrier height with bias voltage (as in the Simmons' model); and, since experiments probe energy depths of ~0.5 eV from the Fermi level, the variation of the density of states of both electrodes with bias voltage. The modeled results agreed quite well with the experimental ones [195].

The effect of the bias dependence of the density of states had been previously introduced in an briefer form [197, 198]. In fact, as voltage increases, new states participating in tunneling are added according to the density of states at the two magnetic electrodes. Because the density of states has a considerable variation near the Fermi level, the difference between the number of majority and minority states decreases, and consequently the polarization (and TMR) also decreases. Such correlation between the TMR(V) decrease and *interfacial* density of states has been shown in References [199, 200].

5.5 Tunnel conductance and Magnetoresistance temperature dependencies

It is known that both the tunnel junction resistance and the tunnel magnetoresistance ratio decrease with increasing temperature (T). The first theoretical model to explain this behavior was derived by Simmons who obtained the temperature dependence of the elastic direct tunneling conductance G_{el} through a tunnel junction [201]. A small variation of tunnel conductance with temperature due to the broadening of the Fermi distribution in the electrodes was then found [201]:

$$G_{el}(T) = G_{el}(0)\frac{CT}{sin(CT)}, \tag{5.33}$$

where $G_{el}(0)$ is the tunnel direct conductance at $T = 0$ K and $C = 1.387 \times 10^{-4}\frac{t}{\sqrt{\varphi - eV/2}}$, t the thickness of the barrier in Å, φ the barrier height in eV and V the applied bias in V.

In Fig. 5.7 one sees the predicted temperature variation of the elastic tunneling current [Equation (5.33)] for different barrier heights and thicknesses. The $G_{el}(T)$ variation is more pronounced in tunnel junctions with thicker and higher barriers. However, one also observes a maximum $G_{el}(300\text{ K})/G_{el}(0)$ ratio of ~3%, which is too small to account for the values usually obtained experimentally ($\gtrsim$20%) [174]. Other mechanisms are then needed to explain such experimental results. Proposed mechanisms include the temperature dependence of the spin polarization, the temperature dependence of hopping conductance through localized states in the barrier, magnon- and phonon-assisted tunneling.

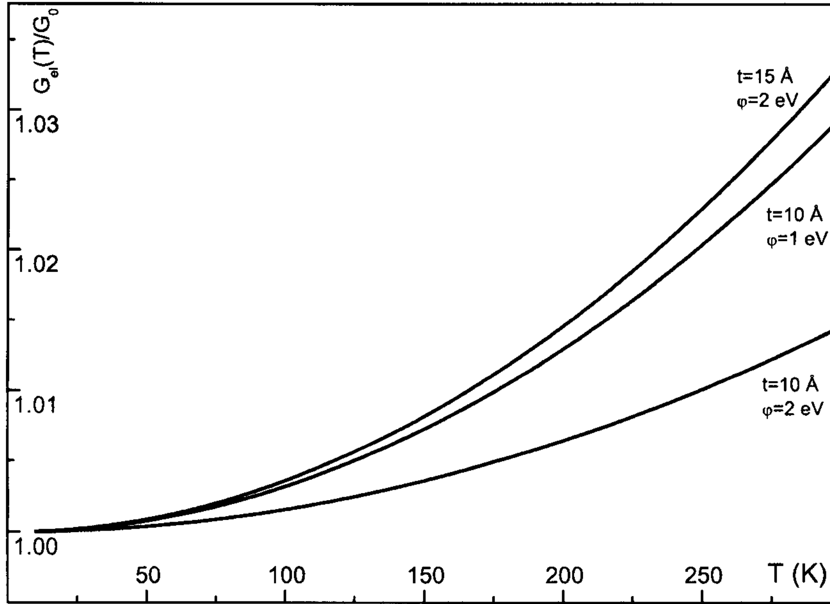

Figure 5.7: Temperature dependence of tunnel conductance due to Fermi broadening.

5.5.1 Spin-polarization temperature dependence

The *surface* magnetization M of a ferromagnetic material decreases with increasing temperature, due to the thermal excitation of magnons, according to

$$M(T) = M(0)(1 - \alpha T^{3/2}), \tag{5.34}$$

where $M(0)$ is the magnetization at zero temperature and α is a material dependent constant called the spin wave parameter [202]. The polarization P is then assumed to vary as the surface magnetization [203]:

$$P(T) = P(0)(1 - \alpha T^{3/2}), \tag{5.35}$$

where $P(0)$ is the polarization at zero temperature. One can then extend Juliere's model to account for the temperature dependence of the spin polarization [204]. The tunneling conductance G^{SP} as derived by Juliere [16] can be written as (assuming equal FM layers, whose magnetizations make an angle θ):

$$G^{SP}(T) = G_{el}[1 + P^2(T)cos\theta]. \tag{5.36}$$

One then obtains for the tunnel magnetoresistance:

$$\begin{aligned} TMR &= \frac{2P^2(T)}{1 - P^2(T)} \\ &= \frac{2P^2(0)(1 - \alpha T^{3/2})^2}{1 - P^2(0)(1 - \alpha T^{3/2})^2}. \end{aligned} \tag{5.37}$$

5.5.2 Hopping conductance

In addition to the direct elastic tunneling conductance [Equation (5.37)], a spin-independent term G^{SI} is added to explain the experimental results. The total conductance is then given by:

$$G(T) = G_{el}[1 + P^2(T)cos\theta] + G^{SI}. \tag{5.38}$$

This additional term then increases the total junction conductance but decreases TMR. It was suggested that the primary mechanism for such term is hopping through localized states in the barrier [203]. The temperature dependence of the hopping contribution can be written as [205]:

$$G^{SI}(T) = \sum_n S_n T^{n-\frac{2}{n+1}}, \tag{5.39}$$

where n is the number of hopping sites and S_n is a prefactor dependent on the density of localized states. As T increases, hopping through more n states is favored. On the other hand, if S_n is kept constant, the decrease of the barrier thickness leads to a decrease of the relative contribution of hopping to the total conductance.

5.5.3 Magnon-assisted tunneling

Magnon-assisted tunneling originates from the *s-d* exchange interaction between tunneling electrons and localized spins at the FM/barrier interfaces [189]. The energy transferred to a spin system results in the propagation of a so called spin wave [12]. The quantum of energy of a spin wave is a magnon, that can be emitted or absorbed by electrons. During such electron-magnon interaction, the energy and *spin* of the electron can be altered. Zhang *et al.* [189] proposed that tunneling electrons with energy above the Fermi level excite magnons at the FM/barrier interface and are responsible for the temperature dependence of the tunnel conductance and magnetoresistance. Han *et al.* [206] further developed this model to include an anisotropic-wavelength magnon cutoff energy.

The excitation energy of a spin wave with wavevector **q** and frequency $\omega(\mathbf{q})$ is $\varepsilon = n_\mathbf{q}\hbar\omega_\mathbf{q}$ [12], where $n_\mathbf{q}$ is the number of excited magnons with wavevector **q** that obeys the Bose-Einstein distribution,

$$n_\mathbf{q}(\omega) = \frac{1}{e^{\hbar\omega_\mathbf{q}/k_BT} - 1}. \tag{5.40}$$

The magnon density of states $\rho^{mag}(\omega)$ is given by:

$$\rho^{mag}(\omega) = (\nu + 1)\frac{\omega^\nu}{\omega_m^{\nu+1}}, \tag{5.41}$$

where ν depends on the type of magnon spectrum ($\nu = 1/2$ for magnons in the bulk of the FM layer and $\nu = 0$ for magnons at the surface) and ω_m is the maximum magnon frequency, which is related to the Curie temperature T_C of the FM:

$$E_m = \hbar\omega_m = \frac{3k_BT_C}{S+1}, \tag{5.42}$$

where S is the spin operator.

One can now obtain the tunnel current involving emission and absorption of magnons at both FM layers. Assuming low applied bias voltage V (< 200 mV) and that the temperature is much smaller than the Fermi energy, one can write for the parallel (P) state [189, 195, 174, 207]:

$$I_P^{mag} = \frac{2\pi e}{\hbar} S \sum_a \left|T_a^J\right|^2 \left[\rho_\downarrow^L \rho_\uparrow^R \int d\omega \rho_a^{mag}(\omega)\left(1 + n_q(\omega)\right)(eV - \hbar\omega)\,\theta(eV - \hbar\omega) + \rho_\uparrow^L \rho_\downarrow^R \int d\omega \rho_a^{mag}(\omega)(eV + \hbar\omega) n_q(\omega)\right], \tag{5.43}$$

where the sum is performed over the two FM electrodes $a = L, R$ and the integral upon the magnon spectrum. $|T^J|$ is the exchange tunneling matrix element for the electron-magnon scattering, $\rho_\downarrow$ ($\rho_\uparrow$) is the spin down (up) electronic density of states of the FM electrodes, and $\theta(x)$ is the step function. The first term in Equation (5.43) refers to magnon emission, while the second refers to magnon absorption.

The tunnel current for the antiparallel (AP) state is given by:

$$\begin{aligned} I_{AP}^{mag} = \frac{2\pi e}{\hbar} S \Big[& \left|T_R^J\right|^2 \rho_\uparrow^L \rho_\uparrow^R \int d\omega \rho_R^{mag}(\omega)\left(1 + n_q(\omega)\right)(eV - \hbar\omega)\,\theta(eV - \hbar\omega) + \\ & \left|T_L^J\right|^2 \rho_\downarrow^L \rho_\downarrow^R \int d\omega \rho_L^{mag}(\omega)\left(1 + n_q(\omega)\right)(eV - \hbar\omega)\,\theta(eV - \hbar\omega) + \\ & \left|T_R^J\right|^2 \rho_\downarrow^L \rho_\downarrow^R \int d\omega \rho_R^{mag}(\omega)(eV + \hbar\omega) n_q(\omega) + \\ & \left|T_L^J\right|^2 \rho_\uparrow^L \rho_\uparrow^R \int d\omega \rho_L^{mag}(\omega)(eV + \hbar\omega) n_q(\omega)\Big], \end{aligned} \tag{5.44}$$

where the first (last) two terms correspond to magnon emission (absorption).

The limits of integration in Equations (5.43) and (5.44) are taken as $[E_c^P,\ E_m]$ and $[E_c^{AP},\ E_m]$, respectively. The magnon cutoff energy $E_c^{P(AP)}$ is introduced to account for anisotropy of the interface spins or a finite coherence length due to, *e.g.* grain boundaries [189]. The use of a magnetic-alignment dependent magnon cutoff energy is justified by the experimentally observed different magnetic excitation energies for the parallel and antiparallel alignments [206]. Considering interfacial magnons with constant density of states [$\nu = 0$ in Equation (5.41)] and two equal FM electrodes, one obtains:

$$G_P^{mag} = -\frac{8\pi e^2 S}{\hbar} \frac{2\rho_\uparrow \rho_\downarrow \left|T^J\right|^2}{E_m} k_B T ln\left(1 - e^{-E_c^P/k_B T}\right), \tag{5.45}$$

and

$$G_{AP}^{mag} = -\frac{8\pi e^2 S}{\hbar} \frac{\left(\rho_\uparrow^2 + \rho_\downarrow^2\right)\left|T^J\right|^2}{E_m} k_B T ln\left(1 - e^{-E_c^{AP}/k_B T}\right). \tag{5.46}$$

Since $\left(\rho_\uparrow^2 + \rho_\downarrow^2\right) > 2\rho_\uparrow\rho_\downarrow$ ($\rho_\uparrow \neq \rho_\downarrow$), the conductance of the AP alignment increases faster with increasing temperature than that of the P alignment, so that the tunnel magnetoresistance ratio decreases with increasing temperature.

5.5.4 Phonon-assisted tunneling

An inelastic spin-conserving contribution to the tunneling current is also sometimes needed to account for experimental results of the temperature dependence of the conductance of tunnel junctions. A possible mechanism responsible for such contribution arises from the excitation and absorption of phonons at the metallic electrodes by tunneling electrons [174].

If energy is transferred to a crystal lattice, an elastic wave propagates through the material. Its energy is quantized and the corresponding quantum of energy is called a phonon [12]. For phonon-assisted tunneling one can write the current for the parallel state [174, 207]:

$$I_P^{ph} = \frac{2\pi e}{\hbar}\sum_{\sigma,a}\rho_\sigma^L\rho_\sigma^R\Big[\int d\omega P_a(\omega)\rho_a^{ph}(\omega)\,(eV-\hbar\omega)\,(1+n_q(\omega))\,\theta(eV-\hbar\omega)+ \int d\omega P_a(\omega)\rho_a^{ph}(\omega)\,(eV+\hbar\omega)\,n_q(\omega)\Big], \tag{5.47}$$

and for the antiparallel state:

$$I_{AP}^{ph} = \frac{2\pi e}{\hbar}\sum_{\sigma,a}\rho_\sigma^L\rho_{-\sigma}^R\Big[\int d\omega P_a(\omega)\rho_a^{ph}(\omega)\,(eV-\hbar\omega)\,(1+n_q(\omega))\,\theta(eV-\hbar\omega)+ \int d\omega P_a(\omega)\rho_a^{ph}(\omega)\,(eV+\hbar\omega)\,n_q(\omega)\Big]. \tag{5.48}$$

Here, $\rho^{ph} = \frac{3\omega^2}{\omega_D^3}$ is the phonon density of states (ω_D is the Debye frequency), $P(\omega) = \gamma\frac{\omega}{\omega_D}$ is the so called phonon vertex (γ is a constant) and n_q is given by Equation (5.40). Again $a = R, L$ and $\sigma =\uparrow,\downarrow$. Two limiting cases arise when integrating Equations (5.47) and (5.48): One for $k_BT \ll \hbar\omega_D$, and the other for $k_BT \gtrsim \hbar\omega_D$. One obtains for the parallel state:

$$G_P^{ph} = \frac{2\pi e^2}{\hbar}\frac{3}{2}\Gamma\left(\rho_\uparrow^2+\rho_\downarrow^2\right)\Gamma\left(\frac{k_BT}{\hbar\omega_D}\right)^\lambda\gamma, \tag{5.49}$$

and for the antiparallel state:

$$G_{AP}^{ph} = \frac{2\pi e^2}{\hbar}\frac{3}{2}\Gamma 2\rho_\uparrow\rho_\downarrow\left(\frac{k_BT}{\hbar\omega_D}\right)^\lambda\gamma, \tag{5.50}$$

where $\Gamma = \frac{8\pi^4}{15}$ ($\Gamma = \frac{8}{3}$) and $\lambda = 4$ ($\lambda = 1$) for $k_BT \ll \hbar\omega_D$ ($k_BT \gtrsim \hbar\omega_D$).

5.5.5 Pinholes

One also has to consider that pinholes may be present in the barrier, providing a metallic path between the two electrodes. The temperature dependence of the electrical resistance of TJs with pinholes should then show a metallic-like behavior, increasing with increasing temperature ($dR/dT > 0$). Such behavior was indeed observed in tunnel junctions with $R \times A \approx 10$ k$\Omega\mu$m^2, although the corresponding I(V) characteristics were well fitted using Simmons' model [184]. However, the same behavior was not observed for tunnel junctions with lower resistance ($R \times A \approx 10$ $\Omega\mu$m^2) [208]. In fact, and although pinholes had been induced, an insulator-like behavior still was observed for R(T), indicating that electrical

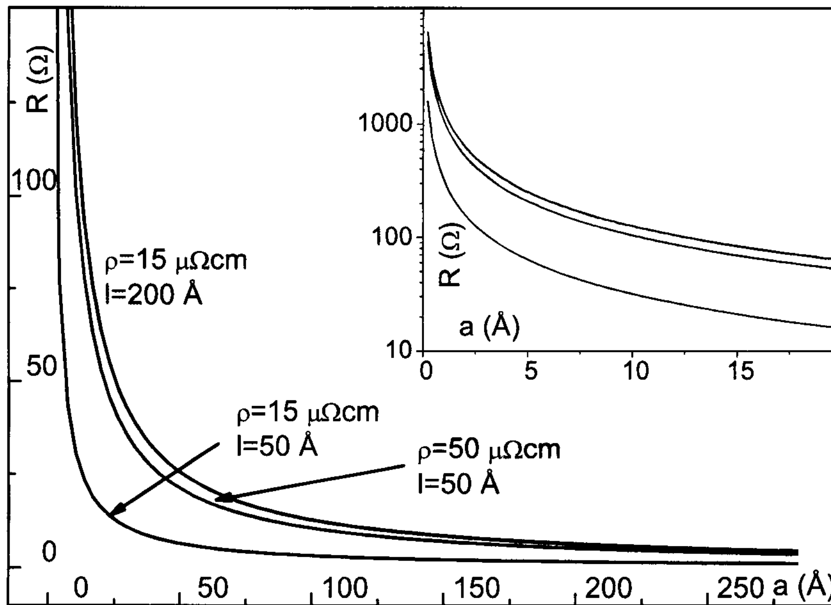

Figure 5.8: Sharvin resistance as a function of nanoconstriction radius a for several ρl products. In the inset the resistance is displayed in a logarithmic scale for small constrictions. Notice however, that the Sharvin resistance holds only for a radius larger than an electron wavelength.

transport was dominated by tunneling. Thus, for low resistance tunnel junctions, the absence of pinholes cannot be ascribed only by the R(T) behavior.

To explain that tunneling can dominate transport in the presence of metallic paths between electrodes, let us consider a nanoconstriction modeled as a circular aperture of radius a between two metallic layers of electrical resistivity ρ. The resistance of such constriction is known as the Sharvin resistance and can be written as [209]:

$$R_{\text{Sharvin}} = \frac{4\rho l}{3\pi a^2}. \tag{5.51}$$

Notice that since $\rho \propto 1/l$, R_{Sharvin} does not depend on the electron mean free path l. Considering typical values for a metal ($\rho \approx 15\ \mu\Omega cm$, $l \approx 50$ Å) and a constriction of radius $a = 50$ Å, one obtains $R_{\text{Sharvin}} \approx 13\ \Omega$, which is at least comparable to the resistance of thin tunnel junctions. In Fig. 5.8 one observes the behavior of the Sharvin resistance as a function of the constriction radius. Obviously, the larger the ρl product, the larger R_{Sharvin}. Notice that for large ρl products, R_{Sharvin} can be considerably large ($\approx 7\ \Omega$) even for $a \approx 200$ Å.

One then expects that the resistance of a tunnel junction with a pinhole can be modeled as a tunnel resistor in parallel with an ohmic resistor. Assuming that the pinhole resistance remains unchanged with increasing pinhole area, one can write the effective $R \times A$ product of a tunnel junction as [208]:

$$R \times A_{\text{eff}}(x) = \frac{A}{\left(\frac{A-x}{R\times A_{\text{tunnel}}}\right) + \left(\frac{x}{R\times A_{\text{pinhole}}}\right)}, \tag{5.52}$$

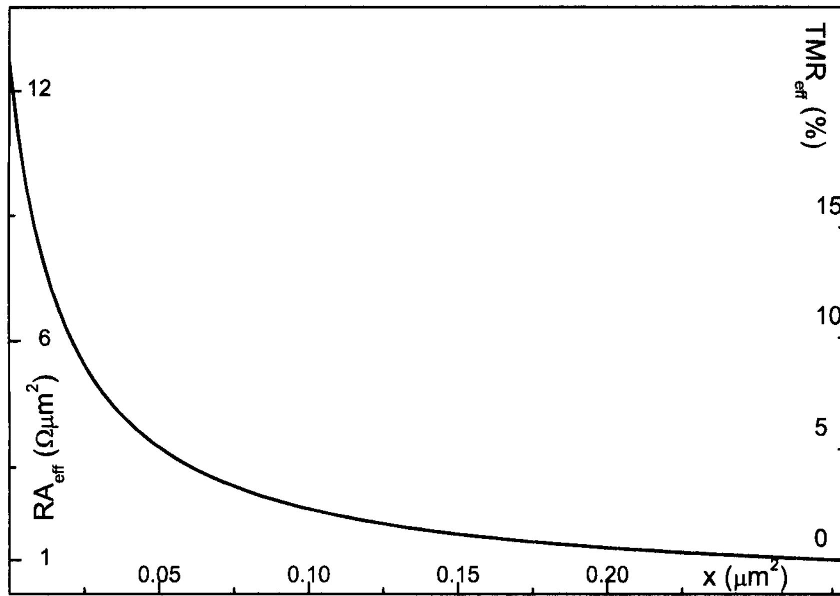

Figure 5.9: $R \times A$ and TMR as a function of pinhole area x. In this case: $A = 0.28\ \mu\text{m}^2$, $R \times A_{\text{tunnel}} = 12.7\ \Omega\mu\text{m}^2$, $R \times A_{\text{pinhole}} = 0.8\ \Omega\mu\text{m}^2$ and $TMR_{\text{tunnel}} = 25\%$.

where $R \times A_{\text{tunnel}}$ is the resistance area product of the TJ in the absence of pinholes, $R \times A_{\text{pinhole}}$ is the resistance area product when all the current passes through the pinhole, x is the area of the pinhole and A is the total area of the tunnel junction. The effective tunnel junction resistance then decreases as a function of pinhole area (Fig. 5.9; left scale) and reaches $R \times A_{\text{pinhole}}$ when $x = A$. The tunnel magnetoresistance also decreases due to the presence of this spin-independent resistance contribution (Fig. 5.9; right scale). The effective TMR is written as [208]:

$$TMR_{\text{eff}}(x) = TMR_{\text{tunnel}} \left(\frac{R \times A_{\text{eff}}(x) - R \times A_{\text{pinhole}}}{R \times A_{\text{tunnel}} - R \times A_{\text{pinhole}}} \right). \tag{5.53}$$

When all the current passes through pinholes, TMR naturally goes to zero.

The temperature dependence of the electrical resistance of the tunnel junction will begin to show a metallic-like behavior when [208]:

$$x > \frac{A \times R \times A_{\text{pinhole}}}{R \times A_{\text{tunnel}} + R \times A_{\text{pinhole}}}. \tag{5.54}$$

For the parameters used in Fig. 5.9, one sees that R(T) exhibits a positive dR/dT (denoting a metallic behavior) only when $x \gtrsim 0.06\ A$. Thus, in low resistance tunnel junctions, an insulating-like behavior of the temperature dependence of the electrical resistance does not rule out the presence of pinholes. Such is not the case for high resistance tunnel junctions, where any metallic short will overcome the tunnel resistance and induce a metallic-like R(T) behavior [184].

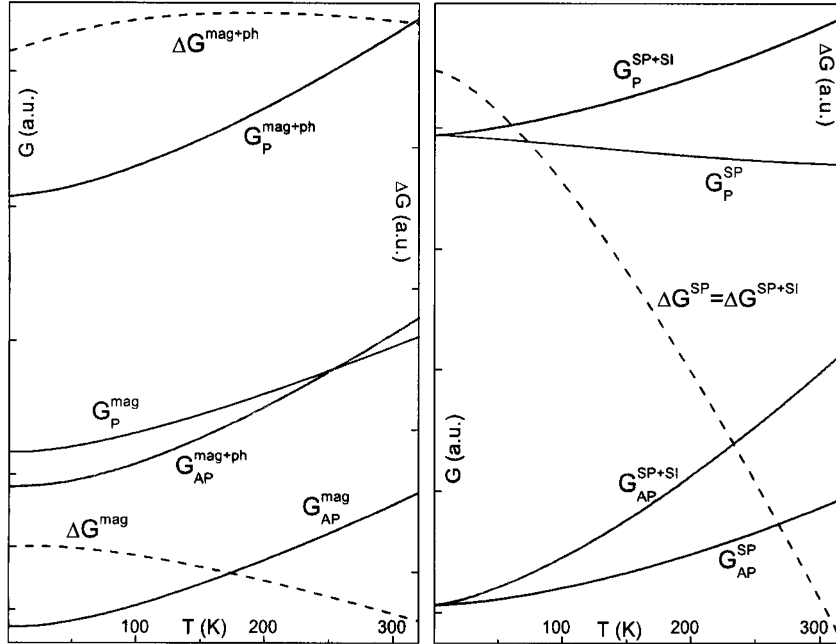

Figure 5.10: Temperature dependence of parallel G_P and antiparallel G_{AP} conductance of a magnetic tunnel junction and corresponding difference ΔG. Obtained from magnon- and phonon-assisted tunneling [Equations (5.45), (5.46), (5.49) and (5.50); left graph] and from the P(T) behavior and hopping conductance [Eqs. (5.38) and (5.39); right graph].

5.5.6 Concluding remarks

As we have seen, several models exist to account for the temperature dependence of the electrical resistance of tunnel junctions. The model derived by Simmons, taking into account only the smearing of the Fermi distribution with temperature, predicts a negligible conductance increase with increasing temperature (a few percent from low to room temperature). This is in contradiction with experiment and other mechanisms have to be considered.

The extension of Juliere's model to account for the decrease of the spin polarization with increasing temperature (section 5.5.1) gives rise to an increase of the parallel conductance G_P^{SP} with increasing temperature (Fig. 5.10; right graph). This contradicts experimental results [174] and a spin-independent tunneling contribution had to be added to the total conductance to obtain good fits [203]. Such contribution was argued to arise from hopping in localized states in the insulator barrier. One sees (Fig. 5.10 right graph; parameters used can be found in Refs. [174] and [203]) that by adding such hopping conductance one in fact obtains a G_P^{SP+SI} that increases with increasing T. However, this model is still not able to fully account for experimental results [174, 210, 211]. One then has to consider magnon- [189, 206] and phonon-assisted [174] tunneling.

As referred in section 5.4, magnon excitation is commonly used to account for the TMR(V) behavior in the low-bias voltage region. Furthermore, phonons in metallic layers are also expected to be excited during measurements in tunnel junctions [174]. Magnon- and phonon-

assisted tunneling are then likely to be the main contributions to the temperature dependence of the electrical resistance of tunnel junctions.

In Fig. 5.10 (left graph) one sees the estimated contributions from magnon- and magnon-phonon-assisted tunneling to the temperature dependence of tunnel conductance. When considering only magnon-assisted tunneling one sees that both parallel and antiparallel conductances increase with increasing temperature, but that the antiparallel contribution increases much more rapidly. Thus, both $\Delta G^{mag} = G_P^{mag} - G_{AP}^{mag}$ and TMR decrease rapidly with increasing temperature. Introducing phonon-assisted tunneling enhances the parallel conductance and (at least at low temperatures) leads to an increase of ΔG^{mag+ph} with increasing temperature. Thus, TMR will decrease slower with increasing T when compared to the case of magnon-assisted tunneling only.

5.6 Dielectric breakdown

Magnetic tunnel junctions to be used in commercial applications (section 1.3) must operate without significant degradation of their transport properties for at least about ten years. However, since the insulating barrier of a MTJ is usually very thin ($\sim$ 5–20 Å), dielectric breakdown is a reliability concern that must always be taken into consideration [208, 212, 213]. In fact, it is known that when sufficiently high electric fields ($\sim 10^7$ V/cm) are applied across the tunnel junction, dielectric breakdown occurs within minutes [214]. The resulting large decrease of the electrical resistance of the tunnel junction is a consequence of the formation of microscopic ohmic shorts in the barrier.

Dielectric breakdown in SiO_2 (used in complementary metal-oxide semiconductors) has been studied for long [215, 216, 217] and several microscopic mechanisms explaining this phenomena were proposed, with varying degrees of success [218, 219, 220]. Nevertheless, research on dielectric breakdown in magnetic tunnel junctions has only recently began to take advantage from such knowledge gathered in past studies on SiO_2 [214, 221]. Furthermore, SiO_2 capacitors have been scaled down to only $\sim$ 40 Å, a value still considerably larger than the typical $\sim$ 10 Å thickness of the insulating barrier of magnetic tunnel junctions. New physics is then encountered when studying dielectric breakdown in thin MTJs, namely the influence of pinholes and local hot-spots on the reliability of MTJs.

5.6.1 Intrinsic and extrinsic breakdown

It is experimentally observed that the breakdown voltage for thin ($\sim$ 10 Å) and ultrathin ($\sim$ 5 Å) tunnel junctions ($\approx$ 0.2 V) is much lower than for thicker ones ($\sim$ 20 Å; $\approx$ 0.6 V) [222], a dependence that is usually attributed to the presence of pinholes in TJs with thin barriers. Two distinct breakdown mechanisms in tunnel junctions are then usually encountered [212].

Intrinsic breakdown occurs in tunnel junctions with well formed oxide layers by the action of the applied electrical field or electrical current (see section 5.6.2), and is characterized by a sudden and large resistance variation at the breakdown point [Fig. 5.11(a)]. It is then associated with the local structure and composition of the oxide.

Extrinsic breakdown is related with the growth of already existing pinholes in the tunneling

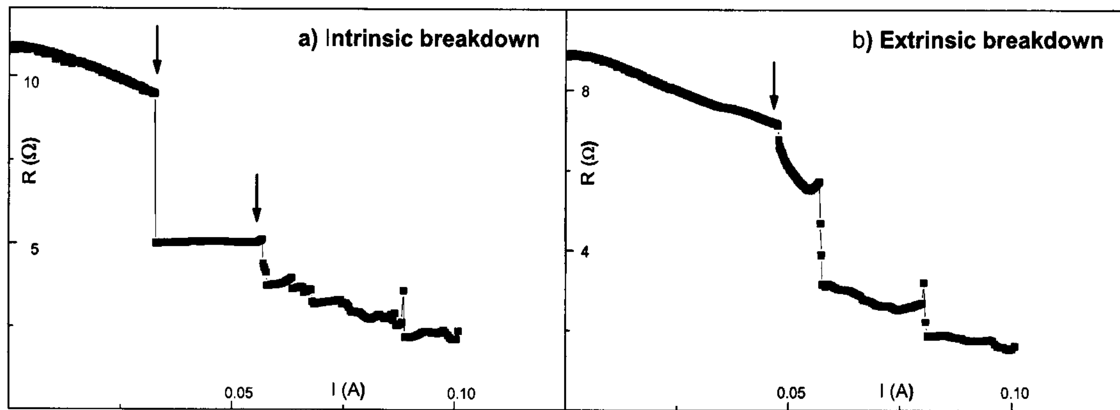

Figure 5.11: (a) Intrinsic breakdown of a tunnel junction with a well formed oxide barrier. (b) Extrinsic breakdown related with defects/pinholes in the barrier of a magnetic tunnel junction. Notice the different resistance variation associated with the two mechanisms: Abrupt for intrinsic, gradual for extrinsic breakdown (see arrows).

barrier and is then a fabrication-related (extrinsic) issue. In breakdown experiments this mechanism is characterized by a gradual variation of the electrical resistance at the breakdown point [Fig. 5.11(b)]. Localized heating near the pinhole then lead to its growth [213]. Tunnel junctions with thicker barriers have a lower concentration of pinholes and thus fail intrinsically more often than thinner ones. Consequently, the TMR value is usually correlated with the breakdown mechanism [212]: TJs that fail due to intrinsic causes show larger TMR than those that break extrinsically.

5.6.2 Microscopic models

Several physical mechanisms have been proposed to account for the observed breakdown in SiO_2 gate oxides, most noticeably the E- and the 1/E-models. All of them account well for the experimental Time Dependent Dielectric Breakdown (TDDB) data within the limited high-electrical field range experimentally available. From the E-model results that the time to breakdown τ_{BD} is expressed as $\tau_{BD} \propto e^{-\gamma E}$ as a consequence of thermochemical breakdown (E the electrical field and γ the field acceleration parameter). The 1/E-model proposes that $\tau_{BD} \propto e^{G/E}$ due to hole-generation after impact ionization (G the field acceleration factor). Today it is believed that both electrical field-induced and electrical current-induced dielectric breakdown mechanisms complement each other and are required to explain all the observed TDDB data over wide ranges of electrical field, voltage, current and temperature [223, 224].

5.6.2.1 The E-model

The E-model [218, 223, 214] is based on thermodynamic free energy considerations and relates breakdown with field-induced distortion of atomic bonds in the oxide layer. When an electrical field is applied, the oxide molecular bonds tend to break with time and tunnel junction breakdown is observed when the localized density of broken bonds is sufficiently

high for a percolative path between the two electrodes to occur.

A large dipole moment directed from the negative oxygen ion to the positive silicon ion exists in SiO_2. In the presence of an applied external electrical field $E = V/t$ (V the applied voltage and t the oxide thickness), the Si-O bonds are distorted because the dipole moments parallel to the field tend to grow while those antiparallel tend to shrink, resulting in a net polarization $\mathbf{P} = \chi\varepsilon_0\mathbf{E}$ (χ the electric susceptibility and ε_0 the electric permittivity of vacuum). The local electrical-field E_{loc} which distorts the molecular bonds in the dielectric is the sum of $\mathbf{E}$ and the surrounding dipolar field due to the polarization $\mathbf{P}$:

$$\mathbf{E}_{loc} = \mathbf{E} + L\frac{\mathbf{P}}{\varepsilon_0} = (1 + L\chi)E, \tag{5.55}$$

where L is the Lorentz factor (=1/3 for cubic symmetry). The local electrical field can then be nearly twice the applied field and dipoles parallel to $\mathbf{E}_{loc}$ have much lower energy than those antiparallel, by an amount $-2\mathbf{p}\cdot\mathbf{E}_{loc}$ where $\mathbf{p}$ is the molecular dipole moment. Antiparallel bonds are then expected to break by thermal processes (related to the finite probability that the molecule receives enough energy to break a bound) and/or hole capture (see 1/E-model), resulting in local defects that ultimately give rise to dielectric breakdown.

The time to breakdown is then given in the E-model by:

$$\tau_{BD} = t_0 e^{\frac{\Delta H}{k_B T}} e^{-\gamma E}, \tag{5.56}$$

where $\gamma = \frac{p(1-L\chi)}{k_B T}$ is the field acceleration factor, t_0 a constant and ΔH is the bond breakage activation energy.

Extrapolating these considerations to the case of amorphous Al_2O_3 [214], one sees that the electric susceptibility of Al_2O_3 ($\chi \approx 7.0$) is larger than that of SiO_2 ($\chi \approx 2.9$), which results in higher polarization and local electrical field and thus on larger field acceleration factor γ. Also, bonds in Al_2O_3 are more ionic than in SiO_2, leading to higher dipole moments in Al_2O_3, and thus also to larger γ. This enhancement of the field acceleration factor was experimentally confirmed [214], giving a solid base for the use of the E-model in magnetic tunnel junctions.

5.6.2.2 The $1/E$-model

The 1/E-model [219, 223] usually fits very well data obtained in high-field/high current tests. In this model, the energy of the electrons arriving at the anode (assumed equal or slightly larger than the barrier height) excites deep-valence band electrons to a state above the Fermi level (impact ionization), producing a hot hole which can tunnel back into the oxide. Most of the injected holes are expected to be collected by the cathode but some remain in the dielectric. This generates an electron trap inside the oxide, leading to an enhancement of local current density. The time to breakdown is then given in the 1/E-model by:

$$\tau_{BD} = t_0 e^{\frac{G}{E}}, \tag{5.57}$$

where G is the field acceleration factor of the 1/E model.

McPherson *et al.* [223] unified the 1/E- and the E-models, by claiming that current-induced holes captured by weak bonds in the dielectric, in fact only lower the required energy for

bond breakage by field-enhanced thermal means. Thus bond breakage can occur either by only field-enhanced thermal means (E-model) or by the sequence mechanism: Hole capture (1/E-model) followed by field enhanced thermal bond breakage (E-model). The effective bond breakage rate is then the sum of the rates of these two mechanisms and dielectric breakdown is dominated by the fastest one. The dominant mechanism depends mainly on the bond strength: If lower than 3 eV, the bond breakage rate is generally dominated by field-enhanced thermal processes, but for bond strengths larger than 3 eV, bond breakage must be hole-catalyzed.

5.7 Current Induced Magnetization Switching

As stated in section 1.3, tunnel junctions are thought to be able to replace common static random-access memories with the advantage of non-volatility. However, several drawbacks are still of concern regarding Magnetic Random Access Memory (MRAM) devices, like cross-talk in the array configuration and the large power consumption, mainly to generate the magnetic field used to commute the resistance between its low and high state. It is thus desirable to replace the usual magnetic field-driven by an alternative resistance switching mechanism. One such mechanism was predicted by Slonczewski [225, 226] and Berger [227] whose studies showed that a spin polarized electrical current can reverse the magnetization of a FM layer by the spin transfer effect: Current Induced Magnetization Switching (CIMS). This effect was recently observed in nanometer-sized pillars [228], exchange-biased spin valves [229] and magnetic tunnel junctions [230, 231] and is thus under intense theoretical [232, 233, 234, 235] and experimental [236, 237] research.

In the model developed by Slonczewski [225, 226], a spin polarized electrical current exerts a torque on the moments of a ferromagnetic layer, if these moments are not collinear with the direction of the current polarization. When polarized electrons from one FM enter a second FM layer, they will start to precess, to align with the magnetization direction of the second FM (Fig. 5.12). Thus, there is a difference of spin angular momentum between incoming and outgoing spins in the second FM layer. The missing spin angular momentum is absorbed by the local moments, which results in a torque exerted on the moments of the second FM layer.

A straightforward physical description of this phenomena is given in, e.g., References [232] and [235]. Let us consider the usual spin-valve type structure formed by two ferromagnetic layers (right and left) separated by a non-magnetic one, and that the magnetization of the right layer ($\mathbf{M}_R$) is tilted with respect to that of the left FM layer ($\mathbf{M}_L$) by an angle θ. The electrical current flows perpendicularly to the plane of the layers (CPP geometry). The FM layers are taken as perfect spin filters, so that incident electrons with spin aligned parallel (antiparallel) to the magnetization are totally transmitted (reflected).

Let us first consider electrons flowing from the right to the left FM layer (with magnetization along $+z$) and thus polarized along $\mathbf{M}_R$ (Fig. 5.12). These electrons can be considered as a linear combination of basis states with spin along $+z$ of amplitude $cos(\theta/2)$ and along $-z$ of amplitude $sin(\theta/2)$. For the perfect spin filter situation considered here, electrons transmitted by the left layer will have their spin solely on the $+z$ direction, while electrons reflected by the left layer will have their spin along the $-z$ direction. The x spin-component is absorbed by the moments of the left FM layer (due to s-d exchange interactions [225, 235]) thus producing

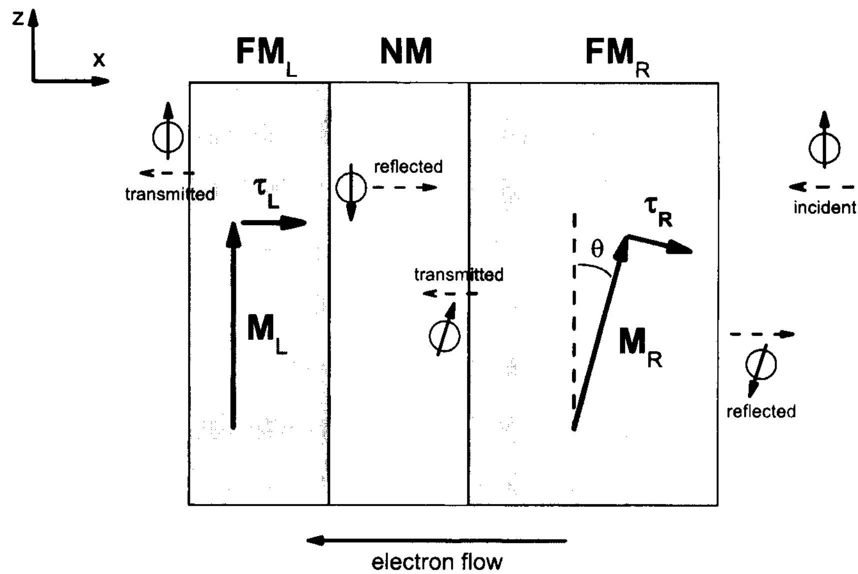

Figure 5.12: Angular momentum transfer. Electrons flow from the right to the left. A torque is exerted in the magnetization of the left FM layer, trying to align it parallel with that of the right layer.

a torque τ_L on $\mathbf{M}_L$. In this case, the torque is applied so as to align the magnetization of the left FM layer parallel to the polarization direction of the incident electrons, and thus to $\mathbf{M}_R$. On the other hand, electrons reflected from the left FM layer have their spin antiparallel to $\mathbf{M}_L$ and exert a torque τ_R on $\mathbf{M}_R$ so as to align it antiparallel to $\mathbf{M}_L$. If no other forces were present in the structure (anisotropy, local fields), the magnetization of both layers would continuously rotate in the same direction [225]. However, if one considers (as schematically represented in Fig. 5.12), that one of the FM layer is much thicker than the other, the direction of the magnetization of such thick layer can be treated as fixed, and only that of the thin layer rotates.

When the current flows in the reverse direction (electrons flow from left to right; Fig. 5.13), the directions of the torques are also reversed. In this case the torque will try to align $\mathbf{M}_R$ parallel to $\mathbf{M}_L$ and $\mathbf{M}_L$ antiparallel to $\mathbf{M}_R$. One then has that, when the current flows in one direction through the thin FM layer, its moments will rotate as to align themselves parallel to the magnetization of the thick FM layer. If the current direction is reversed, the torque will act as to rotate the moments of the thin FM layer antiparallel to $\mathbf{M}_R$. Furthermore, the torque is always non-zero even for small spin dependent scattering [235]. Thus, and although the torque is zero when the magnetizations of both FM layers are parallel or antiparallel, any fluctuation from these orientations is amplified by the current-induced torque.

Recent experiments [238] showed that the CIMS effect does not depend only on the interfacial spin-dependent scattering but that bulk scattering inside the thick FM layer must also be taken into account (see References [226, 232, 233, 239]). It is, however, independent of the scattering inside the thin FM layer.

One then must add an extra spin-transference term to the usual Landau-Lifshitz equation

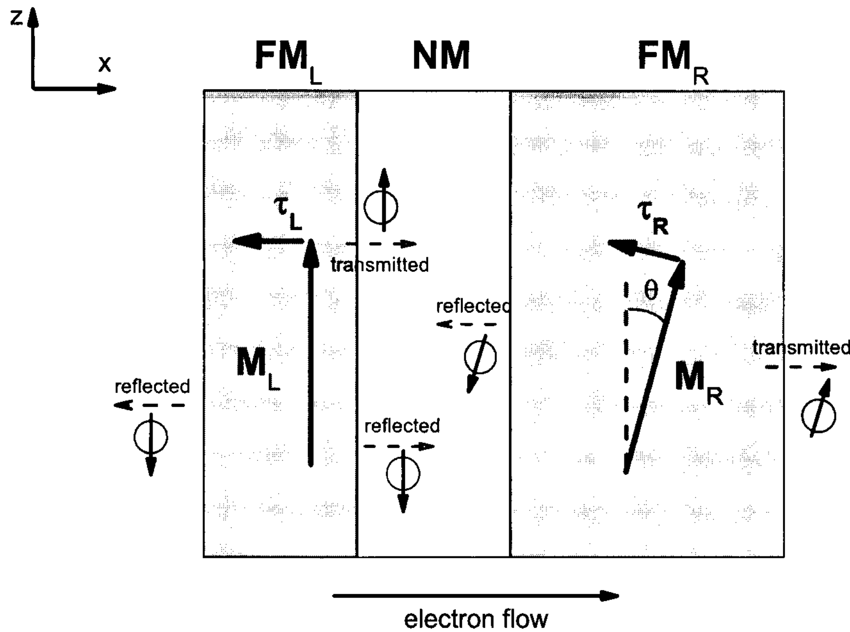

Figure 5.13: Angular momentum transfer. Electrons flow from the left to the right. A torque is exerted in the magnetization of the left FM layer, trying to align it antiparallel with that of the right layer.

that rules magnetization dynamics of the form (see, e.g., References [225, 228, 234, 239]):

$$\frac{d\mathbf{M}_L}{dt} \propto -jg(\theta)\hat{\mathbf{m}}_L \times (\hat{\mathbf{m}}_R \times \hat{\mathbf{m}}_L)\,, \tag{5.58}$$

where j is the electrical current density, $g(\theta)$ is a function that depends on the polarization and increases with θ [225] and $\hat{\mathbf{m}}_{R,L}$ are the unit vectors $\mathbf{M}_{R,L}/M_{R,L}$. It is thus possible to discuss the stability of the parallel and antiparallel states [237], the critical current density needed to induce magnetization reversal through the spin-torque effect [228, 237], as well as the switching time and anisotropy [240].

Such Current-Induced Magnetization Switching was first experimentally observed in nanopillars [228] with two Co layers with different thickness, separated by a Cu spacer. The pillars were lithographically patterned to ~130 nm dots. It was observed that, in low applied magnetic field, a spin polarized current (current density $j \sim 10^8$ A/cm^2), flowing from the thick to the thin layer, switched the magnetization of the thin layer from parallel to antiparallel and from antiparallel to parallel for the reversed current direction.

Since then several other groups have experimentally probed the characteristics of the CIMS effect, including layer thickness [241], magnetic field [237] and temperature [242] dependencies and the effect of coupling between the FM layers [243]. Current induced magnetization switching was also responsible for the observed reversal of the magnetization of the free layer of an exchange-biased spin valve (280×90 nm^2) [229] for high density currents ($\sim 10^8$ A/cm^2). Lower current densities ($\sim 8\times10^6$ A/cm^2) were necessary for current-driven switching of submicron, ellipse-shaped exchange biased tunnel junctions [230, 231].

5.8 Current Induced Resistance Switching

For atomic diffusion to occur an atom needs to surmount the energy barrier E_b separating equilibrium lattice sites. When an electric current flows through a metal the usual, thermally-activated, random motion of atoms is biased by the electrical field (Fig. 5.14), resulting in a net atomic flow. This phenomena is know as electromigration [244] and is currently the major cause of failure of interconnects in integrated circuits [245]. Studies of EM in interconnects are performed under stress conditions, such as high electrical current densities ($\sim 10^7$ A/cm^2) and temperature ($\sim$ 500–700 K) and show that EM can occur through different diffusion paths, such as grain boundary and interfaces, as in Al [246] and Cu [247] interconnects, respectively. The relative importance of the different diffusion paths varies with the material properties (grain size and orientation, interface bonding and structure). In cubic systems, atomic diffusion is usually mediated by vacancies. Since interfaces and grain boundaries are the main sources of vacancies [248], these are usually the paths followed by diffusing atoms. However, interstitial diffusion can also be an important diffusion mechanism [249].

Electromigration is also a concern in magnetic nanostructures, namely spin valves and tunnel junctions [250]. During device operation, local structural inhomogeneities can lead to large current densities, and thus to electromigration (especially in tunnel junctions where the resistance depends exponentially on the barrier thickness and where localized nanoconstrictions can concentrate most of the current). Such high current densities can also lead to intense heating which then results in enhanced electromigration [250]. Discrete electromigration events were observed in metallic nanobridges (for $j \sim 10^8$ A/cm^2) [251]. *Reversible* EM was recently observed in Ni nanoconstrictions ($j \sim 10^{13}$ A/cm^2) [252] and thin tunnel junctions ($j \sim 10^6$ A/cm^2) [62, 253]. It was recently observed that EM in these nanostructures can lead to both an increase and a decrease of the electrical resistance, depending on the sense of the applied electrical current, and thus on the sense of EM-driven atomic motion. This new effect in TJs was called Current Induced Resistance Switching (CIS) and constitutes an important topic systematically investigated in this thesis.

5.8.1 Atomic diffusion

Atomic diffusion in crystals takes place by random discrete atomic jumps from one lattice site to another or, equivalently, from one equilibrium position to another. In a crystal, the regular array of lattice sites provide equilibrium positions for atoms, so during an atomic jump the migrating atom has to overcome repulsive forces from its neighbors. Thus, the migrating atom needs sufficient energy to surmount the energy barrier E_b separating equilibrium positions [Fig. 5.14(a)]. Such energy is occasionally given by a local thermal fluctuation.

Several mechanisms are possible for atomic diffusion [254]. The simplest is the exchange mechanism, that consists in the direct interchange of two neighboring atoms. This is a very unlikely process, since during diffusion each atom would need to be considerably compressed before passing one another. Another mechanism occurs when there are crystal imperfections, such as small interstitial atoms. In this case, diffusion can occur through direct jumps from one interstitial site to another (interstitial mechanism). When the size of the interstitial atom is comparable to that of the lattice atoms, diffusion can occur through the interstitialcy mechanism. Here, the interstitial atom moves to a normal lattice site, while the atom

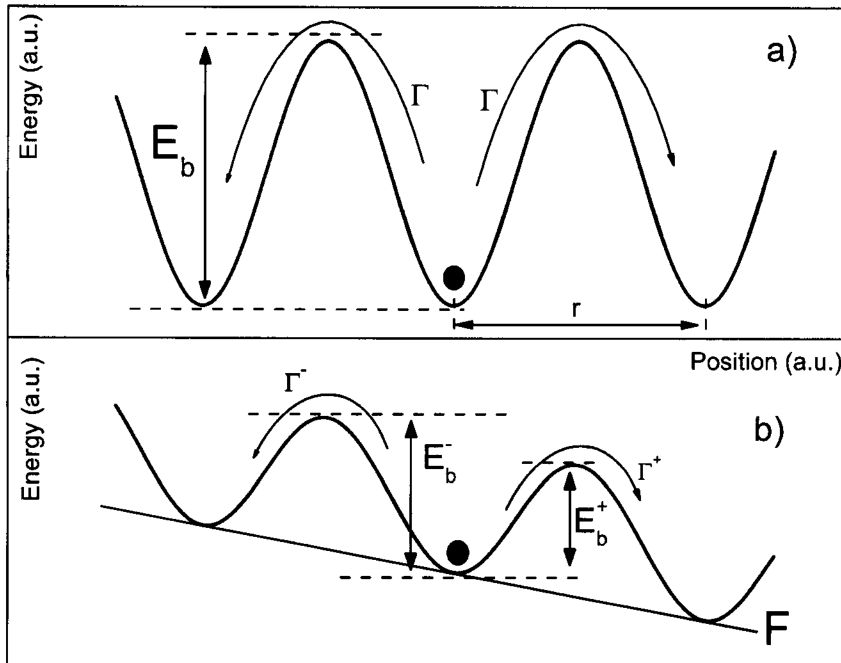

Figure 5.14: (a) Diffusion of an atom in the periodic potential created by the lattice. Notice that the energy barrier for diffusion E_b is isotropic. (b) Diffusion of an atom in the presence of an applied force. Notice the different energy barriers for diffusion and jump frequency to the right (E_b^+, Γ^+) and to the left (E_b^-, Γ^-) .

originally at the lattice site is pushed into a neighboring interstitial site. Another diffusion mechanism is the vacancy mechanism. Vacancies exist in any crystal at a temperature above absolute zero and provide an easy path for diffusion. A migrating atom simply jumps into a neighboring vacancy, exchanging position with it. Vacancy and interstitial mechanisms are the most frequently observed experimentally.

The total displacement per unit time $\mathbf{R}$ of migrating atoms randomly jumping through crystal sites can be written as:

$$\mathbf{R} = \sum_{i=1}^{\Gamma} \mathbf{r}_i, \tag{5.59}$$

where $\mathbf{r}_i$ is the i-th elementary jump vector and Γ is the number of atomic jumps per unit time. Averaging over a large number of jumps one can write the mean square displacement R of a cubic system [255]:

$$\langle R^2 \rangle = \Gamma r^2 f, \tag{5.60}$$

where f is the correlation factor that depends on the crystal structure and diffusion mechanism [256]. However, $f \sim 1$ for most systems of interest, which indicates that the diffusion processes are usually uncorrelated. Thus, successive jumps are completely independent one from another.

Defining the diffusion coefficient as $D = \frac{1}{6} \langle R^2 \rangle$, one can now introduce the two general equations governing diffusion. If C is the concentration of the diffusing atoms, then the

atomic flux J is given by (assuming isotropic diffusion):

$$\mathbf{J} = -D\nabla C. \tag{5.61}$$

Equation (5.61) is the phenomenological Fick's law and states that the flux of the diffusing atoms is proportional to its concentration gradient, *i. e.*, diffusion occurs from regions of high to regions of low concentration. In the absence of a concentration gradient, there will be no net atomic flux.

The conservation of the number of atoms will be given by the continuity equation:

$$\frac{\partial C}{\partial t} = -\nabla \cdot \mathbf{J}. \tag{5.62}$$

For atomic diffusion by a vacancy (interstitial) mechanism the diffusion coefficient D_v (D_i) is given by [255]:

$$D_{v(i)} = \frac{fr^2\Gamma_{v(i)}}{6}, \tag{5.63}$$

where $\Gamma_{v(i)}$ is the jump frequency of an atom into an adjacent vacancy (interstitial site).

The jump frequency can be obtained using straightforward physical arguments. Let us consider a diffusing atom in a periodic potential representing equilibrium lattice sites in the crystal [Fig. 5.14(a)]. The probability that an atom acquires an energy equal or greater than the activation energy for migration (E_b) and thus moves over the barrier into a new equilibrium position is given by the Boltzmann factor. If ν is the vibration frequency of the atom at the equilibrium position (approximately the Debye frequency), then one simply has [255]:

$$\Gamma = \nu e^{-E_b/k_BT}, \tag{5.64}$$

which results in:

$$D_j = D_{0_j} e^{-E_{b_j}/k_BT}, \tag{5.65}$$

where $j = v, i$ (vacancy, interstitial) and $D_{0_j} = \frac{\nu_j r^2 f}{6}$.

Notice that we assumed isotropic jump frequencies, *i. e.*, the jump probability did not depend on its direction [Fig. 5.14(a)]. We will now see how a driving force (*e. g.* an electrical field) affects atomic diffusion [Fig. 5.14(b)].

Let us consider an one-dimensional system, where particles can jump from one site to the right or to the left. In an isotropic system, the jump frequencies Γ to the right and to the left are equal. However, an applied external force F (*e. g.* an electrical field that acts on ions, as in electromigration; see section 5.8.2) introduces an anisotropy on the jump frequency. Such anisotropy arises because the force lowers the potential energy of an atom (by $rF/2$) when it moves by r in the direction of the force [Fig. 5.14(b)]. One thus has to distinguish between the jump frequency to the right Γ^+ and to the left Γ^- . Redefining the (1D) diffusion coefficient as $D = \frac{fr^2}{2}\frac{(\Gamma^+ + \Gamma^-)}{2}$, one can write the flux of the diffusing particle J along the x axis as [257]:

$$J = -D\frac{\partial C}{\partial x} + vC, \tag{5.66}$$

that can be readily generalized for a 3D system. C is the concentration of diffusing atoms and $v = r(\Gamma^+ - \Gamma^-)$ is the drift velocity and is a measure of the bias in the system. Due

to collisions, a linear relation between the drift velocity and the applied force is often found [257, 258]:

$$v = MF, \tag{5.67}$$

where $M = \frac{D}{k_B T}$ is called the mobility.

The flux [Eq. (5.66)] due only to the external force J_F is then given by:

$$J_F = \frac{DC}{k_B T} F. \tag{5.68}$$

The different energy barriers for migration to the right and to the left lead to the jump frequencies (Γ^+, Γ^-) given by:

$$\Gamma^{\pm} = \nu e^{-E_b^{\pm}/k_B T} = \nu e^{-(E_b \mp Fr/2)/k_B T}. \tag{5.69}$$

One now obtains for the diffusion coefficient:

$$D = r^2 \nu e^{-E_b/k_B T} cosh(Fr/2k_B T), \tag{5.70}$$

and the drift velocity:

$$v = 2r\nu e^{-E_b/k_B T} sinh(Fr/2k_B T). \tag{5.71}$$

Noticing that in actual structures diffusion occurs through several paths, an effective diffusion coefficient D_{eff} should be taken into consideration:

$$D_{eff} = f_B D_B + f_{gb} D_{gb} + f_i D_i, \tag{5.72}$$

where the subscripts B, gb, i refer to bulk, grain boundary and interface diffusion, respectively. f_j ($j = B, gb, i$) is the fraction of atoms diffusing through path j and depends on the geometry of the structure considered. Usually $D_{0_B} \ll D_{0_{gb}}, D_{0_i}$. The activation energy also depends on the the migration path. For Aluminium self-diffusion one has 1.5 eV for diffusion in the bulk, 0.6 eV for diffusion along a grain boundary and 0.9 eV for diffusion along an Al/Al_2O_3 interface [259].

5.8.2 Electromigration

When a metal is subjected to an electrical field $\mathbf{E}$, the usual random diffusive motion of atoms is biased by the resulting driving force $\mathbf{F}$, and a net atomic flux can be observed. This phenomena is known as electromigration (EM) [244] and $\mathbf{F}$ can be written as:

$$\mathbf{F} = Z^* e\mathbf{E}, \tag{5.73}$$

where Z^* is the effective valence and e is the elementary charge. The force acting on the migrating ion is usually separated into two components, both linear in the external applied electrical field:

$$\mathbf{F} = \mathbf{F}_d + \mathbf{F}_w = (Z_d + Z_w)e\mathbf{E}. \tag{5.74}$$

The direct force $\mathbf{F}_d$ arises from the electrostatic interactions between the electrical field and the direct valence of the ion Z_d (> 0). The theoretical calculation of the direct force is a

challenging process but $Z_d \approx Z$ (Z the valence of the ion) is usually assumed. The wind force $\mathbf{F}_w$ results from momentum exchange between the current carrying electrons and the migrating ions and it is then exerted in the direction of the electron current (opposite to the electrical field). The wind valence Z_w is simply a convenient term to describe the wind force, arising from the fact that $\mathbf{F}_w$ is proportional to the current density and, in an ohmic material, to $\mathbf{E}$. The competition between wind and direct forces is often dominated by the first, that thus controls the sign and magnitude of the effective valence Z^* and the EM process.

Notice that one can now write the atomic flux [Equation (5.68)] as:

$$J_F = \frac{DC}{k_B T} e Z^* E. \tag{5.75}$$

The most straightforward determination of Z^* is obtained using the so called *ballistic model*, where the direct valence is taken as the valence of the unscreened ion and the wind valence is given by easily obtainable material dependent constants. Other more sophisticated models treat the electromigration driving force self-consistently, without *a priori* separation of the direct and wind contributions.

5.8.2.1 The ballistic model

The ballistic model of electromigration presents the most intuitive picture of the underlying physics of EM [244]. In this model the direct valence is taken to be the (unscreened) ion, for which $Z_d = Z$. The wind force is calculated assuming that all the momentum lost by the scattered electrons is transferred to the migrating ion [251]. Electrons are treated as in the free electron approximation and migrating ions as defects. When an electron is scattered by such impurity ions, the momentum transferred to the ion per second and unit volume is given by $nm\mathbf{v}_d/\tau_i$, where n is the electron density, m is the electron mass, $\mathbf{v}_d$ is the drift velocity of the electron and τ_i is the collision time for electron scattering by the impurity. The force acting on a single impurity ion is then $nm\mathbf{v}_d/\tau_i N_i$, where N_i is the density of impurity ions. The wind force can then be written as [244]:

$$\mathbf{F}_w = -\frac{\mathbf{j}m}{e\tau_i N_i}, \tag{5.76}$$

where $\mathbf{j} = -ne\mathbf{v}_d$. Using $\rho = E/j$, the total resistivity, and $\rho_i = m/ne^2\tau_i$ (resistivity due to the impurity), one obtains:

$$\mathbf{F}_w = -e\frac{n\rho_i}{N_i\rho}\mathbf{E}. \tag{5.77}$$

Equation (5.77) can be further rewritten, so that one obtains $Z_w = -nl\sigma_{tr}$, where n is the electron density, l is the electron mean free path and σ_{tr} is the electron transport cross section for scattering by the ion. The effective valence Z^* in the ballistic model is then given by [244]:

$$Z^* = Z - nl\sigma_{tr}. \tag{5.78}$$

Using typical values for a metal ($n \sim 10^{-1}$ Å^{-3}, $l \sim 100$ Å, $\sigma_{tr} \sim 1$ Å^2; [260]), one finds $Z_w \sim -10$ ($|Z_w| \gg Z_d \approx 1$), showing that the wind force usually dominates electromigration. However, more elaborated electromigration models such as the pseudopotential method give considerably lower Z_w values, by as much as 70% [244]. Also, the ballistic model is difficult to extend to account for band-structure effects.

5.8.2.2 Other models

Other models of electromigration include the pseudopotential method, where each ion is described by its own bare pseudopotential and a neutralizing electron cloud. The neutral atom is described by a screened pseudopotential, allowing the use of perturbation theories. The analysis of such method is complicated because the pseudopotential is non-local and energy dependent. Numerical results give lower wind force values, between 20 and 70% when compared to those obtained using the ballistic model. Such results are in good qualitative agreement with experiment, especially when $Z_d = Z$ is assumed.

Another approach based on the semi-classical Boltzmann equation gives a self-consistent calculation of the electromigration driving force. In this approach the simultaneous presence of the electrical field, electron current and electron scattering is considered. It is found that the electromigration force can be written as [244]:

$$\mathbf{F} = Ze\mathbf{E} - (\mathbf{u} - \mathbf{v}_d)D, \tag{5.79}$$

where $\mathbf{E}$ is the macroscopic electrical field, $\mathbf{u}$ is the velocity of the migrating ion, $\mathbf{v}_d$ is the electron drift velocity and D is a viscosity coefficient.

A quantum-mechanical generalization of the previous result is given by the density matrix analysis. A self-consistent potential V for an electron in the presence of a single impurity and an applied electrical field is considered, $V(\mathbf{r}) = V_0(\mathbf{r}) + V_{sc}(\mathbf{r})$, where V_0 is the bare potential and V_{sc} is the screening potential. The effective valence is given by [244]:

$$\frac{Z^*}{Z} = A - BE_F\tau, \tag{5.80}$$

where τ is the relaxation time and A and B are positive constants. The first term can then be identified with the direct force, while the second one is associated with the wind contribution. One notices that the separation between direct and wind forces is only a matter of convenience, and that the only relevant quantity in EM is the net force acting on the ion. Nevertheless, all electromigration models can be generalized to give a $\mathbf{F}_d + \mathbf{F}_w$ expression.

5.8.2.3 Electromigration in nanoconstrictions

Sorbello [261] first studied electromigration forces in mesoscopic systems. In particular he considered electromigration near a point contact modeled as a circular aperture of radius a between two metallic layers of electrical resistivity ρ. One writes again the Sharvin resistance [209]:

$$R_{Sharvin} = \frac{4\rho l}{3\pi a^2}. \tag{5.81}$$

The direct force is, near the aperture, given by:

$$F_d \approx eZ_d\frac{V}{2a}, \tag{5.82}$$

where V is the voltage across the constriction. On the other hand, the wind force near the aperture can be estimated as:

$$F_w \approx K \frac{I}{\pi a^2}, \tag{5.83}$$

where $K = (F_w/J)_{bulk}$. Both the direct and wind forces are then enhanced near the constriction, when compared to the corresponding bulk values. Using Equations (5.81), (5.82) and (5.83), an estimate on the relative magnitude of the direct and wind forces gives [261, 251]:

$$\frac{F_d}{F_w} \approx -\frac{Z_d}{K}\frac{2\rho l}{3a}. \tag{5.84}$$

The F_d/F_w ratio then depends on the geometry of the constriction: The smaller the constriction radius, the larger the relative magnitude of the direct force compared to the wind force. For self-electromigration in Al, Sorbello [261] estimated $F_d \approx -\frac{1}{2}F_w$ when $a = 14$ Å. Contrarily, in the case of bulk electromigration one generally has $|F_d| \ll |F_w|$, as noticed previously.

Chapter 6

Current Induced Switching in Magnetic Tunnel Junctions

Summary

Tunnel junctions (TJs) consisting of two ferromagnetic (FM) layers separated by an insulator [8] are strong candidates for technological applications as magnetic random-access memories (MRAMs) [155]. The magnetization of one of the FM layers (pinned layer) is fixed by an underlying antiferromagnetic (AFM) layer. The magnetization of the other FM layer (free layer) reverses almost freely when a small magnetic field is applied. Due to spin dependent tunneling [151] one is able to switch the device between two distinct resistance (R) states, when the magnetizations of the pinned and free layers become parallel (R_{P}; low R) or antiparallel (R_{AP}; high R). However, because cross-talk and power consumption are still a concern for MRAM devices, one desires to replace the usual magnetic field-driven by an electrical current-driven R-switching mechanism, as predicted by Slonczewski and Berger [225, 227] (spin torque effect; Current Induced Magnetization Switching). This effect was recently observed in nanometer-sized pillars, exchange-biased spin valves and magnetic tunnel junctions [228, 229, 230, 231], but it required high current densities ($j \sim 10^8 \mathrm{A/cm^2}$).

On the other hand, Liu et al. [62] observed R-changes (switching between high and low R-states) induced by much lower current densities ($j \sim 10^6$ A/cm^2) in thin tunnel junctions. These changes were initially attributed to the Current Induced Magnetization Switching mechanism, caused by the spin-torque exerted by the electrical current on the local moments within the FM layers (section 5.7). However, it was later found [76] that the observed phenomenon did not depend on the relative orientation of the free/pinned layer magnetizations. This new *non-magnetic* effect was then called Current Induced Switching (CIS) and attributed to electromigration of metallic ions in nanoconstrictions in the insulating barrier [253]. In fact, Deac *et al.* [253] observed that, in ultra-thin TJs (barrier thickness $t = 5$ Å), transport in the current-induced high (low) resistance state was tunnel (metallic) dominated. Such change in the transport mechanism was attributed to the opening/closing of metallic pinholes in the insulating barrier, resulting from electromigration of ions from the electrodes into the insulating barrier and vice-versa. For a sufficiently intense current (critical switching current, I_c) high electrical fields occur across the thin insulating layer and may lead

to electromigration of ions from the FM electrodes (Co, Fe) into the barrier, decreasing the effective barrier thickness and consequently the junction resistance ("thin" barrier state; $R = R_b$). If the electrical field is reversed, the previously displaced ions return to the FM electrodes, increasing the tunnel junction electrical resistance ("thick" barrier; R_B). Both CIS and CIMS effects seem to coexist in magnetic tunnel junctions for $j \gtrsim 10^6$ A/cm^2. The reasons for the observed dominance of one effect over the other are still unclear but likely related to structural differences in the studied tunnel junctions.

Here we present a detailed study on the Current Induced Switching effect on a series of low resistance AFM/FM/I/FM (MnIr/CoFe/AlO$_x$/CoFe) tunnel junctions deposited by Ion Beam Deposition (IBD). The AlO$_x$ insulating barrier originally resulted from a 7 Å thick Al layer naturally oxidized. Current Induced Switching cycles performed at room temperature (RT) showed a 6.9% resistance change, and the effect is here discussed in terms of nanostructural rearrangements of metallic ions from the FM electrodes, near their interfaces with the insulating barrier. Notice that electron trapping at localized states in the barrier can also lead to changes in the TJ-resistance (as discussed in chapter 8), but this effect is expected to be small in our MTJs, due to their optimized oxidation.

Just after the initial pronounced current induced switching from the high to the low R-branch (due to atomic migration; under high currents), the subsequent slight reduction of the applied electrical current results in an immediate (small) resistance recovery. This evidences that some displaced ions readily return to their initial sites in the FM electrodes. This particular effect was found to be thermally assisted with a small energy barrier $\Delta_1 \sim 0.13$ eV. A second energy barrier was observed ($\Delta_2 \sim 0.85$ eV), leading to a corresponding exponential temperature dependency, $e^{-\Delta_i/k_BT}$, for the TJ-resistance.

Relaxation phenomena of the CIS effect are also studied in this chapter. After a complete (or *half*) CIS cycle we monitored the R-evolution in time, obtaining a non-monotonic behavior characterized by two distinct relaxation times. First R increases (*decreases*) rapidly, but then a slow relaxation dominates reducing (*increasing*) R. These opposite sign relaxation processes suggest two independent physical mechanisms acting simultaneously inside the TJ, and will be discussed in terms of ion electromigration near the two metal/insulator interfaces.

We also measured the temperature (T) dependence of the electrical resistance (R) and of the current-induced switching effect (CIS) in the 300 – 25 K temperature range. The electrical resistance slightly rises as temperature decreases, indicating tunnel-dominated transport. On the other hand, below room temperature we observe lower CIS signals (*e. g.* ~3.5% at $T = 120$ K instead of 6.9% at RT) and anomalous resistance maxima just preceding resistance switching, near the negative maximum pulse current ($I_{\max}$). At still lower temperatures (*e. g.*, 25 K) the resistance suddenly decreases both at negative and positive high current pulses, indicating barrier degradation effects. Subsequent R(T) measurements showed a positive dR/dT derivative, indicating metallic-like conduction, induced by such degradation processes.

CIS cycles performed under a magnetic field show conclusive evidence that atomic electromigration is assisted by intense heating in narrow nanoconstrictions within the oxide barrier during the CIS cycle. We confirm the existence of local temperatures inside the TJ higher than the blocking temperature (T_B) of the AFM layer. This allows current-reversing of the sign of the exchange bias between the AFM and FM-pinned layers, and thus the use of an electrical current to both induce the CIS effect and locally heat the AFM layer above T_B.

We demonstrate that in addition to the commonly observed two junction R-states, we can obtain a new intermediate R-state, conjugating the nanostructural and thermo-magnetic-driven switchings associated respectively with the CIS and magnetoresistive effects. One can then directly switch the TJ-resistance from the $[R_{AP}, R_B]$ to the $[R_P, R_b]$ state. When large enough current pulses are applied in the opposite direction, electromigration occurs in the reverse sense, increasing R to a new, distinct junction state $[R_P, R_B]$.

6.1 Experimental details

The structure of the IBD series used in this work is [62] Glass/Bottom lead/Ta (90 Å)/NiFe (50 Å)/MnIr (90 Å)/CoFe (80 Å)/AlO_x (3 Å+ 4 Å)/CoFe (30 Å)/NiFe (40 Å)/Ta (30 Å)/TiW(N) (150 Å)/Top lead. The AlO_x barrier was formed by two-step deposition and oxidation processes (50mTorr, 3min; and 100mTorr, 20min). Here NiFe, CoFe, MnIr and TiW(N) stand for $Ni_{80}Fe_{20}$, $Co_{80}Fe_{20}$, $Mn_{78}Ir_{22}$ and $Ti_{10}W_{90}(N)$. The bottom and top leads are made of Al 98.5% Si 1% Cu 0.5%, 600 Å thick and 3000 Å thick respectively, and are 26 μm and 10 μm wide. The junctions were patterned to a rectangular shape with dimensions from 1×2 μm^2 to 2×3 μm^2 by a self-aligned microfabrication process. The samples were annealed at 550 K under an external magnetic field (3 kOe) to impress an exchange bias direction between the AFM and FM pinned layers, taken here as the positive direction. Three samples of this series were extensively studied throughout this work. The temperature dependence of the CIS effect was studied using sample A (area $A = 1 \times 2$ μm^2). Time dependent experiments were performed in sample B (1×2 μm^2). Finally, sample C (1×4 μm^2) was used to study the influence of the magnetic field on the CIS effect.

The electrical resistance and current induced switching were measured with a four-point d.c. method, with a current stable to $1{:}10^6$ and using an automatic control and data acquisition system. Low temperature measurements were performed in a closed cycle cryostat down to 25 K.

CIS cycles were performed using the pulsed current method [76]. The CIS cycles were obtained at constant temperatures between 300 and 25 K. Current pulses ($I_{\rm p}$) of 1 s duration and 5 s repetition period are applied to the junction, starting with increasing negative pulses from $I_{\rm p} = 0$ (where we define the resistance $R_{\rm initial}$), in $-\Delta I_p$ steps up to an extreme $-I_{\rm max}$, dependent of cycle and temperature. One then positively increases the current pulses, following the reverse trend through zero current pulse ($R_{\rm half}$) up to positive $+I_{\rm max}$, and then again to $I_p = 0$ ($R_{\rm final}$), to close the CIS hysteretic cycle. The junction remnant resistance is always measured in the 5 s-waiting periods between consecutive current pulses, using a low current of $I_0 = 1$ mA, providing an $R(I_{\rm p})$ curve for each cycle (see section 2.2.2.2, page 58). This method allows us to discard the non-linear $I(V)$ contributions to the resistance, which would occur if a higher measuring current I_0 was used. Positive current is defined as flowing from the bottom to the top lead in our tunnel junctions.

Using the definitions above, one can define the CIS coefficient as:

$$CIS = \frac{R_{\rm initial} - R_{\rm half}}{(R_{\rm initial} + R_{\rm half})/2}. \tag{6.1}$$

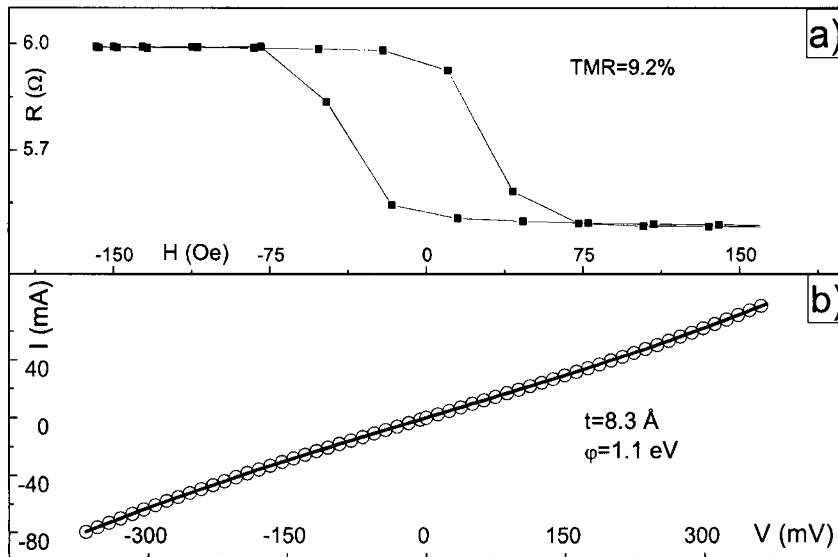

Figure 6.1: (a) Tunnel Magnetoresistance curve and (b) I(V) characteristic of the studied MnIr (90 Å)/CoFe (80 Å)/AlO_x (3 Å+ 4 Å)/CoFe (30 Å)/NiFe (40 Å) tunnel junction.

We also introduce the resistance shift (δ) in each cycle,

$$\delta = \frac{R_{\text{final}} - R_{\text{initial}}}{(R_{\text{initial}} + R_{\text{final}})/2}, \tag{6.2}$$

and the Tunnel Magnetoresistance ratio:

$$TMR = \frac{R_{\text{AP}} - R_{\text{P}}}{R_{\text{P}}}. \tag{6.3}$$

6.2 Experimental results

6.2.1 Current Induced Switching

The studied TJ (Sample A; 1×2 μm^2) had a resistance area product $R \times A \approx 11$ $\Omega\mu\text{m}^2$ and a tunnel magnetoresistance TMR $\sim$ 10% [Fig. 6.1(a)]. Measured I(V) characteristics were fitted using Simmons' model [181], giving a barrier thickness $t = 8.3$ Å and a barrier height $\varphi = 1.1$ eV [Fig. 6.1(b)].

Figure 6.2 displays several Current Induced Switching loops measured consecutively at room temperature (RT) with $I_{\text{max}} = 46$ mA and $\Delta I_p = 2$ mA steps, starting with decreasing current pulses on point S (R_{initial}). In such cycles the resistance remains fairly constant until approximately $I_p = -24$ mA (where we define the *negative* critical switching current, I_c^-). Higher (negative) current pulses lead to a sharp resistance decrease with I_p (resistance switching) until one reaches $-I_{\text{max}}$. The subsequent positive increase of I_{p} from $-I_{\text{max}} = -46$ mA up to $I_p \approx -30$ mA is accompanied by a quick rise of the electrical resistance (ΔR_p; see Fig. 6.2). This will be associated with the existence of small energy barriers (Δ_1) for

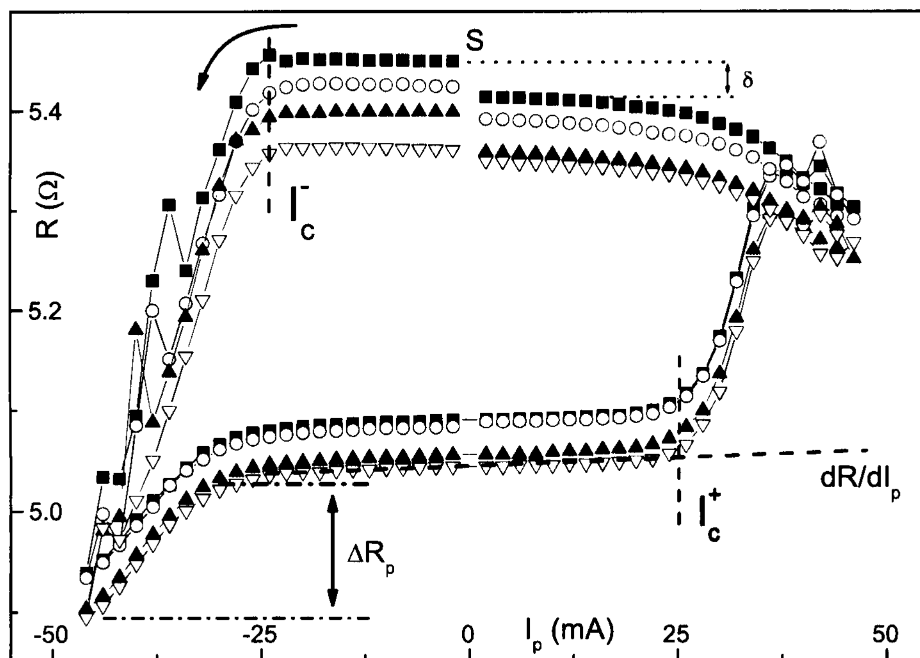

Figure 6.2: Current Induced Switching cycles performed at room temperature in sample A. Resistance switching near $\pm I_{\max}$ is attributed to electromigration of ions from the electrodes into the barrier and back. For $I_{\max} = 46$ mA, we obtained $CIS = 6.9\%$ in the first cycle. Notice the existence of some R-increasing steps during resistance switching to the lower state under negative currents, which can be due to interfacial rearrangements of migrated ions between consecutive current pulses or to the competition between electromigration at the two FM/I interfaces.

electromigration. Further reduction of the negative pulses considerably stabilizes R(I_p), leading to a plateau of (*low*) resistance, for I_p between −26 mA and +26 mA, representing a CIS coefficient of 6.9% with regard to the initial R-value (S point). However, in such current range one still notices the existence of a small positive dR/dI_p slope. As shown below, this will be associated with the existence of large energy barriers (Δ_2) for electromigration.

Around $I_p = +26$ mA (where we define the *positive* critical switching current, I_c^+) the junction resistance starts to rise sharply with the increase of I_p, representing a new resistance switching (barrier and resistance recovering) of the tunnel junction. The resistance reaches however a small maximum around +36 mA and then decreases slightly until $I_{\rm max} = 46$ mA. If we then progressively reduce the positive pulses, we again obtain a (now high resistance) plateau for $I_p \lesssim 26$ mA, which remains until the CIS cycle is closed at $I_p = 0$. The corresponding junction resistance ($R_{\rm final}$) is slightly smaller than at the beginning of the CIS cycle ($R_{\rm initial}$), giving a resistance shift $\delta = -0.7\%$. So the resistance recovery under positive current pulses (starting at I_c^+) almost totally compensates the initial switching under negative current pulses (starting at I_c^-).

These general features are seen in all the subsequent CIS loops measured at room temperature. However, due to the presence of a systematic negative δ-shift, the resistance of the tunnel junction irreversibly decreases from cycle to cycle. Furthermore, one notes that, for the same $I_{\rm max}$, the CIS coefficient slightly decreases with increasing number of cycles; *e. g.* in the first cycle one has a 6.9% resistance variation while in the fourth cycle we observe $CIS = 6.1\%$. The δ-shift amounts to $\approx -0.7\%$ in the three first cycles and is almost zero in the fourth.

6.2.2 Temperature dependent measurements

6.2.2.1 Electrical Resistance

We measured the temperature dependence of the electrical resistance of sample A from 300 K down to 25 K. The resistance of the tunnel junction was 5.5 Ω at room temperature, and increased by about 10% for $T = 25$ K (Fig. 6.3), indicating a tunnel-dominated behavior over the whole temperature range (see section 6.3.1).

6.2.2.2 CIS effect

We then systematically performed CIS cycles as a function of temperature in the 300 – 25 K range, with cycle measurements performed at about 20 K intervals. Figure 6.4 displays the CIS cycles obtained at a few representative temperatures. Between such CIS measuring temperatures, R(T) was continuously monitored and we found that it continued to monotonically rise with decreasing temperature ($dR/dT < 0$, tunnel-like behavior). However, increasing degradation effects were observed under CIS cycling, which changed the R(T) behavior as will be seen below.

Figure 6.4 displays selected Current Induced Switching cycles measured below room temperature. At $T = 280$ K we obtained (for the first cycle) $CIS \approx 6.8\%$ [Fig. 6.4(a)]. However, to achieve resistance switching at this temperature one had to use higher $I_{\rm max}$ values (50 mA in-

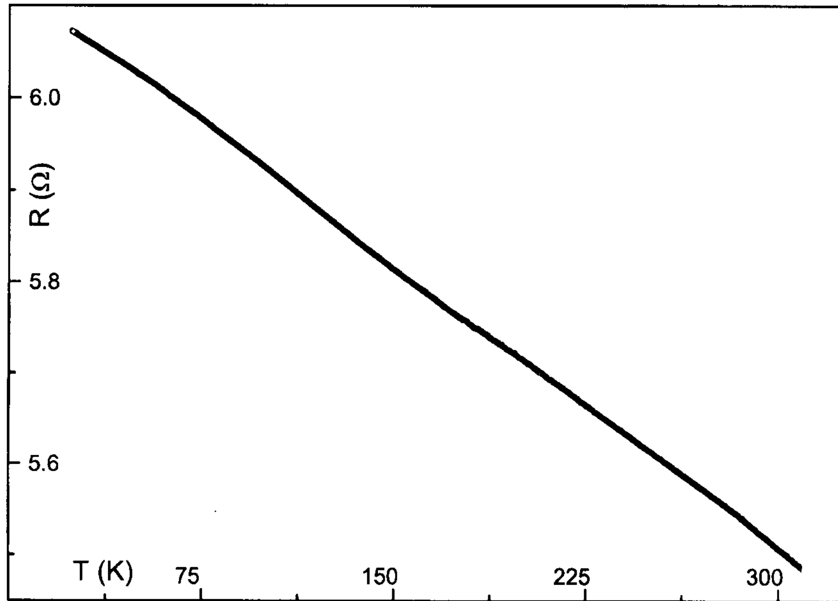

Figure 6.3: Temperature dependence of the electrical resistance of the studied CoFe/AlO_x (7 Å)/CoFe/NiFe TJ (sample A), showing $dR/dT < 0$. This indicates electron tunnelling as the dominant transport mechanism.

stead of 46 mA at room temperature). In fact, at 280 K, the initial plateau of high resistance extends down to $I_c^- \approx -30$ mA (-24 mA at room temperature). Higher negative current pulses lead (as at RT) to a range of resistance switching, from I_c^- down to $-I_{\max}$. Again one subsequently observes a slight R-increase when I_p goes from $-I_{\max}$ until ≈ -30 mA. The low-resistance-plateau is then visible when I_p goes from -30 mA to $+30$ mA. Subsequent higher current pulses lead to a sharp R-increase (resistance recovery) with increasing I_p, leading again to $R_{\text{final}} \lesssim R_{\text{initial}}$.

The same general features are observed at a lower temperature $T = 220$ K [$CIS \approx 6.5\%$; Fig. 6.4(b)] where, to achieve resistance switching, we must now reach $I_{\max} = 58$ mA. An interesting new feature develops now at high positive current pulses (near $+I_{\max}$), where a sharp resistance maximum occurs. For example, in the second CIS cycle the resistance switching at high positive pulses occurs rapidly through an over-resistive state (sharp maximum with $R > R_{\text{initial}}$) before declining to a stable final resistance, which then persists for current pulses down to zero.

Measurements performed at $T = 120$ K give considerably lower CIS signals ($\sim$3.5%), as shown in Fig. 6.4(c). To obtain switching we had to further increase the maximum pulse current applied, using $I_{\max} = 70$ mA in the first two cycles. In addition to the previously observed anomalous maximum preceding the final resistance switch near $+I_{\max}$, a similar effect was also seen under negative pulses near $-I_{\max}$, again giving an over-resistive state. In the third CIS cycle ($I_{\max} = 74$ mA), the resistance suddenly collapses when $I_p \gtrsim 70$ mA, and the resistance irreversibly decreases. This behavior contrasts with the previously recovery behavior near $+I_{\max}$ associated with an increase in R [see *e. g.* Fig. 6.4(a)]. The corresponding low R-value (at 120 K, after $I_p > 70$ mA) persists with the subsequent decrease of

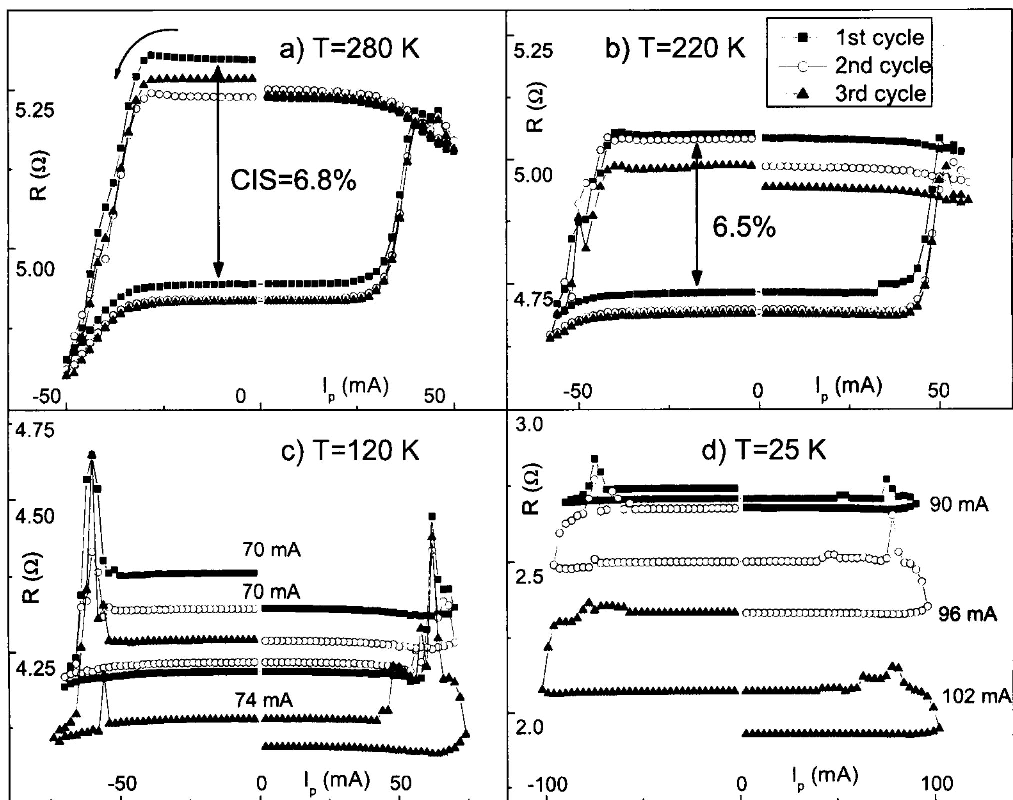

Figure 6.4: Selected CIS cycles performed at constant temperatures in the 280 – 25 K range (sample A).

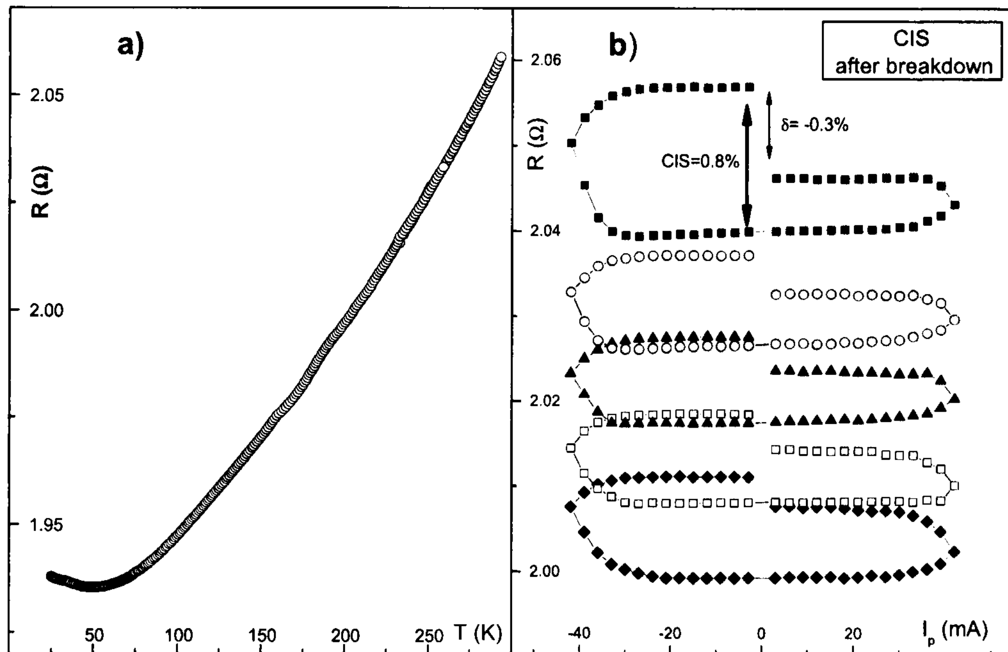

Figure 6.5: (a) Temperature dependence of the electrical resistance R(T) measured after performing CIS cycles between RT and $T = 25$ K, in the A-sample. (b) Selected (non-consecutive) CIS cycles obtained at room temperature after electrical transport across the TJ (sample A) is dominated by pinholes.

I_p to zero. These measurements indicate that sufficiently high I_p values cause irreversible barrier degradation.

We then performed measurements at $T = 25$ K, obtaining the CIS cycles shown in Fig. 6.4(d). To ensure resistance switching we adopted $I_{\text{max}} = 90$ mA in the first cycle. The anomalous resistance maxima near $\pm I_{\text{max}}$ are now much attenuated but the junction resistance systematically shows collapsing steps (irreversible junction degradation) both at positive ***and negative*** high current pulses.

After the CIS cycles at $T = 25$ K we measured the electrical resistance as a function of temperature and the results [Fig. 6.5(a)] show that now R increases with increasing temperature, indicating metal-like conductance in the tunnel junction. This shows that metallic-like paths were opened (through the formation or enlargement of pinholes) across the insulating barrier while performing CIS cycles under high I_{max} values and now dominate the tunnel junction conductance. Such barrier degradation is also visible in the negative δ-shift observed in consecutive CIS cycles. However, if CIS cycles are measured (at room temperature) in this degraded tunnel junction, one still observes both a resistance decrease (near $-I_{\text{max}}$) and a resistance increase (near $+I_{\text{max}}$) induced by an electrical current [Fig. 6.5(b)]. Such cycles with $I_{\text{max}} = 42$ mA now show a much smaller CIS coefficient, of approximately 0.8% and a resistance-shift $\delta = -0.3\%$.

From Fig. 6.4 one intuitively sees that the value of the CIS coefficient depends on the applied

current pulse (notice the continuous R-switching with I_p near $\pm I_{max}$). Therefore, since we had to increase I_{max} with decreasing temperature to induce R-switching, one is not able to correctly extract the CIS(T) behavior from our experimental data. Nevertheless, it is visible that the CIS effect decreases with decreasing temperature. This suggests that the physical mechanism underlying Current Induced Switching is thermally activated. A detailed study on the CIS(I_{max}; T) dependence will be given in Chapter 7.

6.2.3 Time dependent effects

Due to the severe degradation of the tunnel junction revealed in the preceding section, we investigated time dependent effects in another junction of the same series (sample B; $A = 1 \times 2\ \mu\text{m}^2$ and $R \times A \approx 11\ \Omega\mu\text{m}^2$). For this study the electrical resistance was continuously monitored at room temperature over long periods of time (over 15 hours), after performing both complete or half CIS cycles.

After a half CIS cycle [$I_p = 0 \rightarrow -I_{max} = 36$ mA $\rightarrow 0$; A-B in Fig. 6.6(a)], the tunnel junction is left in its low resistance state (point B). We then continuously monitored the resistance evolution in time (t) under the (same) small bias current of 1 mA [Fig. 6.6(a), sequence B-C-D]. The explicit R(t) dependence is displayed in Fig. 6.6(b), where we observe a non-monotonic R(t) behavior characterized by two distinct relaxation times. Initially R *decreases* slightly but very rapidly (B-C), indicating a small relaxation time, but then a slow and opposite relaxation process takes over, gradually *increasing* the electrical resistance (C-D).

Such competing relaxation processes can be described by the combined equation:

$$R(t) = R(\infty) + \Delta R_1 e^{-t/\tau_1} + \Delta R_2 e^{-t/\tau_2}, \tag{6.4}$$

where $R(\infty)$ is the asymptotic resistance, $\tau_{1(2)}$ represent the small (large) relaxation time and $\Delta R_{1(2)}$ represents the associated resistance changes (negative/positive).

Fitting the experimental data gives $\tau_1 \approx 11.7$ min and $\tau_2 \approx 174$ min, and resistance variations of $\Delta R_1 = -0.016\ \Omega$ and $\Delta R_2 = 0.15\ \Omega$. To analyze these effects in more detail we subtracted from the experimental R(t) curve [Fig. 6.6(b)] the long-relaxation time contribution ($\Delta R_2 e^{-t/\tau_2}$), obtaining the initial relaxation $\Delta R(t) = \Delta R_1 e^{-t/\tau_1}$, that clearly evidences the corresponding rapid decrease of R with t [Fig. 6.6(c)].

In the case of a complete CIS cycle [$I_p = 0 \rightarrow -36$ mA $\rightarrow +36$ mA $\rightarrow 0$; A – B in Fig. 6.7(a)] the tunnel junction returns to a high R-state under positive I_p, with a small excess over $R_{initial}$ ($\delta = +0.3\%$). The subsequent R(t) evolution indicates again a non-monotonic two relaxation-time process [Fig. 6.7(b)], but with the R-changes inverted with respect to those obtained after the previous half CIS cycle. In fact, initially the junction resistance *increases* rapidly with a relaxation constant $\tau_1 \approx 2.5$ min ($\Delta R_1 = 0.03\ \Omega$; B – C) and then a slow relaxation process takes over, *decreasing* the electrical resistance with a relaxation time $\tau_2 \approx 125$ min ($\Delta R_2 = -0.05\ \Omega$; C - D). Figure 6.7(c) shows the initial rapid increase of the electrical resistance after subtracting the slow relaxation contribution. Extrapolating the fitted equation into large t, one practically obtains the resistance value previously observed at the beginning of the CIS cycle, showing that reversibility is indeed achieved if one waits long enough to reach the equilibrium state.

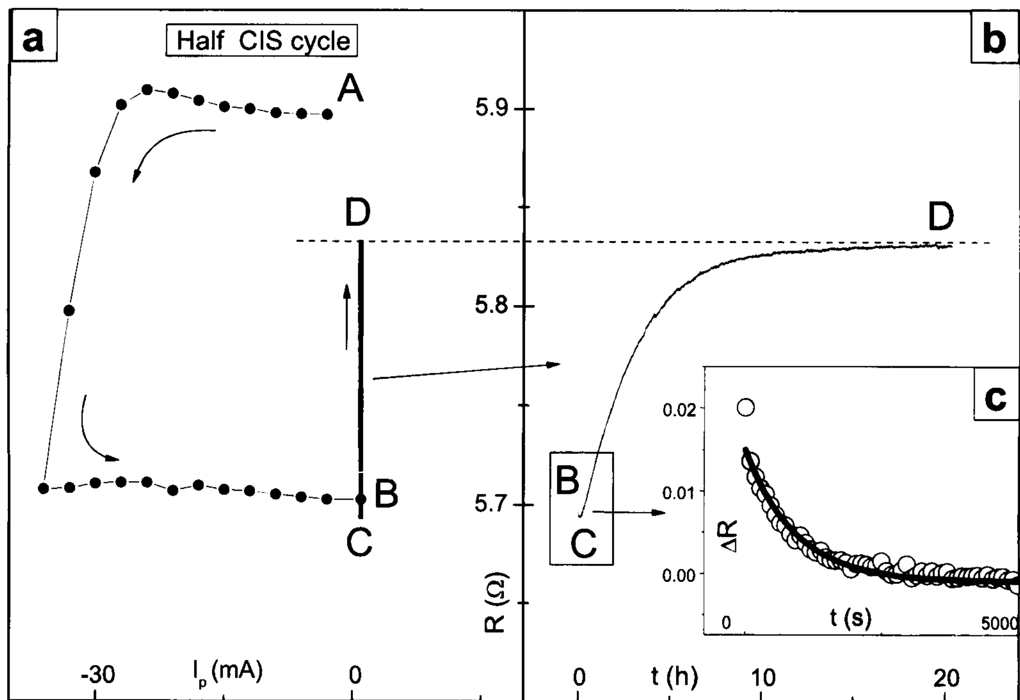

Figure 6.6: (a) Half CIS cycle (A–B) and subsequent relaxation processes (B–C–D). (b) Time evolution of the electrical resistance (B–C–D branch). (c) Slow relaxation processes after subtracting $R(\infty) + \Delta R_2 e^{-t/\tau_2}$. Fitting to Equation (6.4) gives $\tau_1 \approx 11.7$ min and $\tau_2 \approx 174$ min.

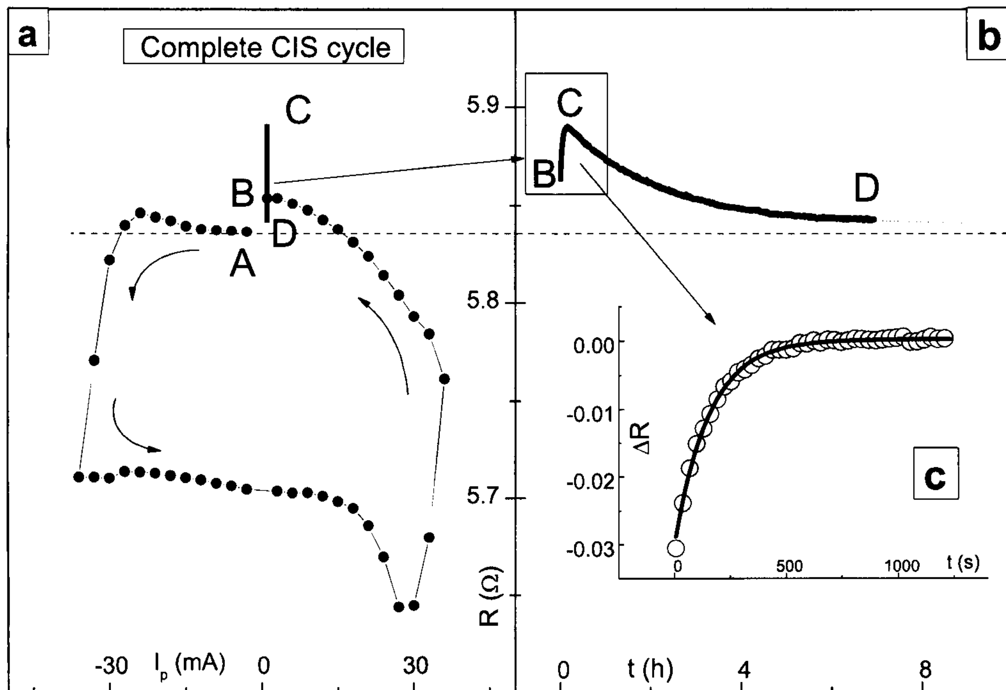

Figure 6.7: Complete CIS cycle and subsequent relaxation effects. Using Equation (6.4), one obtains $\tau_1 \approx 2.5$ min and $\tau_2 \approx 125$ min.

6.2.4 Magnetic field effects

To study the influence of a magnetic field on both the CIS effect and relaxation phenomena, we performed consecutive sets of three measurements [MR, CIS, R(t)] at room temperature, using a new sample (Sample C; $A = 1 \times 4$ μm^2; $R \times A \approx 32$ $\Omega\mu$m^2). First we measured a MR(H) cycle, starting and finishing with $H = -200$ Oe and spanning the ± 200 Oe field range; then we measure CIS cycles (R vs. I_p; $I_{\max} = 39$ mA) under a constant field of ± 200 Oe or zero; finally we studied the R(t) relaxation under $H = \pm 200$ Oe or zero. Figure 6.8 displays the initial sets of consecutive (and representative) MR(H) and CIS measurements performed at room temperature. The relaxation behavior was similar to the one described above and did not show any dependence on the magnetic field. For that reason, the corresponding curves will not be presented here.

(1) In the first MR(H) hysteretic cycle we obtained TMR = 14%, starting and finishing the measurement with $H_{\max} = -200$ Oe [Fig. 6.8(a-1)]. The initial state under $H = -200$ Oe (point A) corresponds to antiparallel pinned and free layer magnetizations (see arrows in Fig. 6.8), giving a ***high-R state*** (R_{AP}). When one increases the magnetic field (towards positive values), one observes the reversal of the magnetization of the free layer, leading to the parallel, low R-state in the positive H-direction (R_P; point B). The reverse sequence occurs when H is decreased from +200 Oe to -200 Oe, closing the MR(H) cycle in the antiparallel state (point A).

The following CIS cycle, R(I_p), was measured under a constant applied field $H = -200$ Oe

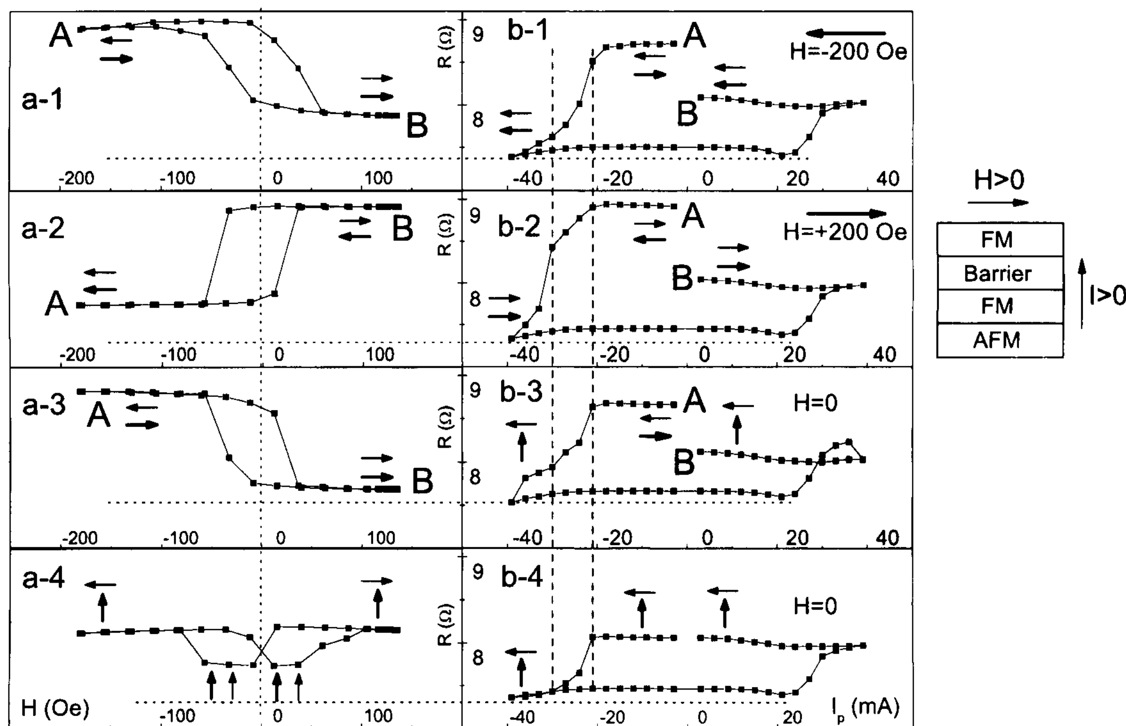

Figure 6.8: Consecutive MR(H) and CIS(I_p) cycles performed under an external magnetic field. The thicker (thinner) arrows refer to the magnetization of the pinned (free) layer.

[Fig. 6.8(b-1)], starting with the antiparallel magnetic state (point A: $R_{\text{initial}} = R_{\text{AP}}$; ***high-R state***). As expected, the resistance remains fairly constant while increasing negatively the current pulses, down to $I_{\text{p}} \approx -21$ mA, where resistance switching to a ***low R-state*** starts. The final R-value attained at $-I_{\text{max}} = -39$ mA is even smaller than the R_{P}-value achieved in the precedent MR(H) cycle shown in Fig. 6.8(a-1) ($CIS = 15\%$). Thus, the observed resistance switching in the CIS cycle cannot be due to a magnetoresistive effect only, but must also have a structural contribution due to electromigration. Also visible is a large resistance shift $\delta = -7\%$.

(2) The second set of MR(H) [Fig. 6.8(a-2)] and CIS(I_p) [Fig. 6.8(b-2)] measurements was then performed. The MR(H) cycle (starting at $H = -200$ Oe; point A) is now *inverted* relatively to that in Fig. 6.8(a-1). The TMR coefficient remains, however, practically unchanged, and when the MR(H) cycle is complete the junction is again left in the parallel magnetic state (point A). The following CIS cycle, R(I_{p}), was performed under a constant positive field $H = +200$ Oe [Fig. 6.8(b-2)]. We then start the R(I_{p}) measurements at point A (antiparallel state) in Fig. 6.8(b-2), and the corresponding curve qualitatively approaches the R(I_{p}) behavior observed in Fig. 6.8(b-1), giving a CIS coefficient of 18% and $\delta = -10\%$.

(3) The third MR(H) cycle [Fig. 6.8(a-3)] is now quite similar to the initial one [Fig. 6.8(a-1)], indicating that the CIS cycle performed under $H = +200$ Oe [Fig. 6.8(b-2)] reverted the sample to its original magnetic behavior. Therefore, at the end of the third MR(H) cycle the junction is left in the antiparallel state. Subsequent R(I_{p}) measurements *without a magnetic field* (starting at point A) led to $CIS = 12\%$ and $\delta = -7\%$ [Fig. 6.8(b-3)]. We notice however that the final magnetic state (point B) differs from the full antiparallel structure (see discussion in section 6.3.3).

(4) As a consequence, the following MR(H) measurement [Fig. 6.8(a-4)] shows a significantly different, double (and shallow) MR loop with a considerably lower MR coefficient (5%). In the subsequent CIS cycle [Fig. 6.8(b-4)], measured under *zero magnetic field*, one has $R_{\text{final}} \approx R_{\text{initial}}$ (negligible resistance shift $\delta = -0.04\%$) and $CIS = 8\%$.

Therefore, important changes can be induced when we perform CIS cycles under adequate constant magnetic fields.

6.3 Discussion

6.3.1 Tunneling versus pinhole conductance

The absence of pinholes in tunnel junctions is usually tested using the three Rowell criteria [262]: Exponential dependence of resistance with insulator thickness, non-linear I(V) characteristics and weak insulating-like temperature dependence of the resistance ($dR/dT < 0$). However, the two first criteria have been shown as non-reliable even in high resistance tunnel junctions ($\sim$k$\Omega\mu$m^2) [184, 185] and the third criterion is insensitive to the presence of few or small pinholes in low resistance tunnel junctions ($\sim 10\ \Omega\mu\text{m}^2$) [208]. Thus the increase of resistance with decreasing temperature observed in our thin junctions (sample A; Fig. 6.3) does not rule out completely the existence of pinholes in the barrier, but shows that tunnel is the dominant transport mechanism.

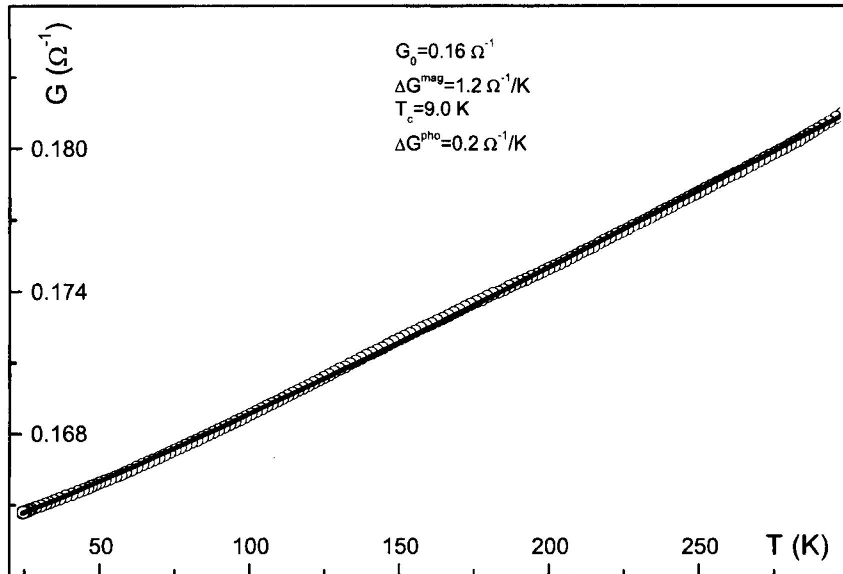

Figure 6.9: Temperature dependence of the conductance of sample A (hollow circles; 300 - 25 K) and corresponding fit using Eq. (6.5) (line).

The temperature dependence of the parallel conductance $G_P(T)$ of sample A is displayed in Fig. 6.9 (hollow circles). As discussed in section 5.5, one can write:

$$G_P(T) = G_P(0) + \Delta G_P^{mag} T ln\left(1 - e^{-T_P^c/T}\right) + \Delta G_P^{ph} T, \tag{6.5}$$

where $G_P(0)$ is the parallel conductance at 0 K, $T_P^c = \frac{E_P^c}{k_B}$ represents the magnon cut-off temperature, below which no magnons are excited, $\Delta G_P^{mag} = -\frac{8\pi e^2 k |T^J|^2}{\hbar E_m}\rho_\uparrow \rho_\downarrow$ and $\Delta G_P^{ph} = \frac{8\pi e^2}{\hbar}\left(\rho_\uparrow^2 + \rho_\downarrow^2\right)\left(\frac{k_B}{\hbar\omega_D}\right)\gamma$. All other parameters are defined in section 5.5.

The fit to the experimental results (line in Fig. 6.9) shows a strong contribution from magnon-assisted tunneling, with a low cut-off temperature of 9 K, which is usually attributed to an overoxidation of the initial Al film when the barrier is under formation [174]. On the contrary, if one considers the temperature dependence of the spin polarization and of the hopping conductance (sections 5.5.1 and 5.5.2), a good fit cannot be achieved.

6.3.2 CIS behavior under zero magnetic field

Room temperature results. Previous data shown in Fig. 6.2 [page 139; see also Fig. 6.10(a)] displayed consecutive CIS cycles measured at $T = 300$ K and using $I_{\max} = 46$ mA. Initially one sees that the TJ resistance remains fairly constant (*high R-state*) when increasingly negative current pulses (starting from $I_\text{p} = 0$) are applied, down to $I_p \approx -24$ mA. At this stage, further negative increase in pulse intensity, to $-I_{\max} = -46$ mA, produces a sharp resistance decrease ($CIS = 6.9\%$), i.e. switching to a lower R-state. This indicates a sudden weakening of the oxide barrier, here associated with the migration of ions from the bottom metallic electrode (Co, Fe) into the insulator. Such migration should occur preferentially

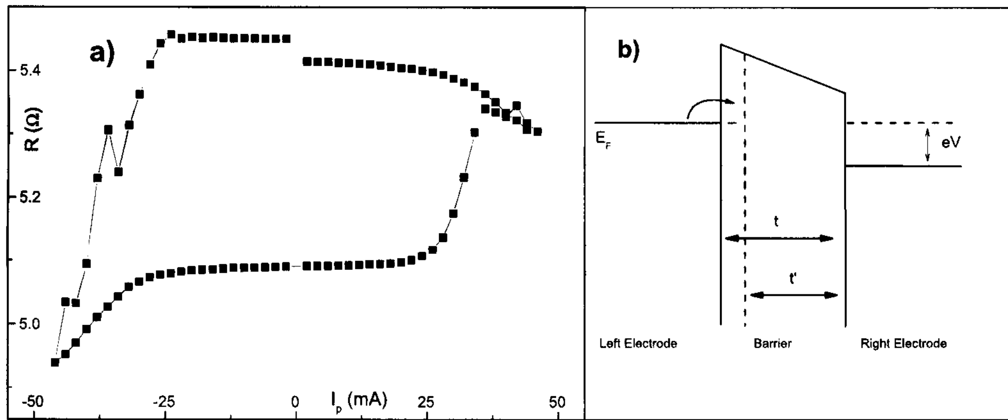

Figure 6.10: (a) Current Induced Switching cycle performed at room temperature in sample A. (b) Electromigration-driven barrier thickness decrease (t→t'), due to the use of a sufficiently high electrical current density across a thin TJ.

in hot-spots [263] (nanoconstrictions where the barrier is thinner) and/or pinholes, and be assisted both by intense electrical fields and local thermal effects. One notices that even a small barrier weakening due to such migration [Fig. 6.10(b)] could considerably lower the tunnel resistance due to its exponential dependence on barrier thickness [181]. For example, for a resistance decrease of 6.9% the effective barrier thickness t needs only to decrease approximately 0.1 Å. The estimated electrical field at the beginning of resistance switching is $E \sim 1.5$ MV/cm, considerably smaller than the electrical field causing dielectric breakdown in thin tunnel junctions ($\sim 5 - 10$ MV/cm) [213]. On the other hand, local temperatures inside the TJ can rise above 520 K (thus considerably increasing atomic mobility), as experimentally confirmed below. In fact, in mesoscopic systems, local heating can be an almost instantaneous process and high temperatures (combined with $E \sim 1.5$ MV/cm) are able to remove an atom out of its lattice potential well in a very short time [264].

Returning to Fig. 6.10(a), one sees that the increase of the $I_{\rm p}$ from $-I_{\max} = -46$ mA to $I_p \approx -30$ mA is accompanied by a significant rise in resistance (ΔR_p). This indicates that the reduction of the migration driving force (electrical field) allows some atoms to easily return to their initial sites in the metallic electrodes, due to the existence of low energy barriers ($\Delta_1 \sim 0.13$ eV, according to the fittings). However, most of the displaced ions remain in their local minima inside the oxide barrier since we still have a *low R-state.* This indicates that the displacement of such ions involves considerably higher energy barriers ($\Delta_2 \sim 0.85$ eV; see below).

Therefore, only when $I_{\rm p}$ reaches a sufficiently high positive value ($I_p \approx +24$ mA) does electromigration start in the reverse sense (previously displaced metal ions now move from the oxide back into the electrode), increasing the effective oxide barrier and the junction electrical resistance. This indicates that at $I_{\rm p} \approx +24$ mA the electrical field (now in the opposite sense) is sufficient to induce the movement of the previously displaced metallic ions under negative $I_{\rm p}$, now from the barrier back into the bottom electrode. We thus have a resistance recovery. Further increase in I_p produces a small resistance maximum around +36 mA. The subsequent resistance decrease (as $I_{\rm p}$ goes up to $+I_{\max}$) could be caused by small displacements of

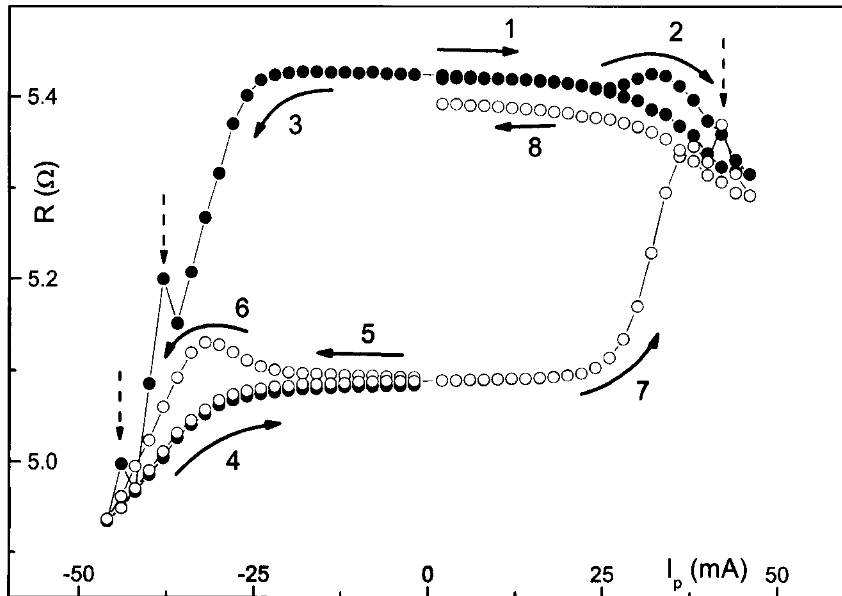

Figure 6.11: Asymmetric CIS R-switching. If a CIS cycle is started with increasingly positive current pulses, no R-switching occurs (full circles). When the tunnel junction is in the low R-branch, only positive current pulses lead to R-recovery (hollow circles).

atoms from the top electrode into the barrier under the high positive electrical fields. If one reduces the positive pulses from $+I_{\text{max}} = 46$ mA to zero, the plateau of high constant resistance again emerges (R_{final}) below $I_{\text{p}} \approx +24$ mA. The small difference between R_{final} and R_{initial} indicates a weak irreversibility, *i. e.*, incomplete nanostructural recovery. The same irreversible changes are also visible when comparing consecutive CIS cycles, where both R_{final} and R_{half} tend to decrease with cycling. Ultimately, consecutive cycling leads to metallic-dominated transport as seen in Fig. 6.5.

Notice that if a CIS cycle is started with increasing positive current pulses, no R-switching is observed (Fig. 6.11; sample A). This indicates asymmetric electromigration between the FM/I (I≡insulating barrier) and I/FM interfaces, likely reflecting the structural differences between such electrode/oxide interfaces. While the top electrode is deposited onto a flat AlO_x surface, the bottom one is deposited onto a rougher MnIr layer and its upper surface is covered with pure Al, subsequently oxidized. In fact, it was experimentally observed by High Resolution Transmission Electron Microscopy that a more irregular interface exists at the FM/I interface [265]. Because the migration of atoms into and out of the barrier should occur preferentially in nanoconstrictions, where higher electrical fields and higher local current densities occur (vacancies and defects more likely to be formed), one expects the bottom electrode/insulating barrier to be more susceptible to atomic migration.

As we have seen in section 5.8, when an electrical field $\mathbf{E}$ is applied to a metal, electromigration can occur as the result of a driving force $\mathbf{F} = eZ^*\mathbf{E}$ (Z^* the effective valence of the ion and e the elementary charge) [244]. The force $\mathbf{F}$ is usually divided into a direct force $\mathbf{F}_d = eZ_d\mathbf{E}$ ($Z_d \approx Z$; arising from electrostatic interactions) and a wind force $\mathbf{F}_w = eZ_w\mathbf{E}$ (arising from momentum exchange; see section 5.8 for a detailed description). Using the ballistic model,

one can write the wind valence as $Z_w = -nl\sigma_{tr}$, where n is the the electron density, l the electron mean free path and σ_{tr} the electron transport cross section for scattering by the ion. Using known values for Fe ($n \sim 10^{-1}$ Å^{-3}, $l \sim 50$ Å, $\sigma_{tr} \sim 3$ Å^2; Refs. [260, 266]), one finds $Z_w \approx -15$. One then has $|Z_w(Fe)| \gg Z_d(Fe) \approx 2$, which shows that, for Fe, the wind force dominates the electromigration (EM) process. The resulting force **F** then has the opposite direction of the electrical field **E** (and current). The observed resistance decrease for negative currents (top to bottom direction; Fig. 6.11) indicates that ions from the bottom electrode migrate into the barrier under the high negative electrical currents applied, and in the opposite direction when the current is reversed.

However, notice that the I/FM interface is also slightly active in electromigration processes. In Fig. 6.11, one sees a small resistance increase (point 2) for $I_{\rm p} \approx +26$ mA, which is here associated with a small electromigration of metallic ions from the *bottom* electrode *away* from the barrier (notice that $I_{\rm c}^{+} \approx +24$ mA). However, for current pulses higher than 34 mA, a small R-decrease is observed, likely due to electromigration of ions from the *top* electrode into the barrier, thus decreasing the effective barrier thickness. When decreasing the applied current pulses from $+I_{\rm max}$, resistance switching is observed for $I_{\rm p} = -24$ mA (point 3). If a $-I_{\rm max} \rightarrow 0 \rightarrow -I_{\rm max}$ sequence is then performed (4–5–6 branch in Fig. 6.11), a small R-maximum is visible for $I_{\rm p} = -32$ mA. This again is likely associated with electromigration of ions from the *top* electrode away from the barrier, increasing R. The subsequent R-decrease results from EM of ions from the opposite (*bottom*) electrode. The observed sharp resistance variations (dashed arrows in Fig. 6.11) then could result from a competition between electromigration in opposite interfaces.

CIS cycles in the metallic R(T) regime. Let us consider the CIS cycles obtained after the tunnel junction (sample A) acquires a metallic-like R(T) behavior (Fig. 6.5). The fact that a measurable CIS coefficient is observed even when pinholes dominate transport through the insulating barrier (and a negligible TMR signal is observed) confirms the different origin of the two phenomena. The measured small CIS coefficient of $\approx 0.8\%$ (compared to $CIS = 6.8\%$ when transport was dominated by tunneling) probably arises from two different factors. First, because we now have large metallic paths, the enlargement of such pinholes through the migration of ions causes a much smaller R-variation than when tunnel dominates (and R depends exponentially on the barrier thickness). Second, one expects smaller local current densities to flow through such large pinholes. This of course leads to smaller electromigration forces acting on metallic ions and thus to a reduced CIS coefficient. Notice that, in this case, we have $I_{\rm c}^{+} \approx 36$ mA, while when tunnel dominated transport we had $I_{\rm c}^{+} \approx 24$ mA.

Relaxation effects after complete and half CIS cycles. We performed one half and one full CIS cycle to study time dependent effects (sample B). After the half CIS cycle [Fig. 6.6(a)], the resistance first starts decreasing rapidly in time, but then a slow R-increase occurs. This indicates that atoms, through thermal fluctuations [the bias measuring current, of 1 mA, is too small ($\ll I_{\rm c}^{+}$) to induce relevant electrical field effects] are returning to a more stable configuration. The higher resistance reached after full relaxation [point D; and asymptotic value in Fig. 6.6(b)] indicates an increase in the effective barrier, which is thus associated with migration of atoms from the barrier back into the electrodes. However, full R-recovery is not completely achieved, remaining some irreversible ΔR change [A-D in Fig. 6.6(a)]. The two relaxation times observed in R(t) suggest two independent mechanisms

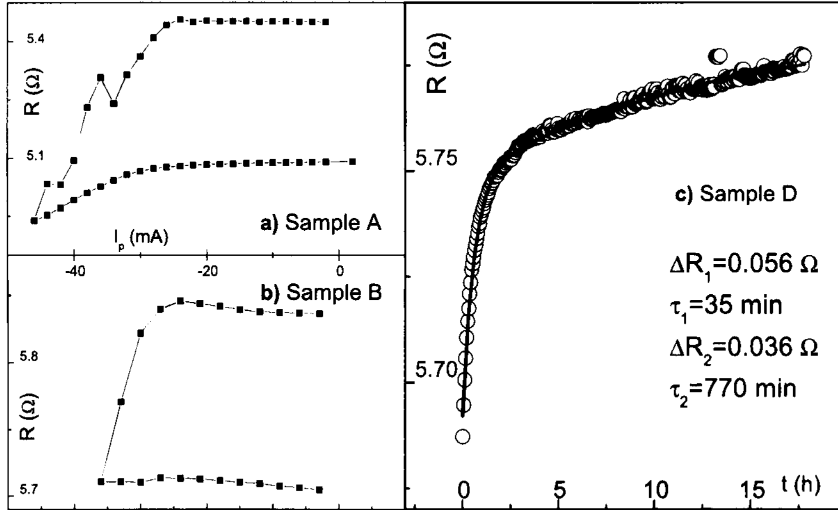

Figure 6.12: Current Induced Switching half cycle of (a) sample A and (b) sample B. (c) Time dependent measurements of the electrical resistance of a tunnel junction (sample D) after negative current pulses have been applied. The fit to Eq. (6.4) reveals the existence of two relaxation times, $\tau_1 = 35$ min and $\tau_2 = 770$ min, both associated with *increasing* R.

acting in the TJ. These could be due to ionic migration near the top and bottom electrodes (occurring at different stages), inducing opposite R-changes under high positive or negative electrical fields.

After a complete CIS cycle [Fig. 6.7(a)] we also observed two relaxation times associated with opposite resistance changes. In this case ions appear to migrate in the reverse sense (when compared to the half CIS case). The final resistances after relaxation (asymptotic values in Figs. 6.6 and 6.7) are practically the same in both cases, indicating that the relaxed TJ nanostructure is the same for both complete and half CIS cycles.

Let us now compare the R($I_{\rm p}$) behavior after switching near $-I_{\max}$ of different samples of the same series [Figs. 6.2 for sample A and 6.7 for sample B; see also Fig. 6.12 (a) and (b)]. Clearly sample A [Fig. 6.12(a)] has a much more pronounced relaxation behavior than sample B [Fig. 6.12(b)]. Since the Current Induced Switching effect depends on local structural details at the electrodes/barrier interfaces, one expects the corresponding physical properties to strongly depend on the measured sample. In particular, the energy barrier which the migrated ions need to surmount to return to their initial positions could be different from sample to sample. Thus, in sample A ions return much quicker to their original sites, indicating a smaller energy barrier than in sample B. Such differences can be further observed in Fig. 6.12(c), displaying the R(t) behavior of a new sample of the same series (sample D) after a large negative current pulse has been applied. The tunnel junction is then in the low R-state (reduced barrier thickness; R_b) and subsequent R(t) data shows metallic ions migrating from the insulating barrier back into the electrode, increasing R. Although two distinct relaxation times are observed, both are associated with R-*increases* ($\tau_1 \approx 35$ min and $\tau_2 \approx 770$ min), which contrasts with the behavior of sample B. No ionic relaxation which decreases R is observed in sample D. In this case, we only observe migrated ions in

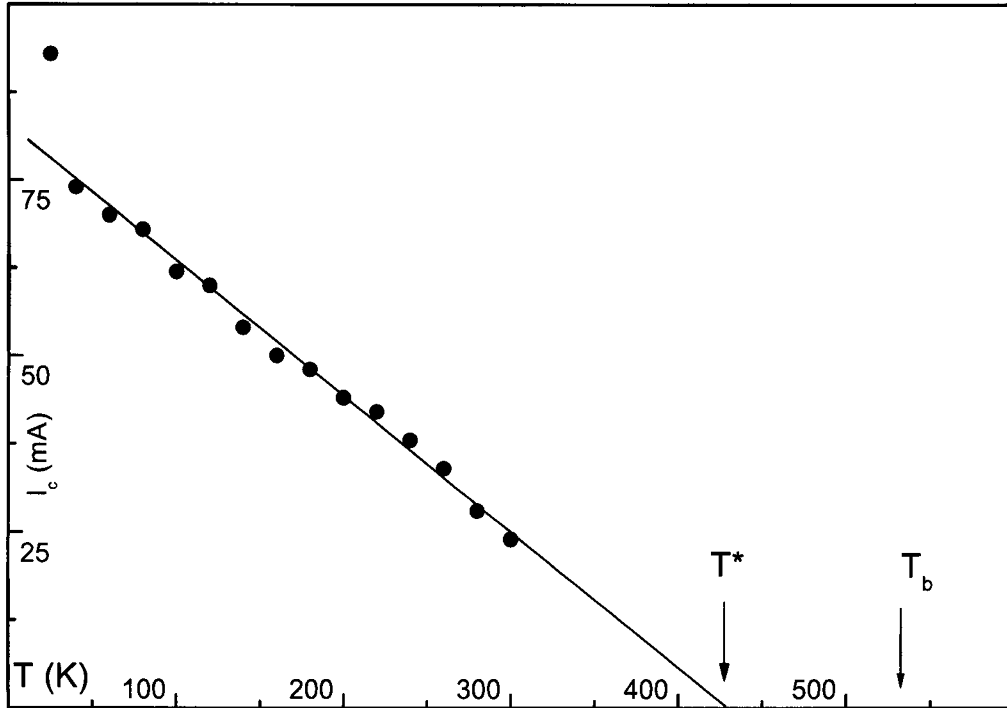

Figure 6.13: Quasi-linear temperature dependence of the critical switching current.

the interface bottom elecrode/insulator returning into the pinned layer and surmounting two different energy barriers. Notice that the initial *R-increase* relaxation process is much faster in this case (sample D) than in the case of sample B (compare the now observed $\tau_1 \approx 35$ min with the corresponding $\tau_2 \approx 125$ min of sample B).

Effects of temperature (300–25 K). The observed decrease of the CIS effect with decreasing temperature suggests a thermally activated mechanism. Also, the anomalous sharp resistance peak which occurs at high positive pulse currents (just below $+I_{\text{max}}$), in the $T = 220$ K and $T = 120$ K curves indicates pre-switching effects. At $T = 120$ K a similar maximum at high negative pulses also appears, probably with the same origin. These effects tend to fade away with further temperature decrease (or cycling). Finally a different effect takes place around $\pm I_{\text{max}}$ at low temperatures ($T = 25$ K), where the resistance sudden and irreversibly decreases, indicating progressive barrier breakdown.

Another interesting point concerns the temperature dependence of the critical current I_c needed to induce resistance switching (notice that $I_c^+ \approx |I_c^-|$ throughout the studied temperature range). Our data indicates that I_c decreases quasi-linearly with increasing temperature, extrapolating to zero at $T^* \approx 425$ K (Fig. 6.13). Such behavior can be understood if one considers the expression for the effective barrier modified by electromigration [251] $\Delta_0 - \xi I$, where Δ_0 is the zero-bias electromigration-energy barrier, ξ is a parameter that measures the change of such activation energy as a result of the electromigration force [267] and I is the applied current. Electromigration then occurs when the effective barrier becomes comparable to the thermal energy. The temperature dependence of the critical current (I_c) is then given

by [268]:

$$I_c \approx \frac{\Delta_0}{\xi} - \frac{k_B T}{\xi}, \tag{6.6}$$

where k_B is the Boltzmann constant. Although our data could be well fitted using this simple model, one should notice that the effective temperature inside the tunnel junctions is larger than that at which the measurement takes place (see below), which limits the quantitative understanding of our results. Nevertheless, we refer here the obtained results: $\Delta_0 \approx 0.036$ eV and $\xi \approx 0.4$ eV/A.

On the other hand, the localized resistance increase (ΔR_p) observed just after switching at high negative current pulses (Fig. 6.2) shows an exponential temperature dependence $e^{-\Delta_1/K_B T}$ with $\Delta_1 \approx 0.13$ eV (Fig. 6.14). This is attributed to local low barrier channels for atomic migration of displaced metal ions, from the barrier into the electrode. Because in the current pulse range where ΔR_p is obtained electromigration is certainly active ($|I_\mathrm{p}| \geq |I_\mathrm{c}^-|$; see Fig. 6.2), the estimated Δ_1-value should be taken only as a limiting maximum value for the low-energy barrier. Additionally, the slope of the CIS cycles near $I_\mathrm{p} = 0$ (in the low R-branch; dR/dI_p in Fig. 6.2), gives an indication on the remaining high energy barriers, with $\Delta_2 \approx 0.85$ eV. This value is fairly close to the diffusion activation energy of atoms through grain boundaries in CoFe/Cu multilayers (0.90 eV) [269]. One concludes that ionic electromigration can occur through two microscopic processes with different energy barriers. These channels may be associated with electromigration of ions with different binding energies (and migration energies [270]), or trapped at different potential sites in the AlO_xlattice [271, 272].

6.3.3 CIS(H) cycles and current written multi R-states

Let us now return to CIS cycles performed under an applied magnetic field, using sample C, which exhibits a standard magnetoresistance MR(H) cycle with TMR = 14% [Fig. 6.8(a-1); measured under $I = 1$ mA $\ll I_c$]. In the CIS cycle shown in Fig. 6.8(a-2), starting with the high resistance state under a permanent applied field of -200 Oe ($R_\mathrm{initial} = R_\mathrm{AP}$, point A), the application of increasing negative current pulses leaves the resistance virtually unchanged until $I_p = -21$ mA, where a considerable R-decrease starts. As before, this suggests a gradual weakening of the oxide barrier, associated with the migration of atoms from the metallic electrodes into the barrier. One also notices that R becomes smaller than the lowest resistance achieved in the previous MR(H) cycle [Fig. 6.8(a-1)] and thus ΔR at switching cannot be only due to a magnetic effect.

The following MR(H) cycle appears *inverted* [Fig. 6.8(a-2)] with respect to that presented in Fig. 6.8(a-1). Therefore, while measuring the CIS(I_p) cycle under $H = -200$ Oe [Fig. 6.8(b-1); **H** opposite to the initial exchange bias], the magnetization of the pinned layer was reversed and the junction switched from the antiparallel to the parallel *magnetic* state (see Fig. 6.15). This magnetic switch was certainly caused by a significant heating effect under high current pulses, so that local temperatures inside the TJ increase above the blocking temperature of the 90 Å thick MnIr AFM layer ($T_B \approx 520$ K [273]; see section 6.4). The corresponding magnetization then easily aligns with the applied (negative) magnetic field. Subsequent cooling below T_B [when $|I_p|$ is reduced in the CIS(I_p) cycle] leaves the TJ in such inverted exchange bias direction, *i. e.*, in the parallel (low resistance) state. This effect has

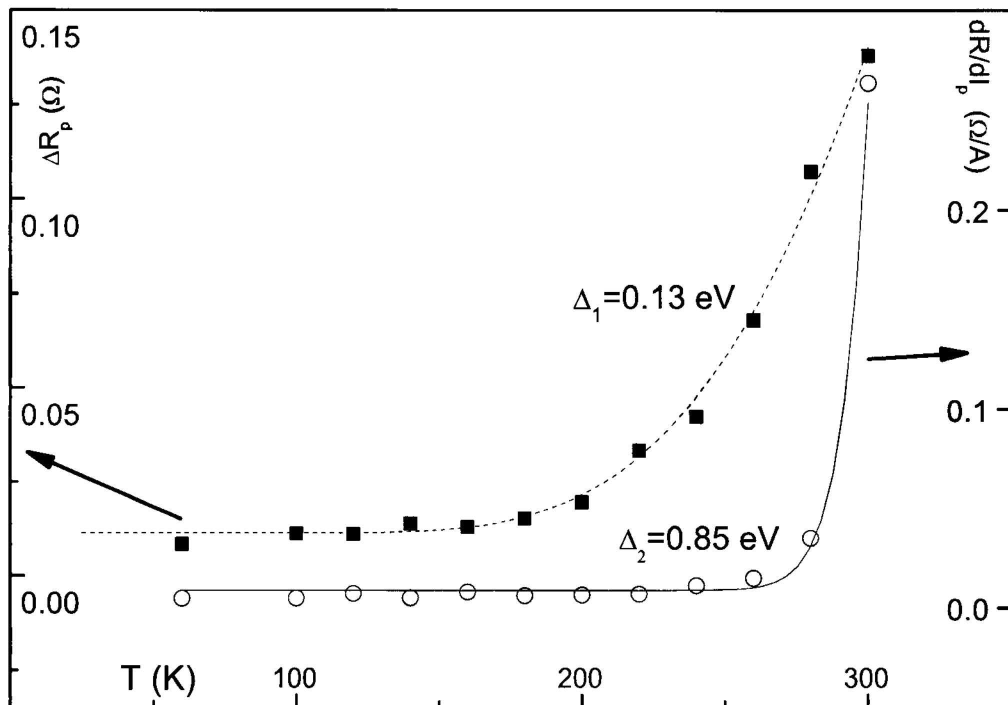

Figure 6.14: Temperature dependence of the resistance increase observed after switching (ΔR_p; left scale) and of the dR/dI_p slope near zero current pulse in the low-R branch (scale on the right); both processes are attributed to relaxation phenomena.

already been considered for pinned-layer writing under current pulses [274]. On the other hand, such temperature rise also enhances electromigration effects, due to the increase in the thermal motion of atoms [275].

Therefore, the additive resistance effects of magnetic switching and electromigration explain the large ΔR change near $-I_{\text{max}}$ in the CIS(I_{p}) cycle performed under $H = -200$ Oe. Comparing the MR(H) and CIS(I_p) data, we estimate a resistance decrease of ~12% due to magnetic switching and ~7% due to electromigration.[1]

Proceeding with the CIS(I_p; $H = -200$ Oe) cycle [Fig. 6.8(b-1)], the subsequent decrease of I_{p} towards positive values does not change R. However, when the current pulse reaches $I_p \approx$ 21 mA, ***thermally assisted*** electromigration occurs again, this time increasing the effective oxide barrier (and the electrical resistance) since the electrical field is now reversed (see Fig. 6.15 for a schematic representation of a CIS cycle under an applied negative magnetic field). If pinned-layer magnetic switching had not taken place under strong negative I_{p}, one would had simply a recovered barrier and a low δ-shift. However, since the junction persists in the parallel state (due to the magnetic switching near $-I_{\text{max}}$), a large difference between R_{initial} and R_{final} ($\delta = -7\%$) is observed and enables us to obtain an ***intermediate R-state.*** This large difference between R_{initial} and R_{final} is mainly due to the previous magnetic switching under sufficiently negative I_{p} (antiparallel to parallel state). The CIS(I_{p}) cycles measured under $H = +200$ Oe [Fig. 6.8(b-2); **H** now opposite to the ***previously impressed*** exchange bias direction] and $H = 0$ [Fig. 6.8(b-3)] show essentially the same features.

Three well separated (~ 7%) resistance states are therefore demonstrated in the same TJ, when one adequately plays with the thermo-magnetic and electromigration effects. Starting in the ***antiparallel, thick barrier*** state [R_{AP}, R_B], one can directly obtain a ***parallel, thin barrier*** state [R_P, R_b] using simultaneously a large electrical current and an external magnetic field opposite to the exchange bias direction. When a current pulse of opposite direction is applied, the ***parallel, thick barrier*** state is obtained [R_P, R_B].

The lower CIS coefficients observed when cycles are performed under zero field (12% and 8%), in relation to the cycles under ±200 Oe (18% and 15%), cannot be attributed to differences in electromigration (the magnetic field does not drive ion migration), but to magnetic effects. In fact, notice that when the temperature rises above T_B, the pinned layer magnetization (under $H = 0$) develops a complex multi-domain structure. Accordingly, the following MR measurement under $H = -200$ Oe [Fig. 6.8(a-4), see arrows; ↑ denotes a domain-like state] shows a double MR loop with a considerably lower TMR (5%) due to the lack of full parallelism between the free and pinned layer magnetizations.

Finally, in the subsequent CIS cycle [Fig. 6.8(b-4)], measured under ***zero magnetic field***, one has $R_{\text{final}} \approx R_{\text{initial}}$ (resistance shift $\delta = -0.04\%$) and $CIS = 8\%$. The observed R-switching is now only due to the migration of ions into/out of the barrier (thermally driven magnetization reversal of the pinned layer does not occur) and the negligible resistance shift

[1]One notices that temperatures even higher than 520 K have been observed by thermographic analysis during electromigration in Al interconnects, for current densities $\gtrsim 27$ MA/cm^2 [276]. In our measurements, if the current would flow uniformly across the barrier, a much smaller current density (~1 MA/cm^2, for $I_{\text{max}} \sim 40$ mA) would result. However, atomic force microscopy studies on slightly different tunnel junctions showed the existence of hot-spots in the barrier that concentrate most of the current flowing through the TJ, leading to much higher local current densities. Further arguments suggesting the existence of hot-spots will be given in section 6.4.1, using numerical simulation of heating in tunnel junctions.

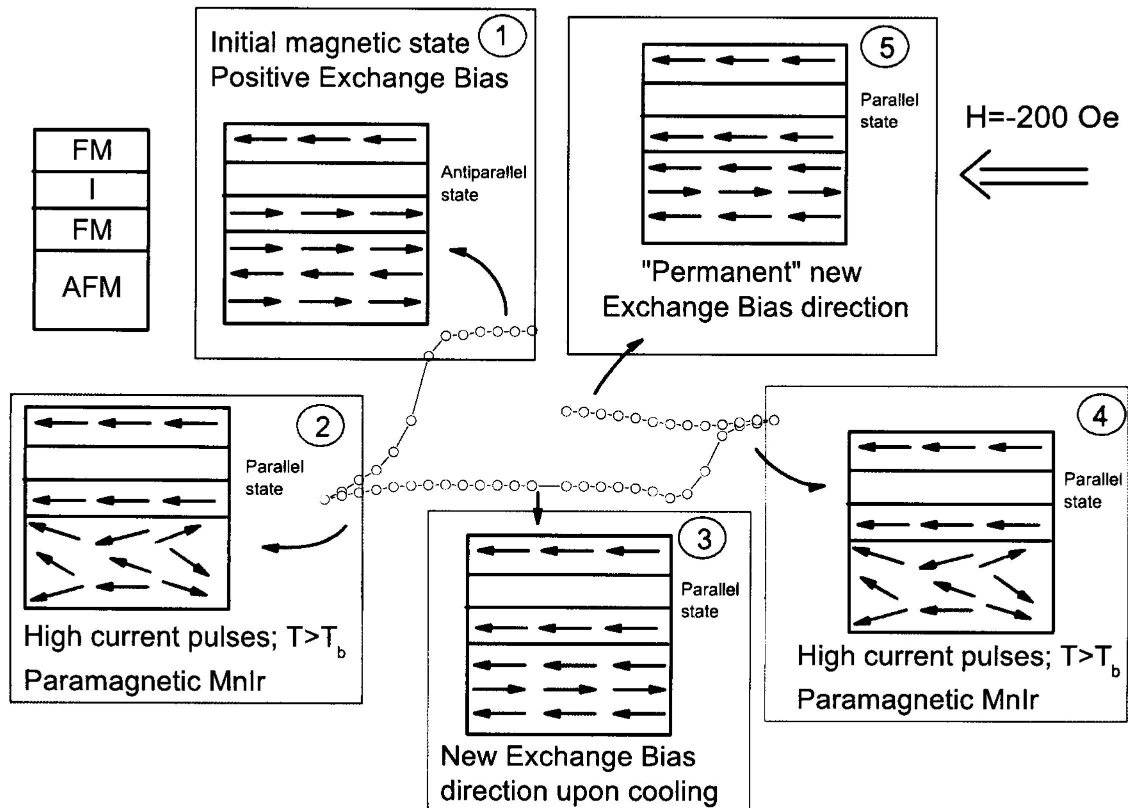

Figure 6.15: Exchange bias reversal when CIS cycles are performed under an external magnetic field. (1) The TJ is in its antiparallel state due to the applied negative magnetic field. (2) High current densities lead to intense heating above the blocking temperature of the AFM layer. The pinned layer magnetization then reverses and the TJ is in its parallel state. Electromigration of ions from the bottom electrode into the barrier further reduces the electrical resistance of the TJ below R_P. (3) Under lower current densities the TJ is cooled below T_B and a new exchange bias direction is impressed in the AFM layer. (4) High temperatures above T_B again occur, but leading to no magnetic-state changes, since the TJ is already aligned with the applied magnetic field. Electromigration of ions from the barrier into the bottom electrode increases R. (5) When I_p is again reduced, the exchange bias direction is "permanently" impressed, opposite to the initial one.

is attributed to small barrier degradation. Notice that in both CIS cycles under $H = 0$ and $H \neq 0$, R-switching always occurs at $I_{\rm p} \approx -21$ mA, indicating that the structural effect precedes the magnetic one (see corresponding vertical lines in Fig. 6.8, column b).

Development of irreversibility under current cycling. The presence of irreversible changes under cycling in the barrier can be followed by monitoring $R_{\rm P}$ and $R_{\rm AP}$ along the successive MR(H) curves (not shown). Both values show an overall 3% decrease (between the first and 7-th cycles; the latter not shown). The increase of the magnitude of the magnetic interlayer coupling [also deduced from the MR(H) curves] with the number of cycles (see column a in Fig. 6.8) is another sign of irreversible changes in the oxide barrier. Comparing only similar-shape MR(H) curves, one sees that the coupling field rises from 2.3 Oe [Fig. 6.8(a-1)] to 9.0 Oe [Fig. 6.8(a-3)] and continues to rise in subsequent measurements (not shown). This increase in the magnitude of the coupling field is related to a degradation of the barrier properties (more or larger hot-spots/pinholes), producing a larger exchange contribution to the coupling between the free and pinned layers.

6.3.3.1 Four state resistance

Four-resistance states can be further envisaged as illustrated in Fig. 6.16. For each MR state (R_P or R_{AP}) two R-states due to electromigration are possible: The low resistance state characterized by a thin barrier (R_b) and the high resistance state characterized by a thick barrier (R_B). The alternative process can also be envisaged: For each structural state in the CIS effect (large or small barrier), two distinct MR states can still be produced using an external magnetic field and thermally induced switching. The magnetic antiparallel, and "thick"-barrier state is obtained with a small negative magnetic field and a large, positive electrical current pulse [R_{AP}, R_B]. The antiparallel and "thin"-barrier state [R_{AP}, R_b] can be obtained with a small negative magnetic field (to reverse the free layer magnetization) and a high enough negative electrical current (to return ions to the electrodes). The [R_P, R_B] state can be obtained with a small positive magnetic field and a sufficient positive electrical current. Finally the [R_P, R_b] state can be obtained with a positive magnetic field and a high enough negative electrical current.

6.4 Heating in tunnel junctions

The standard way to switch between R-states in MRAMs is to use magnetic fields generated by current lines. However, the undesirable switching of half-selected bits is a concern for MRAM devices. Furthermore, as the size of a memory cell decreases, the magnetic field needed to induce switching greatly increases. To overcome such limitations, a thermally-induced pinned layer switching mechanism was proposed [274, 277]. As we have seen, when a sufficiently high electrical current flows through the insulating barrier, local temperatures can increase above the blocking temperature of the AFM layer ($T_B \sim 500$ K). One is then able to switch the magnetization of the pinned layer with a small magnetic field H and, upon cooling (under H), a new exchange-bias pinning direction is impressed.

Heat generation in tunnel junctions arises from two processes [263]: Usual Joule heating

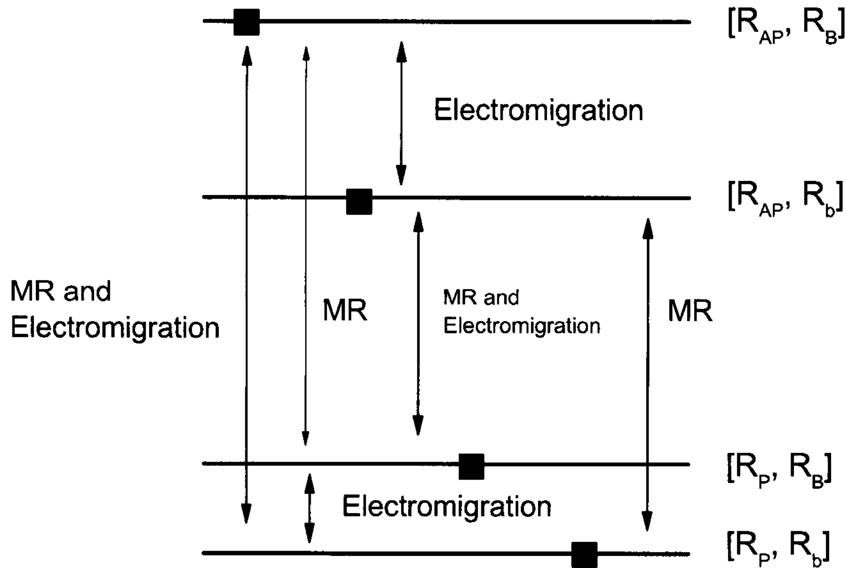

Figure 6.16: Envisaged four resistance states in thin tunnel junctions using both CIS and MR effects; R_B (R_b) stand for thick (thin) barrier and R_P (R_{AP}) for parallel (antiparallel) magnetic states.

in the metallic layers and electron inelastic scattering upon ballistic tunneling. The heat equation can then be written as [263]:

$$d.c_p\frac{\partial T}{\partial t} - K\frac{\partial^2 T}{\partial^2 x} = \rho.j^2 + \frac{j.V}{l_{in}}e^{-x/l_{in}}, \tag{6.7}$$

where c_p is the heat capacity, d is the mass density, K is the heat conductivity, T is the temperature, x is the stack position, $j = V/(RA)$ is the current density, V is the bias voltage and l_{in} is the inelastic scattering mean free path. Numerical results were obtained assuming that the current density is constant throughout the junction stack. Two different simulations were performed. In the first (second), one disregards (includes) the top and bottom leads and the temperature at the bottom and top of the tunnel junction stack (leads) is assumed fixed at 300 K. Other boundary conditions do not alter much the results obtained by the simulation [263]. Values of the parameters used can be found in Ref. [263].

In section 6.3.3 we induced a current-driven pinned layer switching effect in thin MTJs with $T_B = 520$ K [273] using *mean* current densities $j \sim 1 \times 10^6$ A/cm^2 through a tunnel junction. Our numerical results on heat generation in such TJ (with assumed *uniform* j) show however that, for $j \sim 1 \times 10^6$ A/cm^2, heating would be fairly small (see section 6.4.1). In fact, only much larger uniform current densities (~ 15 MA/cm^2) would lead to heating above the blocking temperature of the AFM layer. One concludes that the experimental observation of thermally driven pinned layer reversal is due to *localized heating* in nanoconstrictions that concentrate most of the electrical current and lead to high local current densities. Furthermore, we will present dynamical simulations that show that both heating and cooling (above and below T_B respectively) occur over very small time scales ($\lesssim$ ns), making current-written pinned layer switching a competitive mechanism for technological implementation.

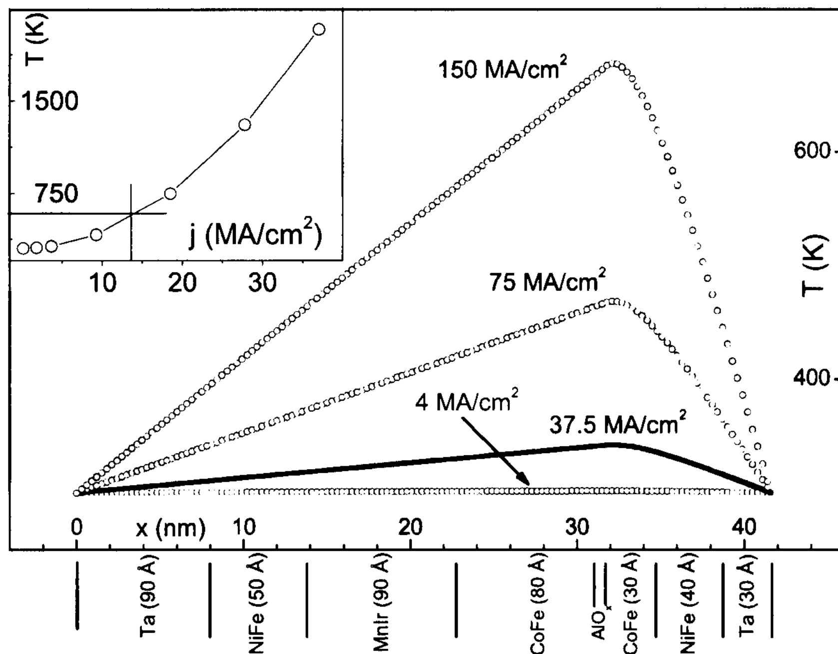

Figure 6.17: Simulation of heating processes inside the studied tunnel junctions, under different electrical current densities (1 MA= 10^6 A). Inset: Temperature increase as a function of current density passing through the junction. The results shown in the figure (inset) were obtained disregarding (taking into consideration) the top and bottom leads.

6.4.1 Steady-state regime

Our numerical results (Fig. 6.17) indicate that large heating can occur near the insulating barrier for high current densities. The results presented in the figure were obtained disregarding the top and bottom leads but are here depicted because they allow us to have a more detailed knowledge on the temperature increase in the region of interest. More accurate results are shown in the inset of Fig. 6.17, where both leads were included. Notice that the simulated temperature increase is (for the same current density) higher when the leads are present.

The expected T-increase arising from an uniform current density $j = I/A \approx 1$ MA/cm^2 is small (~ 30 K; inset of Fig. 6.17), and to reach $T_B = 520$ K our numerical results suggest $j_{\rm num} \sim 15 \times 10^6$ A/cm^2. This corresponds to an effective area through which current flows $A_{\rm eff} = I/j_{\rm num} \approx 0.3$ μm^2, *i.e.*, about 7% of the total tunnel junction area. These results then suggest that the obtained current density $j \approx 1 \times 10^6$ A/cm^2 is only an *average* value and that nanoconstrictions concentrate most of the current flowing through the barrier. Such hot-spots have been revealed by atomic force microscopy [263] and correlate well with results presented here.

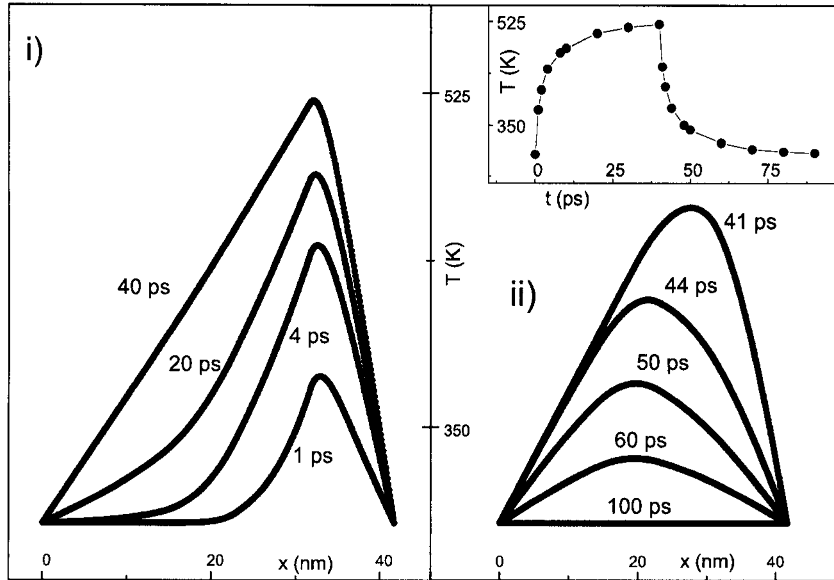

Figure 6.18: (a) Simulation of dynamical heating processes for $j = 112.5$ MA/cm^2. (b) Cooling under zero applied current. Inset: Maximum temperature inside the tunnel junction as a function of time during heating and cooling. All simulations were performed disregarding the top and bottom leads.

6.4.2 Dynamic regime

For MRAM application, write operations should occur in the ns-time frame. For that reason we performed dynamical simulations of heating and cooling (above and below T_B respectively) to predict if time was a constrainment when using the current-written pinned layer switching scheme. Figure 6.18 shows the obtained results using $j = 112.5$ MA/cm^2 (disregarding the top and bottom leads). One observes that both heating up to T_B and cooling back to room temperature occur in a very small time frame of less than 1 ns, making current-written pinned layer switching a competitive mechanism for actual technological applications.

6.5 Conclusions

We presented a detailed study of the Current Induced Switching effect on thin, low resistance (7 Å barrier) CoFe/AlO$_x$/CoFe tunnel junctions. We consistently traced the evolution of resistance switching in consecutive CIS(I_p) cycles between two (or three) states, driven by an electrical current, both under $H = 0$ and $H \neq 0$. Such evolution is controlled by the nanostructural rearrangements of ions at the electrodes/barrier interfaces (electromigration) and also by magnetic switching in the pinned layer under sufficiently high current pulses (under $H \neq 0$).

The temperature dependence of the junction resistance showed a weak non-metallic behavior from 300 to 25 K. This indicates proximity to the electrical continuity limit, so that several

competing mechanisms may be simultaneously operative. Current induced resistance switching was observed over the same temperature range, decreasing with temperature (e.g. ~7% at room temperature and ~3.5% at $T = 120$ K). At low temperatures we observed irreversible resistance decreases near $\pm I_{\text{max}}$, indicating barrier degradation. The CIS measurements as a function of temperature (300 – 25 K) showed that this effect is thermally assisted. Low ($\Delta_1 \sim 0.13$ eV) and high ($\Delta_2 \sim 0.85$ eV) energy barriers were estimated. Such differences are here associated with electromigration involving different types of ions and sites/defects. Notice that the comparison between the energy-barrier obtained from the temperature dependence of the critical switching current ($\Delta_0 \approx 0.04$ eV) and Δ_1 is made difficult because of the observed large temperature increase in our tunnel junction. In fact, taken this increase into account, Δ_0 would also increase considerably, being much closer to Δ_1. Furthermore, as we noticed before, the estimated Δ_1-value should be taken only as an upper limit, since it was obtained while large current pulses were being applied. We then conclude that the actual low-energy barrier value would fall between the obtained Δ_0 and Δ_1 values.

Time dependent measurements were also performed after a complete or a one-half CIS cycle, revealing two distinct relaxation times associated with opposite resistance changes. This experimental evidence on two opposite sign relaxation processes was explained by electromigration involving ions from the two FM/I interfaces.

If CIS cycles are measured under an external magnetic field, one is able to current-induce a change in the sign of the exchange bias of the TJ, and the corresponding magnetic state (antiparallel to parallel). This effect was shown to arise from excessive local heating in the tunnel junction, and enables us to obtain a CIS cycle with three different electrical resistance states. The magnetic dependence of the CIS effect results from an indirect effect related to excessive heating in nanoconstrictions. In the presence of a magnetic field, the pinned layer magnetization can rotate if $T > T_B$, thus decreasing the TJ-resistance.

Finally, we notice that, since the CIS effect depends on the structural characteristics of the electrode/oxide interfaces, differences in the measured properties are likely to occur between samples of the same series. In fact, even the most optimized characteristics of tunnel junctions (resistance and magnetoresistance) always show some dispersion in the same deposition batch [64].

Chapter 7

Current Induced Switching in non-Magnetic Tunnel Junctions

Summary

In the previous chapter we studied the Current Induced Switching (CIS) effect in thin, low resistance magnetic tunnel junctions (MTJs). In a CIS cycle, the resistance commutes between two resistance (R) states due to electromigration of ions from the electrodes into the barrier (decreasing R) and from the barrier back into the electrodes (increasing R). However, we saw that cycling also produces irreversible R-decreases that ultimately lead to metallic-dominated conduction. Time dependent measurements showed that (under a low measuring current), previously displaced metallic ions relax into their initial positions in the electrodes. CIS cycles performed under an external magnetic field provided conclusive evidence that high temperatures occur inside the TJ, likely due to the existence of nanoconstrictions carrying fairly large current densities.

Here we study three different series of tunnel junctions with a Ta non-magnetic (NM) amorphous thin layer deposited i) just below, ii) just above and iii) just below-and-above the insulating barrier (fully non-magnetic TJ in this case; in cases i, ii one of the electrodes was magnetic). In particular, we investigate the influence of the Ta non-magnetic layers in the Current Induced Switching effect.

Interestingly, we found that, in tunnel junctions having a Ta layer deposited below the barrier (FM/NM/I/FM or FM/NM/I/NM/FM), the current direction needed to induce R-switching is opposite to that required in FM/I/FM or FM/I/NM tunnel junctions. In the first case switching occurs for *positive* current pulses whereas in the later it occurs only for *negative* currents (as discussed in chapter 6). Using the ballistic model of electromigration (EM), we will show here that the direct force likely dominates electromigration in Ta (NM) layers, while the wind contribution is dominant in CoFe (FM) layers. The different switching directions are then associated with the dominance of different EM forces (direct or wind) in these two types of tunnel junctions.

Another important difference between tunnel junctions with and without a Ta layer deposited *below* the insulating barrier occurs in the relaxation phenomenon. Following the displacement

of CoFe ions into the barrier by the action of an electrical field (in FM/I/FM and FM/I/NM tunnel junctions), subsequent relaxation R(t) measurements always show the return of such ions to their initial positions in the electrodes. On the other hand, electromigrated Ta ions (in FM/NM/I/FM and FM/NM/I/NM tunnel junctions) remain inside the barrier and thus the thin- and thick-barrier R-states (R_b and R_B states respectively) remain stable when measured (under low bias current) over periods above 4 hours. This indicates that Ta ions need to surmount much larger energy barriers than CoFe ions to return to the electrodes.

We measured the electrical resistance, magnetoresistance and CIS effect in the 300 – 20 K temperature range for all the TJ series here studied. We used the current pulse method to measure the CIS effect, and V(I_p) characteristics were also obtained while applying the current pulse I_p. The temperature dependence of the electrical resistance of the studied series always shows an initial negative dR/dT derivative, indicating an insulator-like behavior in the TJ virgin state. The Current Induced Switching effect was found to be strongly dependent on both maximum pulse current (I_{max}) and temperature. At constant temperature, the CIS effect increases with increasing I_{max}, until a plateau of constant CIS is observed. The temperature dependence of the CIS coefficient was obtained in the 300 – 20 K range and, for the same I_{max}, it decreases with decreasing temperature.

We measured the temperature dependence of the electrical resistance of the thin- and thick-barrier states (R_b and R_B), observing a smaller R(T) variation when the tunnel junction is in the R_b state. Studies on barrier degradation (irreversible resistance decrease; caused by sufficiently high I_{max} values) showed a gradual transition from tunnel- to metallic-dominated transport, related to the formation and subsequent increase of pinhole size. Time evolution electrical resistance measurements under both low and high electrical currents allowed us to probe the dynamics of our system as electromigration proceeds. At low temperatures we found a rapid but quasi-continuous R(t) evolution in the early stages of EM. However, as time increases this smooth dependence gradually disappears and the resistance starts to vary by discontinuous steps, denoting a different dynamical EM-process. The increase of temperature definitely enhances this trend, and R(t) then reveals the existence of many active fluctuators.

7.1 Experimental details

To further study Current Induced Switching, new series of tunnel junctions with one or two non-magnetic electrodes were measured. Here we present our results on three series of tunnel junctions deposited by Ion Beam Deposition (IBD), with a non-magnetic Ta layer deposited just below (series 834), just above (series T1) and on both sides (series 835) of the insulating AlO_x barrier (Table 7.1).

The structure of the tunnel junctions of series 834 was Glass/Bottom lead/Ta (90 Å)/NiFe (50 Å)/MnIr (90 Å)/CoFe (40 Å)/Ta (20 Å)/AlO_x (3 Å+ 4 Å)/CoFe (30 Å)/NiFe (40 Å)/Ta (30 Å)/TiW(N) (150 Å)/Top lead. The tunnel junctions of series 835 differed from those of series 834 by the addition of a 20 Å Ta layer immediately above the AlO_x barrier. Series T1 had the structure Glass/Bottom lead/Ta (90 Å)/NiFe (70 Å)/MnIr (80 Å)/CoFe (30 Å)/Al (3 Å+ 4 Å)/Ta (100 Å)/TiW(N) (150 Å)/Top lead.

The barrier was, in all series, formed by a two-step deposition and oxidation processes [62];

Series	Non-magnetic layer
834	20 Å Ta *pinned* layer
835	20 Å Ta *pinned* + *free* layers
T1	100 Å Ta *free* layer

Table 7.1: Tunnel junction series with non-magnetic electrodes studied in this chapter.

NiFe, CoFe, MnIr and TiW(N) stand for $Ni_{80}Fe_{20}$, $Co_{80}Fe_{20}$, $Mn_{78}Ir_{22}$ and $Ti_{10}W_{90}(N)$. The bottom and top leads are made of Al 98.5% Si 1% Cu 0.5%, and are 600 Å (26 μm) and 3000 Å (10 μm) thick (wide) respectively. The junctions were patterned to a rectangular shape with dimensions ranging from 1×1 μm^2 to 6×2 μm^2 by a self-aligned microfabrication process.

The electrical resistance, magnetoresistance and current induced switching were measured with a four-point d.c. method, with a current stable to 1:10^6 and using an automatic control and data acquisition system. Low temperature measurements were performed in a automatically controlled closed cycle cryostat. CIS cycles were performed using the pulsed current method [76] allowing us to measure the *remnant* resistance of the tunnel junction after each current pulse. The CIS cycles were obtained at constant temperatures between 300 K and 20 K. Details to the measuring sequence were given in sections 2.2.2.2 and 6.1. However, notice that the voltage across the TJ was now also measured while applying the current pulse I_p, enabling us to obtain the (non-linear) V(I_p) characteristic for each CIS cycle.

Recall that the CIS coefficient is defined as:

$$CIS = \frac{R_{\text{initial}} - R_{\text{half}}}{(R_{\text{initial}} + R_{\text{half}})/2}. \tag{7.1}$$

The resistance shift (δ) in each cycle is given by:

$$\delta = \frac{R_{\text{final}} - R_{\text{initial}}}{(R_{\text{initial}} + R_{\text{final}})/2}. \tag{7.2}$$

7.2 Tunnel junctions with a non-magnetic Ta layer covering the pinned CoFe layer (series 834)

*Here we study how a Ta non-magnetic thin layer (20 Å) deposited just below the insulating barrier affects Current Induced Switching. We measured the electrical resistance, magnetoresistance and CIS cycles in the 320–20 K temperature range. The CIS coefficient was found to be strongly enhanced by increasing $I_{\max}$ (30–80 mA range), reaching almost 60% for the maximum applied current pulse, $I_{\max} = 80$ mA. However, severe R-degradation occurs for $I_{\max} \gtrsim 65$ mA. We found that, as in the case of magnetic tunnel junctions (chapter 6), EM of metallic ions occurs in the bottom electrode/insulating barrier interface (Ta/AlO_x in the TJs studied here; CoFe/AlO_x in chapter 6). However, the current direction inducing resistance variations are different in the two cases: While in magnetic TJs one sees that R-decrease or switching (*R-increase or recovery*) occurs only for negative (*positive*) current pulses, in FM/NM/I/FM tunnel junctions these changes are inverted: Switching (*recovery*) occurs*

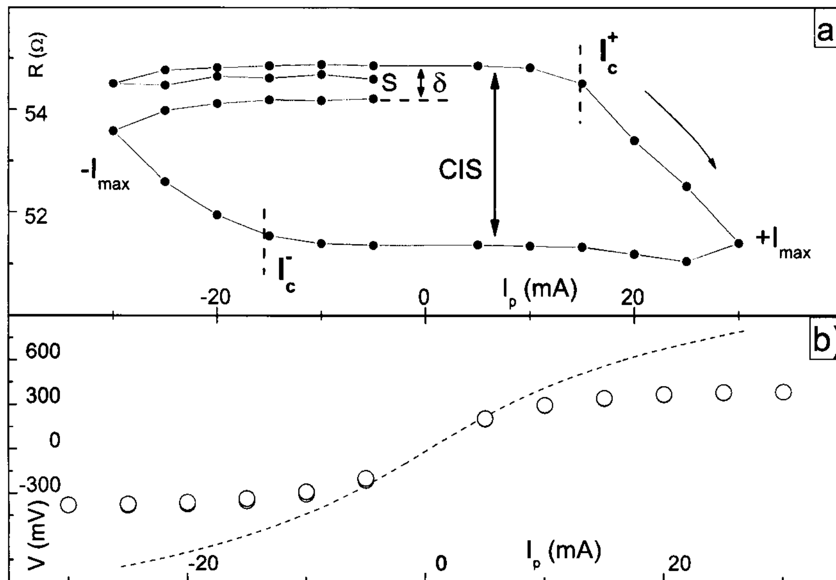

Figure 7.1: (a) Current Induced Switching cycle for $I_{\mathrm{max}} = 30$ mA and (b) corresponding V(I_{p}) characteristic (hollow circles). The dashed line is a V(I) characteristic calculated using Simmons' model ($\varphi = 1$ eV; $t = 9$ Å).

*under positive (*negative*) currents. The ballistic model of electromigration will enable us to associate these differences with the dominance of the direct (wind) EM-contribution in Ta (CoFe). Voltage-current characteristics show strong anomalous non-linearities, that are here associated with heating effects. One estimates that the temperature inside the tunnel junction reaches ~600 K for* $I_{\mathrm{max}} = 80$ *mA. Numerical results from a model of heat generation and diffusion in tunnel junctions again show that such high temperatures can only occur if local current densities much larger than uniform* $j = I/A$ *(I is the current and A the total tunnel junction area) flow through the barrier. No time dependent (relaxation) effects were observed and the CIS effect did not depend on the applied magnetic field (up to* $H = 250$ *Oe). The temperature dependence of the Current Induced Switching coefficient was also obtained: For the same maximum current pulse, the CIS coefficient decreases with decreasing temperature, showing its thermally activated nature.*

7.2.1 Room temperature results

7.2.1.1 Current Induced Switching

The initial resistance at RT of the studied tunnel junction was 54.9 Ω and the corresponding resistance area product $R \times A = 220$ $\Omega\mu\mathrm{m}^2$. No magnetoresistance was observed, due to the loss of interfacial polarization (Ta layer deposited just below the barrier). In fact, the tunnel magnetoresistance of a TJ is known to strongly decrease with the thickness of a non-magnetic layer inserted just below the insulating barrier [278, 279] and TMR goes rapidly to zero within the first monolayers of the non-magnetic material.

We measured CIS cycles with increasing $I_{\max}$, starting with a cycle up to $I_{\max} = 30$ mA [Fig. 7.1(a); cycle starting at point S] from which we obtained $CIS = 6.6\%$ and $\delta = -1.2\%$. No resistance switching was observed under the initial negative current pulses ($0 \to -I_{\max}$). However, upon reversing the current ($-I_{\max} \to 0 \to +I_{\max}$) one observes that for $I_{\rm p} \gtrsim 15$ mA [where we define the positive critical current I_c^+; see Fig. 7.1(a)] the resistance starts to decrease, a trend that becomes increasingly enhanced (switching) up to $I_{\max} = 30$ mA. This switching is associated with electromigration of metallic ions from the electrodes into the barrier [253], decreasing the effective barrier thickness and consequently the junction resistance. The absence of R-switching under negative current pulses again indicates an electromigration asymmetry with respect to the electrode/oxide interfaces, *i.e.* only ions from one interface appear actively involved in EM. Physically such asymmetry arises not only from the different materials deposited just below (Ta) and above (CoFe) the insulating barrier, but also from the deposition and oxidation processes used during tunnel junction fabrication; in particular the top electrode is deposited over an oxidized *smooth* surface (see also discussion in section 6.3.2). Since the migration of ions into and out of the barrier should occur preferentially in nanoconstrictions the asymmetry in EM must be related to the structural details inherent to the deposition and oxidation processes. Electromigrating ions then likely belong to the bottom electrode. The (assumed uniform) current density and electrical field at R-switching can be estimated as $j_c \sim 0.4 \times 10^6$ A/cm^2 and $E_c \sim 3$ MV/cm, respectively.

Returning to Fig. 7.1(a), the decrease of $I_{\rm p}$ from $I_{\max}$ to zero hardly affects the low resistance state. However, for $I_{\rm p} \leq -15$ mA ($\equiv I_c^-$), the resistance gradually increases until $I_{\rm p} = -I_{\max}$, recovering a significant fraction of the previous R-switching near $+I_{\max}$. This indicates that, under a reversed electrical field, most ions return to their initial sites in the metallic electrodes. The subsequent change of $I_{\rm p}$ from $-I_{\max}$ to zero (to close the CIS cycle) produces no significant change in the resistance. However, the final δ-shift ($R_{\rm final} < R_{\rm initial}$; $\delta = -1.2\%$) indicates some irreversible effects in this CIS cycle ($I_{\max} = 30$ mA), associated with barrier degradation.

The voltage across the junction was also measured for each applied current pulse, providing the V($I_{\rm p}$) characteristic depicted in Fig. 7.1(b) (hollow circles). The use of Simmons' model [181] to fit this curve does not give reasonable fitting parameters. The unsatisfactory dashed line in Fig. 7.1(b) was obtained using the Simmons' model and adequate thin TJ barrier parameters [253] (barrier thickness $t = 9$ Å, barrier height $\varphi = 1$ eV). Large discrepancies are thus observed, particularly near $\pm I_{\max}$, which will be related to the effects of localized heating inside the tunnel junction. Similarly, the use of the Brinkman model for asymmetric tunnel junctions [187] does not yield good fits.

We then performed CIS cycles with increasing $I_{\max}$, from 30 to 80 mA, in $\Delta I_p = 5$ mA steps as shown in Fig. 7.2 for selected cycles. Notice the enhanced R-switching and R-recovering stages (versus $I_{\rm p}$), occurring from I_c^+ to $I_{\max}$ and from I_c^- to $-I_{\max}$, respectively. From this data we can obtain the CIS and δ-shift in each cycle, extracting the corresponding dependence on $I_{\max}$, as shown in Fig. 7.3(a). The CIS coefficient rises non-linearly with $I_{\max}$ until ~65 mA ($CIS = 57.4\%$), saturating for higher current pulses. On the other hand, δ remains fairly small below $I_{\max} \sim 60$ mA (-0.4%), but increases rapidly for higher $I_{\max}$ ($\delta = -9.6\%$ for $I_{\max} = 80$ mA). The CIS increase with increasing $I_{\max}$ indicates that electromigrated ions are further pushed into the barrier (further lowering R) or/and more ions become active in the EM processes. Such processes lead to irreversible damage of the barrier, as reflected

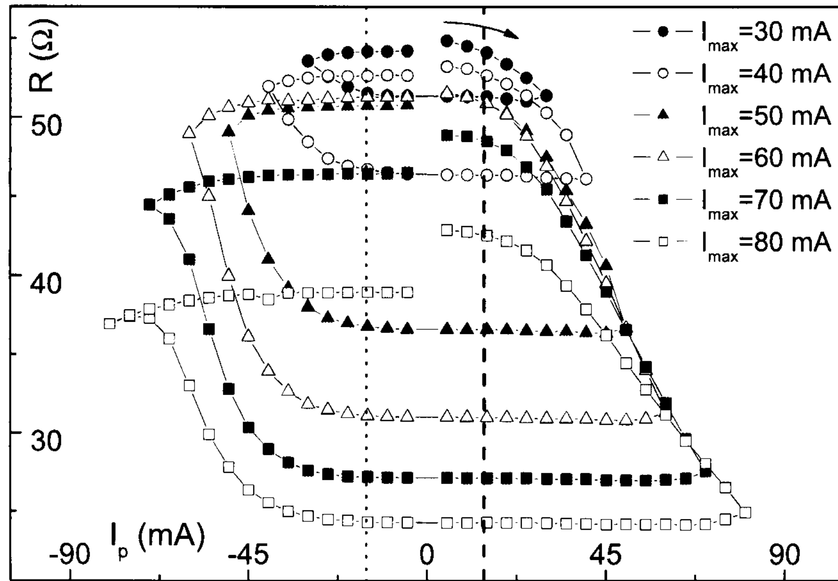

Figure 7.2: Selected CIS cycles performed with $I_{\max}$ up to 80 mA. Notice the enhanced R-switching occurring under increasing $I_{\max}$.

in the δ-shift enhancement observed for $I_{\max} \geq 65$ mA [Fig. 7.3(a)].

In the $R(I_{\max})$ graph [Fig. 7.3(b)] we confirm that both R_{initial} and R_{final} show an overall irreversible decrease with increasing $I_{\max}$. In particular, R_{initial} decreases by more than 30% from the first CIS cycle ($I_{\max} = 30$ mA; $R = 54.9$ Ω) to the last one ($I_{\max} = 80$ mA; $R = 38.9$ Ω). Such decrease is, however, small until $I_{\max} = 60$ mA, but gets sharper at higher currents. Another interesting feature is the fact that R_{half} decreases rapidly whit $I_{\max}$ until ~65 mA. This then leads to large $\Delta R = R_{\text{initial}} - R_{\text{half}}$ and, consequentially, to the observed CIS coefficient enhancement in this $I_{\max}$ range. When $I_{\max}$ is larger than 65 mA, ΔR decreases slightly, and a plateau of constant CIS coefficient is observed.

7.2.1.2 Discussion

The observed resistance switching (R-decrease) occurs only for ***positive*** current pulses in the here studied FM/NM/I/FM tunnel junctions (R-recovery occurs under negative I_p). However, in FM/I/FM tunnel junctions switching (recovery) occurs under ***negative*** (positive) currents (Fig. 7.4; see chapter 6). To explain such difference, we compare the electromigration direct and wind forces in the Ta (NM) and CoFe (FM) layers. Due to the lack of relevant data in the literature, one rewrites the characteristic wind force valence in the ballistic model, $Z_w = -nl\sigma_{tr}$ ($n \equiv$ electron density, $l \equiv$ electron mean free path and $\sigma_{tr} \equiv$ electron transport cross section) to obtain the ratio:

$$\frac{Z_w(Ta)}{Z_w(CoFe)} = \frac{\rho(CoFe)v_F(Ta)}{\rho(Ta)v_F(CoFe)}\frac{\sigma_{tr}(Ta)}{\sigma_{tr}(CoFe)}, \tag{7.3}$$

where ρ is the electrical resistivity and v_F the Fermi velocity. Inserting the parameters given in Table 7.2 [260, 266, 280, 23], one obtains $Z_w(Ta) \sim 0.07 \times Z_w(CoFe)$, so the wind

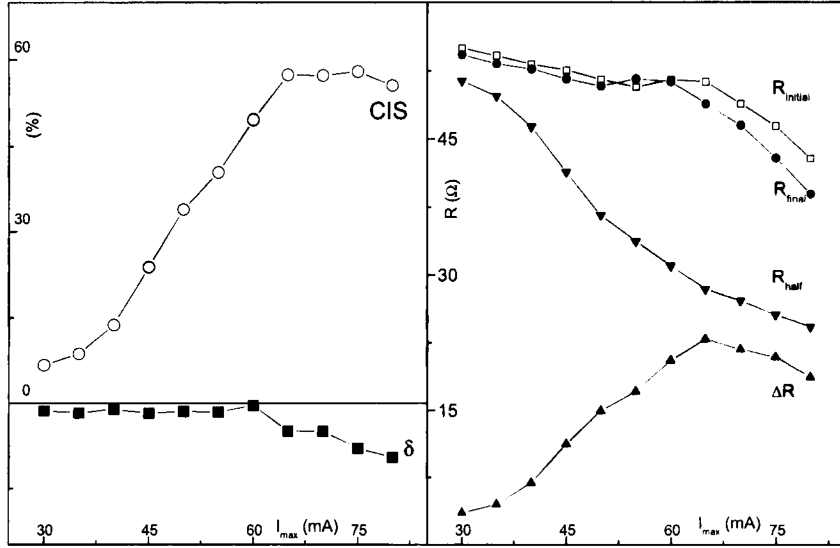

Figure 7.3: (a) Current Induced Switching coefficient and δ-shift as a function of maximum applied current. The CIS coefficient is enhanced with $I_{\max}$ but large negative δ-shift values occur for $I_{\max} > 60$ mA, indicating progressive barrier degradation. (b) Maximum applied current pulse dependence of characteristic tunnel junction resistances in a CIS cycle.

	ρ ($\mu\Omega cm$) [23]	σ_{tr} (Å^2) [266]	v_F (cm/s) [260, 280]
CoFe	17.1	~3	~2
Ta	154.0	~6	0.67

Table 7.2: Electrical resistivity, electron transport cross section for scattering and Fermi velocity used to estimate $Z_w(Ta)/Z_w(CoFe)$.

force is much larger in CoFe (where it dominates electromigration) than in Ta. On the contrary, because Ta is in an amorphous state (notice its high electrical resistivity in Table 7.2), the small electron mean free path prevents large momentum gains by electrons between consecutive collisions and thus a large wind force.

Using the value estimated in section 6 for $Z_w(Fe)$ (≈ -15), one finds $Z_w(Ta) \approx -1.4$ [$\approx Z_d(Ta)$]. Remembering that the magnitude of the direct force is enhanced relatively to the wind force in nanoconstrictions (section 5.8.2) and that the ballistic model usually overestimates Z_w, one expects the direct force to dominate the wind force in the Ta layers. Thus, the likely cause for the observed difference in the R-switching directions is different dominant electromigration forces in Ta and CoFe.

Figure 7.5 (left scale) shows the Current Induced Switching R(I_p)-cycle obtained at RT, with $I_{\max} = 80$ mA ($CIS = 55.5\%$; $\delta = -9.6\%$). Notice again the R(I_p)-switching from $I_c^+ = 15$ mA to $I_{\max} = 80$ mA and from $I_c^- = -35$ mA to -$I_{\max} = -80$ mA. The V(I_p) characteristic is also displayed (hollow circles; right scale), showing an anomalous plateau with a slight negative dV/dI_p slope for $|I_\text{p}| \geq 30$ mA. This effect cannot be explained by tunnel

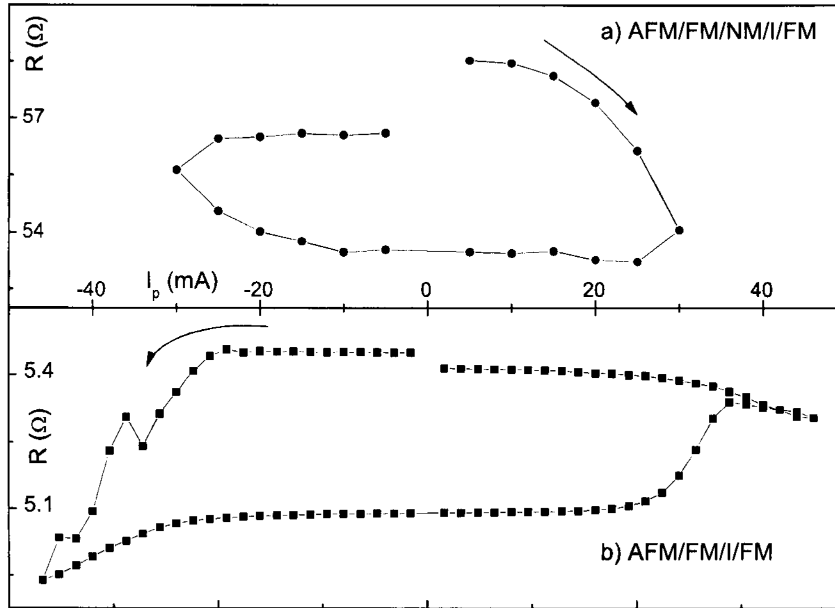

Figure 7.4: Different resistance switching directions in a CIS experiment for tunnel junctions with (a) AFM/FM/NM/I/FM (MnIr/CoFe/Ta/AlO$_x$/CoFe/NiFe) and (b) AFM/FM/I/FM (MnIr/CoFe/AlO$_x$/CoFe/NiFe; see also chapter 6).

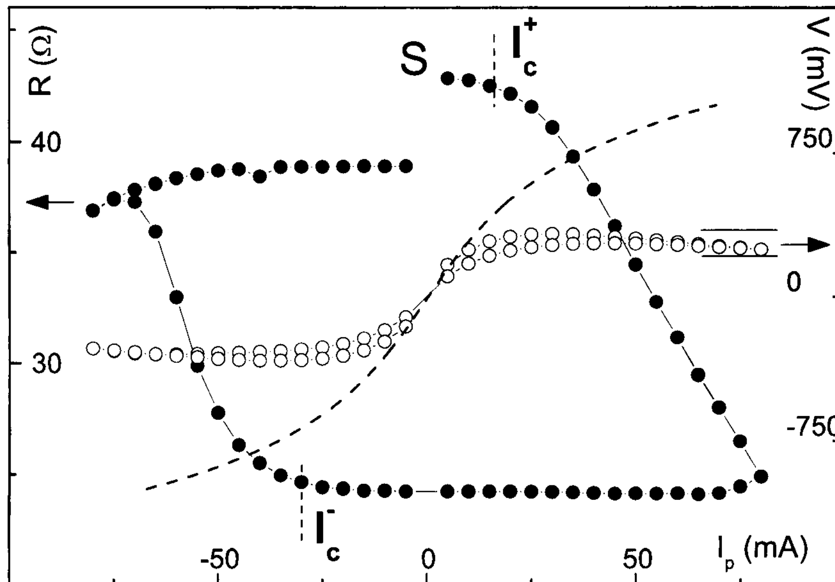

Figure 7.5: CIS cycle and corresponding V(I_p) characteristic for $I_\mathrm{max} = 80$ mA. Notice the decrease of $|V|$ near $\pm I_\mathrm{max}$. The dashed line depicts a V(I) curve calculated using Simmons' model.

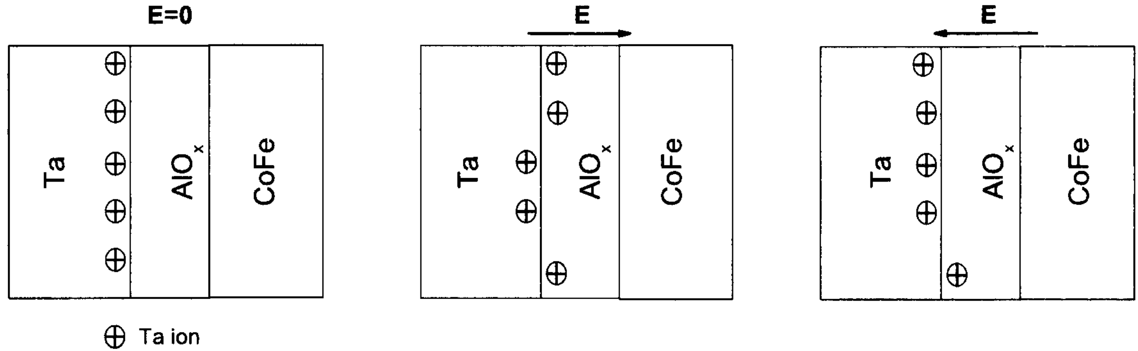

Figure 7.6: Schematic electromigration of Ta ions into and out of the insulating AlO_x barrier. Notice that some Ta ions may remain in the barrier when the electrical current is reversed.

transport theories and is here related to heating inside the junction. Using our temperature dependent R-data (see below), the temperature inside the tunnel junction is estimated as ~600 K. Such high temperatures confirm the results obtained in FM/I/FM tunnel junctions (chapter 6), where temperatures larger than 520 K where shown to occur.

Numerical results of heat generation in tunnel junctions were obtained using the method described in section 6.4. The steady-state heat equation can be written as [263]:

$$-K\frac{\partial^2 T}{\partial^2 x} = \rho j^2 + \frac{jV}{l_{in}}e^{-x/l_{in}}, \tag{7.4}$$

where all terms were defined in section 6.4. The top and bottom leads were not included in the simulation and the temperature at the bottom and top of the tunnel junction stack is assumed fixed at 300 K.

Our results (not shown; see Ref. [281]) indicate that the temperature increase expected from an uniform $j_c = I_c/A \sim 0.4 \times 10^6$ A/cm^2 is negligible (~ 1 K), and to reach 600 K one needs $j_{\rm num} \sim 2 \times 10^7$ A/cm^2. This corresponds to an effective area through which current flows $A_{\rm eff} = I_c/j_{\rm num} \approx 0.1$ μm^2, *i.e.*, about 2.5% of the total tunnel junction area. We again conclude that nanoconstrictions concentrate most of the current flowing through the barrier.

One can now describe the observed electromigration in thin FM/NM/I/FM tunnel junctions with NM=Ta (amorphous; Fig. 7.4a). Under increasing positive current pulses, the dominating EM direct force induced by the electrical field pushes Ta atoms from the bottom electrode into the barrier (Fig. 7.6; center), a process thermally assisted by heating generated by the high current densities flowing in nanoconstrictions. This rises the probability that an atom surmounts the energy barrier for migration E_b (inset of Fig. 7.7), exponentially enhancing atomic mobility. Even a small barrier weakening (due to such migration) considerably lowers the tunnel resistance due to its exponential dependence on barrier thickness [181]. Using the Simmons' model one can calculate the resistance variation due to a barrier thickness reduction from t to $t - \delta t$ ($\delta t \ll t$):

$$\begin{aligned} &\frac{R(t) - R(t-\delta t)}{R(t)} = \\ =&\frac{R_{\rm initial} - R_{\rm half}}{R_{\rm initial}} \approx 1 - e^{-0.72\sqrt{\varphi/2}\delta t} \approx 0.72\sqrt{\varphi/2}\delta t. \end{aligned} \tag{7.5}$$

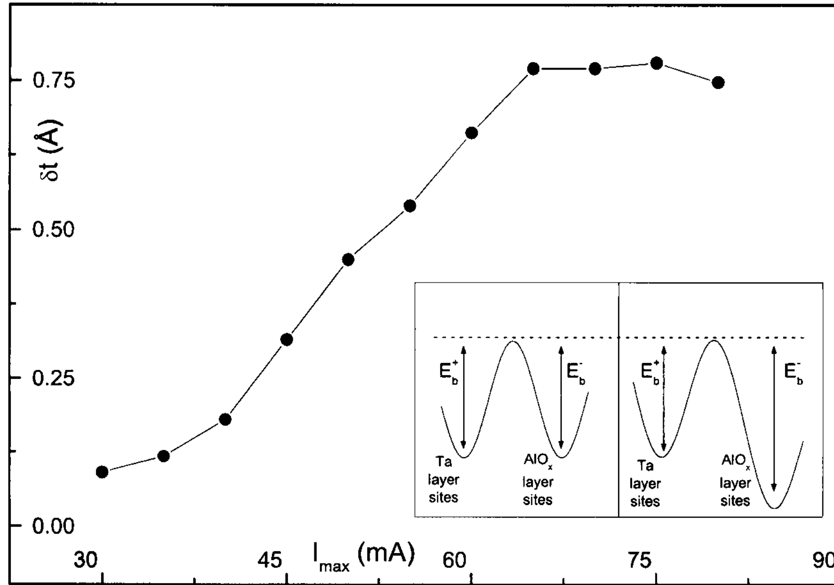

Figure 7.7: Dependence of the barrier thickness decrease (δt) on the maximum applied current pulse, as obtained from the CIS(I_{max}) curve (Fig. 7.3) and Eq. (7.5) (for $\varphi = 1$ eV). Inset: Energy barrier for migration from Ta into the barrier (E_b^+) and vice-versa (E_b^-), in the first (left) and last (right) CIS cycles.

For a CIS coefficient of $\sim$ 60%, and assuming $\varphi = 1$ eV, the barrier thickness has to decrease by $\delta t \sim 0.8$ Å. [Notice that the barrier height φ is also expected to decrease with electromigration of ions from the electrodes into the barrier. That effect was not considered above for simplicity, but would lead to the decrease of the δt value estimated from Eq. (7.5).] One can then plot the expected barrier thickness decrease δt as a function of the maximum applied current I_{max} using the experimental R_{initial} and R_{half} values (Fig. 7.7). We see that the $\delta t(I_{\text{max}})$ dependence follows the same trend as the CIS coefficient (Fig. 7.2). In particular, a non-linear behavior (as more clearly visible at low temperatures) is observed for $I_{\text{max}} \leq 60$ mA, that is, while the δ-shift is small and electromigration is mainly reversible. In atomic diffusion processes one often has [257] $\frac{\partial x}{\partial t'} \propto F$ (x the position and t' the time). Therefore, in electromigration in tunnel junctions one has $\delta t \propto j\delta t'$, *i.e.* the barrier thickness decrease is proportional to the electrical current density. Following this simple analysis, one obtains $[R(t) - R(t - \delta t)]/R(t) \propto j$. The CIS effect then depends on how local current densities behave near nanoconstrictions and its dependence on nanostructural atomic rearrangements.

Time dependent measurements (over 4 h) showed no relaxation phenomena after performing half [Fig. 7.8(a)] or complete [Fig. 7.8(b)] CIS cycles at $T = 300$ K. This is also visible in Figs. 7.2 (page 170) and 7.4, where no R-increase is observed after switching to the low R-state in the case of AFM/FM/NM/I/FM tunnel junctions [Fig. 7.4(a); near $+I_{\text{max}}$], contrasting with the AFM/FM/I/FM case [see R-increase near $-I_{\text{max}}$ in Fig. 7.4(b)]. Thus, under a reduced driving force, displaced Ta ions remain trapped in deep enough local energy minima inside lattice potential barriers ($E_b \gg k_B T$), so that mere thermal fluctuations cannot return them to the electrodes. In the CIS cycle of Fig. 7.4(a) one observes that

the low resistance state persists for I_p from I_{max} down to I_c^-. However, when $I_p < I_c^-$ the driving force gets strong enough to return most of the previously displaced ions back into their initial positions in the NM layer (Fig. 7.6; right). The final resistance does not exactly reaches its initial value, indicating progressive barrier degradation. Such barrier degradation can result from metallic ions that remain in the barrier after the CIS cycle is completed. Notice also that in the initial CIS cycle with $I_{max} = 30$ mA [Fig. 7.4(a)] one has $I_c^+ \approx |I_c^-|$. This indicates that the driving forces for electromigration into and out of the insulating barrier are approximately equal, *i.e.* the lattice sites where ions migrate from and to are energetically similar ($E_b^+ \approx E_b^-$; inset of Fig. 7.7). Furthermore, Fig. 7.2 (see dashed line) shows that $I_c^+ \approx 15$ mA throughout all CIS cycles performed, indicating that cycling does not alter the EM force needed to induce atomic migration from Ta ions into the barrier. In other words, the energy barrier which the Ta ions surmount (when migrating into the barrier) is kept constant. This contrasts with electromigration in the opposite direction, for which $|I_c^-|$ increases with cycling (Fig. 7.2; see dotted line). Therefore, the force needed to return Ta ions from the barrier back into the electrodes has to be increased ($E_b^+ < E_b^-$; inset of Fig. 7.7), indicating that under increasingly higher current pulses, Ta ions are pushed further into the interior of the barrier, being harder to remove from the insulator.

Finally notice in Fig. 7.8(c), where we present the R(t) behavior after a complete CIS cycle, that the electrical resistance fluctuates between several discrete levels. These levels are attributed to the migration of ions from the barrier into the electrodes (R-increases) and vice-versa (R-decreases) as we will study in more detail in section 7.3.3.

7.2.2 Temperature dependent results

7.2.2.1 Electrical resistance

The electrical resistance of the studied TJ (series 834) rises with decreasing temperature, indicating tunnel-dominated transport (Fig. 7.9). At $T = 20$ K, the electrical resistance was 108.0 Ω, indicating a 97% increase above the room temperature value (54.9 Ω). Such strong R(T) dependence is usually associated with a contribution from hopping conductance [282]. We then fitted the R(T) curve using magnon- and phonon-assisted tunneling and a two step hopping contribution (see section 5.5.2) having an associated temperature dependance $G^{hop}(T) = S_2 T^{4/3}$. The fit result (line in Fig. 7.9) reproduces quite well the experimental curve. Notice however that if one adds three-step-hopping for temperatures above $T \approx 150$ K, the obtained fit clearly improves. This confirms the current knowledge that higher order hopping contributions are enhanced by temperature [205]. Magnetoresistance was also measured at $T = 20$ K and no MR signal was observed.

7.2.2.2 CIS effect

We then measured CIS cycles in the 30–80 mA I_{max} range, at temperatures below room temperature, down to 25 K.

For $T = 200$ K and $I_{max} = 30$ mA, we obtained $CIS = 1.3\%$ and $\delta = -0.5\%$ [Fig. 7.10(a)]. This indicates that, for the same I_{max}, the CIS coefficient decreases with temperature, as

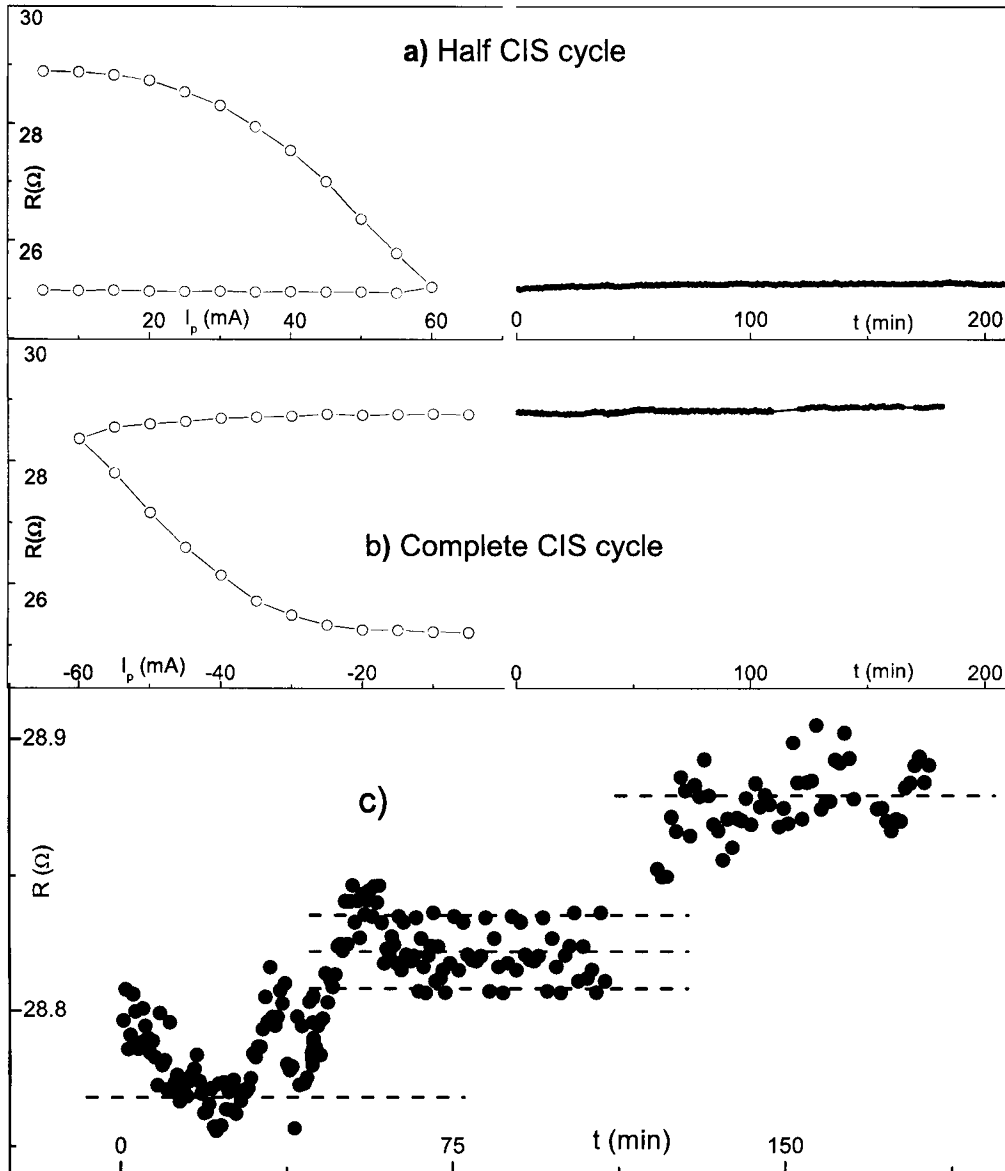

Figure 7.8: (a) Half and (b) complete CIS cycles performed at $T = 300$ K, and subsequent R(t) measurements. (c) Enlarged view of R(t) measurements performed after a complete CIS cycle.

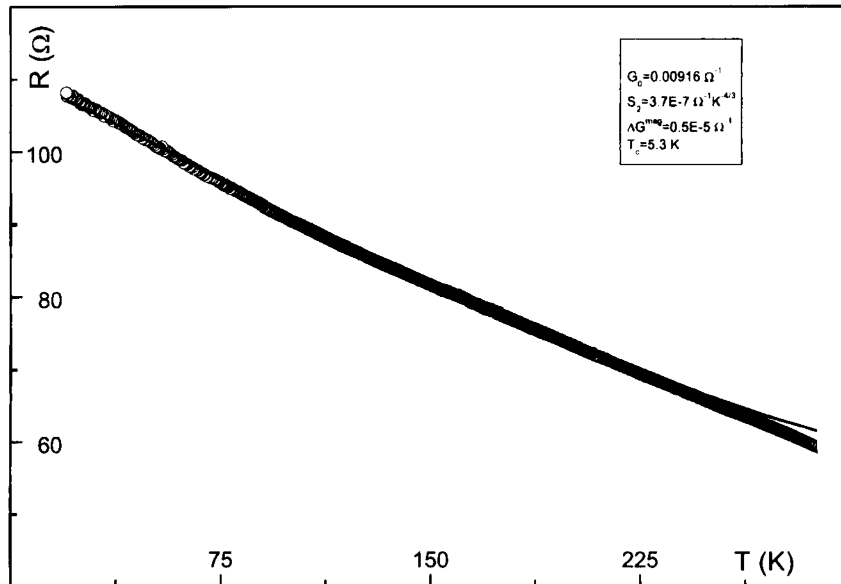

Figure 7.9: Experimental temperature dependence of the electrical resistance and corresponding fit (red line; series 834).

does the δ-shift (compare with $CIS = 6.6\%$, and $\delta = -1.2\%$ obtained at $T = 300$ K). For $I_{\text{max}} = 80$ mA, we obtained $CIS = 37.3\%$ and $\delta = -0.1\%$ ($CIS = 55.5\%$, and $\delta = -9.6\%$ at RT). Nevertheless, at $T = 200$ K one still observes a non-linear $R(I_{\text{p}})$ behavior in the $I_{\text{c}}^{+} \rightarrow +I_{\text{max}}$ and $I_{\text{c}}^{-} \rightarrow -I_{\text{max}}$ current pulse ranges (for $I_{\text{max}} = 40$ mA, one has $I_{\text{c}}^{+} = 20$ mA and $I_{\text{c}}^{-} = -20$ mA). Notice that the I_{c}^{+} and I_{c}^{-} switching currents again vary with I_{max}, consistently with what was observed at RT (see below).

Interestingly, one observes negligible negative or even small *positive* δ-shifts (the later in the 60–80 mA I_{max} range), indicating that the resistance at the end of a CIS cycle is higher than at the beginning [see also Fig. 7.12(a)]. This *healing* is also sometimes observed at RT and likely reflects the stochastic nature of atomic diffusion processes. In fact, the main R-degradation induced in previous CIS cycles (at the same or at higher temperatures) is likely due to migrated ions from the electrodes which remained trapped in the barrier. In subsequent CIS cycles with higher I_{max}, these ions have increasing probability to return to the electrodes, producing then a positive δ-shift. One also sees that the CIS coefficient (at $T = 200$ K) continuously rises with I_{max} and does not saturate for $I_{\text{max}} = 80$ mA [Fig. 7.11(a)], in contrast to what was observed at $T = 300$ K. Considering the absolute R-values [Fig. 7.12(a)], we observe that, in the 60–80 mA I_{max} range, R_{initial} and R_{final} increase with increasing I_{max} (positive δ-shift) and that ΔR (R_{half}) increases (decreases) strongly above $I_{\text{max}} = 50$ mA.

Further lowering the temperature shows overall the same general features: For the same I_{max}, the CIS coefficient is smaller at lower temperature; in the 30–80 mA I_{max} range, the CIS coefficient continuously rises with I_{max}; the δ-shift is always small, taking both positive and negative values, but following no clearly defined trend [Fig. 7.11(a)]. The initial and final resistance values then remain fairly constant in these I_{max} and temperature ranges; the

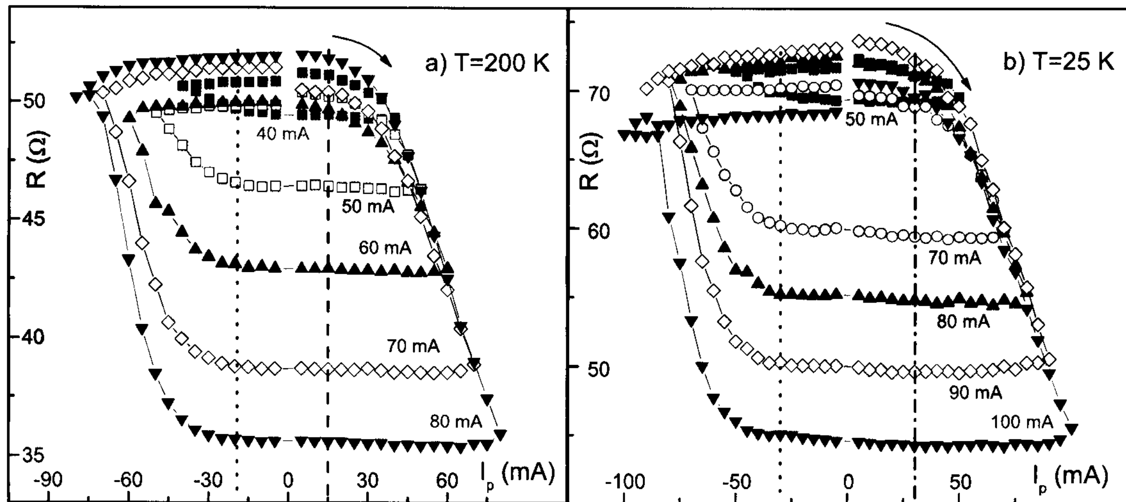

Figure 7.10: CIS cycles performed at (a) $T = 200$ K and (b) $T = 25$ K.

rise of the CIS coefficient is always related with the increase in ΔR [decrease of R_{half}; Fig. 7.12(a)].

At $T = 25$ K, we increased I_{max} up to 100 mA, obtaining the selected R(I_{p}) cycles shown in Fig. 7.10(b). For $I_{\text{max}} = 30$ mA we obtained $CIS = 1.0\%$ and $\delta = -0.5\%$; for $I_{\text{max}} = 80$ mA we obtained $CIS = 26.6\%$ and $\delta = 0.7\%$ and for $I_{\text{max}} = 100$ mA, $CIS = 45.3\%$ and $\delta = -3.1\%$. These cycles are mainly reversible in the 30–90 mA I_{max} range with a CIS coefficient as high as 38%. However, for higher maximum pulse currents ($I_{\text{max}} = 100$ mA), a trend towards CIS coefficient saturation and a (negative) increase of δ starts to appears [see Fig. 7.11(a)].

Figures 7.11(a) and 7.12 summarize the results obtained in the temperature and maximum pulse current ranges used. One observes in Fig. 7.12(b) that the CIS coefficient is increasingly enhanced with both increasing current pulses and temperature. The CIS(T) behavior follows approximately the same trend when plotted for several I_{max} values [Fig. 7.12(b)]. Finally, V(I_{p}) characteristics below room temperature (not shown; $I_{\text{max}} = 80$ mA) all show a similarly anomalous behavior as that displayed in Fig 7.5. In particular, the temperature increase calculated from the V(I_{p}) curves is approximately equal for all temperatures ($\Delta T \approx 300$ K).

Electromigration energy barriers. Recall from chapter 6 that for electromigration to occur, the effective energy barrier modified by electromigration ($\Delta_0 - \xi I$) has to be comparable to the thermal energy. Thus, as T decreases, the critical switching current must increase according to:

$$I_c \approx \frac{\Delta_0}{\xi} - \frac{k_B T}{\xi}, \tag{7.6}$$

where all parameters were defined in chapter 6.3.2, page 149. Recall that ξ measures the total change of the activation energy due to the electromigration force. In fact, we observe experimentally that both I_{c}^{+} and $\mid I_{\text{c}}^{-} \mid$ (driving force for ionic electromigration) increase quasi-linearly with decreasing temperature (*e. g.* $I_{\text{c}}^{+} = 35$ mA and $I_{\text{c}}^{-} = -50$ mA at $T = 25$ K and

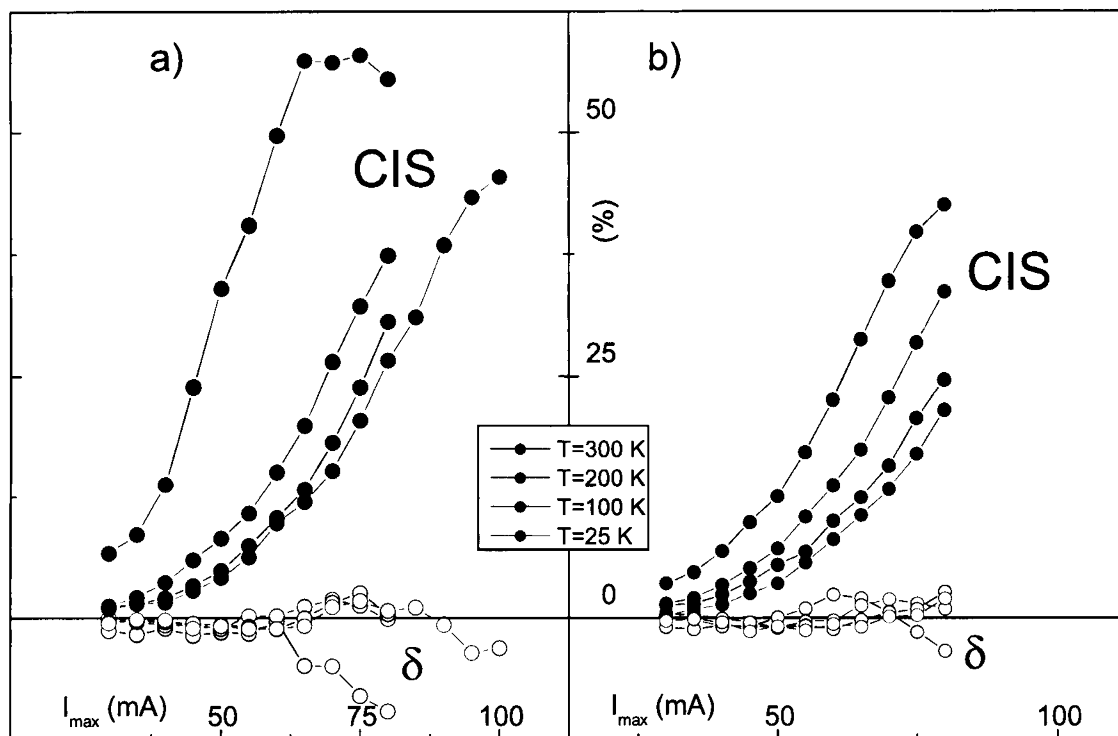

Figure 7.11: CIS coefficient as a function of I_{max} over the 300–25 K temperature range for two different samples of the same series (a) and (b).

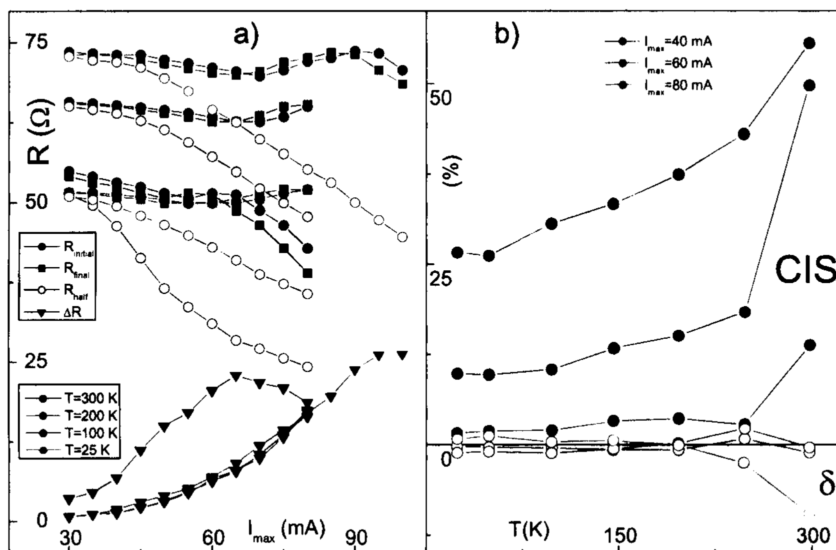

Figure 7.12: (a) $R_{initial}$, R_{half} and R_{final} as a function of I_{max} over the 300–25 K temperature range and (b) CIS coefficient as a function of temperature (300–25 K) for the 30–80 mA I_{max} range.

for $I_{\rm max} = 80$ mA), extrapolating to zero current at $T = 500$ K (I_c^+) and $T = 850$ K (I_c^-) for $I_{\rm max} = 80$ mA (not shown). Note that, as in the RT case, we again observe (at constant temperature) that I_c^- gradually increases with increasing $I_{\rm max}$, while I_c^+ remains fairly constant (see vertical lines in Fig. 7.10 and below). The fit of the $I_c^{\pm}(T; I_{\rm max} = 80 \text{ mA})$ data to Eq. (7.6) gives, $\Delta_0^+ \approx 0.042$ eV and $\xi^+ \approx 1.1$ eV/A (obtained from I_c^+) and $\Delta_0^- \approx 0.071$ eV and $\xi^- \approx 1.4$ eV/A (from I_c^-). Notice that the $I_c^+(T)$ dependence is the same for all $I_{\rm max}$ and equal to the $I_c^-(T)$ curve for low $I_{\rm max}$ (≈ 50 mA).

We should notice that, also in this case, the effective temperature inside the tunnel junction rises with the applied current, so that the Δ_0 value obtained should be taken only as a lower limit. However, such temperature increase does not affect the obtained value (from the fit) of the EM-parameter ξ, which should then be taken as a correct estimative. Furthermore, it is know that, when an atom in a nanobridge fluctuates between two metastable positions, the ξ-parameter is different for each of them [251, 267]. This effect is associated with the change of the effective EM-valence (direct+wind valences) with the atom-surrounding environment [251]. Thus, in our study, as ions migrate into the barrier, they experience a change in the lattice environment that in turn leads to the observed change in the ξ-parameter ($\xi^+ \neq \xi^-$).

We observe fairly different activation energies when migration occurs from the electrode into the barrier or from the barrier into the electrodes (for $I_{\rm max} = 80$ mA). This confirms our conclusions above that the force needed to return Ta ions from the barrier into the electrodes gets higher when $I_{\rm max}$ increases, *i. e.* Ta ions migrate further inside the barrier. This then leads to large differences in the atomic surroundings of the migrating ions and thus to different EM-parameters ($\Delta_0^{\pm}$ and $\xi^{\pm}$). On the other hand, for low $I_{\rm max}$ the driving force for electromigration into and out of the insulating barrier is approximately equal [$I_c^+(T) \approx |I_c^-(T)|$], *i.e.* the lattice sites where ions migrate (from and to) are energetically similar, and thus so is the temperature dependence of the critical switching current and the corresponding EM-parameters.

CIS($I_{\rm max}$) behavior. We turn now to the non-linear increase of the CIS coefficient with $I_{\rm max}$ (and $I_{\rm p}$) observed at all measured temperatures (see Fig. 7.11). Such enhancement of R-switching with applied current can be associated with two factors likely to occur: i) Atoms migrating under low currents are continuously pushed further into the barrier with increasing current and, ii) an increasing number of ions take part in the EM processes as $I_{\rm max}$ increases.

In fact, the initial decrease of R due to EM of ions near a nanoconstriction is expected to further lower the local barrier thickness and consequently increase the current density through such hotspots. This would lead to an increase of the force acting on both migrated and surrounding ions (increased ξI factor), and of the local temperature (increased $k_B T$ energy). Such enhancements would then lead to the participation of ions with higher EM-energy barriers in the EM process [see Eq. (7.6)], leading to the enhancement of the measured R-switching.

One also expects other TJ-regions to become active (in EM), with the increase of $I_{\rm max}$ and T, due to the likely existence of a distribution of EM-energy barriers. In fact, a broad distribution of such activation energies was observed in studies of electromigration in aluminium test lines [283]. Our present studies (see section 7.3.3) also show a wealth of energy barriers when performing R versus time measurements under large applied *continuous* electrical currents.

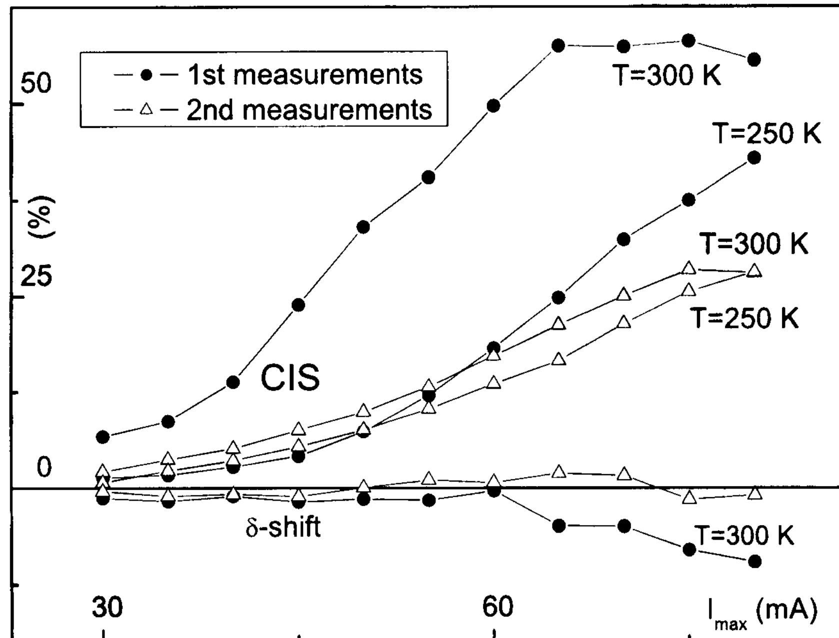

Figure 7.13: CIS coefficient and δ-shift as a function of $I_{\max}$ (first and second set of measurements) at $T = 300$ K and 250 K.

At the early stages of EM one observes a sharp resistance variation associated with the electromigration of a great number of ions. At later stages ($t \gtrsim 5$ min) we still observe a fairly large number of actively migrating ions displaying different EM-characteristics (R-variation amplitude and switching rates), likely associated with EM through different energy barriers.

Reproducibility of the CIS behavior. After such a long series of studies in the same TJ (54.9 Ω and $R \times A = 220\ \Omega\mu\text{m}^2$), we re-measured CIS cycles, at $T = 300$ K and 250 K, obtaining the results displayed in Fig. 7.13 (open triangles; compare with the initial measurements displayed in full circles). The corresponding CIS coefficients (open triangles) are considerably lower than the initial ones (solid circles). Also, the new δ-shift does not show the sharp negative increase above 60 mA, rather remaining fairly small, taking both positive and negative values. The CIS saturation at large $I_{\max}$ has been shifted to higher current values. Although the electrical resistance is now fairly smaller (due to the irreversible barrier degradation which occurred in previous measurements) the shapes of the re-measured CIS cycles are similar to the initial ones.

Finally, Fig. 7.11(b) displays the CIS($I_{\max}$) behavior obtained for a new sample ($R \approx 40\ \Omega$; $R \times A \approx 240\ \Omega\mu\text{m}^2$ at RT) of the same series, studied at several temperatures. A comparison of these results with those presented in Fig. 7.11(a) denotes a similar CIS($I_{\max}$) trend in both samples for all temperatures. We observe for this sample $CIS = 23\%$, which is lower than that of the previously presented one ($CIS = 49\%$; for $I_{\max} = 60$ mA and at RT). Furthermore, we do not observe any CIS saturation above a certain current value. Nevertheless, the CIS coefficient still decreases with decreasing temperature (for the same $I_{\max}$) and a non-linear

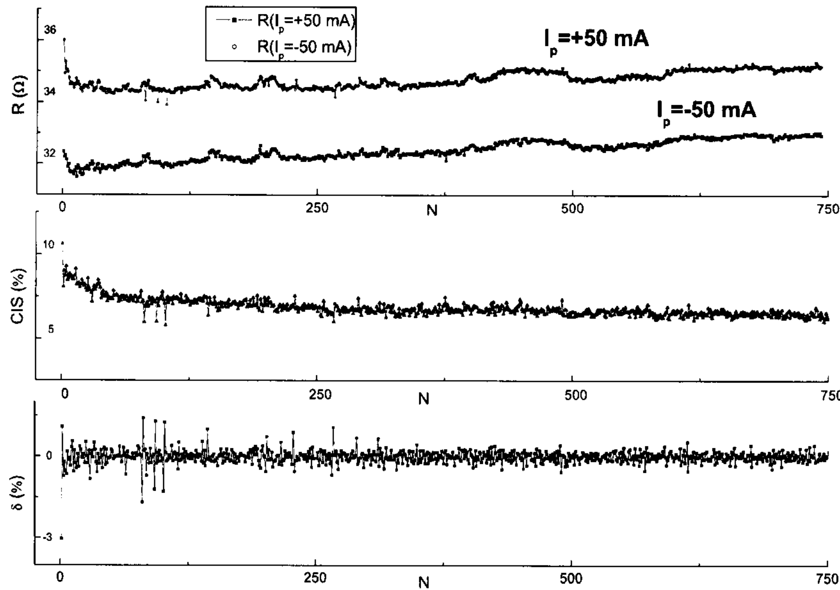

Figure 7.14: CIS coefficient as a function of the cycle number using $I_{\mathrm{p}} = \pm 50$ mA and room temperature measurements.

CIS(I_{max}) behavior is always observed.

7.2.3 Direct ($+I_{\mathrm{max}}$, $-I_{\mathrm{max}}$) Current Induced Switching

We also performed measurements applying only two current pulses (repeated about 800 cycles), but large enough to produce resistance switch ($I_{\mathrm{p}} = +50$ mA and -50 mA; Fig. 7.14; in the TJ with $R \approx 40\ \Omega$ and $R \times A \approx 240\ \Omega\mu\mathrm{m}^2$). As expected, one observes one low R-state after applying a positive +50 mA current pulse and a high R-state after applying a negative -50 mA current pulse. Both resistances start by declining sharply over the first set of measurements (36.0 Ω →34.5 Ω), but then a small gradual rise is observed (34.5 Ω →35.3 Ω). The CIS coefficient (Fig. 7.14, middle graph) also starts by declining, but stabilizes after about 250 cycles (9.2%→6.4%). In Fig. 7.14 (lower graph) we observe the δ-shift as a function of pulse number revealing a near zero δ-shift with an erratic fluctuating behavior. The δ-shift was defined in these measurements as the difference in resistances between consecutive +50 mA pulses, divided by their average value. The same overall features are seen when $I_p = \pm 65$ mA ($CIS = 18.5\%\rightarrow$ 13.8%; not shown) with a trend towards a constant CIS value. A near zero δ-shift (average $\overline{\delta} = -0.003\%$) is obtained, although the average δ-shift decreases with cycling ($\overline{\delta} = -0.006\%$ in the first 200 pulses and $\overline{\delta} = -0.002\%$ in the last 200 pulses). These data indicate that irreversible resistance switching is being progressively exhausted and that, after many CIS cycles with the same I_{max}, R-switching occurs mainly through reversible processes.

When ±80 mA pulses are applied (Fig. 7.15), one observes $CIS = 17.3\%$ ($R \sim 35\ \Omega$). However, when the number of pulses is just above 100, a small decrease in resistance is seen ($R \sim 30\ \Omega$). This is followed by a large irreversible R-decrease after a few more

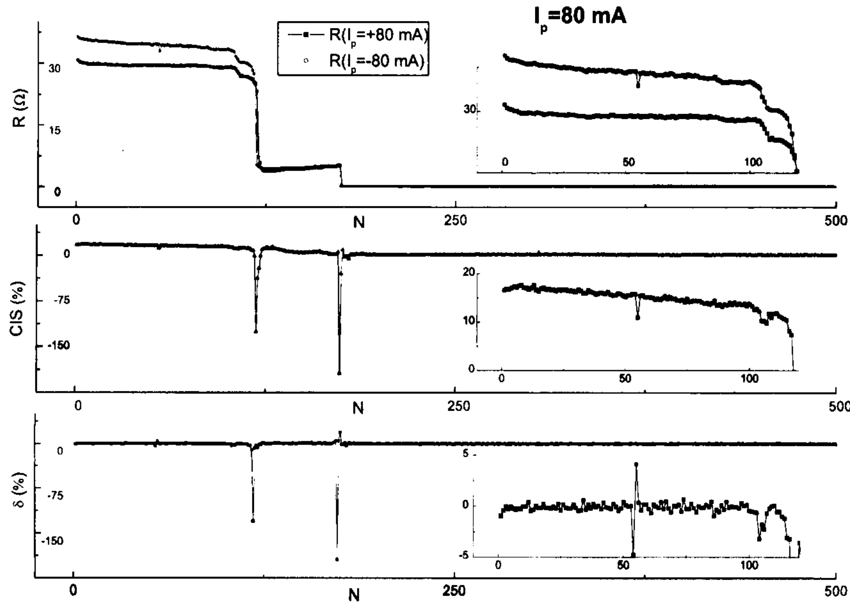

Figure 7.15: CIS coefficient as a function of the cycle number, for $I_\mathrm{p} = \pm 80$ mA at room temperature.

pulses ($R \sim 4.5\ \Omega$). Before N reaches 200, another (final) decline in the resistance is seen, practically bringing it to zero ($R \sim 0.1\ \Omega$). One notices that it is the *positive* +80 mA pulse (which usually *slightly* and *reversibly* decreases R) that always causes this dramatic change in conductance. Thus, the migration of ions from the electrode into the barrier (decreasing R) under high electrical currents can severely damage the structural integrity of the insulator. The CIS coefficient is also influenced by such R-degradation. Initially, it decreases from 17.3% to 13.7% (for $N \sim 100$). A slight change in CIS is observed after the second R decrease ($CIS \sim 10$ % for $N = 130$) but a rapid decrease ($CIS \sim 4$ % for $N > 140$) then occurs. When the resistance approaches zero, so does the CIS coefficient.

7.3 Tunnel junctions with non-magnetic *pinned* and *free* layers (series 835)

The CIS effect was also studied in MTJs with two thin (20 Å) non-magnetic Ta electrodes, above and below the insulating barrier (series 835). We observe that R-switching in CIS cycles occurs for the same current direction as in the previously studied AFM/FM/NM/I/FM tunnel junctions (section 7.2), and that no time dependent relaxation phenomenon occurs (Ta ions remain in deep energy minima inside the barrier). This enabled us to measure the temperature dependence of the electrical resistance of both the thin- and thick-barrier states (R_b and R_B). Experiments show a smaller $R(T)$ variation when the tunnel junction is in the R_b state. The temperature dependence of the CIS effect essentially corroborates the results in section 7.2. In particular we again find that the CIS coefficient increases as $I_{\max}$ and T increase. For this reason, we will only briefly describe those results. CIS cycles with increasingly higher

maximum current pulses produce increasing barrier degradation (resistance decrease). This enabled us to study how $R(T)$ behaves as a function of barrier degradation and its smooth passage from tunnel- to metallic-dominated transport. We also studied the time evolution of the electrical resistance under both low and high electrical currents, to probe the dynamics of our system as electromigration proceeds. At low temperatures and in the early stages of EM, we found a rapid quasi-continuous R-trend (decrease for positive currents and increase for negative currents). However, as time increases, this trend gradually disappears and the resistance varies by discontinuous steps, associated with different EM-processes. The increase of temperature leads to very complex $R(t)$ signals, with many active fluctuators.

7.3.1 Current Induced Switching

The electrical resistance of the studied sample of series 835 was 32.9 Ω at room temperature (and $R \times A = 197.4\ \Omega\mu\text{m}^2$). As in the previous series 834, we again observed that R rises with decreasing temperature, indicating tunnel-dominated transport (not shown). At $T = 20$ K, the electrical resistance was 61.6 Ω, indicating a 87.2% resistance increase above the room temperature value.

We then measured CIS cycles at $T = 300$ K, with increasingly higher maximum pulse currents I_{max}, ranging from 30 mA to 60 mA [Fig. 7.16(a)]. We again observe a CIS effect ($CIS = 6.5\%$ and negligible δ-shift for $I_{\text{max}} = 40$ mA). As also observed in series 834, increasing I_{max} results both in an increase of the CIS coefficient and of the δ-shift ($CIS = 12.2\%$ and $\delta = -4.1\%$ for $I_{\text{max}} = 60$ mA). The voltage across the junction was again measured while applying the current pulses, to obtain the I(V) characteristic. These I(V) curves are also anomalous, again due to heating effects in the TJ.

As we decrease the measuring temperature, the same general features described previously are observed: CIS cycles performed in the same I_{max} range displayed lower CIS coefficients and δ-shifts at smaller temperature [Fig. 7.16(b)]. For example, at $T = 25$ K we only obtained $CIS = 1.1\%$ and $\delta = -0.2\%$ for $I_{\text{max}} = 60$ mA. Furthermore, the critical switching current again increases quasi-linearly with decreasing temperature and a numerical fit to Eq. (7.6) gives $\Delta_0 \approx 0.050$ eV (corresponding to $T^* \approx 600$ K) and $\xi \approx 1.0$ eV/A. These values compare fairly well with those obtained for series 834 ($\Delta_0 \approx 0.042$ eV and $\xi \approx 1.1$ eV/A). The similitude of the Δ_0 and ξ parameters obtained in both 834 and 835 series (having a Ta layer deposited below the insulating barrier) shows that electromigration in these samples occurs through similar processes.

7.3.2 Influence of EM-induced barrier state on the R(T) behavior

7.3.2.1 R_B and R_b temperature dependence

Taking advantage of the fact that no relaxation phenomena occur in this series, we measured the temperature dependence of the electrical resistance of both *thick* (R_B) and *thin* (R_b) barrier states [Fig. 7.17(a)]. A new tunnel junction with $R \approx 43\ \Omega$ ($R \times A \approx 170\ \Omega\mu\text{m}^2$) was used in this study. A CIS coefficient of $\approx 25\%$ for $I_{\text{max}} = 50$ mA was obtained [Fig. 7.17(b)].

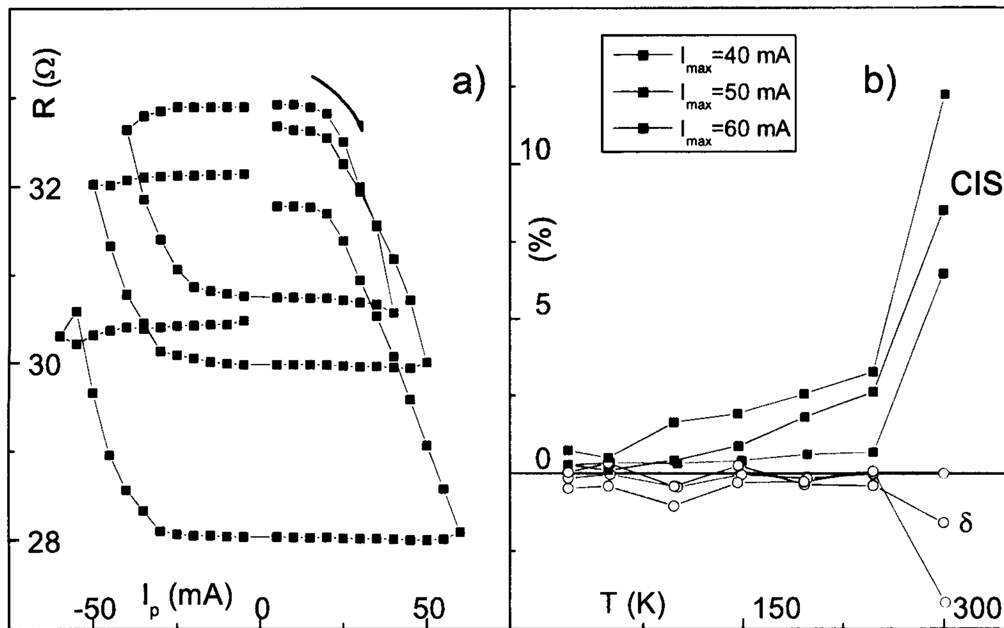

Figure 7.16: (a) Selected CIS cycles performed at RT. (b) CIS coefficient as a function of temperature for several selected I_{max}.

The electrical resistance of the R_B state increased with decreasing T from $R_B = 43\ \Omega$ at RT to 76 Ω at $T = 20$ K [Fig. 7.17(a)]. If we define the relative resistance change between RT and 20 K as:

$$\alpha = \frac{R_{300K} - R_{20K}}{R_{300K}}, \tag{7.7}$$

so that $\alpha < 0$ (> 0) indicates tunnel (metallic) dominated transport, we obtain for the thick barrier state, $\alpha_B = -78\%$.

On the other hand, after performing one half CIS cycle at RT [Fig. 7.17(b); open circles], the tunnel junction is left in its thin barrier state with $R_b \approx 32\ \Omega$. Our measurements of the temperature dependence of the electrical resistance of such thin barrier state reveal a smaller R-increase from RT down to 20 K than in the $R_B(T)$ case. In fact, $R_b \approx 53\ \Omega$ at $T = 20$ K which gives $\alpha_b = -66\%$. Thus, the electrical resistance of the thick barrier state increases more with decreasing temperature than in the thin barrier state ($\alpha_B < \alpha_b < 0$). We relate this observation to a larger tunnel contribution when the TJ is in the R_B state, as will be discussed below.

Fitting the $R_B(T)$ and $R_b(T)$ curves using phonon-assisted tunneling and two and three step hopping, revealed a decrease of both hopping contributions and a slight increase of the phonon-assisted tunneling term when the R-state changed from R_B to R_b. This is attributed to the decrease of the barrier thickness (which leads to a decrease of the hopping contribution) and to enhanced excitation of phonons at the electrodes/barrier interface by tunneling electrons.

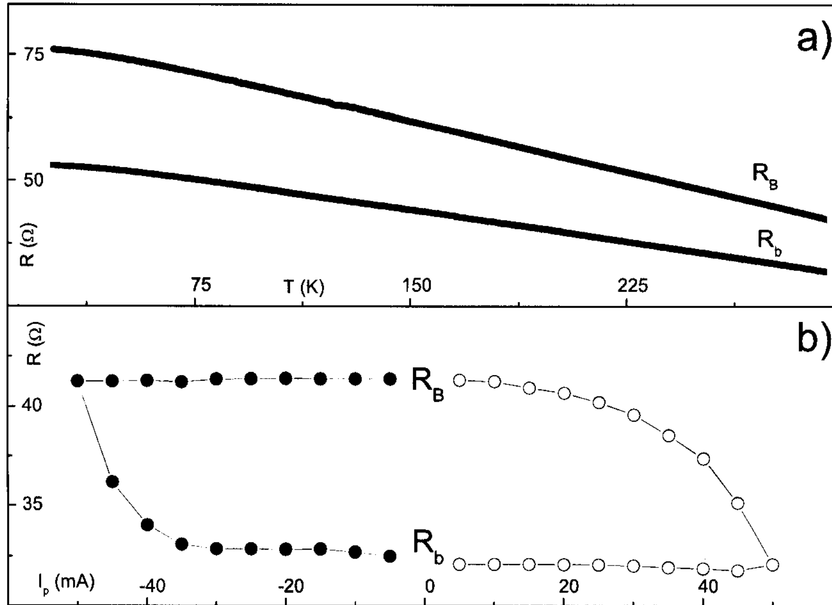

Figure 7.17: (a) Temperature dependence of the electrical resistance in the low (R_b; thin barrier) and high (R_B; thick barrier) CIS states. (b) Half CIS cycle performed with $I_{\max} = 50$ mA (open circles) that enabled us to change from the thick to the thin barrier state.

7.3.2.2 Evolution of R(T) with barrier degradation

We studied how the temperature dependence of the electrical resistance of a tunnel junction evolves with increasing barrier degradation. For this we performed CIS cycles with high $I_{\max}$ (in the 80–110 mA range) which usually lead to large negative δ-shifts ($R_{\text{final}} < R_{\text{initial}}$), indicating that the barrier is being progressively weakened. After each CIS cycle n, we measured R(T) in the 300–20 K range. We will show that the tunnel junction transport changes progressively from a tunnel- ($dR/dT < 0$) to a metallic-dominated ($dR/dT > 0$) behavior. Two tunnel junctions were used to perform this study: TJ1 with $R = 11.3\ \Omega$ ($R \times A = 67.8\ \Omega\mu\text{m}^2$) and TJ2 with $R = 21.6\ \Omega$ ($R \times A = 259.2\ \Omega\mu\text{m}^2$).

Both tunnel junctions initially ($n = 0$; before any CIS cycle was performed) displayed a tunnel-dominated R(T) behavior, with $\alpha = -20\%$ and -75% for samples TJ1 and TJ2 respectively. Subsequent CIS cycles performed with increasing maximum applied current pulses (if CIS cycles were performed with the same $I_{\max}$ they soon became almost completely reversible, with low δ-shifts) lead to the irreversible decrease of the TJs electrical resistance and to the steady increase of α in both samples [Fig. 7.18(a)]. Nevertheless, our R(T) measurements still showed tunnel-dominated transport ($\alpha < 0$) down to $R \times A \approx 20\ \Omega\mu\text{m}^2$. The last R(T) measurement with such tunnel dominated behavior displayed $\alpha = -3\%$ for TJ1 ($n = 6$; $R \approx 2.5\ \Omega$) and $\alpha = -15\%$ for TJ2 and $n = 10$ ($R \approx 5\ \Omega$). Finally, further EM-induced decrease of R leads to a metallic-dominated transport [$\alpha = 47\%$ for TJ1 ($n = 10$; $R = 0.65\ \Omega$) and $\alpha = 40\%$ for TJ2 and $n = 12$ ($R = 1.9\ \Omega$)].

We then normalized our R(T) data, according to $\frac{R - R_{300K}}{|R_{20K} - R_{300K}|}$. Figure 7.18(b) displays

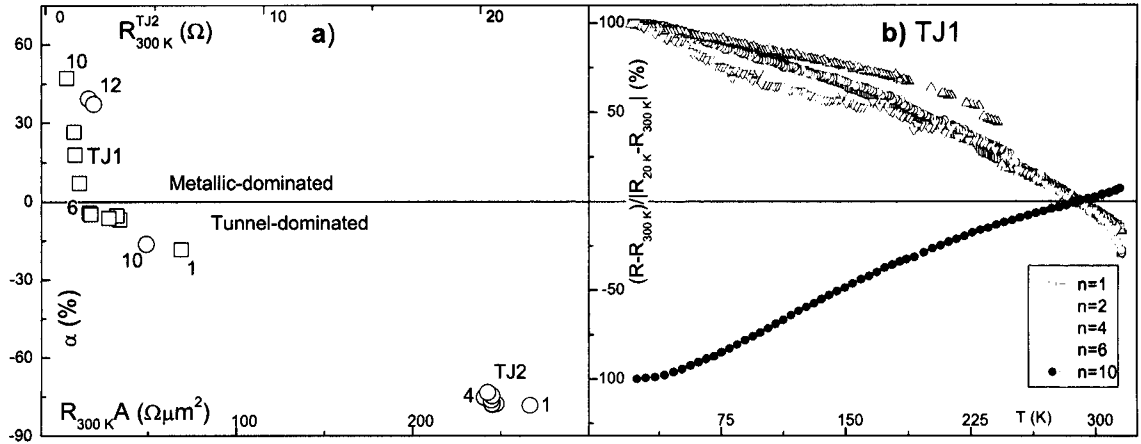

Figure 7.18: (a) The relative resistance change from 300 K to 20 K (α) as a function of the $R \times A$ product (lower scale; for TJ1 and TJ2) or R_{300K} (upper scale; TJ2 only) as changed by EM-induced barrier degradation (TJ1, open squares and TJ2, open circles). The numbers in the Figure are the number of CIS cycles measured up to the considered R(T) run. (b) Selected normalized R(T) curves in the 300–20 K range (TJ1).

selected curves for different stages of barrier degradation (sample TJ1), obtained after performing CIS cycle n (see legend). Although the shapes of the (tunnel dominated) curves are almost equal, some display increasing R-steps. On the other hand, the normalized metallic-dominated transport curves ($n > 6$) are all identical.

7.3.2.3 Discussion and conclusions

Electromigration-driven irreversible resistance decrease allowed us to progressively change the dominant transport mechanism of the studied junctions from tunnel to metallic. We will now show that such transition occurs due to the decrease of barrier thickness and to the formation and subsequent enlargement of pinholes.

Electrical transport will then have two contributions: Tunnel through the undamaged part of the barrier (with resistance R_t) and metallic transport through pinholes (resistance R_m). We write for the measured resistance (R):

$$\frac{1}{R} = \frac{1}{R_t} + \frac{1}{R_m}. \tag{7.8}$$

We can also estimate the evolution of the pinhole size with decreasing tunnel junction electrical resistance [Fig. 7.19(a)]. As stated in section 5.5.5, the Sharvin theory allows us to calculate the resistance of a nanoconstriction modeled as a circular aperture of radius a between two metallic layers of electrical resistivity ρ and electron mean free path ℓ [209]. We then have in the ballistic limit ($\ell >> a$):

$$R_{\text{Sharvin}} = \frac{4\rho\ell}{3\pi a^2}. \tag{7.9}$$

Notice that the Ta layers of the studied TJs have a high resistivity ($\rho \approx 150\ \mu\Omega$cm), so we do not expect the electron mean free path ℓ to be very large ($\ell \lesssim a$). We then write the electrical resistance of a constriction in the diffusive transport regime, known as the Maxwell resistance:

$$R_{\text{Maxwell}} = \frac{\rho}{2a}. \tag{7.10}$$

A good approximation for the actual resistance of the nanoconstriction of a sample with finite ℓ is simply [284]:

$$R_{\text{constriction}} = R_{\text{Maxwell}} + R_{\text{Sharvin}}. \tag{7.11}$$

To calculate the pinhole radius, let us assume that i) a pinhole is formed just after the first irreversible resistance decrease; ii) only one pinhole is formed and grows in the tunnel junction and, iii) the tunnel resistance remains constant throughout the CIS degrading stages (the only R-variation factor arises from the enhancement of the metallic contribution). R_t is thus simply the tunnel junction resistance measured before EM-induced barrier degradation (for TJ1, $R_t \approx 11\ \Omega$ and for TJ2, $R_t \approx 22\ \Omega$). This then allows us to estimate the metallic resistance [R_m; see Fig. 7.19(b)]. Identifying Eq. 7.11 as the metallic contribution (R_m) to the measured electrical resistance, and based on the above simplifications, we obtain for the pinhole radius:

$$a = \frac{3\pi\rho + \sqrt{3\pi\rho}\sqrt{64\ell R_m + 3\pi\rho}}{12\pi R_m}. \tag{7.12}$$

Using the values mentioned for our Ta layers ($\rho \approx 150\ \mu\Omega$cm, $\ell \approx 5$ Å), we can estimate the value and evolution of the pinhole radius [Fig. 7.19(a)].

Let us first consider the results obtained for TJ2: As expected, a increases with decreasing resistance from about 30 Å for $n = 4$ ($R_m = 250\ \Omega$), to 1500 Å for $n = 10$ ($R_m = 5\ \Omega$) and finally up to 4300 Å for $n = 12$ ($R_m = 1.7\ \Omega$). Notice however that this simple model does not describe our data in a fully satisfactory way. In particular the model underestimates the metallic resistance: For $n = 10$ (for which we still observe tunnel dominated transport; $\alpha < 0$) we obtain $R_m \approx 5\ \Omega$, which is already smaller than the (assumed constant) tunnel resistance, $R_t \approx 22\ \Omega$. Our model then predicts a metallic R(T) behavior for $n = 10$, which is in contradiction to our experimental data. Notice that the obtained R_m depends only on the R_t value used in Eq. (7.8).

We conclude that the initial EM-driven irreversible resistance decrease is not due to the formation of pinholes but to the progressive weakening of the tunnel barrier (decreasing barrier thickness) and that the minimum experimental R-value without pinholes ($R = R_t$) is considerably lower than the initial TJ resistance of 22 Ω. Using Eq. (7.8), we predict that, to ensure $R_t > R_m$ up to $n = 10$ we must have $R_t \approx 8\ \Omega$. Then, the initial 22 Ω → 8 Ω R-decrease corresponds only to a barrier thickness decrease (δt) without the formation of pinholes. We estimate $\delta t \approx 1.3$ Å [using Eq. (7.5), with $\varphi = 1$ eV].

Assuming then $R_t \approx 8\ \Omega$, we calculated the new pinhole radius using Eq. (7.12). For $n = 10$ we obtain $a = 900$ Å ($R_m = 8.3\ \Omega$) and for $n = 12$, $a = 3700$ Å ($R_m = 2.0\ \Omega$), which, nevertheless, is fairly close to the value obtained above considering $R_t \approx 22\ \Omega$. Still, the results presented here must be taken as qualitative only. In fact, $R_t \approx 8\ \Omega$ is not the only value that adequately adapts to the observed $\alpha(R)$ dependence and we estimate $3.5\ \Omega \lesssim R_t \lesssim 8\ \Omega$. For $R_t \approx 3.5\ \Omega$ one has pinhole appearance only for $n = 11$, already having $R_m < R_t$

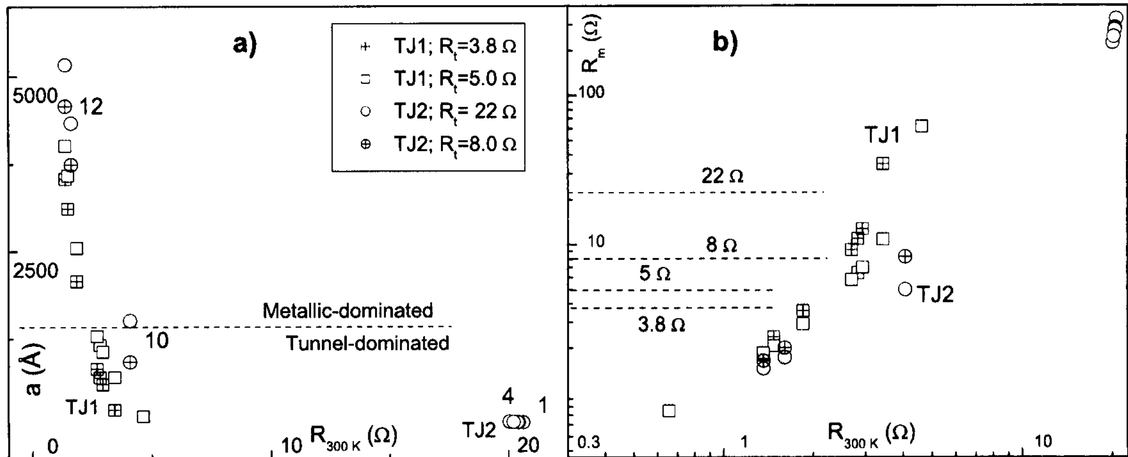

Figure 7.19: (a) Pinhole radius as a function of the tunnel junction electrical resistance [TJ1 using $R_t = 3.8\ \Omega$ (open squares) and $R_t = 5\ \Omega$ (squares with crosses) and TJ2 using $R_t = 22\ \Omega$ (open circles) and $R_t = 8\ \Omega$ (circles with crosses); see discussion for details]. (b) Corresponding metallic resistance R_m, as calculated from Eq. (7.8).

($a = 2500$ Å). In this case ($R_t \approx 3.5\ \Omega$), the formation of a pinhole immediately leads to metallic-dominated transport.

In the case of TJ1, we have more α-values near the tunnel/metallic transition. We can thus limit the R_t estimate to a narrower interval. First, notice that, as in the case of TJ2, if we use the initial TJ-resistance ($R_t \approx 11\ \Omega$) to calculate R_m, we again obtain $R_m < R_t$ for a R(T) data showing that transport is still dominated by tunneling ($\alpha < 0$). Thus, we again conclude on the initial progressive weakening of the tunnel barrier (decreasing barrier thickness) leading to the decrease of the tunnel junction electrical resistance. We predict [using Eq. (7.8)] that $3.8\ \Omega \lesssim R_t \lesssim 5\ \Omega$, which corresponds to a barrier thickness decrease of 1.1 Å$\lesssim \delta t \lesssim 1.3$ Å. Using the two mentioned limiting resistances, we observe that R_m decreases with decreasing TJ electrical resistance [Fig. 7.19(b)], denoting the increase of pinhole radius [Fig. 7.19(a)]. In the case of TJ1, we observe that pinholes are already formed ($a \approx 1000$ Å) while $\alpha < 0$ is still experimentally obtained (demonstrating tunnel dominated transport; $R_m > R_t$). Further current-induced decrease of the tunnel junction resistance is seen to be due to the growth of the pinhole size which enhances the metallic electrical conductance contribution, and ultimately leads to metallic-dominated transport ($\alpha > 0$).

In conclusion, we showed that the initial insulating barrier degradation arises from irreversible barrier thickness decrease ($\delta t \approx 1.3$ Å; no pinholes were present in the barrier in the as deposited state), without formation of pinholes. Such barrier weakening leads to higher α values. The same α-increase trend was observed in our $R_b(T)$ and $R_B(T)$ measurements ($\alpha_b > \alpha_B$), which suggests that irreversible and reversible switching arise from the same physical mechanism. Under adequate experimental conditions we might even reversibly switch between $\alpha_B < 0$ (tunnel-dominated transport) to $\alpha_b > 0$ (metallic-dominated transport), and vice-versa, by electromigration. Such phenomenon was in fact recently observed by Deac *et al.* [253] in ultra-thin TJs (barrier thickness $t = 5$ Å).

We further observed that increasing barrier degradation leads to the formation of metallic paths between the two electrodes that, however, *do not lead to a metallic dominated transport* for small enough pinhole radius. The increase of such radius leads to the decrease of the metallic (Sharvin+Maxwell) resistance and thus to the ultimate dominance of metallic over tunnel transport.

7.3.3 Probing individual EM-driven atomic motion events

7.3.3.1 Introduction

A general observation in nanobridges when their electrical resistance is measured versus time [R(t)], is the appearance of *two-level resistance fluctuations* (TLFs) [251, 267], originating from reversible motion of single atoms between two metastable states in the nanobridge region. Depending on the applied bias current and measuring temperature, a variety of phenomena can be observed, including the change of fluctuation rates and number of active fluctuators with applied current and temperature and interaction between different fluctuators (in which the reconfiguration of one affects the fluctuation rates or even the amplitude of another). For sufficiently high applied electrical current, a net resistance variation is observed due to atomic electromigration [251]. Subsequent decrease of the current to low bias reveals a variation of the previously observed (also under low current) TLF characteristics: EM leads to irreversible atomic reconfigurations. Nevertheless, the dynamical processes exhibited by the electrical resistance under large currents were never studied in great detail.

We now present a study on the time evolution of the electrical resistance of a tunnel junction (series 835), subjected to both low and high electrical currents (compared to the critical switching current I_c). Studies performed with a R-acquisition time of 10 ms allowed us to probe both two-level fluctuations and to follow the dynamics of our system as electromigration proceeds. We found a rapid quasi-continuous R-trend (decrease for positive and increase for negative currents) in the early stages of EM (just after $I > I_c$ was applied; $T = 25$ K). However, at later stages this trend gradually disappears, showing the decrease of the fluctuation rates and the appearance of resistance discontinuous steps that are within the bandwidth of our experimental setup. Such steps occur through different EM-paths, including sharp R-steps, switching preceded by fluctuations between two R-levels and dumped fluctuations (possibly associated with collective processes involving several atoms). With increasing temperature we observe more complex R(t) signals, with many active fluctuators. After long periods with the current applied (for $I > I_c$), no net resistance variation is observed, although many fluctuators remain active.

7.3.3.2 Experimental details

Changes in the atomic arrangement at the electrode/barrier interfaces in the measured tunnel junction were monitored by real-time data acquisition. In our setup, the sample is current-biased by a constant DC current source (Time Electronics 9818 with $\Delta I/I = 1/10^6$). The voltage drop across the sample is measured each 10 ms with a Keithley 182 nanovoltmeter. Data is stored in the buffer of the voltmeter, allowing the recording of 1024 points. Acquisition is then stopped (although the current is still applied) for the stored data to be retrieved by

a personal computer. Such data transference takes about 20 s, after which acquisition is resumed. This procedure is repeated for a given number of sets, allowing us to obtain the intended R(t) evolution.

Measurements were performed from room temperature down to 25 K and applied electrical currents ranged from 0.1 mA to 60 mA. This allowed us to span the current region where no net atomic flow occurs (no net resistance variation is observed below the critical switching current; low applied electrical current) to that where electromigration is visible (sharp variation of the electrical resistance). Data-acquisition starts about 1 s after the current is applied to the sample. All R(t) measurements under negative currents were performed after one half CIS cycle, so that the TJ is in the thin, low resistance state. The tunnel junction studied initially had $R = 20\ \Omega$ ($R \times A = 240\ \Omega\mu\text{m}^2$).

We define the maximum resistance variation within one complete measurement (constituted by n sets of 1024 data points) under the same applied current, R(t,I), as:

$$\frac{\delta R}{R} = \frac{R_{\text{max}} - R_{\text{min}}}{(R_{\text{max}} + R_{\text{min}})/2}, \tag{7.13}$$

where R_{max} (R_{min}) is the maximum (minimum) measured electrical resistance.

7.3.3.3 Experimental results

Low temperature. Figure 7.20 displays R(t) measurements performed at $T = 25$ K for selected applied electrical currents ($I = 10$, 40, 60, -10, -40 and -60 mA, corresponding to maximum resistance variations of $\delta R/R \approx 0.03\%$, 0.7%, 2.3%, 0.04%, 1.0% and 1.5%, respectively).

As expected, for $I < I_c$ (≈ 35 mA at $T = 25$ K), we observe a small resistance variation with no defined trend [Fig. 7.20(a); $I = 10$ mA; $\delta R/R \sim 0.03\%$]. When the applied current is just above the critical switching current [Fig. 7.20(b); $I = 40$ mA], a clear R-decrease is visible ($\delta R/R \approx 0.7\%$), associated with electromigration of ions from the bottom electrode into the barrier. Such R-decreasing trend is enhanced for higher applied currents [larger $\delta R/R$; Fig. 7.20(c) for $I = 60$ mA]. A similar behavior is observed for negative currents: For $|I| < I_c$, no R-switching is visible [Fig. 7.20(d); $I = -10$ mA], but for $I = -40$ mA and $I = -60$ mA [Figs. 7.20(e) and 7.20(f), respectively], the electrical resistance steadily increases with time. Previously displaced ions now return to the electrodes [recall that R(t) measurements under negative current were performed after one half CIS cycle, so that ions have migrated into the barrier].

For low bias current, TLFs are sometimes observed, but no net resistance variation occurs. Unfortunately, the R-fluctuation rates are at the edge of time resolution in our setup, so that a detailed analysis cannot be performed. Also, even at low temperature and bias, many fluctuators are seen at all times. In fact, fairly complex dynamic R(t) behaviors are observed [see inset of Fig. 7.20(b) for selected time frame of measurements with $I = 0.2$ mA], including multi-level R-fluctuations or the sudden appearance and disappearance of different fluctuators. For larger positive currents, true electromigration occurs and a net resistance decrease is observed. Although the R(t) dynamics is apparently still dominated by discrete R-fluctuations (see below), the motion of ions is now strongly biased by the applied positive

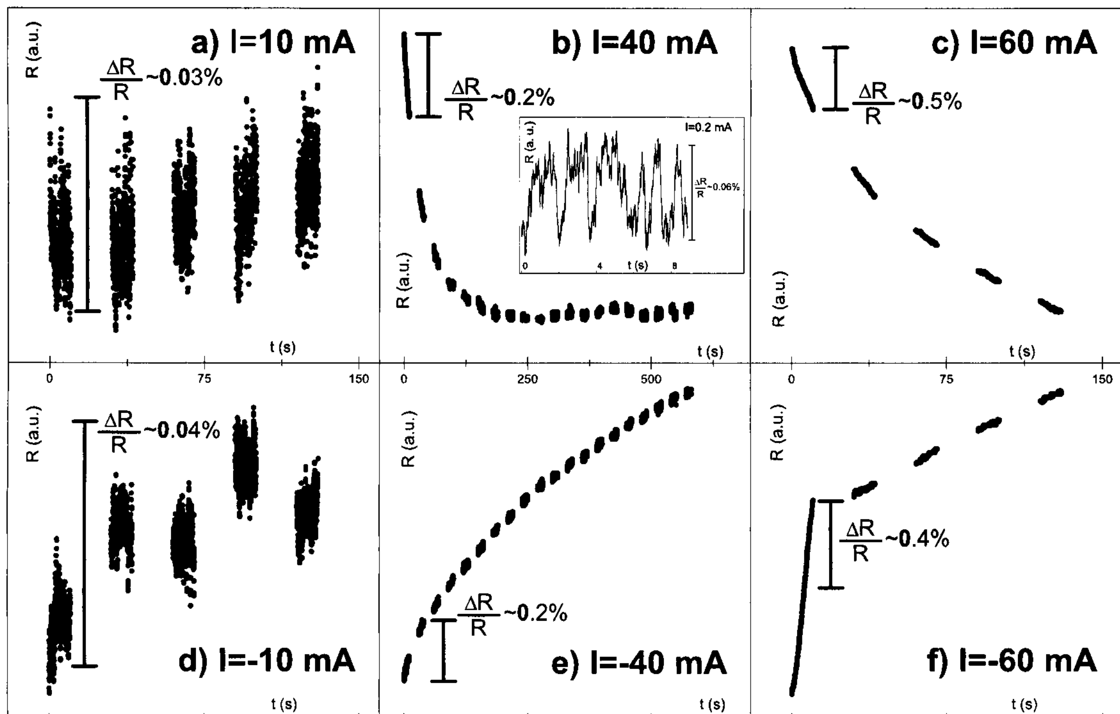

Figure 7.20: Time-evolution of the electrical resistance of the studied tunnel junction for $T = 25$ K and several applied electrical currents: (a) $I = 10$ mA, (b) $I = 40$ mA, (c) $I = 60$ mA, (d) $I = -10$ mA, (e) $I = -40$ mA and (f) $I = -60$ mA.

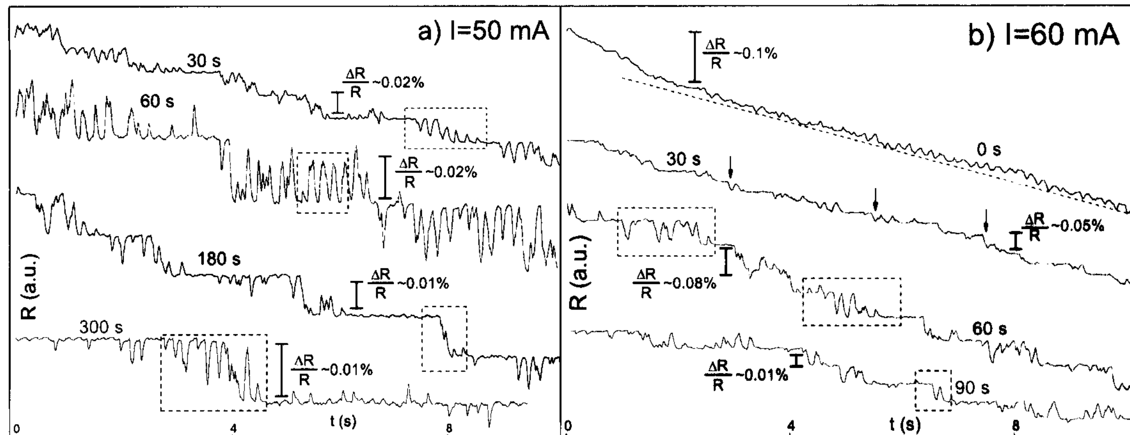

Figure 7.21: Selected sets of 10 s of the R(t) evolution for (a) $I = 50$ mA and (b) $I = 60$ mA, obtained at $T = 25$ K. The times in the figure correspond to the time approximately passed since the current was applied.

current, and an overall R-decrease is observed. Figure 7.21 displays representative sets of 1024 experimental R(t) data points obtained for $I = 50$ and 60 mA. In the case of $I = 60$ mA [Fig. 7.21(b)], we see a continuous R-decrease in the top curve (obtained just after the electrical current was applied), associated with the fast diffusion of a large number of ions, beyond the experimentally available bandwidth. If, however, one subtracts a linear average curve from the experimental data, we more clearly observe several small R-fluctuations of different amplitude and rate (not shown), although (as in the low-bias case) the corresponding rates are close to the time resolution of our setup.

With increasing time [second curve of Fig. 7.21(b), obtained 30 s after the current was applied], the overall switching rates clearly decrease and, what were mainly unobservable fast switching events, are now often within the bandwidth of our setup (see several R-decreasing steps in curve). Although we still observe an overall continuous decreasing trend, several discrete, discontinuous R-fluctuations, are now also observed and associated with individual EM-events. We conclude on the existence of at least two different EM-driven resistance decrease processes, one that leads to a fast and strong decrease of the electrical resistance and another characterized by lower switching rates which lead to an overall small R-decrease.

Measurements performed at later times (two bottom curves, obtained 60 and 90 s after the current was applied) allowed us to observe several terraces of constant resistance. We sometimes observe that the resistance evolves from one terrace to the next (with a lower resistance), fluctuating between them, before such fluctuations disappear and the resistance is left in the state favored by the applied electrical current (in the case of a positive current, that of lower resistance; see R-fluctuations in boxes and subsequent terraces). Furthermore, other R-switching processes are also observed, like sharp R-decreases without fluctuations between two R-levels.

The same general properties are observed under $I = 50$ mA [Fig. 7.21(a)]: With increasing time the overall net resistance variation decreases (less ions active in EM); several R-switching processes are visible (see boxes in 30, 60 and 300 s curves); two-level fluctuations

are occasionally observed but rapidly disappear (box in 60 s curve). Returning to how the resistance switches between terraces, Fig. 7.21(a) gives clear evidence on the existence of several different processes. In the upper curve (obtained 30 s after the current was applied; see box), we see that R switches between two different levels through what appears to be *dumped* fluctuations. This can result from a collective process where several atoms are migrating between metastable energy minima, although the applied current is biasing the whole system. Note that such collective motion of atoms has been observed experimentally [285] and predicted by computer simulations [286]. Other processes are visible: In the third curve (180 s; see box), we observe *e. g.* a sharp, single R-decrease; in the bottom curve (see box), we see a complex R-switching between two terraces, where several fluctuators are apparently active before the electrical resistance finally settles at a low level.

Two explanations can be given for the observed wealth of active fluctuators. First, interaction between migrating ions, for which the reconfiguration of one atom can induce the appearance or disappearance of other fluctuators, influencing both their switching rates and amplitude [251]. In fact, Ralls *et al.* [251] found complex R(t) signals above $T \approx 150$ K (the effect of increasing temperature was found to be quite similar to that of increasing the applied electrical current), associated with constantly changing rate, amplitude and number of active fluctuators, having strong interactions between them. Also, ions from (constantly changing in time) different regions of the electrode/barrier interfaces can be independently active in electromigration.

Room temperature. Figure 7.22 shows the time-evolution of the electrical resistance of the studied TJ at RT for different bias currents: A positive, low current ($I < I_c \approx 25$ mA at RT) that does not induce electromigration [$I = 10$ mA; Fig. 7.22(a)] and a positive, high current ($I > I_c$) that clearly results in a pronounced R-decrease [$I = 40$ mA; Fig. 7.22(b)], due to electromigration of ions from the electrodes into the barrier. For $I = 10$ mA, the electrical resistance remains fairly constant throughout all the measurement ($t \approx 7$ min) and the R-variation observed is small ($\delta R/R \approx 0.1\%$). On the other hand, for $I = 40$ mA, we clearly observe a R-decreasing trend ($\delta R/R \approx 1.5\%$) that is still visible even at the end of our measurement. For negative currents, we observe a fairly similar picture: For low applied electrical current ($I = -10$ mA) R remains fairly constant ($\delta R/R \approx 0.2\%$); for $I = -40$ mA, we observe a R-increase ($\delta R/R \approx 4.2\%$) associated with electromigration of ions from the barrier back into the electrodes.

If one again studies the individual R(t) curves more closely, we see that for small current bias, we have no time resolution to observe TLFs. This is expected because the fluctuating rates and number of fluctuators increase strongly with temperature. In fact, we expect that the temperature increase leads to complex noise signals, that we believe are still composed of discrete resistance fluctuations, but with rapid switching times, outside our experimental bandwidth. Figure 7.23(a) clearly shows for the top curve (obtained just after the 40 mA electrical current was applied) mainly a continuous R-decreasing trend, but not the corresponding individual R(t)-discontinuous fluctuations, denoting that the 10 ms acquisition time is not low enough for its observation.

As time increases, we observe smaller overall resistance variations, but a fairly complex R(t) behavior is still visible, like multi-level resistance fluctuations [box in Fig. 7.23(a)]; the sudden appearance of new fluctuators; or discrete, irreversible (within the time frame of our

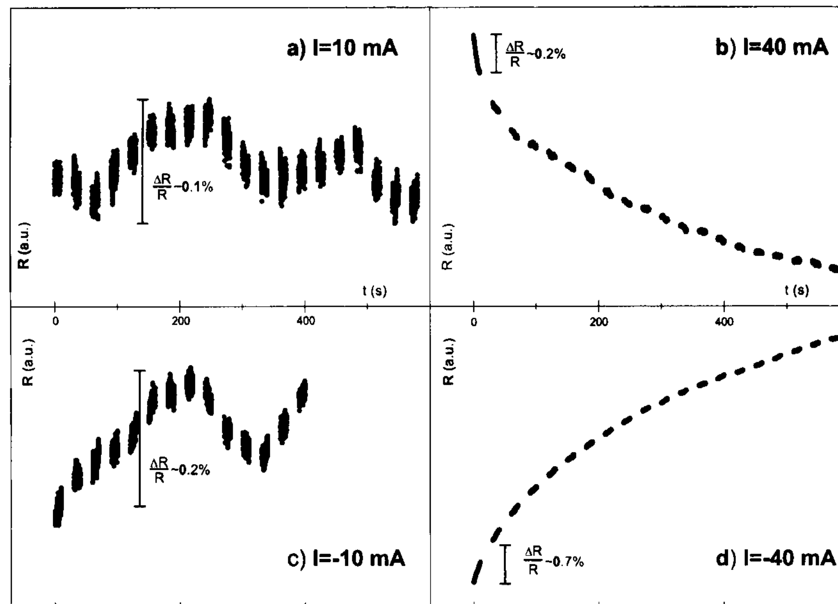

Figure 7.22: Time-evolution of the electrical resistance of the studied TJ for several applied electrical currents: (a) $I = 10$ mA, (b) $I = 40$ mA, (c) $I = -10$ mA and (d) $I = -40$ mA.

measurements) R-decreases (see arrows). After even longer times we can see more clearly the R-fluctuations [Fig. 7.23(b); curves obtained for $t > 200$ s]. Although many R-fluctuations are still visible, the net resistance decrease is now fairly small (sharp R-switches; see arrows). Furthermore, we observe in the bottom curve no net resistance variation, although a complex R(t) signal is seen, with at least six different fluctuating levels. Thus, even after applying an electrical current for such a long time, many atoms are still actively contributing to R-fluctuations (due to the thermal energy), although leading to no net resistance variation. This contrasts with the results at $T = 25$ K, where we observed terraces of fairly constant resistance. We also notice that the ions involved in electromigration at the earlier stages are likely those that we observe to fluctuate at low bias currents, having lower EM-energy barriers. The presence of still many active fluctuators at the last stages of EM indicate the existence of a distribution of energy barriers for electromigration.

For the $I = -40$ mA case (Fig. 7.24), we again observe that the first set of measurements (top curve; corresponding to the first 10 s after the current was applied) reveals only a quasi-continuous R-increase, associated with the return of ions from the barrier into the electrode. The two middle curves, corresponding to 60 and 120 s after the current was applied, still show the same quasi-continuous R-increase, although we observe some discontinuous R-steps (see arrows). This again confirms that two EM-processes are contributing to the observed phenomena: Fast R-increasing EM-events that are outside our acquisition bandwidth, and other, slower events, that distinguish themselves as R-increasing steps in our curves. After large periods (bottom curve) the fast R-increasing trend disappears and R-fluctuations are the main cause for the observed resistance variation.

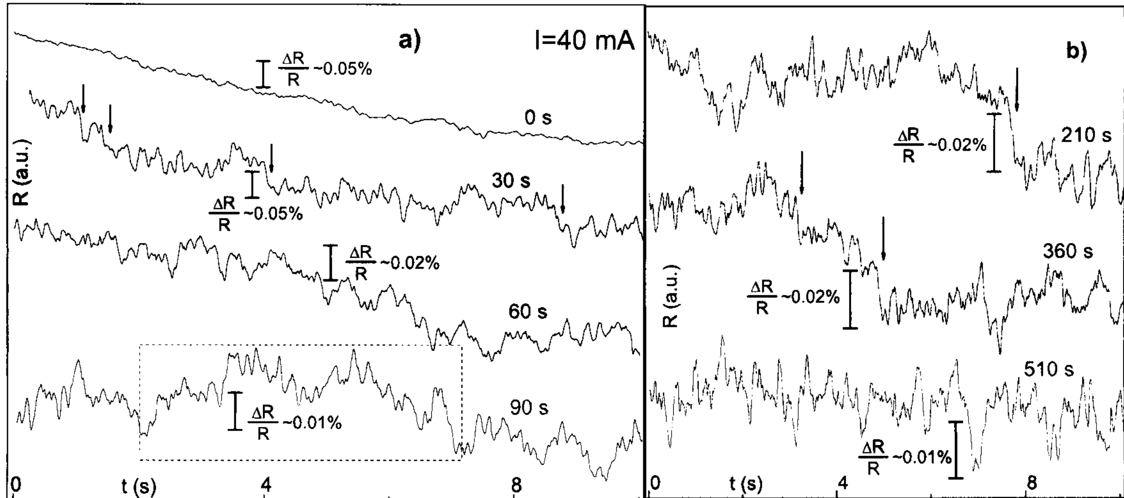

Figure 7.23: Time-evolution of the electrical resistance of the studied tunnel junction for $I = 40$ mA for several periods of 1024 data points acquired every 10 ms; (a) In the beginning of the data acquisition and (b) at the end.

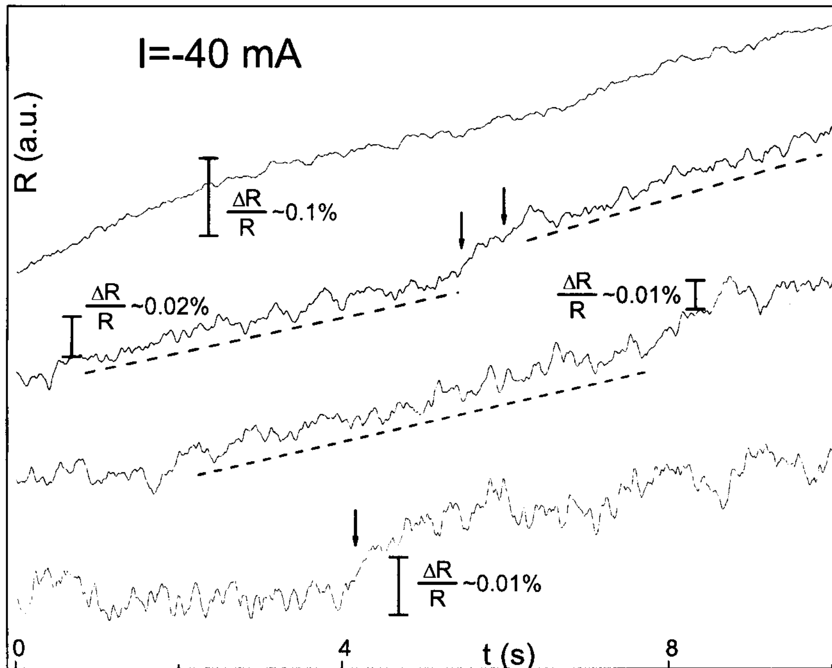

Figure 7.24: Time-evolution of the electrical resistance of the studied tunnel junction for $I = -40$ mA for several periods of 1024 data points acquired every 10 ms; the top three in the beginning of the data acquisition and the bottom one at the end.

7.4 Tunnel junctions with non-magnetic free layer (series T1)

We now briefly present our studies on the current-induced switching effect in tunnel junctions having a ferromagnetic pinned layer and a non-magnetic free layer (FM/I/NM; series T1), with the structure MnIr (80 Å)/CoFe (30 Å)/AlO_x (7.0 Å)/Ta (100 Å). We observed a CIS effect of ≈ 0.4% *at room temperature. In this case (as in FM/I/FM tunnel junctions), resistance switching occurs for negative* $I_{\rm p}$ *(R-recovery for positive applied current pulses). We again associate this effect with EM of CoFe ions from the bottom electrode into the barrier. Also, we observe that the CIS effect depends on* $I_{\rm max}$ *and large applied electrical currents lead to visible R-lowering. Electrical resistance measurements as a function of time were also performed and, after half a CIS cycle, R(t) follows a typical relaxation behavior with a single relaxation time of approximately 4.5 min. We measured the temperature dependence of the electrical resistance and current-induced switching in the 300 - 25 K temperature range. We observed that R slightly increases with decreasing temperature, while the CIS coefficient, for the same* $I_{\rm max}$, *decreases with decreasing temperature.*

7.4.1 Electrical resistance

We measured the temperature dependence of electrical resistance in the 300–25 K temperature range (not shown). We observed a small R-increase in the studied temperature range of approximately 6% [3.65 Ω at RT ($R \times A = 14.6\ \Omega\mu{\rm m}^2$) and 3.88 Ω at 30 K]. Such marginal tunnel behavior indicates close proximity to the barrier-continuity limit, so that several competing transport mechanisms may be simultaneously operative, although tunnel is the dominant one.

7.4.2 Current Induced Switching

Figure 7.25 shows CIS($I_{\rm p}$) cycles obtained at selected temperatures for a FM/I/NM sample of series T1. A 0.4% CIS signal was observed at 300 K [for $I_{\rm max} = 39$ mA; Fig. 7.25(a)]. Under increasingly negative current pulses the junction resistance remains constant until $I_p \approx -21$ mA ($\equiv I_c^-$), where a rapid decrease in R starts to occur, down to $-I_{\rm max} = -39$ mA. This indicates enhanced junction conductivity after negative current pulses of increasing intensity are applied. As discussed throughout chapters 6 and 7, this results from enhanced current paths, due to electromigration of metallic atoms into the insulating barrier so as to slightly reduce the effective thickness of the TJ. Notice that the observed resistance decrease occurs only for negative $I_{\rm p}$, as in FM/I/FM tunnel junctions. On the other hand, in FM/NM/I/FM and FM/NM/I/NM/FM tunnel junctions, R-decrease was observed for positive current pulses. Thus, we associate R-switching with EM of CoFe ions from the bottom electrode into the barrier. The critical switching current and critical electric field can be estimated as $j_c \approx 1.0 \times 10^6$ A/cm^2 and $E_c \approx 1.0$ MV/cm, respectively.

If one then increases the negative current pulses from $-I_{\rm max}$, we observe a significant R-increase, although R remains below its initial value. For $I_p \gtrsim +21$ mA ($\equiv I_c^+$), switching occurs to a high R-state, and at the end of the CIS cycle one has $R_{\rm final} \approx R_{\rm initial}$. Previously displaced metallic atoms have returned to their positions in the electrode.

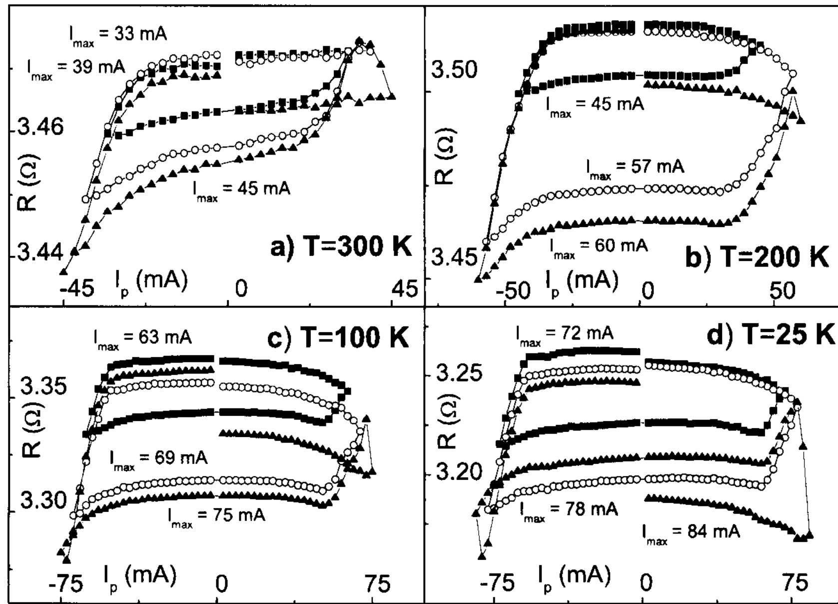

Figure 7.25: Selected Current Induced Switching cycles obtained in a sample of series T1, at representative temperatures.

Notice that the CIS cycle performed at RT with $I_{\max} = 45$ mA [Fig. 7.25(a)] shows a R-maximum at $I_p \approx 36$ mA (for which one has the initial R-value). This indicates that the migration of ions under negative current pulses was completely reversed for positive $I_{\rm p}$. However, further increasing pulse intensity produces a R-decrease, and a non-negligible δ-shift is observed ($\delta = -0.2\%$). Also, no significant changes in either I_c^- or I_c^+ were observed as $I_{\max}$ was increased. This behavior in FM/I/NM tunnel junctions was also observed in FM/I/FM tunnel junctions. Such behavior contrasts with that observed in FM/NM/I/FM and FM/NM/I/NM/FM TJs, where $I_{\rm c}^-$ increased with $I_{\max}$. We relate the observed $I_c^- \approx I_c^+$ to the existence of relaxation phenomena in FM/I/FM and FM/I/NM tunnel junctions (see below): Because ions gradually return to the electrode as soon as the negative current starts to be decreased, changes in the atomic surroundings are small and thus $I_c^+ \approx |I_c^-|$ for all $I_{\max}$.

CIS cycles measured at lower temperatures [Fig. 7.25(b) – (d)] show essentially the same features. In particular, the R-increase observed after switching to the low R-state is still visible, although its amplitude is smaller than at RT. We also observe that, for the same $I_{\max}$, the CIS coefficient is smaller than at RT. Furthermore, as expected, the critical switching current I_c increases with decreasing temperature (*e. g.* $I_c \approx 60$ mA at $T = 25$ K.).

As observed in all the other series, the CIS coefficient increases with increasing $I_{\max}$ (Fig. 7.26), but a trend towards saturation is visible for large $I_{\max}$. Furthermore, increasing the maximum current pulse used also leads to the (negative) increase of the δ-shift. In fact, δ is almost zero for low $I_{\max}$, decreasing sharply above a given current (Fig. 7.26). The critical switching current was seen to increases quasi-linearly with decreasing temperature, extrapolating to zero at $T^* \approx 425$ K. Fitting the data to Eq. (7.6), we obtained $\Delta_0 \approx 0.036$ eV and $\xi \approx 0.5$ eV/A.

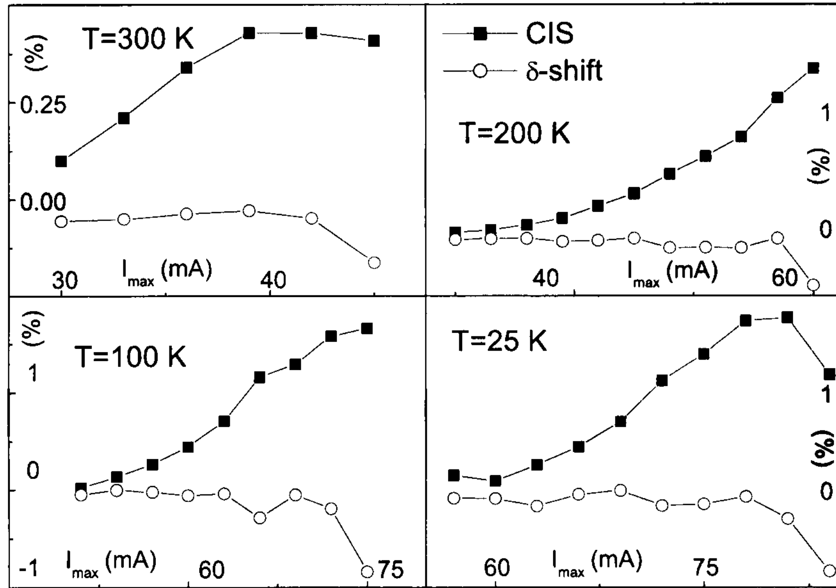

Figure 7.26: CIS coefficient and resistance shift δ as a function of I_{max} at selected temperatures for a sample of series T1.

7.4.3 Time dependent effects

As in the fully magnetic tunnel junctions studied in chapter 6, TJs of series T1 also presented time dependent resistance variations under a low bias current. To investigate such effects we performed several consecutive CIS cycles at RT ($I_{\text{max}} = 42$ mA; Fig. 7.27). The last one (red circles) was stopped after only one half cycle ($0 \rightarrow -42$ mA $\rightarrow 0$) and we then monitored the electrical resistance of the TJ over a period of time of about one hour (under a low bias current $I = 1$ mA). As shown in the inset of Fig. 7.27, a typical relaxation behavior with a single time constant is observed:

$$R(t) = R(\infty) + \Delta R e^{-t/\tau}, \tag{7.14}$$

where $R(\infty)$ (ΔR) is the asymptotic resistance (resistance change) and τ is the relaxation time. The corresponding rise in R is displayed by the vertical bar in Fig. 7.27, at $I = 1$ mA. We obtained $\tau \approx 4.5$ min and the fitted ΔR value indicate that about 80% of the *initial* resistance (that of the first cycle; black triangles) is recovered by this relaxation phenomenon. In fact, after the R(t) measurements the electrical resistance had a higher value than at the beginning of the corresponding CIS cycle. Thus, some of the barrier degradation produced at high negative current pulses (as seen by the R-decrease from cycle to cycle) is healed if one allows sufficient time for the system to relax to its stable configuration.

One can also observe these relaxation processes in the CIS cycles presented above [notice the significant rise in resistance ΔR_p observed just after the current pulses are decreased from $-I_{\text{max}}$, and the positive (dR/dI_p) slope at the low R-state near $I_p = 0$; see Fig. 7.25]. As in the MTJs case, CoFe ions that have migrated into the barrier under negative current pulses return to the electrode surmounting two energy barriers (Δ_1, Δ_2). In fact, both ΔR_p and (dR/dI_p) follow an exponential temperature dependence ($e^{-\Delta/k_B T}$; not shown) with

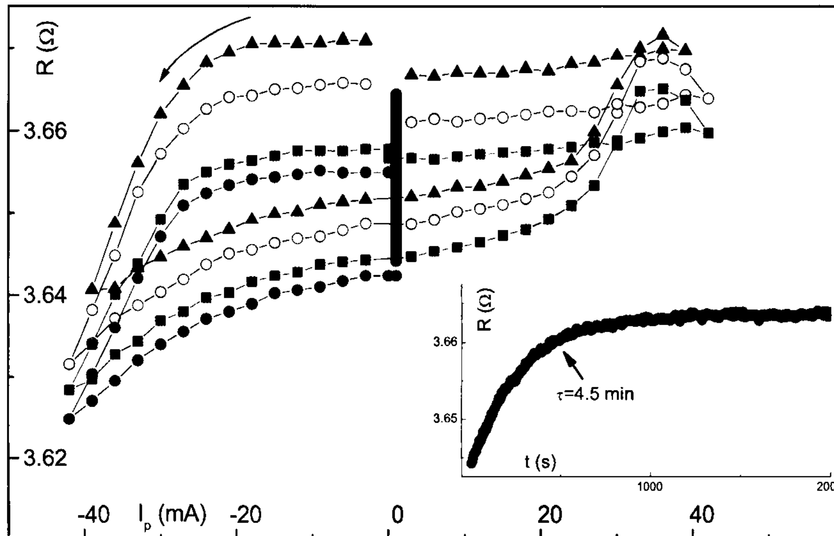

Figure 7.27: CIS cycles performed at room temperature and relaxation phenomena (inset).

$\Delta_1 \approx 0.11$ eV (when the electrical current is slightly decreased, some CoFe ions present in the barrier easily return to the electrode, through a low energy barrier) and $\Delta_2 \approx 0.25$ eV (a slightly higher energy barrier is responsible for the observed low R-state), respectively. (Recall the discussion in section 6.5, page 162, regarding a comparison of Δ_0 with Δ_1 and Δ_2.)

7.4.4 Discussion

As stated above, we associate the observed R-switching to migration of CoFe ions from the bottom electrode into the barrier (decreasing R) and their return to the FM layer (increasing R). The current direction for which resistance decreases is the same as that observed in FM/I/FM tunnel junctions. Thus, we again attribute the Current Induced Switching effect to EM of CoFe ions from the bottom electrode. Confirming the CIS effect similarities in both FM/I/FM and FM/I/NM tunnel junctions, we note that only in these two series were relaxation phenomena observed. [Compare Figs. 6.2 and 6.6 with Figs. 7.25(a) and 7.27 (pages 139, 145, 198 and 200, respectively)]. Thus, CoFe ions always relax back to the electrodes after migrating into the barrier under negative applied currents, as inferred from the lower Δ_0 ($\approx k_B T^*$) value given by the fit of the $I_c(T)$ data in this type of TJs, when compared to FM/NM/I/FM and FM/NM/I/NM/FM tunnel junctions. (Remember, however, that the obtained Δ_0 values are in fact their lower limits, since heating occurs in the studied samples, making a comparison between different series of TJs rather difficult.)

We can now compare the main results concerning the CIS effect in magnetic (chapter 6) and non-magnetic (series T1) tunnel junctions. Table 7.3 summarizes such comparison. First notice the smaller CIS coefficient observed for the non-magnetic tunnel junctions ($CIS = 0.4\%$ versus $CIS = 2.8\%$ for $I_{\max} \approx 35$ mA). However, the critical switching current, critical switching current density and critical switching electrical field are similar in both series,

	CIS (%)	j_c (MA/cm^2)	E_c (MV/cm)	$\Delta_0 \approx k_B T^*$ (eV)	τ (min)	Δ_1 (eV)	Δ_2 (eV)	ξ (eV/A)
MTJ	2.8	1.2	1.5	0.04	174	0.13	0.85	0.4
nMTJ	0.4	1.0	1.0	0.04	4.5	0.11	0.25	0.5

Table 7.3: Comparison of relevant CIS-parameters obtained for FM/I/FM (chapter 6) and FM/I/NM (series T1) tunnel junctions.

indicating that the forces needed to induce electromigration of CoFe ions are the same in the two series. Furthermore, the temperature dependence of I_c is also quite similar and, in particular, extrapolates to zero current at the same temperature ($\approx$ 425 K). Thus, the EM-energy barriers observed in these two series are also much the same ($\Delta_0 \approx 36$ meV). However the resistance relaxation seen in these series shows quite different behaviors, particularly concerning the relaxation times ($\tau \approx 174$ min and ≈ 4.5 min for the magnetic and non-magnetic tunnel junctions respectively) and the EM-energy barriers calculated from the dR/dI_p slopes ($\Delta_2 \approx 0.85$ eV and $\Delta_2 \approx 0.25$ eV). Similar differences in the relaxation phenomena were also observed within magnetic tunnel junctions of the same series (chapter 6) and should be related to structural differences in the measured tunnel junctions. However, further studies are still required to better understand these results.

7.5 Conclusions

We presented a detailed study on the Current Induced Switching effect in three different series of tunnel junctions with a Ta non-magnetic (NM) layer deposited i) just below, ii) just above and iii) just below and above the insulating barrier.

In CoFe/Ta/AlO$_x$/CoFe low resistance (7 Å barrier) tunnel junctions we observed that the CIS coefficient increases with increasing maximum applied current pulses, reaching ~60% for $I_{\max} = 80$ mA. Such effect is controlled by nanostructural rearrangements at the electrodes/barrier interfaces, due to ion electromigration (reversible and irreversible). When high currents are applied, one observes large irreversible resistance decreases. The V(I_p) characteristics showed an anomalous behavior near $\pm I_{\max}$ due to heating effects inside the tunnel junction. The analysis of these effects shows that nanoconstrictions indeed concentrate most of the tunneling current through the barrier, forming local hot-spots. One further demonstrates that the R-switching direction is related to a competition between dominant electromigration contributions (direct/wind forces): The direct (wind) force dominates electromigration in Ta (CoFe) layers.

Our studies on CoFe/AlO$_x$/Ta (CoFe/Ta/AlO$_x$/Ta/CoFe) showed the opposite (same) R-switching direction when compared to that of CoFe/Ta/AlO$_x$/CoFe. Furthermore, tunnel junctions without a Ta layer deposited *below* the insulating barrier always showed R-relaxation phenomenon. Thus, the diffusion of CoFe ions into the barrier always lead to return of such ions to their initial positions in the electrodes. On the other hand, Ta ions remain inside the barrier in both the thin- and thick-barrier R-states.

Our measurements of R_b(T) and R_B(T) in FM/NM/I/NM/FM tunnel junctions showed a

smaller increase of the electrical resistance of the thin barrier state state when the temperature decreased from 300 to 25 K. We related this fact to a smaller tunnel-contribution for the overall conductance. In fact, with increasing barrier degradation we smoothly changed the R(T) behavior from tunnel- to metallic-dominated, due to the formation and increase of pinhole sizes. We also studied the R(t) behavior when electromigration occurs in a tunnel junction. At $T = 25$ K and at the earlier stages of EM we observed a rapid quasi-continuous R-trend that gradually disappears. We then observe discontinuous R-steps denoting different EM-processes. For high temperatures we observe an increase in the number of fluctuators and complex R(t) signals.

Chapter 8

Underoxidized Magnetic Tunnel Junctions

Summary

Magnetic tunnel junctions (MTJ) consisting of two ferromagnetic (pinned and free) layers separated by an insulating barrier are strong candidates for magnetoresistive sensors in high-density storage devices [287]. Requirements for actual MTJ-sensors implementation [288] include low resistance-area product (R×A<1 $\Omega\mu m^2$) and reasonable tunnel magnetoresistance (TMR>20%). Such goals are being intensively pursuit, usually by decreasing the thickness of the insulating barrier well below 10 Å (ultrathin barriers; ~5–6 Å). However, this can also lead to the formation of pinholes (regions of direct contact between the two FM electrodes) and to the undesirable enhancement of the corresponding coupling field.

A different approach recently showed that similar TJ-characteristics (high TMR, low R×A) can be obtained by only partially oxidizing thicker (9 Å) AlO_x-barriers [289], *i. e.*, by decreasing the oxidation time (see Fig. 8.1; taken from Ref. [289]). Fairly high TMR ($\sim$ 20%; $R \times A \sim$ 2–5 $\Omega\mu m^2$) are still observed even when the oxidation process is performed with the shutter closed. Furthermore, a small number of MTJs showed very low $R \times A$ values ($\sim 0.5\ \Omega\mu m^2$) while preserving similar tunnel magnetoresistance ratios.

Here we study the magneto-transport of such low-resistance, underoxidized MTJs. Under a low bias current, the electrical resistance in both parallel (R_P) and antiparallel (R_{AP}) states presents jumps between two closely separated ($\delta R/R \sim 0.6\%$) stable levels. These jumps are about 10 times more frequent for the antiparallel alignment of the ferromagnetic (FM) layers. This effect is here associated with spin-dependent electron tunneling through localized defects in the insulating barrier [290, 291, 292]. In fact, we observe a clear dependence of the fluctuation amplitude and rate on the degree of oxidation, and thus on the number of defects on the barrier. For a low oxidation time (high transparency barrier) we see no fluctuations; however, a slight increase of the oxidation time leads to the appearance and subsequent enhancement of such fluctuations; ultimately they gradually disappear with further enhancement of the oxidation time.

We also studied dielectric breakdown (DB) in these underoxidized $CoFeB/AlO_x/CoFeB$

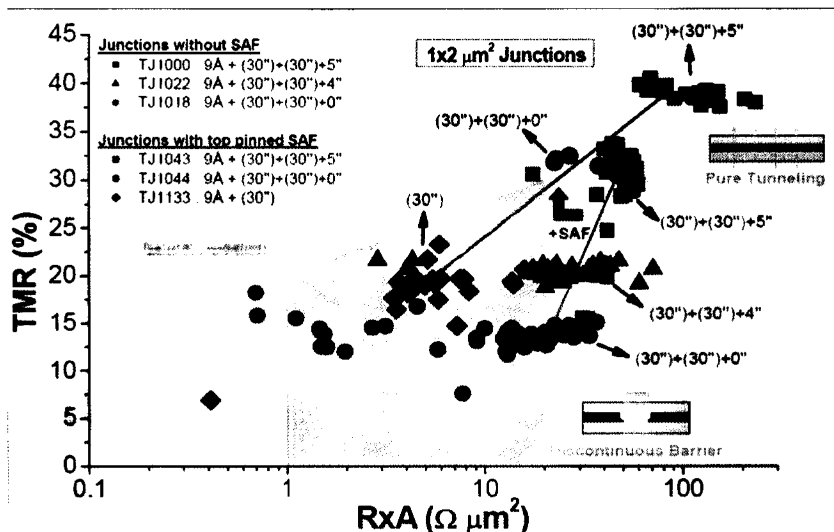

Figure 8.1: Tunnel magnetoresistance versus $R \times A$ for magnetic tunnel junctions with different oxidation times.

MTJs. We will show that breakdown occurs at localized spots of the barrier, likely where a large concentration of defects (oxygen vacancies due to the underoxidation of the barrier) exists. Furthermore, a relation between TJ-area and breakdown mechanism is seen for the MTJs with the largest studied oxidation time: While failure in junctions with large areas ($A \sim 10$ μm^2) is usually of an extrinsic nature (smooth R-decrease at DB), MTJs with small areas ($A \sim 1$ μm^2) fail mainly by an intrinsic mechanism (abrupt R-decrease). In fact, with increasing MTJ-area, we expect more defects to appear in the barrier, leading to the observed change in the breakdown mechanism from intrinsic to extrinsic. However, with decreasing oxidation time we observe that extrinsic breakdown becomes the dominant failure mechanism, independently of MTJ-area.

We measured the temperature dependence of the electrical resistance and TMR in the 300-20 K range. In the low resistance MTJs with AlO_x-barriers formed during extremely small oxidation times (25 s, with the shutter closed) we found different R(T) behaviors for different samples: Tunnel-dominated transport (dR/dT<0), metallic-like R(T) behavior (dR/dT>0) and a mixture of the two. However, the magnetoresistance ratio is still fairly large in all samples even at room temperature ($\sim$ 20%). This suggests a competition between tunneling and diffusive/ballistic transport, showing that metallic nanoconstrictions (unoxidized Al) play an important role in the magneto-transport of underoxidized tunnel junctions. We conclude that these metallic-transport channels are spin dependent and are likely the reason for the fairly large MR values observed for extremely underoxidized tunnel junctions. This effect will be discussed in terms of ballistic magnetoresistance through non-magnetic nanoconstrictions.

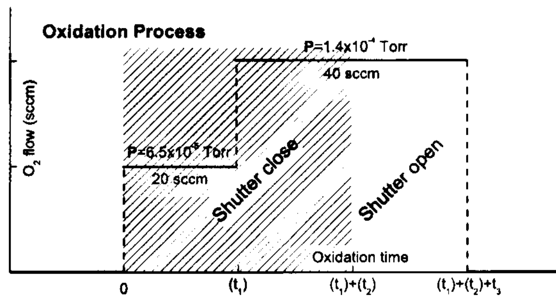

Figure 8.2: Schematic representation of the oxidation process used to fabricate the here studied tunnel junctions.

8.1 Experimental details

We studied several series of ion beam deposited magnetic tunnel junctions with different oxidation times [289, 293]. Before actual TJ stack deposition, a $Al_{98.5}Si_1Cu_{0.5}$ low resistance buffer is smoothed with a grazing angle ion beam. The complete structure of the tunnel junctions studied was glass/Al (70 Å)/Ta (90 Å)/NiFe (70 Å)/CoFeB (50 Å)/AlO_x (9 Å)/X/MnIr (250 Å)/Ta (90 Å)/TiW(N) (150 Å). The top electrode X is either a FM CoFeB layer or a synthetic antiferromagnetic (SAF or SyAFM) CoFeB (40 Å)/Ru (6 Å)/CoFeB (40 Å) structure. NiFe, MnIr, CoFeB and TiW(N) stand for $Ni_{80}Fe_{20}$, $Mn_{78}Ir_{22}$, $Co_{73.5}Fe_{16.5}B_{10}$ [130] and $Ti_{10}W_{90}$(N). The junctions were patterned to a rectangular shape with areas between 1×1 μm^2 and 3×8 μm^2 by a self-aligned microfabrication process. The fabrication of these MTJs was performed at INESC-MN.

The AlO_x barrier was formed by a remote Ar/O_2 plasma (110 W RF in a 20 cm diameter assist ion gun), 60 cm away from the sample [289]. Ions drift to the chamber due to pressure gradient only (no acceleration voltage on the gun grids). The oxidation is divided into three consecutive stages with total oxidation time $(t_1)+(t_2)+t_3$. During the first two stages $(t_1)+(t_2)$ the sample is protected by a shutter preventing most of the oxygen from reaching the sample. The plasma O_2 content is also progressively increased. During the first stage the plasma is created with 4 sccm (Ar)+20 sccm (O_2) at a pressure $P = 6.5 \times 10^{-5}$ Torr and in the following two stages (2, 3) one has 4 sccm (Ar)+40 sccm (O_2) at $P = 1.4 \times 10^{-4}$ Torr (Fig. 8.2). Stage 3 occurs without shutter, *i. e.* with the sample directly exposed to the O_2 plasma.

The dependence of the tunnel magnetoresistance on the applied electrical current, TMR(I), and the current-voltage V(I) characteristics were simultaneously measured at room temperature (RT) with a fully automated KLA10007E wafer probe station. Measurements were performed as follows: under the electrical current I one measures the resulting voltage drop in both the magnetic parallel (V_P) and antiparallel (V_{AP}) states. A small current $I_0 \approx 0.1$ mA is then adopted and $V_P(I_0)$ and $V_{AP}(I_0)$ measured again. The same procedure is performed for $-I$. The electrical current I is then step increased and the above set of measurements repeated at each step. This method allows us to obtain detailed data on each tunnel junction: the corresponding $V_P(I)$ and $V_{AP}(I)$ characteristics, the TMR(I) behavior and the TMR under I_0, after application of I (allowing a more detailed study of dielectric breakdown).

Series	Structure	Oxidation time
TJ1001	$NiFe_{70}/CoFeB_{50}/Al_8$+Ox/$CoFeB_{40}/MnIr_{250}$	(30")+(30")+5"
TJ1018	$NiFe_{70}/CoFeB_{50}/Al_9$+Ox/$CoFeB_{40}/MnIr_{250}$	(30")+(30")+0"
TJ1019	$NiFe_{70}/CoFeB_{50}/Al_9$+Ox/$CoFeB_{40}/MnIr_{250}$	(30")+(30")+1"
TJ1022	$NiFe_{70}/CoFeB_{50}/Al_9$+Ox/$CoFeB_{40}/MnIr_{250}$	(30")+(30")+4"
TJ1043	$NiFe_{70}/CoFeB_{50}/Al_9$+Ox/SyAFM/$MnIr_{250}$	(30")+(30")+5"
TJ1135	$NiFe_{70}/CoFeB_{50}/Al_9$+Ox/SyAFM/$MnIr_{250}$	(25")+(00")+0"

Table 8.1: Series of magnetic tunnel junction studied during this work. Here, SyAFM is a $CoFeB_{40}/Ru_6/CoFeB_{40}$ synthetic antiferromagnetic structure. The numbers in subscript are the layer thickness in Å.

Such room temperature measurements were performed at INESC-MN by Ricardo Ferreira. Temperature dependent measurements were performed using the four-point d.c. method, with a current stable to $1{:}10^6$ and an automatic control and data acquisition system.

The Tunnel Magnetoresistance is, as usual, defined as

$$TMR = \frac{R_{\rm AP} - R_{\rm P}}{R_{\rm P}}. \tag{8.1}$$

8.2 Experimental results

Figure 8.1 (taken from Ref. [289]) shows the tunnel magnetoresistance ratio versus $R \times A$ of tunnel junctions with different oxidation times [289, 293]. Decreasing oxidation time leads to a decrease of TMR and $R \times A$. Nevertheless, fairly high TMR ($\sim 20\%$; $R \times A \sim 5\ \Omega\mu\text{m}^2$) is still obtained, even when all the oxidation process is performed with the shutter closed. We will here study in detail the transport properties of the magnetic tunnel junctions displayed in Table 8.1, having different oxidation times.

8.2.1 Dielectric Breakdown

The dependence of the tunnel magnetoresistance on the applied bias current TMR(I) of a MTJ with $(30'')$+$(30'')$+$5''$ oxidation time ($A = 1 \times 1\ \mu\text{m}^2$; $R \times A \approx 10\ \Omega\mu\text{m}^2$) is displayed in Fig. 8.3(b) (solid squares; series TJ1001). Also shown are the TMR values measured under $I_0 \approx 0.1$ mA, after the current I was applied (open circles). Figure 8.3(c) depicts the V(I) characteristics in both the parallel and antiparallel states. Using Simmons' model [181], one obtains the barrier thickness ($t \sim 9$ Å) and height ($\varphi \sim 0.25$ eV) of the tunnel junction. The small barrier height is indicative of underoxidation of the barrier. Figure 8.3(a) displays the electrical resistance obtained under I and I_0 for both parallel and antiparallel states.

The TMR(I) curve [Fig. 8.3(b); solid squares] displays the usual gradual TMR decrease with increasing bias current. However, increasing I also leads to a sharp TMR decrease (sudden discontinuity at $|I| \approx 32$ mA), visible in both measurements under I and I_0. At such breakdown point, all TMR(I), V_P(I) and V_{AP}(I) [and R_P(I), R_{AP}(I)] curves show an

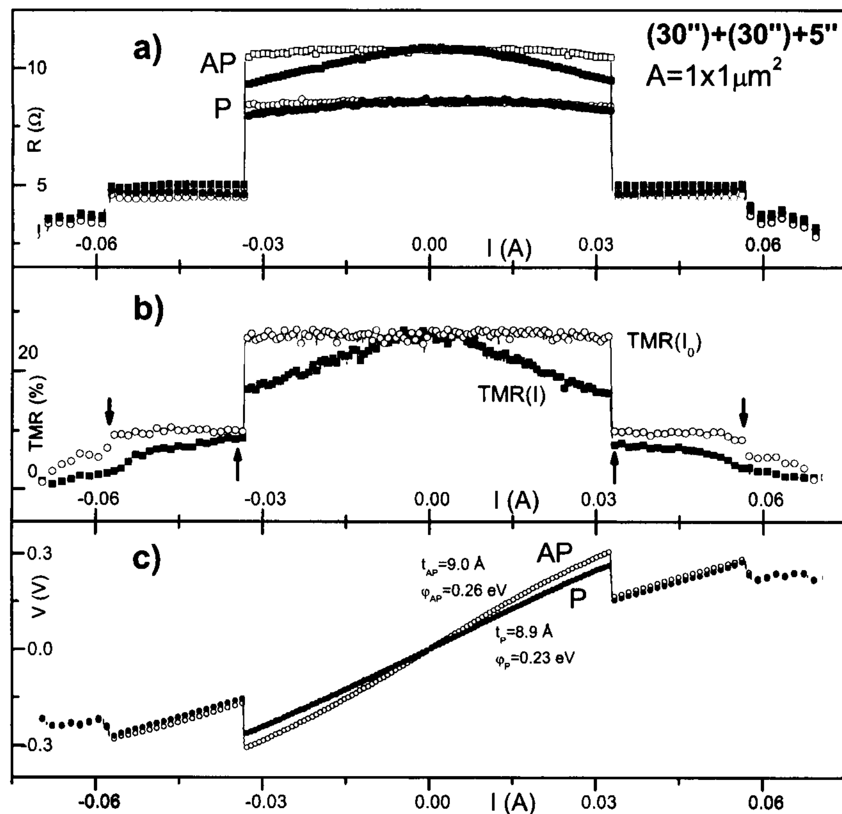

Figure 8.3: (a) Electrical resistance versus bias current of a MTJ with $(30'')+(30'')+5''$ oxidation time (series TJ1001; $A = 1 \times 1\ \mu\text{m}^2$), under both I (black curves) and I_0 (red curves) and for both parallel (P) and antiparallel (AP) states. (b) Tunnel magnetoresistance versus bias current [TMR(I); solid squares]. Open circles display the TMR ratio obtained under a low bias current $I_0 \approx 0.1$ mA after I is applied. (c) V(I) characteristics in the P and AP states. Notice the abrupt decrease in the measured electrical resistance and TMR observed at $|I| \approx 32$ mA, denoting the intrinsic breakdown of the barrier.

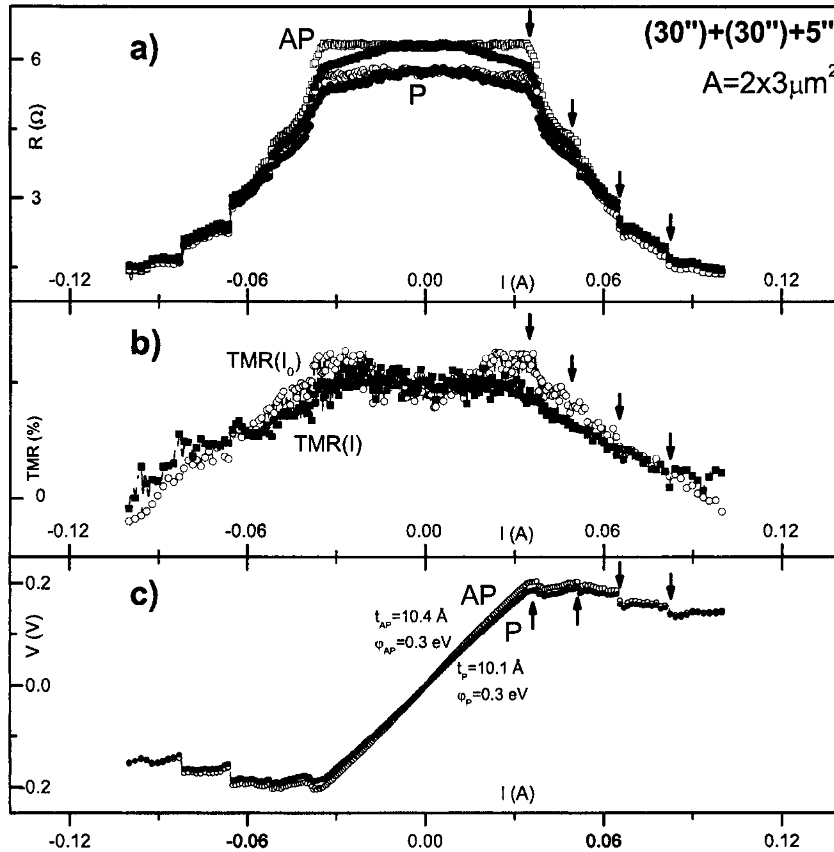

Figure 8.4: (a) Electrical resistance versus bias current of a MTJ with (30″)+(30″)+5″ oxidation time (series TJ1001; $A = 2 \times 3\ \mu\text{m}^2$), under both I (black curves) and I_0 (red curves) and for P and AP states. (b) TMR(I) (solid squares) and TMR obtained under a low bias current $I_0 \approx 0.1$ mA after I is applied (open circles). (c) V(I) characteristics in the parallel and antiparallel states. Notice the gradual R- and TMR-decrease observed at and/or just after the breakdown of the barrier.

abrupt decrease, associated with the *intrinsic* breakdown of the studied sample [212], through the formation of a pinhole in the barrier under the high applied electrical field (see section 5.6). As I is further increased, a new breakdown event is seen (at $|I| \approx 55$ mA), related with the formation of a new pinhole (see arrows in Fig. 8.3).

On the other hand, tunnel junctions with larger area show a fairly different behavior. Figure 8.4 displays the obtained results for a MTJ with $A = 2 \times 3\ \mu\text{m}^2$ ($R \times A \approx 50\ \Omega\mu\text{m}^2$). In this case we observe several breakdown events characterized by smooth R-decreases (see arrows in Fig. 8.4). At the first breakdown point ($|I| \approx 35$ mA), all TMR(I), TMR(I_0), V_P(I) and V_{AP}(I) [Fig. 8.4(c); see also R_P, R_{AP} in Fig. 8.4(a)] show a slight and gradual decrease, a behavior that we associate with defect-driven extrinsic breakdown of the barrier [212], reflecting the growth of existing pinholes with the applied current [213]. Three more breakdown events are visible at higher currents ($|I| \approx 50$ mA, ≈ 65 mA and ≈ 80 mA), bringing TMR to zero and further reducing V_P and V_{AP} (lower R-values). These new breakdown points

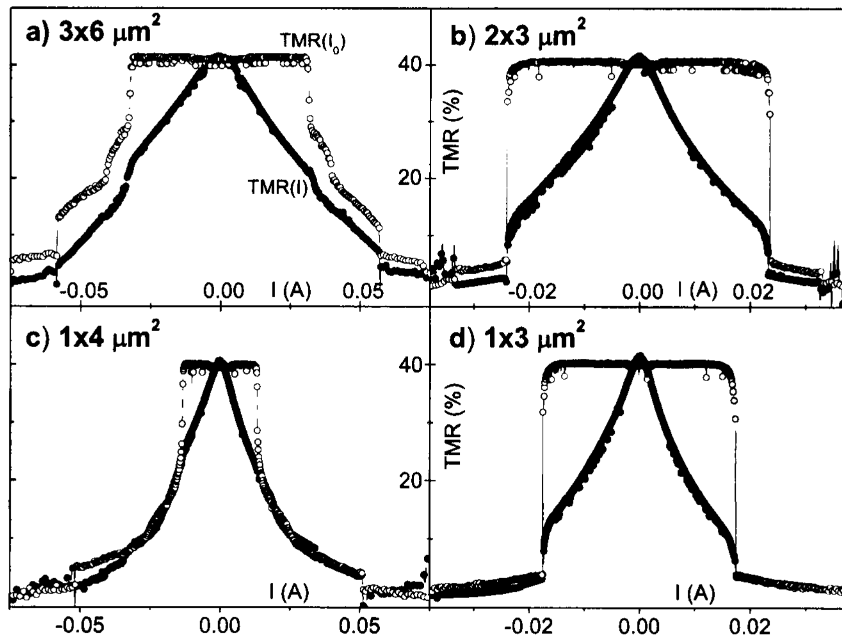

Figure 8.5: Tunnel magnetoresistance measured under I (full squares) and I_0 (open circles) for MTJs of series TJ1043 [(30″)−(30″)+5″] with different areas. Notice the gradual TMR-decreases observed for MTJs with (a) $A = 3 \times 6\ \mu\text{m}^2$ and (c) $A = 1 \times 4\ \mu\text{m}^2$, contrasting with the sharp ones for MTJs with (b) $A = 2 \times 3\ \mu\text{m}^2$ and (d) $A = 1 \times 3\ \mu\text{m}^2$.

are characterized by a small but sharp R-decrease, followed by a gradual one. We believe that this is due to the formation of new pinholes in the barrier at localized weak-spots (sharp R-variations) and their subsequent current-induced growth (smooth R-decrease). Moreover, after the first breakdown point [$|I| \approx 35$ mA; Fig. 8.4(a)] the electrical resistance decrease is not constant but shows a trend towards saturation, suggesting progressive pinhole-growth exhaustion. Breakdown in this MTJ then also seems to occur at different, localized spots of the barrier, likely where a large concentration of defects (oxygen vacancies due to the underoxidation of the barrier) exists.

As stated above, the extrinsic breakdown mechanism is dominant in large area MTJs of series TJ1001. In fact, with increasing MTJ-area, defects are more likely to appear in the barrier, leading to the observed change in the breakdown mechanism from intrinsic to extrinsic. This is also seen in MTJs of series TJ1043 (SAF pinned layer structure), where most of the junctions with large areas fail by an extrinsic mechanism, while those with small areas ($A \lesssim 1 \times 4\ \mu\text{m}^2$) fail mainly through an intrinsic one. This can be observed in Fig. 8.5 for MTJs of series TJ1043 with different areas [(30″)+(30″)+5″]. Samples with $A = 3 \times 6\ \mu\text{m}^2$ and $1 \times 4\ \mu\text{m}^2$ display a slight and gradual TMR-decrease at breakdown (also visible in the electrical resistance; not shown), while those with $A = 2 \times 3\ \mu\text{m}^2$ and $1 \times 3\ \mu\text{m}^2$ show an abrupt change of TMR (and R).

Magnetic tunnel junctions with smaller oxidation times fail mostly through an extrinsic mechanism, independently of the area, although some samples of series TJ1022 [(30″)+(30″)−4″] still display intrinsic breakdown [see Fig. 8.6(a) and (c); $A = 1 \times 2\ \mu\text{m}^2$]. Figures 8.6(b) and

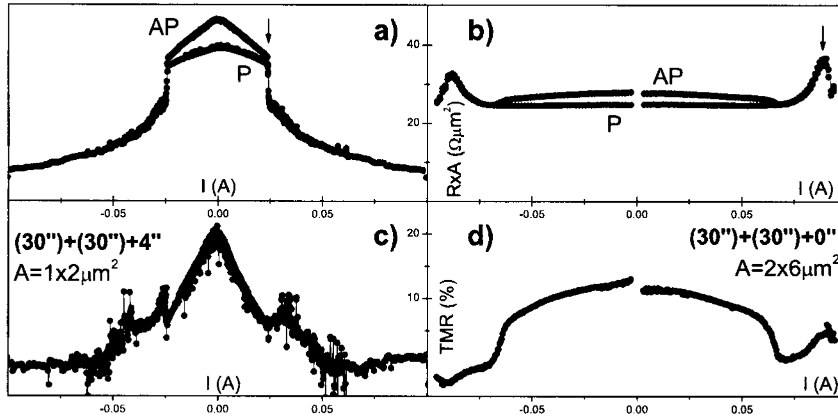

Figure 8.6: $R \times A$ product (for the parallel and antiparallel states) versus applied current of MTJs of series (a) TJ1022 [(30″)+(30″)+4″] and (b) TJ1018 [(30″)+(30″)]; (c) and (d) display the corresponding TMR bias dependence.

(d) show $R \times A$ and TMR electrical current bias dependencies for a sample of series TJ1018 [(30″)+(30″)+0″; $A = 2 \times 6$ μm^2], where extrinsic breakdown is observed (see arrow). Also notice the fairly large R-increase seen before TJ-dielectric breakdown, associated with heating due to large current densities flowing through metallic pinholes across the barrier (see below).

Figure 8.7(a) displays a typical TMR(I) dependence of tunnel junctions with extremely small oxidation time [(25″)+(00″)+00″; series TJ1135], giving TMR∼ 15% under low bias current. At $|I| \approx 70$ mA, both TMR(I) and TMR(I_0) sharply decrease to zero. Corresponding V(I) characteristics for the parallel and antiparallel magnetic states [Fig. 8.7(c)] show a quasi-linear behavior also up to $|I| \approx 70$ mA. Fitting our data to Simmons' model allows us to estimate the corresponding barrier thickness ($t \approx 4.5$ Å) and barrier height ($\varphi \approx 0.4$ eV). The extremely small values obtained indicate that only part of the initially deposited Al layer (9 Å) was oxidized (low barrier thickness) and that the oxidized Al is likely not stequiometric (low barrier height). The decrease of TMR to zero is due to the abrupt drop of the electrical resistance of the antiparallel state (R_{AP}). However, the electrical resistance of the parallel state (R_{P}) remains constant [see Fig. 8.7(c) and inset]. Notice again the increase of the electrical resistance observed at high applied electrical current [inset of Fig. 8.7(b)], related to heating in the measured tunnel junction, indicating a metallic R(T) behavior, dR/dT>0 (see below). Figures 8.7(b) and 8.7(d) display TMR(I) and TMR(I_0) and V(I) characteristics for a MTJ of the same series with $A = 2 \times 4$ μm^2. In this case we clearly see that TMR(I) and TMR(I_0) do not go to zero at the same applied current. Thus, such decrease appears not to be related with junction breakdown. In fact, one again observes [inset of Fig. 8.7(d)] that R_{P} is not affected by this applied current (I), and only R_{AP} is decreased. This phenomenon then seems to be of a magnetic origin, but further investigations are needed for us to fully explain it. Further increasing the applied electrical current again leads to a fairly large R-increase (due to heating). Only at higher electrical currents (see arrows) is the electrical resistance seen to decrease, due to the extrinsic breakdown of the barrier.

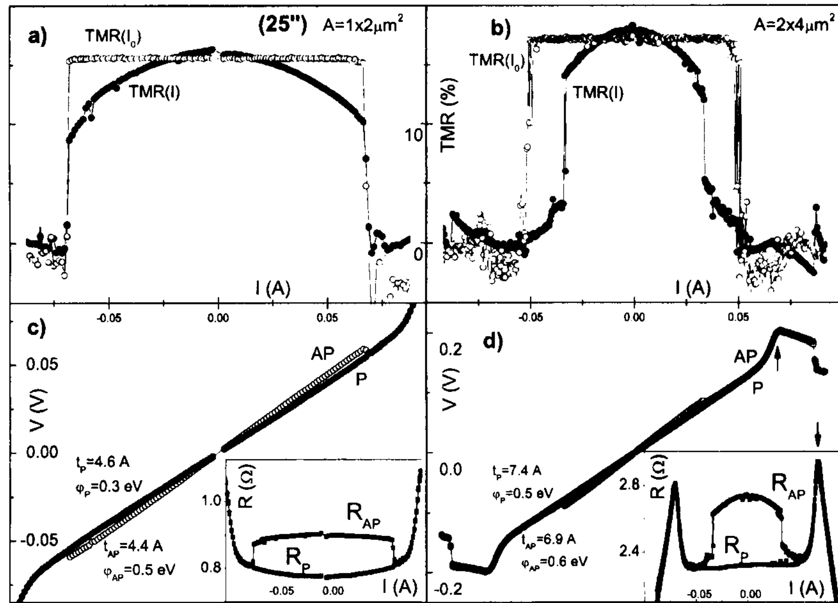

Figure 8.7: (a) Tunnel magnetoresistance versus bias current [TMR(I)] of a MTJ with (25″) oxidation time. (b) V(I) characteristics in the parallel and antiparallel states. Inset: Corresponding electrical resistance (V/I).

8.2.2 Spin dependent resistance fluctuations

The electrical resistance of the parallel ($R_{\rm P}$) and antiparallel ($R_{\rm AP}$) states (Fig. 8.8; measured under I_0) of a a MTJ with (30″)+(30″)+5″ oxidation time (series TJ1043; $A = 3 \times 8$ μm^2) is observed to fluctuate between two closely separated ($\delta R/R \sim 0.6\%$) stable levels. While $R_{\rm P}$ is most of the times in the low R-level, with rare fluctuations to the higher R-level, $R_{\rm AP}$ is preferentially in the higher R-level. These fluctuations are about 10 times less frequent for the parallel alignment of the pinned and free layers, indicating that this phenomenon is spin-dependent. Consequently, TMR also shows similar fluctuations (inset of Fig. 8.8).

The above phenomenon is likely related with transport through localized defects in the insulating barrier, leading to the closing/opening of conductance channels [290, 291, 292] through the trapping/untrapping of electrons by oxygen vacancies in the AlO_x underoxidized barrier. When an electron is captured by the barrier, conduction within a volume $\propto t^3$ is blocked [292], thus decreasing the overall MTJ conductance. When the MTJ is in the antiparallel state, there is an electron trapped in a defect most of the times (the higher R-level is more frequent) because (spin dependent) tunneling to the other electrode is less probable in this magnetic configuration. However, in the parallel state the tunneling probability is higher and electrons are not so often trapped.

Because the experimental procedure in some of the here studied MTJ-series did not include measurements under I_0, we will present our results on R-fluctuations in MTJs with different oxidation times using only measurements obtained under the applied electrical current I. We also notice that the presented data does not include the study of the dynamics of the

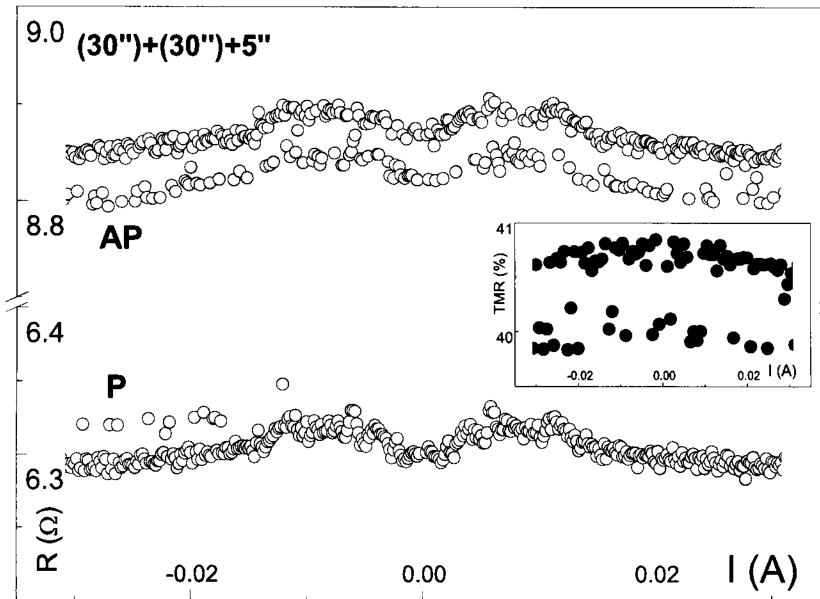

Figure 8.8: Electrical resistance of the antiparallel (AP) and parallel (P) states and corresponding TMR values (inset) of a MTJ with (30″)+(30″)+5″ oxidation time (series TJ1043; measured under I_0). Notice the two R-levels existent in both R_P and R_AP.

observed phenomenon. Such study as a function of TJ-magnetic state, temperature and applied electrical current is currently underway.

Our results indicate that the amplitude and frequency of the resistance fluctuations depend on the tunnel junction oxidation time (Fig. 8.9). Tunnel junctions with the lowest oxidation times [performed with the shutter closed, (25″)+(00″)+00″ and (30″)+(30″)+00″] reveal small and rare resistance fluctuations (Fig. 8.9, first row). A slightly higher oxidation time [(30″)+(30″)+1″; Fig. 8.9, second row] leads to large, frequent and multi-level R-fluctuations. However, such fluctuations are then seen to decrease with increasing oxidation time [third and fourth rows for MTJs with (30″)+(30″)+4″ and (30″)+(30″)+5″ oxidation time, respectively]. In fact, for (30″)+(30″)+5″ tunnel junctions only two level fluctuations are observed.

These results can be understood as follows. When the oxidation is performed for small time periods and with the shutter closed, few oxygen atoms reach the Al layer and only a superficial, discontinuous (see section 8.2.3) AlO_x insulating barrier is formed. Thus, electrons will either flow through the metallic part of the barrier or tunnel between the two electrodes through the incipient barrier and defects are not expected to have an important effect in the overall TJ-conductance. When the shutter is opened, more oxygen reaches the sample and a thicker barrier is formed [as seen by the increase of the barrier thickness, obtained from fittings to the corresponding I(V) characteristics]. The barrier formed during (30″)+(30″)+1″ is very inhomogeneous (low barrier height) and should have a large amount of oxygen vacancies where electrons can be trapped. This then leads to fluctuations between several resistance levels, likely due to the simultaneous trapping of electrons at different defects. When the oxidation time is further increased, a more uniform oxidation of the Al layer is obtained and the number of defects decreases. The corresponding resistance fluctuations then also decrease

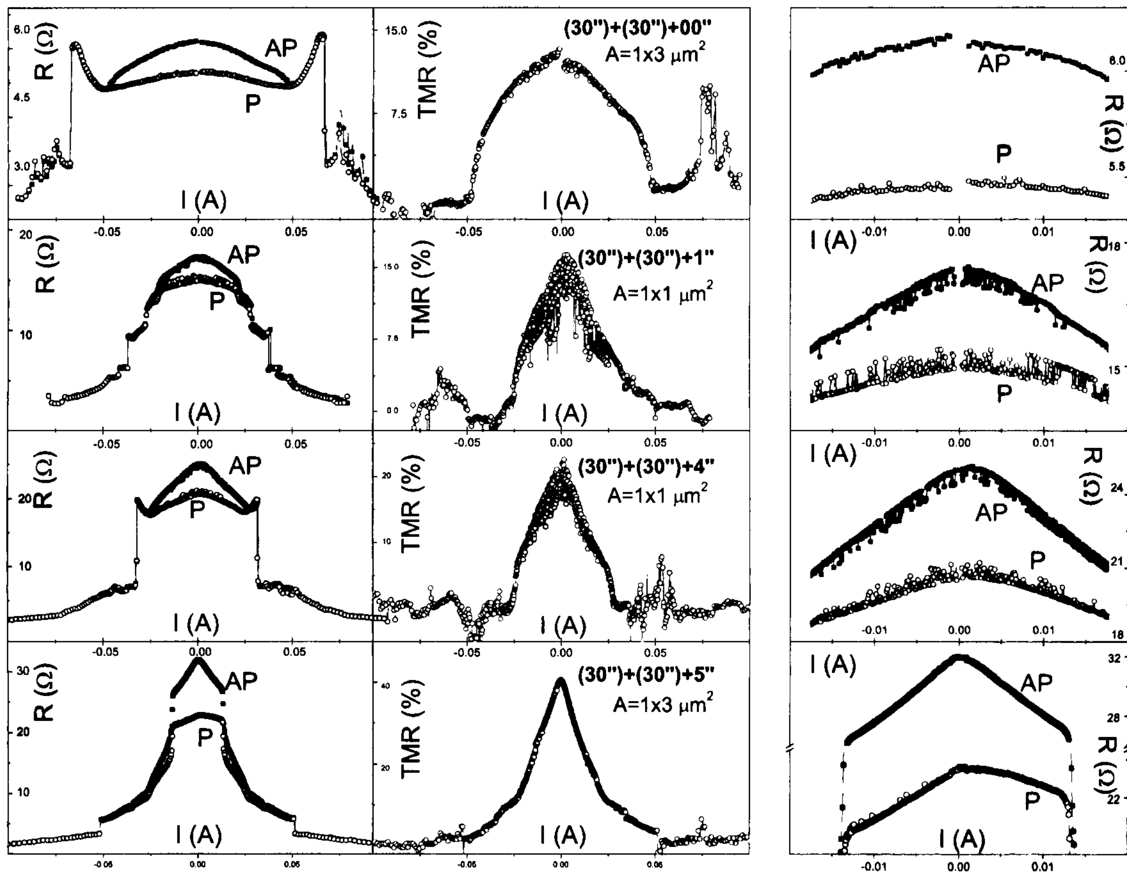

Figure 8.9: Electrical resistance of the antiparallel and parallel states (column 1), corresponding TMR values (column 2) and enlarged low current region (column 3) for MTJs with different oxidation times.

in amplitude and, for (30″)+(30″)+5″ oxidation time, we observe only two level resistance fluctuations.

8.2.2.1 Electron trapping and 1/f noise

We will here briefly review some basic considerations on the relation between electron trapping, defects and 1/f noise in TJs, following the reference work of C. T. Rogers [294].

1/f noise is a general phenomena that appears in a wide variety of electronic devices. In fact, the power spectrum of many systems (in the low frequency regime) follows a $1/f^{\alpha}$ dependence (usually $0.85 < \alpha < 1.15$). 1/f noise can then deteriorate device performance if one is interested in low frequency signals. The early models of 1/f noise started by considering an individual noise source characterized by an exponential relaxation. The corresponding power spectrum is Lorentzian and, if many noise sources are active, having a wide distribution of relaxation times, 1/f noise arises.

Rogers studied small area tunnel junctions at low temperatures, so that only few noise sources

were active, thus allowing the study of the corresponding individual spectra. In fact, if the bandwidth of the measuring system is limited so that only one Lorentzian is active, one is able to see discrete jumps between two R-levels (state 1 and 2) in the time evolution of the tunnel junction electrical resistance [R(t)]. The Lorentzian power spectrum was then proved to arise from the switching on and off of single microscopic scattering centers of some kind. In fact, if the system under study has an exponentially decaying probability (in time) of remaining in a given state (1 or 2), one finds a Lorentzian spectrum with a roll-off frequency given by $1/\tau_{eff} = 1/\tau_1 + 1/\tau_2$, where $\tau_{1(2)}$ is the mean lifetime of the system in state 1 (2).

Rogers then concentrated on the origin of the TJ electrical resistance fluctuations. He focused on the variation of the TJ-barrier height φ_0 arising from changes in the local charge distribution in the barrier, via capture and/or emission of electrons. Schmidlin [295] was the first to consider the effect of point ionic charges on the TJ electrical resistance and was able to determine how a trapped charge in the barrier changes the corresponding barrier height. To perform a qualitative analysis of his data, Rogers considered the effect of an uniform sheet of charge in the barrier. The effective barrier height φ_q upon capture of a charge q is then given by:

$$\varphi_q = \varphi_0 \left(1 + \frac{\phi}{2\varphi_0}\right)^2, \tag{8.2}$$

with

$$\phi = \frac{3q}{2\epsilon A} z_0 \left(1 - \frac{z_0}{t}\right), \tag{8.3}$$

where ϵ is the insulating barrier permittivity, A is the tunnel junction area, z_0 is the position of the uniform sheet of charge in the barrier and t the barrier thickness. The change in the barrier height then depends on the position of the trapped charge and is maximum for $t/2$. The resulting change in TJ-conductance can be approximated by:

$$\frac{\delta j}{j} \approx -\alpha\sqrt{\varphi_0}\, t \frac{\phi}{\varphi_0}, \tag{8.4}$$

where $\alpha = \frac{4\pi}{h}\sqrt{2me}$. The estimations of ϕ ($\approx 5 \times 10^{-6}$ V) and $\delta j/j$ ($\approx 5 \times 10^{-5}$) were in fair agrement with the experimental results obtained by Rogers.

8.2.3 Temperature dependent measurements

We will now present our studies on the temperature dependence of the electrical resistance and magnetoresistance of tunnel junctions with extremely small $(25'')+(00'')+00''$ oxidation time. Figure 8.10 displays the R_P, R_{AP} and TMR (insets) temperature dependencies of four different tunnel junctions of series TJ1135 $[(25'')+(00'')+00'']$. In Fig. 8.10(a) we observe that the electrical resistance of MTJ1 ($A = 3 \times 8$ μm^2 and $R \times A \approx 12$ $\Omega\mu$m^2) *decreases* with decreasing temperature, denoting a metallic-like behavior (dR/dT>0). This effect is more pronounced for the parallel than for the antiparallel magnetic state. Recall that we can define the relative resistance change between 300 K and 25 K as:

$$\alpha = \frac{R_{300K} - R_{20K}}{R_{300K}}. \tag{8.5}$$

For the MTJ1 sample we obtain $\alpha_P = 10.2\%$ and $\alpha_{AP} = 1.4\%$ for the parallel and antiparallel states respectively (see table 8.2). Nevertheless, TMR increases with decreasing temperature

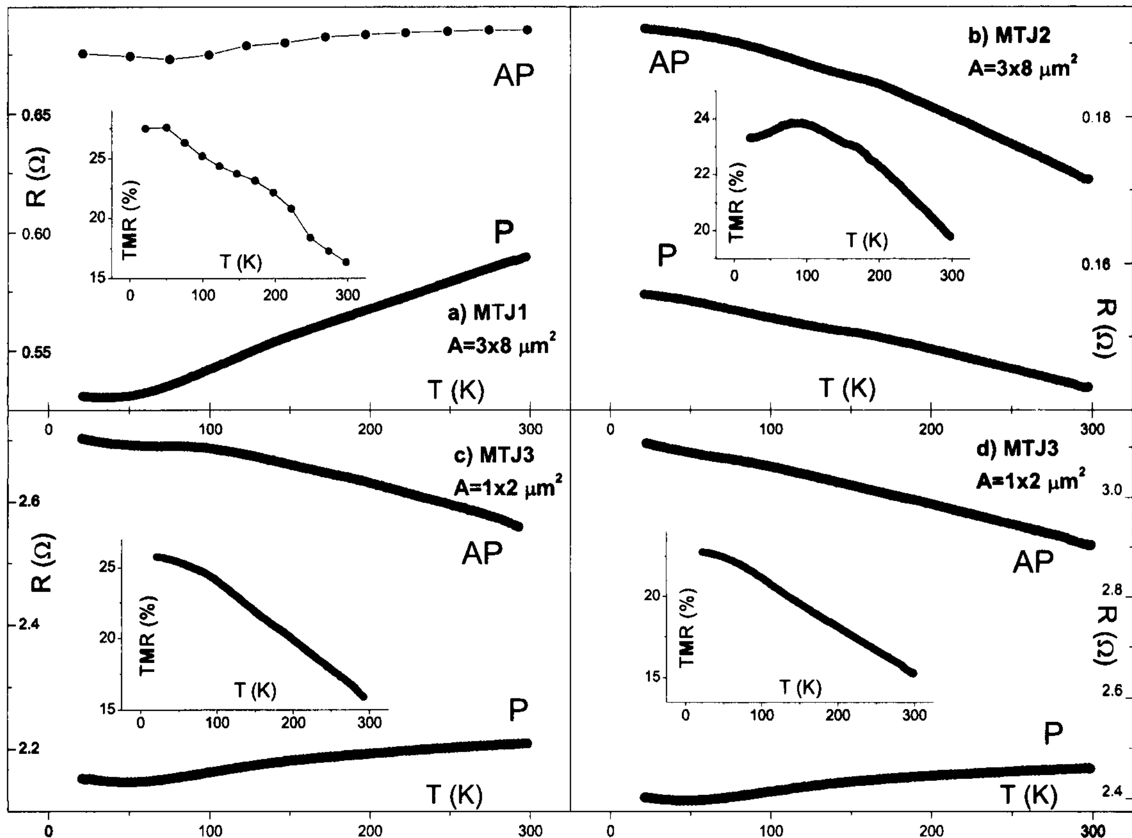

Figure 8.10: Temperature dependence of the electrical resistance and magnetoresistance (insets) of four different tunnel junctions of the same series, with (25″)+(00″)+00″ oxidation time.

($\sim$ 16% at RT and $\sim$ 27% at $T = 20$ K). Thus, although tunnel (which would lead to dR/dT<0) is not the dominating transport mechanism in this MTJ, a large magnetoresistance is still observed.

On the other hand, a different TJ of the same series and with the same area (MTJ2; $A = 3 \times 8\ \mu m^2$) displays a different R(T) behavior: Both R_P and R_{AP} show a small, negative dR/dT slope, indicating tunnel dominated transport [Fig. 8.10(b); $R \times A \approx 3.4\ \Omega\mu m^2$]. This occurs even though the electrical resistance (and R×A product) of MTJ2 is smaller than that of MTJ1. Also, TMR slightly increases with decreasing temperature (20% at RT and 23% at 25 K).

Strikingly, in MTJ3, MTJ4 [Figs. 8.10(c) and (d)] and MTJ5 (not shown; see table 8.2) samples we observe negative dR/dT for the antiparallel state ($\alpha_{AP} = -5.5\%$, -7.2% and -2.6%) and positive dR/dT for the parallel state ($\alpha_P = 2.3\%$, 2.4% and 3.1%).

We conclude on the existence of two parallel conductance channels, tunnel (with resistance R_t) and metallic (with resistance R_m), in the studied tunnel junctions (with $R_t \approx R_m$). The dominance of one over the other is expected to be due to small structural and composition variations in the underoxidized AlO_x layer. In particular, nanobridges of metallic unoxidized

	A (μm^2)	R_{300K} P/AP (Ω)	R_{25K} P/AP (Ω)	α_P (%)	α_{AP} (%)	TMR$_{300K}$ (%)	TMR$_{25K}$ (%)
MTJ1	3×8	0.59/0.69	0.53/0.68	10.2	1.4	16.3	27.4
MTJ2	3×8	0.14/0.17	0.16/0.19	-8.7	-11.8	20.0	23.3
MTJ3	1×2	2.20/2.56	2.15/2.70	2.3	-5.5	16.6	26.0
MTJ4	1×3	2.46/2.90	2.40/3.11	2.4	-7.2	18.5	27.7
MTJ5	2×3	1.95/2.29	1.89/2.35	3.1	-2.6	17.4	24.3

Table 8.2: Transport characteristics of the measured tunnel junctions of series TJ1135.

Al connecting both electrodes must play an important role in the transport properties of these extremely underoxidized MTJs. Differences in the measured TJ-electrical resistance and corresponding temperature dependence should then arise either from incipient barrier thickness or height variations (changing R_t) or from different Al-nanobridge area (changing R_m). The question then arises if the measured large magnetoresistance originates only from tunneling, or also from some other mechanism, like ballistic [296] or diffusive [297] MR through narrow non-magnetic constrictions, as discussed further below.

8.2.3.1 Impact of barrier and constriction parameters on MTJ-electrical resistance and corresponding temperature dependence

We can model the electrical resistance of underoxidized tunnel junctions as two resistors in parallel, one arising from metallic paths through unoxidized Al and another from tunneling through the oxidized AlO_x. If the electrical resistance of an oxidized tunnel junction is given by R_{t0}, one can write $R_t = \frac{R_{t0} \times A}{A - \pi a^2}$, where a is the radius of the unoxidized part of the junction (in our case a has only a small impact on R_t, so that it can be neglected in the equation above; $\pi a^2 \ll A$, see below). The $R_{t0} \times A$ product depends only on the thickness (t) and height (φ) of the insulating barrier [181]. On the other hand, the electrical resistance of the metallic contribution is, for simplicity, considered to be given only by the Maxwell formulation [298], $R_{\text{Maxwell}} = \frac{\rho}{2a}$ (ρ the electrical resistivity).

As stated above, the observed different R(T) behaviors for different MTJs of the same series are expected to be the outcome of small variations in t, φ or a. Let us then consider the case of MTJ3 for which one expects $R_t \approx R_m$. Consequently one has (for the parallel state and at 25 K), $R_m \approx R_t \approx 2R_P = 4.3\ \Omega$. Using $A = 1 \times 2\ \mu\text{m}^2$, $\varphi = 1$ eV and $\rho = 10\ \mu\Omega$cm, we obtain $t \approx 7.6$ Å and $a \approx 115$ Å.

Figure 8.11 shows how the variation of t (a) changes R_t (R_m) and the total resistance $R^{-1} = R_t^{-1} + R_m^{-1}$. Clearly, a small variation of t [Fig. 8.11(a)] may lead to a change in the dominant transport mechanism for the set of parameters here considered. If t increases just from 7.6 to 7.8 Å, R_t increases by more than 25% and changes from below to above $R_m = 2R_P = 4.3\ \Omega$. On the other hand, with increasing constriction radius a [Fig. 8.11(b)], we can also observe a change in the dominant transport mechanism from tunnel to metallic. Thus, in our underoxidized tunnel junctions with nanobridges of metallic Al embedded in the AlO_x barrier, the interplay between metallic and tunneling transport is likely the cause of the observed wealth of R(T) behaviors for different MTJs.

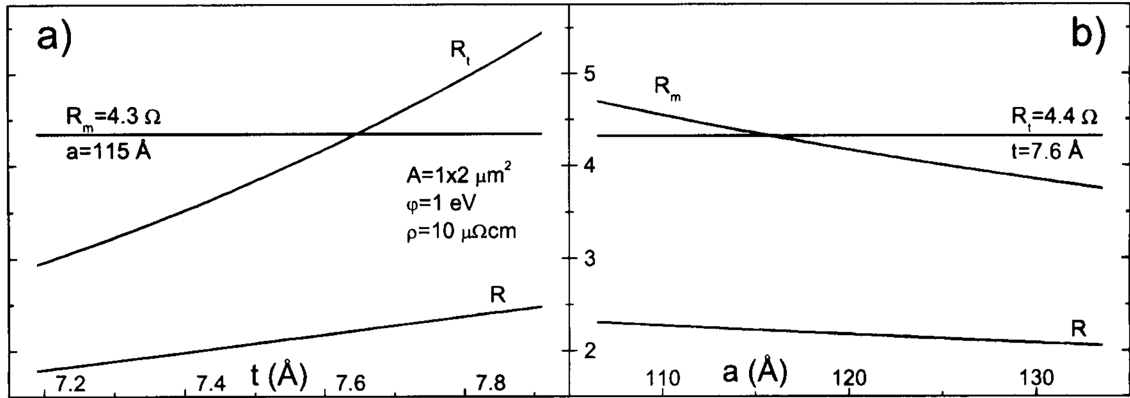

Figure 8.11: Effects of small variations of (a) t and (b) a in the overall tunnel junction resistance.

In the case of MTJ1 $[R_P(25K) = 0.53\ \Omega]$ one has $R_m < R_t$ $(\alpha_{P,AP} > 0)$. Considering the $R_m \ll R_t$ hypothesis, we obtain $a \approx 940$ Å, corresponding to a metallic constriction area $A_m \approx 28000\ \text{nm}^2$ or $\approx 0.1\%$ of the total TJ-area. However, this is the upper limit of a since the tunnel-resistance arising from the oxidized part of the junction should also be included. If we now assume $R_m \approx R_t$, and using $\varphi = 1$ eV and $\rho = 10\ \mu\Omega$cm, we obtain $t \approx 9$ Å $(R_t \approx 1.13\ \Omega)$ and $a \approx 500$ Å $(R_m \approx 1.0\ \Omega)$, corresponding to an equivalent resistance $R \approx 0.53\ \Omega$. Further notice that, for the parameters used, one obtains $R_m < R_t$ corresponding to a metallic R(T) behavior. The extremely small area of the unoxidized Al ($\approx 0.03\%$ of the total area of the junction) leads to fairly high current densities across the TJ-metallic constriction ($j \approx 13$ MA/cm^2 for $I = 1$ mA), although the voltage drop is small ($V \approx 1$ mV).

Let us now return to the inset of Fig. 8.7(c) where we display the R(I) dependence of a MTJ of series TJ1135 in a dielectric breakdown experiment. Clearly, the electrical resistance (parallel state) increases with increasing current magnitude, denoting Joule heating due to high current densities flowing through metallic nanoconstrictions (dR/dT>0).[1] Using the linear dR/dT of our R(T) experiments (dR/dT$\approx$ 0.16 mΩ/K for MTJ3) and the ΔR values between R(I=0) and R for which TMR goes to zero ($|I| \approx 70$ mA) we obtain $\Delta T \approx 190$ K. Such temperature increase can then be the cause for the observed TMR disappearance before the onset of dielectric breakdown.[2]

The two resistances in parallel model can also account for the negative dR/dT observed in MTJ2 if one considers that the decrease of the barrier thickness or height leads to reduced R_t values (so that $R_t < R_m$).

[1]Notice that, if tunneling was the dominant transport mechanism, a decrease of R with increasing $|I|$ would be observed [see Fig. 8.3(a)].

[2]For the maximum applied current ($|I| \approx 95$ mA) we would obtain $\Delta T \approx 2000$ K. Such high temperatures also result from simplified numerical simulations of Joule heating in nanoconstrictions (performed using Eq. (6.7); *e. g.*, $\Delta T \approx 1500$ K for $j \approx 1000$ MA/cm^2; corresponding to $I \approx 80$ mA and $a = 500$ Å). The results obtained are, as expected, very sensitive to the constriction radius. On the other hand, the extremely high temperature values predicted should be taken with great caution, in face of the severe simplification underlying such analysis.

8.2.3.2 Magnetoresistance origin

In theory, one would expect the presence of unoxidized Al constrictions in the insulating barrier to result in the sharp decrease of the measured tunnel magnetoresistance [208]. However in the here study underoxidized tunnel junctions, we still observe fairly large TMR ($\sim$ 20%) even when dR/dT>0 is observed. If transport through our metallic constrictions was spin-independent and considering $R_m \approx R_t$, the effective magnetoresistance of a MTJ with similar barrier-parameters but without metallic constrictions would then have to be $\sim$ 50%.

Notice that this TMR value is even larger than that observed for the highest used oxidation time (see Fig. 8.1) and similar to those obtained in MTJs with optimized oxidation processes. Furthermore, we expect the oxidized barrier of MTJs with (25")+(00")+0" oxidation time to be substantially different from those with (30")+(30")+5" (lower barrier thickness and height). With decreasing insulating thickness the effective spin polarization of a MTJ system is known to decrease [160]. The metallic Al remaining after oxidation should also lead to the decrease of TMR due to the loss of interfacial spin polarization [278]. Consequently, for underoxidized MTJs, TMR should naturally decrease with decreasing oxidation time, leading to the conclusion that the metallic conductance through nanobridges in our system is spin dependent.

To reinforce this statement, we now refer in more detail the $R_{P,AP}$(T) results of MTJ3 and MTJ4 (and MTJ5) presented in Figs. 8.10(c) and (d). For these MTJs we observed $\alpha_P > 0$ and $\alpha_{AP} < 0$. Since one obviously has $R_t^P < R_t^{AP}$, if transport through the metallic nanobridges was spin-independent ($R_m^P = R_m^{AP}$) we would expect the metallic conductance to be further visible in the antiparallel state. [Since $R_m^P < R_t^P$ ($\alpha_P > 0$), we would have $R_m^P = R_m^{AP} < R_t^P < R_t^{AP}$ (which would then lead to $\alpha_{AP} > 0$).] The change from metallic to tunnel dominated transport when the MTJ-magnetic configuration goes from parallel to antiparallel can then only be explained if we assume spin dependent metallic transport across Al nanoconstrictions. Furthermore, $R_m^{AP} - R_m^P > R_t^{AP} - R_t^P$, *i. e.*, the *magnetoresistance arising from metallic transport is larger than that arising from tunnel.* In other words, the tunnel magnetoresistance is in fact limiting the MR obtained in our system. Because giant magnetoresistance in the current perpendicular to the plane configuration is usually small ($\approx$ 0.5%), other magnetoresistive mechanisms must be taken into account, such as ballistic and diffusive (spin dependent) transport through nanoconstrictions.

Ballistic magnetoresistance. Although ballistic magnetoresistance (BMR) is in fact theoretically predicted, its experimental observation is still a topic surrounded by controversy [299, 300]. Ballistic magnetoresistance [301, 302, 303, 304] experiments are performed in FM-nanocontacts (with physical dimension generally in the range 10–100 Å) between two FM electrodes and is theoretically explained in terms of domain wall, scattering. If a domain wall is trapped in the nanobridge region (so that the constriction radius is much smaller than the mean electron free path) and the FM-magnetizations (M) are antiparallel, polarized electrons will be strongly reflected at such sharp domain wall resulting in a large resistance. On the other hand, if the magnetizations at the two sides of the nanocontact are parallel, electrons with their spin along M cross the domain wall without scatter (small resistance).

Experimentally, BMR values of more than 3000% have been reported [304] but other results

suggested that such large resistance variations may be due to artifacts (magnetostatic forces, magnetostriction) that can mimic true BMR [305, 306, 307]. However, recent experiments on single atom conductors showed large BMR values that apparently cannot be attributed to any such artificial phenomena [299].

The similitude between BMR and TMR was discussed by N. Garcia [296]. He argued that pinholes can be present in thin tunnel junctions and give rise to large ballistic MR. In fact, BMR [296] (for spin conserving transport) and TMR [16] depend equally on the spin polarization P of the FM-electrodes:

$$MR = \frac{2P^2}{1-P^2}, \tag{8.6}$$

so that based in MR measurements alone, one cannot distinguish between (spin-dependent) currents arising from tunneling or from pinholes.

Notice that the values of a estimated above for our underoxidized MTJs (a ~100–500 Å) are larger than the electron mean free path in Al ($a > \ell$). However, we expect the relevant parameter in our system to be the spin flip mean free path, which can be much larger than the mean electron free path. Also, notice that the estimated values of a are in fact an upper limit, since it is likely that several nanobridges are present in the MTJ-system (and not a single one as assumed above). We then have several (N) constrictions with radius a_i ($< a$) acting in parallel (so that $R_m^{-1} = \sum_{i=1}^{N} R_{m_i}^{-1}$; $R_{m_i} = \frac{\rho}{2a_i}$). Both situations lead to the recovery of the ballistic regime in the case here studied.

In Ballistic Magnetoresistance experiments performed in nanocontacts, the magnitude of the BMR effect is a function of contact area, decreasing sharply with its increase [308, 309]. This occurs because the width of the domain wall scales with the nanocontact size (and thus with the sample resistance). However, this is not the case for our underoxidized tunnel junctions, where the existence of the BMR effect does not depend on any domain wall. Thus, BMR in non-magnetic nanobridges does not scale with contact area the same way it does in FM-nanocontacts. In fact, transport through non-magnetic nanoconstrictions does not even need to be ballistic for very large MR to be observed [297, 310]. A smooth BMR decrease is predicted when the transport regime goes from ballistic to diffusive, and values as high as 100% have been predicted in the diffusive regime [310]. The theoretical study of Yang *et al.* [297] of non-magnetic nanoconstrictions connecting two large magnetic electrodes also predicted a decrease of MR with increasing constriction radius, but MR values of ~ 60% are still obtained for $a = 200$ Å. They concluded that the presence of non-magnetic constriction in tunnel junctions does not necessarily leads to the suppression of the magnetoresistance and that, by playing with the constriction parameters, it is possible to obtain large MR values while controlling the electrical resistance. For all the above, whether the system under study is in the ballistic ($a_i < \ell$) or diffusive ($a_i > \ell$) regime, the BMR effect should be observable in our non-magnetic Al nanobridges and is likely the origin of the metallic, spin-dependent transport in underoxidized tunnel junctions.

8.3 Conclusions

We showed that transport in underoxidized MTJs is controlled by nanoconstrictions and defects in the AlO_x barrier. We observed that TMR and both R_P and R_{AP} fluctuate between

two closely separated levels, and this effect was associated with spin dependent transport through localized defects in the barrier. Furthermore, we observed that the fluctuations amplitude and rate depend on the barrier oxidation time, due to the variation of the number of defects on the barrier.

We showed that dielectric breakdown in underoxidized MTJs occurs at different, localized spots in the barrier, likely where a large concentration of defects exists. Furthermore, we observed a clear dependence of the breakdown process on the MTJ area: Failure in MTJs with large areas is usually of an extrinsic nature, while small-area junctions fail mainly by an intrinsic mechanism. Nevertheless, with decreasing oxidation time the extrinsic breakdown becomes dominant, independently of the MTJ-area.

R(T) measurements on MTJs with extremely small oxidation times (25 s, with the shutter closed) show different R(T) behaviors for different samples: Tunnel-dominated transport ($dR/dT<0$), metallic-like R(T) behavior ($dR/dT>0$) and a mixture of the two. Nevertheless, a fairly large magnetoresistive ratio is still observed in all samples. We attribute this to spin dependent transport through nanoconstrictions of unoxidized Al and discussed this effect in terms of ballistic magnetoresistance through non-magnetic nanoconstrictions.

Chapter 9

Conclusions and Outlook

This Thesis presents an extensive investigation on the transport properties of magnetoresistive devices, namely specular spin valves and tunnel junctions. In the following we summarize our main results and conclusions.

1. Our comparative study of conventional (non-oxidized) and specular (oxidized) spin valves allowed us to conclude that:

    - The introduction of the nano-oxide layers formed by the partial oxidation of the pinned and free layers greatly enhances the GMR ratio, due to specular electron reflection at the FM/NOL interfaces. In fact, the observed break of the correlation between magnetic and transport processes in the studied specular spin valve indicates the extreme importance of interfacial scattering in this type of GMR nano-structure.
    - The (CoFe) nano-oxide layers are AFM with $T_B \approx 175$ K (likely Fe_2O_3), that lead to the large increase of the exchange and pinned layer coercive fields below such temperature. A broad distribution of blocking temperatures in the nano-oxide layer was experimentally inferred. We then obtained the temperature dependence of the exchange bias arising from the MnIr and AFM-NOL layers.
    - The MR(H) curves are strongly influenced by the paramagnetic/antiferromagnetic transition in the NOL. Field cooling measurements showed that the MR(H) curves depend strongly on the sign and value of the cooling field H_0. Furthermore, the MR(T,H_0) curves departed from the zero field cooling situation below T_B. We relate all these features to the effects of H_0 on the AFM ordering and AFM domain structure of the NOL below its blocking temperature.
    - We showed the importance of the domain structure of the NOL on the residual magnetoresistance observed at large positive fields, using training effect measurements.
    - We extended a model based on the total energy of a conventional spin valve to the case of a NOL SV, and related the observed anomalous bump in the MR(H) curve with the presence of the FM_b layer in the NOL SV.

2. Our detailed studies on the recently discovered Current Induced Resistance Switching effect on thin, low resistance magnetic tunnel junctions allowed us to:

- Attribute the CIS effect to nanostructural rearrangements of metallic ions from the FM electrodes near the interface with the insulating barrier. At high maximum applied electrical currents we observed irreversible resistance decreases due to barrier degradation. Because electromigration (EM) of ions into and out of the barrier should occur preferentially in nanoconstrictions and/or pinholes, we expect the bottom electrode/insulating barrier to be more susceptible to ionic migration.
- Show that the current induced resistance switching effect is thermally assisted (it decreases with decreasing temperature while the critical switching current increases with decreasing temperature). We then estimated two electromigration-energy barriers, $\Delta_1 \sim 0.13$ eV and $\Delta_2 \sim 0.85$ eV, associated with EM involving different types of ions sites/defects. Furthermore, time dependent measurements after a complete or one half CIS cycle enabled us to observed two distinct relaxation times, associated with opposite resistance changes. This evidence on two opposite sign relaxation processes was explained by electromigration involving ions from the two FM/I interfaces.
- Trace the evolution of resistance switching in consecutive CIS cycles, between two (or three) states, driven by an electrical current, both under $H = 0$ and $H \neq 0$. We attributed such evolution to a conjugation of electromigration-driven and magnetic field-driven switching. In fact, if CIS cycles are measured under an external magnetic field, one is able to current-induce a change in the sign of the exchange bias of the TJ, and the corresponding magnetic state (antiparallel to parallel). This effect arises from excessive local heating in the tunnel junction, and enables us to obtain a CIS cycle with three different electrical resistance states. We then attributed the observed excessive heating to localized high current densities flowing through nanoconstrictions in the barrier.

3. We further studied the Current Induced Switching effect on series of tunnel junctions with one or two non-magnetic electrodes, observing that:

   - Tunnel junctions with a Ta layer deposited below the barrier had opposite current switching direction compared to that obtained with a CoFe pinned layer. We attributed this difference to a competition between the direct and wind electromigration forces in Ta and CoFe layers.
   - Tunnel junctions with a Ta layer deposited *below* the insulating barrier show no relaxation phenomenon: Ta ions remain inside the barrier and both the thin- and thick-barrier R-states are stable. On the other hand, the diffusion of CoFe ions into the barrier always allowed their later return to the initial positions in the electrodes.
   - When the TJ is in the low barrier state, the electrical resistance decrease with temperature is smaller than in the thick barrier state, denoting a smaller tunnel-contribution to the overall conductance. Furthermore, with increasing barrier degradation we smoothly changed the R(T) behavior from tunnel- to metallic-dominated transport, due to the formation of pinholes and subsequent increase of pinhole size.
   - The earlier EM-stages at low temperatures occur through a rapid quasi-continuous R-trend that gradually disappears. We then observe discontinuous R-steps denoting different EM-processes. For high temperatures we observe an increase in the number of fluctuators and complex R(t) signals.

4. Finally, our study of underoxidized tunnel junctions led to the following conclusions:

    - Transport in underoxidized MTJs is controlled by defects within the AlO_x barrier. In fact, TMR and both resistances in the parallel and antiparallel states fluctuate between two closely separated levels, and this effect was associated with spin dependent transport through localized defects in the barrier. Such fluctuations (both amplitude and frequency) depend on the oxidation state of the barrier.
    - Dielectric breakdown in these TJs occurs at different, localized spots in the barrier, likely where a large concentration of defects (oxygen vacancies due to the underoxidation of the barrier) exists. Furthermore, we observed a clear dependency of the breakdown process on the MTJ area.
    - R(T) measurements on different MTJs with extremely small oxidation times show a wealth of behaviors: metallic-like behavior ($dR/dT>0$), insulating-like behavior ($dR/dT<0$) and a mixture of the two (metallic for the parallel and insulating for the antiparallel states). Therefore, unoxidized Al plays an important role in the magneto-transport of such tunnel junctions, and can be usefully exploited for device optimization. In particular, transport through Al nanobridges was found to be spin dependent, allowing us to attributed the fairly large MR values observed in extremely underoxidized tunnel junctions to ballistic magnetoresistance through non-magnetic nanoconstrictions.

5. Although not being a main objective of this thesis, our results have important implications for the performance of actual devices. We emphasize the following:

    - The domain structure of the AFM-NOL was seen to clearly influence the Giant Magnetoresistance and, with H-cycling below the NOL blocking temperature, both GMR and exchange field decrease. This effect can have important consequences in device performance if T_B of the NOL is above room temperature. Although in our results we observed $T_B \approx 175$ K, the formation of thicker NOLs (to further enhance specularity and GMR) should lead to the increase of T_B, deteriorating GMR-sensor performance, including long term stability (due to the training effect).
    - We demonstrated that Current Induced Switching could be used to obtain three resistance-states in magnetic tunnel junctions. However, electromigration is also a reliability concern for MTJs used in Magnetic Random Access Memories or read head sensors. This is particularly true for MRAMs where industry currently researches the spin torque effect aiming to replace H-driven switching of TJ-magnetic configuration. High current densities must then be used and electromigration can be a major reliability issue.
    - The presence of defects in the barrier of underoxidized tunnel junctions was linked to the dielectric breakdown observed at high applied electrical currents. Such defects are then also a reliability concern in MTJs. Furthermore, they are likely the origin of the observed resistance fluctuations that may in fact decrease device performance. Also, the presence of a spin-dependent metallic channel was confirmed by our R(T) measurements which could help in MTJ-sensor optimization.

The work performed in the last four years and presented in this thesis has opened several new possible lines of research in the near future. The spin-torque effect is seen for current densities

$j \gtrsim 10^7$ A/cm^2, an order of magnitude higher than those we need to induce electromigration-driven resistance changes. Why recent spin-torque studies do not reveal the CIS effect is still a rather open question that could possibly be answered by studying e-beam lithographed samples. Nevertheless, some reports on dielectric breakdown have revealed resistance changes due to electromigration in MTJs, but systematic studies were never developed. We just notice that, as demonstrated, the Current Induced Switching effect is strongly dependent on the topography of the electrode/barrier interface. This was experimentally confirmed in TJs with different barrier thicknesses and different insulating barrier materials [253].

Also, a deeper study of the differences observed in the CIS effect on TJs from the same deposition batch should be performed. This would include experiments with a large number of samples to obtain statistical data on the CIS coefficient, critical switching currents, relaxation times and corresponding distributions, so as to obtain a more complete understanding of the CIS effect. One should also deepen the knowledge on the dynamics of current-driven electromigration, trough the use of ultra-fast data-acquisition boards. The implementation of such new setup (allowing data acquisition every 3 μs) is planed for the near future.

Such implementation can also be very helpful in studies of resistance fluctuations in under-oxidized MTJs, arising from the trapping/untrapping of electrons in defects in the insulating barrier. Measurements as a function of TJ-magnetic state (parallel/antiparallel), temperature and applied current can help the understanding of the mechanisms behind this phenomenon. Furthermore, the development of magnetic tunnel junctions with MgO barriers displaying very large TMR can further complement this study, because of the enhanced sensitivity of their transport properties on the corresponding crystalline structure. For TMR$>$200% one envisages the emergence of a wide new field of very low magnetic field ($\sim 10^{-12}$ T) sensor applications, namely biosensing.

Studies on the temperature dependence of the electrical resistance and TMR of tunnel junctions with low oxidation times should also be continued, in particular to separate different conductance contributions (tunnel/metallic/diffusive/ballistic) and to optimize Al nanoconstriction characteristics to enhance MTJ-magnetoresistance.

List of publications

1. *Comparative study of magnetoresistance and magnetization in nano-oxide-specular and non-specular MnIr/CoFe/Cu/CoFe spin-valves from 10 to 300 K*, J. B. Sousa, J. O. Ventura, M. A. Salgueiro da Silva, P. P. Freitas and A. Veloso, J. Appl. Phys. **91**, 5321 (2002).

2. *Anomalous MR (H) behavior of CoFe nano-oxide spin valves at low temperatures*, J. O. Ventura, J. B. Sousa, M. A. Salgueiro da Silva, P. P. Freitas and A. Veloso, J. Appl. Phys. **93**, 7690 (2003). Selected for Journal of Nanoscale Science and Technology.

3. *Peculiar magnetic and electrical properties near structural percolation in metal-insulator granular layers*, J. B. Sousa, J.A.M. Santos, R.F.A. Silva, J.M. Teixeira, J. Ventura, Yu.G. Pogorelov, G.N. Kakazei, S. Cardoso and P. P. Freitas, E. Snoeck, J. Appl. Phys. **96**, 3861 (2004).

4. *Exchange bias of MnPt/CoFe films prepared by ion beam deposition*, M. Rickart, P. P. Freitas, I. G. Trindade, N. P. Barradas, E. Alves, M. Salgueiro, N. Muga, J. Ventura, J. B. Sousa, G. Proudfoot, D. Pearson, and M. Davis, J. Appl. Phys. **95**, 6317 (2004).

5. *Ferromagnetic coupling field reduction in CoFeB tunnel junctions deposited by Ion Beam*, S. Cardoso, R. Ferreira and P. P. Freitas, M. MacKenzie and J. Chapman, J. O. Ventura, J. B. Sousa and N. P. Barradas, IEEE Trans. Magn. **40**, 2272 (2004).

6. *Impact of the magnetism of nano oxide layers on the GMR effect in specular spin valves*, J. O. Ventura, J. B. Sousa, P. P. Freitas and A. Veloso, J. Magn. Magn. Mat. **272-276**, 1892 (2004).

7. *Electromigration in thin tunnel junctions with ferromagnetic/nonmagnetic electrodes: nanoconstrictions, heating, and direct and wind forces*, J. Ventura, J. B. Sousa, Y. Liu, Z. Zhang and P. P. Freitas, Phys. Rev. B **72**, 094432 (2005).

8. *Exchange coupling of bilayers and synthetic antiferromagnets pinned to MnPt*, M. Rickart, A. Guedes, B. Negulesco, J. Ventura, J. B. Sousa, P. Diaz, M. MacKenzie, J. N. Chapman and P. P. Freitas, Eur. Phys. J. B **45**, 207-212 (2005).

9. *Blocking temperature in exchange coupled MnPt/CoFe bilayers and synthetic antiferromagnets*, M. Rickart, A. Guedes, J. Ventura, J. B. Sousa, P. P. Freitas, J. Appl. Phys. **97**, 10K110 (2005).

10. *Relaxation Phenomena in Current Induced Switching in Thin Magnetic Tunnel Junctions*, J. Ventura, J. P. Araujo, F. Carpinteiro, J. B. Sousa, Y. Liu, Z. Zhang, P. P. Freitas, J. Magn. Magn. Mat. **290-291**, 1067 (2005).

11. *Domain imaging, MOKE and AMR in CoFeB films for MRAM applications*, J. M. Teixeria, R. Silva, J. Ventura, J.P. Araujo, J. B. Sousa, S. Cardoso, R. Ferreira and P. P. Freitas, Mat. Sci. Eng. B **126**, 180 (2006).

12. *Spin-dependent two-level resistance fluctuations in underoxidized tunnel junctions*, J. Ventura, J. M. Teixeira, Yu. Pogorelov, J. B. Sousa, R. Ferreira and P. P. Freitas, accepted in J. Appl. Phys.

13. *Electromigration-driven resistance switching in non-magnetic tunnel junctions*, J. Ventura, A. Pereira, J. M. Teixeira, F. Carpinteiro, J. P. Araujo, J. B. Sousa, Y. Liu, Z. Zhang and P. P. Freitas, accepted in J. All. Comp.

14. *Short-range effects and magnetization reversal in $Co_{80}Fe_{20}$ thin films: a MOKE magnetometry/domain imaging and AMR study*, J. M. Teixeria, R. F. A. Silva, J. Ventura, A. Pereira, J. P. Araujo, M. Amado, F. Carpinteiro, J. B. Sousa, S. Cardoso, R. Ferreira and P. Freitas, accepted in Mat. Sci. Forum

15. *Heat generation in tunnel junctions for current-written pinned layer switching*, J. Ventura, A. Pereira, J. M. Teixeira, J. P. Araujo, F. Carpinteiro, J. B. Sousa, Y. Liu, Z. Zhang and P. P. Freitas, accepted in Mat. Sci. Forum.

16. *Nanoscopic origin of Current Induced Switching in thin tunnel junctions*, J. Ventura, J. P. Araújo, J. B. Sousa, Y. Liu, Z. Zhang and P. P. Freitas, accepted in IEEE Trans. Nanotechnol.

17. *Magnetic characterization of MnPt/CoFe bilayers using the MOKE technique*, J.M. Teixeira, A. M. Pereira, J. Ventura, R.F.A. Silva, F. Carpinteiro, J.P. Araujo, J.B. Sousa, M. Rickart, S. Cardoso, R. Ferreira and P. P. Freitas, submitted to Vacuum.

Bibliography

[1] P. Grünberg, R. Schreiber, Y. Pang, M. B. Brodsky, and H. Sowers, "Layered magnetic structures: Evidence for antiferromagnetic coupling of Fe layers across Cr interlayers", *Phys. Rev. Lett.*, vol. 57, pp. 2442–2445, November 1986.

[2] S. S. P. Parkin, N. More, and K. P. Roche, "Oscillations in exchange coupling and magnetoresistance in metallic superlattice structures: Co/Ru, Co/Cr, and Fe/Cr", *Phys. Rev. Lett.*, vol. 64, pp. 2304–2307, May 1990.

[3] B. Heinrich, Z. Celinski, J. F. Cochran, W. B. Muir, J. Rudd, Q. M. Zhong, A. S. Arrott, K. Myrtle, and J. Kirschner, "Ferromagnetic and antiferromagnetic exchange coupling in bcc epitaxial ultrathin Fe(001)/Cu(001)Fe(001) trilayers", *Phys. Rev. Lett.*, vol. 64, pp. 673–676, February 1990.

[4] P. P. Freitas, L. V. Melo, I. Trindade, M. From, J. Ferreira, and P. Monteiro, "Antiferromagnetic exchange and magnetoresistance enhancement in Co-Re superlattices", *Phys. Rev. B*, vol. 45, pp. 2495–2498, February 1992.

[5] M. N. Baibich, J. M. Broto, A. Fert, F. Nguyen van Dau, F. Petroff, P. Etienne, G. Creuzet, A. Friederich, and J. Chazelas, "Giant magnetoresistance of (001)Fe/(001)Cr magnetic superlattices", *Phys. Rev. Lett.*, vol. 61, pp. 2472–2475, November 1988.

[6] G. Binasch, P. Grünberg, F. Saurenbach, and W. Zinn, "Enhanced magnetoresistance in layered magnetic structures with antiferromagnetic interlayer exchange", *Phys. Rev. B*, vol. 39, pp. 4828–4830, March 1989.

[7] B. Dieny, V. S. Speriosu, S. S. P. Parkin, B. A. Gurney, D. R. Wilhoit, and D. Mauri, "Giant magnetoresistive in soft ferromagnetic multilayers", *Phys. Rev. B*, vol. 43, pp. 1297–1300, January 1991.

[8] J. S. Moodera, L. R. Kinder, T. M. Wong, and R. Meservey, "Large magnetoresistance at room temperature in ferromagnetic thin film tunnel junctions", *Phys. Rev. Lett.*, vol. 74, pp. 3273–3276, April 1995.

[9] T. Miyazaki and N. Tezuka, "Giant magnetic tunneling effect in Fe/Al_2O_3/Fe junction", *J. Magn. Magn. Mater.*, vol. 139, pp. L231–L234, January 1995.

[10] S. Yuasa, T. Katayama, T. Nagahama, A. Fukushima, H. Kubota, Suzuki Y., and Ando K., "Giant tunneling magnetoresistance in fully epitaxial body-centered-cubic Co/MgO/Fe magnetic tunnel junctions", *Appl. Phys. Lett.*, vol. 87, pp. 222508, November 2005.

[11] J. Hong, H. Kanai, and Y. Uehara, "Very large GMR of spin valve with specularly reflective layers", Presented at the 47th MMM Conference, Seattle, WA, Nov. 13, 2001, 2005.

[12] C. Kittel, *Introduction to solid state physics*, New York: Wiley, 1976, 5th ed., 1976.

[13] T. R. McGuire and R. I. Potter, "Anisotropic magnetoresistance in ferromagnetic 3d alloys", *IEEE Trans. Magn.*, vol. 11, pp. 1018–1038, July 1975.

[14] R. von Helmolt, J. Wecker, B. Holzapfel, L. Schultz, and K. Samwer, "Giant negative magnetoresistance in perovskitelike $La_{2/3}Ba_{1/3}MnO_x$ ferromagnetic films", *Phys. Rev. Lett.*, vol. 71, pp. 2331–2333, October 1993.

[15] S. S. P. Parkin, Z. G. Li, and D. J. Smith, "Giant magnetoresistance in antiferromagnetic Co/Cu multilayers", *Appl. Phys. Lett.*, vol. 58, pp. 2710–2712, June 1991.

[16] M. Julliere, "Tunneling between ferromagnetic films", *Phys. Lett. A*, vol. 54, pp. 225–226, September 1975.

[17] D. Wang, C. Nordman, J. M. Daughton, Q. Zhenghong, and J. Fink, "70% TMR at room temperature for SDT sandwich junctions with CoFeB as free and reference layers", *IEEE Trans. Magn.*, vol. 40, pp. 2269–2271, July 2004.

[18] W. H. Meiklejohn and C. P. Bean, "New magnetic anisotropy", *Phys. Rev.*, vol. 102, pp. 1413–1414, June 1956.

[19] J. Nogués and I. K. Schuller, "Exchange bias", *J. Magn. Magn. Mater.*, vol. 192, pp. 203–232, February 1999.

[20] T. G. S. M. Rijks, R. Coehoorn, J. T. F. Daemen, and W. J. M. de Jonge, "Interplay between exchange biasing and interlayer exchange coupling in Ni(80)Fe(20)/CU/Ni(80)Fe(20)/Fe(50)Mn(50) layered systems", *J. Appl. Phys.*, vol. 76, pp. 1092–1099, July 1994.

[21] B. A. Everitt, D. Wang, and J. M Daughton, "Spin valves with NiO pinning layer", *IEEE Trans. Magn.*, vol. 32, pp. 4657–4659, September 1996.

[22] N. Hasegawa, A. Makino, F. Koike, and K. Ikarashi, "Spin-valves with antiferromagnetic α-Fe_2O_3 layers", *IEEE Trans. Magn.*, vol. 32, pp. 4618–4620, September 1996.

[23] V. Gehanno, P. P. Freitas, A. Veloso, J. Ferreira, B. Almeida, J. B. Sousa, A. Kling, J. C. Soares, and M. F. da Silva, "Ion beam deposition of Mn-Ir spin valves", *IEEE Trans. Magn.*, vol. 35, pp. 4361–4367, September 1999.

[24] J. R. Childress, M. M. Schwickert, R. E. Fontana, M. K. Ho, P. M. Rice, and B. A. Gurney, "Low-resistance IrMn and PtMn tunnel valves for recording head applications", *J. Appl. Phys.*, vol. 89, pp. 7353–7355, June 2001.

[25] A. E. Berkowitz and K. Takano, "Exchange anisotropy - a review", *J. Magn. Magn. Mater.*, vol. 200, pp. 552–570, October 1999.

[26] W. J. Gallagher, S. S. P. Parkin, Y. Lu, X. P. Bian, A. Marley, K. P. Roche, R. A. Altman, S. A. Rishton, C. Jahnes, T. M. Shaw, and G. Xiao, "Microstructured magnetic tunnel junctions (invited)", *J. Appl. Phys.*, vol. 81, pp. 3741–3746, April 1997.

[27] M. Kiwi, "Exchange bias theory: a review", cond-mat/0107097, 2001.

[28] W. H. Meiklejohn and C. P. Bean, "New Magnetic Anisotropy", *Phys. Rev.*, vol. 105, pp. 904–913, February 1957.

[29] A. P. Malozemoff, "Random-field model of exchange anisotropy at rough ferromagnetic-antiferromagnetic interfaces", *Phys. Rev. B*, vol. 35, pp. 3679–3682, March 1987.

[30] U. Nowak, K. D. Usadel, J. Keller, P. Miltényi, B. Beschoten, and G. Güntherodt, "Domain state model for exchange bias. I. Theory", *Phys. Rev. B*, vol. 66, no. 1, pp. 014430, July 2002.

[31] J. Keller, P. Miltényi, B. Beschoten, G. Güntherodt, U. Nowak, and K. D. Usadel, "Domain state model for exchange bias. II. Experiments", *Phys. Rev. B*, vol. 66, no. 1, pp. 014431, July 2002.

[32] C. Tsang, R. E. Fontana, T. Lin, D. E. Heim, V. S. Speriosu, B. A. Gurney, and M. L. Williams, "Design, fabrication and testing of spin valve read heads for high density recording", *IEEE Trans. Magn.*, vol. 30, pp. 3801–3806, November 1994.

[33] J. C. S. Kools, W. Kula, D. Mauri, and T. Lin, "Effect of finite magnetic film thickness on Néel coupling in spin valves", *J. Appl. Phys.*, vol. 85, pp. 4466–4468, April 1999.

[34] M. D. Stiles, "Interlayer exchange coupling", *J. Magn. Magn. Mater.*, vol. 200, no. 1, pp. 322–337, October 1999.

[35] J. Zhang and R. M. White, "Topological coupling in spin valve type multilayers", *IEEE Trans. Magn.*, vol. 32, pp. 4630–4635, September 1996.

[36] S. S. P. Parkin, N. More, and K. P. Roche, "Oscillations in exchange coupling and magnetoresistance in metallic superlattice structures: Co/Ru, Co/Cr, and Fe/Cr", *Phys. Rev. Lett.*, vol. 64, pp. 2304–2307, May 1990.

[37] P. Bruno, "Theory of interlayer magnetic coupling", *Phys. Rev. B*, vol. 52, pp. 411–439, July 1995.

[38] J. L. Leal and M. H. Kryder, "Interlayer coupling in spin valve structure", *IEEE Trans. Magn.*, vol. 32, pp. 4642–4644, September 1996.

[39] R. Coehoorn, "Period of oscillatory exchange interactions in Co/Cu and Fe/Cu multilayer systems", *Phys. Rev. B*, vol. 44, pp. 9331–9337, November 1991.

[40] J. C. S. Kools, Th. G. S. M. W. Rijks, A. E. M. De Veirman, and R. Coehoorn, "On the ferromagnetic interlayer coupling in exchange-biased spin-valve multilayers", *IEEE Trans. Magn.*, vol. 31, pp. 3918–3920, November 1995.

[41] V. S. Speriosu, B. Dieny, P. Humbert, B. A. Gurney, and H. Lefakis, "Nonoscillatory magnetoresistance in Co/Cu/Co layered structures with oscillatory coupling", *Phys. Rev. B*, vol. 44, pp. 5358–5361, September 1991.

[42] J. C. Slonczewski, "Conductance and exchange coupling of two ferromagnets separated by a tunneling barrier", *Phys. Rev. B*, vol. 39, pp. 6995–7002, April 1989.

[43] C. Heide, R. J. Elliott, and N. S. Wingreen, "Spin-polarized tunnel current in magnetic-layer systems and its relation to the interlayer exchange interaction", *Phys. Rev. B*, vol. 59, pp. 4287–4304, February 1999.

[44] J. Faure-Vincent, C. Tiusan, C. Bellouard, E. Popova, M. Hehn, F. Montaigne, and A. Schuhl, "Interlayer magnetic coupling interactions of two ferromagnetic layers by spin polarized tunneling", *Phys. Rev. Lett.*, vol. 89, no. 10, pp. 107206, August 2002.

[45] J. Hong, J. Kane, J. Hashimoto, M. Yamagishi, K. Noma, and H. Kanai, "Spin valve heads with specularly reflective oxide layers for over 100 Gb/in^2", *IEEE Trans. Magn.*, vol. 38, pp. 15–19, January 2002.

[46] C. Haginoya, M. Hatatani, K. Meguro, C. Ishikawa, N. Yoshida, K. Kusukawa, and K. Watanabe, "Side-Shielded Tunneling Magnetoresistive Read Head for High-Density Recording", *IEEE Trans. Magn.*, vol. 40, pp. 2221–2223, July 2004.

[47] S. Mao, Y. Chen, F. Liu, X. Chen, B. Xu, P. Lu, M. Patwari, H. Xi, C. Chang, B. Miller, D. Menard, B. Pant, J. Loven, K. Duxstad, S. Li, Z. Zhang, A. Johnston, R. Lamberton, M. Gubbins, T. McLaughlin, J. Gadbois, J. Ding, B. Cross, S. Xue, and P. Ryan, "Commercial TMR Heads for Hard Disk Drives: Characterization and Extendibility At 300 Gbit/in^2", *IEEE Trans. Magn.*, vol. 42, pp. 97–102, February 2006.

[48] M. Lohndorf, T. Duenas, M. Tewes, E. Quandt, M. Ruhrig, and J. Wecker, "Highly sensitive strain sensors based on magnetic tunneling junctions", *Appl. Phys. Lett.*, vol. 81, pp. 313–315, July 2002.

[49] P. P. Freitas, F. Silva, N. J. Oliveira, L. V. Melo, L. Costa, and N. Almeida, "Spin valve sensors", *Sensors and Actuators A - Physical*, vol. 81, pp. 2–8, April 2000.

[50] R. Richter, L. Bär, J. Wecker, and G. Reiss, "Nonvolatile field programmable spin-logic for reconfigurable computing", *Appl. Phys. Lett.*, vol. 80, pp. 1291–1293, February 2002.

[51] H. A. Ferreira, D. L. Graham, P. P. Freitas, and J. M. S. Cabral, "Biodetection using magnetically labeled biomolecules and arrays of spin valve sensors (invited)", *J. Appl. Phys.*, vol. 93, pp. 7281–7286, May 2003.

[52] D. L. Graham, H. A. Ferreira, and P. P. Freitas, "Magnetoresistive-based biosensors and biochips", *Trends in Biotechnology*, vol. 22, pp. 455–462, September 2004.

[53] B. F. Cockburn, "Tutorial on Magnetic Tunnel Junction Magnetoresistive Random-Access Memory", *Records of the 2004 International Workshop on Memory Technology, Design and Testing*, pp. 46–51, August 2004.

[54] P. P. Freitas, S. Cardoso, R. Sousa, W. Ku, R. Ferreira, V. Chu, and J. P. Conde, "Spin Dependent Tunnel Junctions for Memory and Read-Head Applications", *IEEE Trans. Magn.*, vol. 36, pp. 2796–2801, September 2000.

[55] B. N. Engel, N. D. Rizzo, J. Janesky, J. M. Slaughter, R. Dave, M. DeHerrera, M. Durlam, and S. Tehrani, "The Science and Technology of Magnetoresistive Tunneling Memory", *IEEE Trans. Nanotechnol.*, vol. 1, pp. 32–38, March 2002.

[56] S. Tehrani, J. M. Slaughter, M. DeHerrera, B. N. Engel, N. D. Rizzo, J. Salter, M. Durlam, R. Dave, J. Janesky, B. Butcher, K. Smith, and G. Grynkewich, "Magnetoresistive Random Access Memory Using Magnetic Tunnel Junctions", *Proc. IEEE*, vol. 91, no. 5, pp. 703–714, May 2003.

[57] S. Maekawa and T. Shinjo, *Spin dependent transport in magnetic nanostructures*, New York and London: Taylor & Francis, 2002.

[58] M. Takagishi, K. Koi, M. Yoshikawa, H. Iwasaki, and M. Sahashi, "The applicability of CPP GMR heads for magnetic recording", *IEEE Trans. Magn.*, vol. 38, pp. 2277–2282, September 2002.

[59] D. Song, J. Nowak, R. Larson, P. Kolbo, and R. Chellew, "Demonstrating a tunneling magneto-resistive read head", *IEEE Trans. Magn.*, vol. 36, pp. 2545–2548, September 2000.

[60] G. A. Prinz, "Magnetoelectronics applications", *J. Magn. Magn. Mater.*, vol. 200, pp. 57–68, October 1999.

[61] D. R. Baselt, G. U. Lee, M. Natesan, S. W. Metzger, P. E. Sheehan, and R. J. Colton, "A biosensor based on magnetoresistance technology", *Biosens. Bioelectron.*, vol. 13, no. 7, pp. 731–739, October 1998.

[62] Y. Liu, Z. Zhang, P. P. Freitas, and J. L. Martins, "Current-induced magnetization switching in magnetic tunnel junctions", *Appl. Phys. Lett.*, vol. 82, pp. 2871–2873, April 2003.

[63] S. Cardoso, *Dual-Stripe GMR and Tunnel Junction Read Heads and Ion Beam Deposition and Oxidation of Tunnel Junctions*, PhD thesis, Instituto Superior Técnico, 2003.

[64] R. Costa e Sousa, *Magnetic Random Access Memory (MRAM) based on Spin Dependent Tunnel Junctions*, PhD thesis, Instituto Superior Técnico, 2003.

[65] J. Zhang, *Low-resistance tunnel junctions for read head applications*, PhD thesis, Instituto Superior Técnico, 2003.

[66] S. Li, T. S. Plaskett, P. P. Freitas, P. Wei, N. Barradas, B. Almeida, and J. B. Sousa, "The effect of substrate bias on the properties of NiO/NiFe and NiO/CoFe exchange biased spin-valve sensors", *IEEE Trans. Magn.*, vol. 34, pp. 3772–3777, September 1998.

[67] J. Moreira, *Estudo Experimental do Efeito Hall, Magnetoresistência e Resistividade Eléctrica em Metais e Ligas Magnéticas (3d, 4f)*, PhD thesis, Universidade do Porto, 1985.

[68] V. Amaral, *Localização electrónica e magnetismo em amorfos metálicos*, PhD thesis, Universidade do Porto, 1993.

[69] M. Salgueiro da Silva, *Estudo experimental de estruturas magnéticas moduladas nos compostos intermetálicos NdRu2Si2 e TbRu2Si2*, PhD thesis, Universidade do Porto, 1999.

[70] B. Almeida, *Filmes finos e multicamadas metálicas magnéticas*, PhD thesis, Universidade do Porto, 1997.

[71] J. Araujo, *Local Probe and Bulk property Studies of Highly Correlated Electron Systems: High-Tc superconductores and CMR magnetic Oxides*, PhD thesis, Universidade do Porto, 2001.

[72] B. A. Hands, *Cryogenic Engineering*, New York: Academic Press, 1986, 1986.

[73] G. Walker, *Cryocoolers*, New York: Plenum Press, 1983, 1983.

[74] M. W. Zemansky, *Heat and thermodynamics*, New York: McGraw-Hill, 1957, 1957.

[75] L. B. Valdes, "Resistivity measurements on Germanium for transitors", *Proc. IRE*, vol. 42, pp. 420–423, 1954.

[76] Y. Liu, Z. Zhang, and P. P. Freitas, "Hot-spot mediated current-induced resistance change in magnetic tunnel junctions", *IEEE Trans. Magn.*, vol. 39, pp. 2833–2835, September 2003.

[77] "http://msdn.microsoft.com/vbasic/".

[78] "www.ni.com/mstudio/".

[79] J. M. Teixeria, R. F. A. Silva, J. Ventura, A. Pereira, J. Araujo, M. Amado, F. Carpinteiro, J. B. Sousa, S. Cardoso, R. Ferreira, and P. P. Freitas, "Short-range effects and magnetization reversal in Co80Fe20 thin films: a MOKE magnetometry/domain imaging and AMR study", Submitted to Mat. Sci. Forum, 2005.

[80] K. Fuchs, "The conductivity of thin metallic films according to the electron theory of metals", *Proc. Camb. Phil. Soc.*, vol. 34, pp. 100, October 1938.

[81] E. H. Sondheimer, "The mean free path of electrons in metals", *Adv. Phys.*, vol. 1, pp. 1–42, 1952.

[82] J. M. Ziman, *Electrons and phonons*, Oxfor, Clarendon press, 1967.

[83] S. B. Soffer, "Statistical Model for the Size Effect in Electrical Conduction", *J. Appl. Phys.*, vol. 38, pp. 1710–1715, March 1967.

[84] R. E. Camley and J. Barnaś, "Theory of giant magnetoresistance effects in magnetic layered structures with antiferromagnetic coupling", *Phys. Rev. Lett.*, vol. 63, pp. 664–667, August 1989.

[85] J. Barnaś, A. Fuss, R. E. Camley, P. Grünberg, and W. Zinn, "Novel magnetoresistance effect in layered magnetic structures: Theory and experiment", *Phys. Rev. B*, vol. 42, pp. 8110–8120, November 1990.

[86] A. Fert and I. A. Campbell, "Electrical resistivity of ferromagnetic nickel and iron based alloys ", *J. of Phys. F Metal Phys.*, vol. 6, pp. 849–871, May 1976.

[87] R. Q. Hood, L. M. Falicov, and D. R. Penn, "Effects of interfacial roughness on the magnetoresistance of magnetic metallic multilayers", *Phys. Rev. B*, vol. 49, pp. 368–377, January 1994.

[88] E. E. Fullerton, D. M. Kelly, J. Guimpel, I. K. Schuller, and Y. Bruynseraede, "Roughness and giant magnetoresistance in Fe/Cr superlattices", *Phys. Rev. Lett.*, vol. 68, pp. 859–862, February 1992.

[89] B. Dieny, V. S. Speriosu, and S. Metin, "Thermal variation of the magnetoresistance of soft spin-valve multilayers".

[90] P. Dieny, A. Granovsky, A. Vedyaev, C. Cowache, N. Ryzhanova, and L. G. Pereira, "Recent results on the giant magnetoresistance in magnetic multilayers (anisotropy, thermal variation and CCP-GMR)", *J. Magn. Magn. Mater.*, vol. 151, pp. 378–387, December 1995.

[91] A. Vedyayev, B. Dieny, and N. Ryzhanova, "Quantum-theory of giant magnetoresistance of spin-valve sandwiches", *EuroPhy. Lett.*, vol. 19, pp. 329–335, June 1992.

[92] A. Vedyayev, C. Cowache, N. Ryzhanova, and B. Dieny, "Quantum effects in the giant magnetoresistance of magnetic multilayered structures ", *J. Phys. Cond. Matt.*, vol. 5, pp. 8289–8304, November 1993.

[93] H. E. Camblong and P. M. Levy, "Novel results for quasiclassical linear transport in metallic multilayers", *Phys. Rev. Lett.*, vol. 69, pp. 2835–2838, November 1992.

[94] H. E. Camblong, P. M. Levy, and S. Zhang, "Electron transport in magnetic inhomogeneous media", *Phys. Rev. B*, vol. 51, pp. 16052–16072, June 1995.

[95] P. M. Levy, S. Zhang, and A. Fert, "Electrical conductivity of magnetic multilayered structures", *Phys. Rev. Lett.*, vol. 65, pp. 1643–1646, September 1990.

[96] S. Zhang, P. M. Levy, and A. Fert, "Conductivity and magnetoresistance of magnetic multilayered structures", *Phys. Rev. B*, vol. 45, pp. 8689–8702, April 1992.

[97] X.-G. Zhang and W. H. Butler, "Conductivity of metallic films and multilayers", *Phys. Rev. B*, vol. 51, pp. 10085–10103, April 1995.

[98] W. F. Egelhoff, P. J. Chen, C. J. Powell, M. D. Stiles, R. D. McMichael, J. H. Judy, K. Takano, and A. E. Berkowitz, "Oxygen as a surfactant in the growth of giant magnetoresistance spin valves", *J. Appl. Phys.*, vol. 82, pp. 6142–6151, December 1997.

[99] W. F. Egelhoff, P. J. Chen, C. J. Powell, M. D. Stiles, R. D. McMichael, J. H. Judy, K. Takano, A. E. Berkowitz, and J. M. Daughton, "Specular electron scattering in giant magnetoresistance spin valves", *IEEE Trans. Magn.*, vol. 33, pp. 3580–3582, September 1997.

[100] W. F. Egelhoff, T. Ha, R. D. K. Misra, Y. Kadmon, J. Nir, C. J. Powell, M. D. Stiles, R. D. McMichael, C.-L. Lin, J. M. Sivertsen, J. H. Judy, K. Takano, A. E. Berkowitz, T. C. Anthony, and J. A. Brug, "Magnetoresistance values exceeding 21% in symmetric spin valves", *J. Appl. Phys.*, vol. 78, pp. 273–277, July 1995.

[101] H. J. M. Swagten, G. J. Strijkers, P. J. H. Bloemen, M. M. H. Willekens, and W. J. M. de Jonge, "Enhanced giant magnetoresistance in spin-valves sandwiched between insulating NiO", *Phys. Rev. B*, vol. 53, pp. 9108–9114, April 1996.

[102] H. J. M. Swagten, G. J. Strijkers, R. H. J. N. Bitter, W. J. M. de Jonge, and J. C. S. Kools, "Specular reflection in spin valves bounded by NiO layers", *IEEE Trans. Magn.*, vol. 34, pp. 948–953, July 1998.

[103] H. Sakakima, M. Satomi, Y. Sugita, and Y. Kawawake, "Enhancement of MR ratios using thin oxide layers in PtMn and α-Fe_2O_3-based spin valves", *J. Magn. Magn. Mater.*, vol. 210, pp. 20–24, February 2000.

[104] A. Veloso, P. P. Freitas, P. Wei, N. P. Barradas, J. C. Soares, B. Almeida, and J. B. Sousa, "Magnetoresistance enhancement in specular, bottom-pinned, $Mn_{83}Ir_{17}$ spin valves with nano-oxide layers", *Appl. Phys. Lett.*, vol. 77, pp. 1020–1022, August 2000.

[105] Y.-G. Wang, F. Shen, Z. Zhang, J.-W. Cai, and W.-Y. Lai, "Determination of the Potential Barrier at the Metal/Oxide Interface in a Specular Spin Valve Structure with Nano-oxide Layers Using Electron Holography", *Chin. Phys. Lett.*, vol. 19, pp. 1480–1482, October 2002.

[106] H. Fukuzawa, K. Koi, H. Tomita, H. N. Fuke, H. Iwasaki, and M. Sahashi, "Specular spin-valve films with an FeCo nano-oxide layer by ion-assisted oxidation", *J. Appl. Phys.*, vol. 91, pp. 6684–6690, May 2002.

[107] K. Li, Y. Wu, J. Qiu, G. Han, Z. Guo, H. Xie, and T. Chong, "Suppression of interlayer coupling and enhancement of magnetoresistance in spin valves with oxide layer", *Appl. Phys. Lett.*, vol. 79, pp. 3663–3665, November 2001.

[108] M. Mao, C. Cerjan, and J. Kools, "Physical properties of spin-valve films grown on naturally oxidized metal nano-oxide surfaces", *J. Appl. Phys.*, vol. 91, pp. 8560–8562, May 2002.

[109] C.-H. Lai, C. J. Chen, and T. S. Chin, "Giant magnetoresistance enhancement in spin valves with nano-oxide layers", *J. Appl. Phys.*, vol. 89, pp. 6928–6930, June 2001.

[110] J. Hong, J. Kane, J. Hashimoto, M. Yamagishi, K. Noma, and H. Kanai, "Spin-valve head with specularly reflective oxide layers for over 100 Gb/in^2", *IEEE Trans. Magn.*, vol. 38, pp. 15–19, January 2002.

[111] C. C. Hu, M. Mao, A. J. Devasahayam, C. L. Lee, J. C. S. Kools, W. Skinner, and J. Hautala, "Nano-oxide layer formed on Ruthenium of synthetic pinned-structure spin valve by ion beam and cluster ion beam oxidation", *IEEE Trans. Magn.*, vol. 40, pp. 2203–2205, July 2004.

[112] D. M. Jeon, J. P. Lee, D. H. Lee, S. Y. Yoon, J. H. Kim, D. H. Yoon, and S. J. Suh, "Nano-oxide layer and magnetic properties in Mn-Ir-Pt-baserd spin valve multilayers", *Thin Sol. Films*, vol. 475, pp. 243–245, October 2004.

[113] L. Wang, J. J. Qiu, W. J. McMahon, K. B. Li, and Y. H. Wu, "Nano-oxide-layer insertion and specular effects in spin valves: Experiment and theory", *Phys. Rev. B*, vol. 69, no. 21, pp. 214402, June 2004.

[114] J. L. Leal and M. H. Kryder, "Spin valves exchange biased by Co/Ru/Co synthetic antiferromagnets", *J. Appl. Phys.*, vol. 83, pp. 3720–3723, April 1998.

[115] J. G. Zhu, "Spin valve and dual spin valve heads with synthetic antiferromagnets", *IEEE Trans. Magn.*, vol. 35, pp. 655–660, March 1999.

[116] B. Dieny, M. Li, S. H. Liao, C. Horng, and K. Ju, "Quantitative interpretation of the magnetoresistive response (amplitude and shape) of spin valves with synthetic antiferromagnetic pinned layers", *J. Appl. Phys.*, vol. 87, pp. 3415–3420, April 2000.

[117] G. W. Anderson, Y. Huai, and M. Pakala, "Spin-valve thermal stability: The effect of different antiferromagnets", *J. Appl. Phys.*, vol. 87, pp. 5726–5728, May 2000.

[118] J.-S. Park, S.-R. Lee, and Y. K. Kim, "Spin-valves with modified synthetic antiferromagnets exhibiting an enhanced bias point control capability at submicrometer dimensions", *J. Magn. Magn. Mater.*, vol. 279, pp. L1–L4, August 2004.

[119] Y. Huai, G. Anderson, and M. Pakala, "IrMn based spin-filter spin-valves", *J. Appl. Phys.*, vol. 87, pp. 5741–5743, May 2000.

[120] B. A. Gurney, V. S. Speriosu, J.-P. Nozieres, H. Lefakis, D. R. Wilhoit, and O. U. Need, "Direct measurement of spin-dependent conduction-electron mean free paths in ferromagnetic metals", *Phys. Rev. Lett.*, vol. 71, pp. 4023–4026, December 1993.

[121] M. Ueno, H. Nishida, K. Mizukami, F. Hikami, K. Tabuchi, and T. Sawasaki, "Read-write performance of spin-filter-spin-valve heads", *IEEE Trans. Magn.*, vol. 36, pp. 2572–2574, September 2000.

[122] H. Fukuzawa, H. Iwasaki, Y. Kamiguchi, K. Koi, and M. Sahashi, "Spin-filter spin-valve films with an ultrathin CoFe free layer", *J. Appl. Phys.*, vol. 89, pp. 5581–5584, May 2001.

[123] A. Al-Jibouri, M. Hoban, Z. Lu, and G. Pan, "Spin-filter spin valves with nano-oxide layers for high density recording heads", *J. Appl. Phys.*, vol. 91, pp. 7098–7100, May 2002.

[124] B. Dieny, "Classical theory of giant magnetoresistance in spin-valve multilayers: influence of thicknesses, number of periods, bulk and interfacial spin-dependent scattering ", *J. Phys. Cond. Matt.*, vol. 4, pp. 8009–8020, October 1992.

[125] M. F. Gillies and A. E. T. Kuiper, "Enhancement of the giant magnetoresistance in spin valves via oxides formed from magnetic layers", *J. Appl. Phys.*, vol. 88, pp. 5894–5898, November 2000.

[126] M. R. Parker, H. Fujiwara, S. Hossain, and W. E. Webb, "Magnetic vector model of spin-valves", *IEEE Trans. Magn.*, vol. 31, pp. 2618–2620, November 1995.

[127] J. Barnas, "The influence of outer boundary conditions on the interlayer exchange coupling in magnetic sandwich structures", *J. Magn. Magn. Mater.*, vol. 167, pp. 209–222, March 1997.

[128] A. Chaiken, T. M. Tritt, D. J. Gillespie, J. J. Krebs, P. Lubitz, M. Z. Harford, and G. A. Prinz, "Temperature dependence of magnetoresistance in Fe-Cr-Fe sandwiches", *J. Appl. Phys.*, vol. 69, pp. 4798–4800, April 1991.

[129] F. Shen, Q. Y. Xu, G. H. Yu, W. Y. Lai, Z. Zhang, Z. Q. Lu, G. Pan, and A. Al-Jibouri, "A specular spin valve with discontinuous nano-oxide layers", *Appl. Phys. Lett.*, vol. 80, pp. 4410–4412, June 2002.

[130] S. Cardoso, R. Ferreira, P. P. Freitas, M. MacKenzie, J. Chapman, J. O. Ventura, J. B. Sousa, and U. Kreissig, "Ferromagnetic coupling field reduction in CoFeB tunnel junctions deposited by ion beam", *IEEE Trans. Magn.*, vol. 40, pp. 2272–2274, July 2004.

[131] S. Y. Yoon, D. H. Lee, D. M. Jeon, Y. S. Kim, D. H. Yoon, and S. J. Suh, "Microstructure and magnetic properties of Mn-Ir based specular spin valve multilayer with nano oxide layer", *Sensors and Actuators A - Physical*, vol. 115, pp. 91–95, June 2004.

[132] D. H. Lee, S. Y. Yoon, J. H. Kim, and S. J. Suh, "Characterization of nano-oxide layer in specular spin valve multilayer", *Thin Sol. Films*, vol. 475, pp. 251–255, October 2004.

[133] J. Qiu, P. Luo, K. Li, Y. Zheng, L. H. An, and Y. Wu, "Optimization of nano-oxide layer in CIP spin valves", *IEEE Trans. Magn.*, vol. 40, pp. 2260–2262, July 2004.

[134] M. Doi, M. Izumi, N. F. Hiromi, H. Iwasaki, and M. Sahashi, "Magnetism of $Co_{1-x}Fe_x$-NOL in specular spin-valves", *IEEE Trans. Magn.*, vol. 40, pp. 2263–2265, July 2004.

[135] P. J. van der Zaag, Y. Ijiri, J. A. Borchers, L. F. Feiner, R. M. Wolf, J. M. Gaines, R. W. Erwin, and M. A. Verheijen, "Difference between Blocking and Néel Temperatures in the Exchange Biased Fe_3O_4/CoO System", *Phys. Rev. Lett.*, vol. 84, pp. 6102–6105, June 2000.

[136] M. Pan, B. You, Y. Zhao, M. Lu, A. Hu, H. Zhaia, and S. Zhou, "Thermal stability of exchange bias in FeMn based bilayers", *J. Appl. Phys.*, vol. 91, pp. 5272–5274, April 2002.

[137] L. Tang, D. E. Laughlin, and S. Gangopadhyay, "Microstructural study of ion-beam deposited giant magnetoresistive spin valves", *J. Appl. Phys.*, vol. 81, pp. 4906–4908, April 1997.

[138] C. Tsang and K. Lee, "Temperature dependence of unidirectional anisotropy effects in the Permalloy-FeMn systems", *J. Appl. Phys.*, vol. 53, pp. 2605–2607, March 1982.

[139] S. Soeya, T. Imagawa, K. Mitsuoka, and S. Narishige, "Distribution of blocking temperature in bilayered $Ni_{81}Fe_{19}$/NiO films", *J. Appl. Phys.*, vol. 76, pp. 5356–5360, November 1994.

[140] M. D. Stiles and R. D. McMichael, "Temperature dependence of exchange bias in polycrystalline ferromagnet-antiferromagnet bilayers", *Phys. Rev. B*, vol. 60, pp. 12950–12956, November 1999.

[141] S. Brems, D. Buntinx, K. Temst, C. Haesendonck, F. Radu, and H. Zabel, "Reversing the training effect in exchange biased CoO/Co bilayers", *Phys. Rev. Lett.*, vol. 95, pp. 157202, October 2005.

[142] F. Radu, M. Etzkorn, R. Siebrecht, T. Schmitte, K. Westerholt, and H. Zabel, "Interfacial domain formation during magnetization reversal in exchange-biased CoO/Co bilayers", *Phys. Rev. B*, vol. 67, no. 13, pp. 134409, April 2003.

[143] A. Hochstrat, C. Binek, and W. Kleemann, "Training of the exchange-bias effect in NiO-Fe heterostructures", *Phys. Rev. B*, vol. 66, no. 9, pp. 092409, September 2002.

[144] C. Binek, "Training of the exchange-bias effect: A simple analytic approach", *Phys. Rev. B*, vol. 70, no. 1, pp. 014421, July 2004.

[145] D. L. Peng, K. Sumiyama, T. Hihara, S. Yamamuro, and T. J. Konno, "Magnetic properties of monodispersed Co/CoO clusters", *Phys. Rev. B*, vol. 61, pp. 3103–3109, January 2000.

[146] M. Gruyters, "Spin-Glass-Like Behavior in CoO Nanoparticles and the Origin of Exchange Bias in Layered CoO/Ferromagnet Structures", *Phys. Rev. Lett.*, vol. 95, pp. 077204, April 2005.

[147] C. Schlenker, S. S. P. Parkin, J. C. Scott, and K. Howard, "Magnetic disorder in the exchange bias bilayered FeNi-FeMn system", *J. Magn. Magn. Mater.*, vol. 54, pp. 801–802, February 1986.

[148] A. Veloso and P. P. Freitas, "Spin valve sensors with synthetic free and pinned layers", *J. Appl. Phys.*, vol. 87, pp. 5744–5746, May 2000.

[149] P. M. Tedrow and R. Meservey, "Spin-dependent tunneling into ferromagnetic Nickel", *Phys. Rev. Lett.*, vol. 26, pp. 192–195, January 1971.

[150] P. M. Tedrow and R. Meservey, "Spin polarization of electrons tunneling from films of Fe, Co, Ni, and Gd", *Phys. Rev. B*, vol. 7, pp. 318–326, January 1973.

[151] R. Meservey and P. M. Tedrow, "Spin-polarized electron tunneling", *Phys. Rep.*, vol. 238, pp. 173–243, March 1994.

[152] S. Yuasa, T. Nagahama, A. Fukushima, Y. Suzuki, and K. Ando, "Giant room-temperature magnetoresistance in single-crystal Fe/MgO/Fe magnetic tunnel junctions", *Nature Mat.*, vol. 3, pp. 868–871, December 2004.

[153] S. S. P. Parkin, C. Kaiser, A. Panchula, P. M. Rice, B. Hughes, M. Samant, and S. H. Yang, "Giant tunnelling magnetoresistance at room temperature with MgO (100) tunnel barriers", *Nature Mat.*, vol. 3, pp. 862–867, December 2004.

[154] S. Tehrani, J. M. Slaughter, E. Chen, M. Durlam, M. DeHerrera, and J. Shi, "Progress and outlook for MRAM technology", *IEEE Trans. Magn.*, vol. 35, pp. 2814–2819, September 1999.

[155] S. Tehrani, B. Engel, J. M. Slaughter, E. Chen, M. DeHerrera, M. Durlam, P. Naji, R. Whig, J. Janesky, and J. Calder, "Recent developments in magnetic tunnel junction MRAM", *IEEE Trans. Magn.*, vol. 36, pp. 2752–2757, September 2000.

[156] R. Coehoorn, S. R. Cumpson, J. J. M. Ruigrok, and P. Hidding, "The electrical and magnetic response of yoke-type read heads based on a magnetic tunnel junction", *IEEE Trans. Magn.*, vol. 35, pp. 2586–2588, September 1999.

[157] D. Song, J. Nowak, R. Larson, P. Kolbo, and Chellew R., "Demonstrating a tunneling magneto-resistive read head", *IEEE Trans. Magn.*, vol. 36, pp. 2545–2548, September 2000.

[158] M. Beth Stearns, "Simple explanation of tunneling spin-polarization of Fe, Co, Ni and its alloys", *J. Magn. Magn. Mater.*, vol. 5, pp. 167–171, April 1977.

[159] J. A. Hertz and K. Aoi, "Spin-dependent tunnelling from transition-metal ferromagnets", *Phys. Rev. B*, vol. 8, pp. 3252–3256, October 1973.

[160] M. Münzenberg and J. S. Moodera, "Superconductor-ferromagnet tunneling measurements indicate sp -spin and d -spin currents", *Phys. Rev. B*, vol. 70, no. 6, pp. 060402, August 2004.

[161] E. Y. Tsymbal, I. I. Oleinik, and D. G. Pettifor, "Oxygen-induced positive spin polarization from Fe into the vacuum barrier", *J. Appl. Phys.*, vol. 87, pp. 5230–5232, May 2000.

[162] J. M. de Teresa, A. Barthélémy, A. Fert, J. P. Contour, R. Lyonnet, F. Montaigne, P. Seneor, and A. Vaurès, "Inverse tunnel magnetoresistance in $Co/SrTiO_3/La_{0.7}Sr_{0.3}MnO_3$: New ideas on spin-polarized tunneling", *Phys. Rev. Lett.*, vol. 82, pp. 4288–4291, May 1999.

[163] M. Sharma, S. X. Wang, and J. H. Nickel, "Inversion of spin polarization and tunneling magnetoresistance in spin-dependent tunneling junctions", *Phys. Rev. Lett.*, vol. 82, pp. 616–619, January 1999.

[164] S. F. Alvarado, "Tunneling potential barrier dependence of electron spin polarization", *Phys. Rev. Lett.*, vol. 75, pp. 513–516, July 1995.

[165] E. Y. Tsymbal and D. G. Pettifor, "Modelling of spin-polarized electron tunnelling from 3d ferromagnets", *J. Phys.: Condens. Matter*, vol. 9, pp. L411–L417, July 1997.

[166] S. Zhang and P. M. Levy, "Models for magnetoresistance in tunnel junctions", *Eur. Phys. J. B*, vol. 10, pp. 599–606, August 1999.

[167] Y. Asano, A. Oguri, and S. Maekawa, "Parallel and perpendicular transport in multilayered structures", *Phys. Rev. B*, vol. 48, pp. 6192–6198, September 1993.

[168] J. Bardeen, "Tunnelling from a many-particle point of view", *Phys. Rev. Lett.*, vol. 6, pp. 57–59, January 1961.

[169] W. A. Harrison, "Tunneling from an independent-particle point of view", *Phys. Rev.*, vol. 123, pp. 85–89, July 1961.

[170] J. Mathon and A. Umerski, "Theory of tunneling magnetoresistance in a junction with a nonmagnetic metallic interlayer", *Phys. Rev. B*, vol. 60, pp. 1117–1121, July 1999.

[171] E. Y. Tsymbal and D. G. Pettifor, "Spin-polarized electron tunneling across a disordered insulator", *Phys. Rev. B*, vol. 58, pp. 432–437, July 1998.

[172] C. Choen-Tannoudji, B. Diu, and F. Laloe, *Quantum mechanics*, New York: John Wiley & Sons, 1977.

[173] X. Zhang, B. Li, G. Sun, and F. Pu, "Spin-polarized tunneling and magnetoresistance in ferromagnet/insulator(semiconductor) single and double tunnel junctions subjected to an electric field", *Phys. Rev. B*, vol. 56, pp. 5484–5488, September 1997.

[174] T. Dimopoulos, *Transport polarise en spins dans le jontions tunnel magnetiques: le role des interfaces metal/oxyde dans le processus tunnel*, PhD thesis, Universite Louis Pasteur de Strasbourg, 2002.

[175] M. Arbramowitz and I. A. Stegun, *Handbook of mathematical functions*, New York: Dover Publications, 1965, 1965.

[176] N. Tezuka and T. Miyazaki, "Barrier height dependence of MR ratio in Fe/Al-oxide/Fe junctions", *J. Magn. Magn. Mater.*, vol. 177, pp. 1283–1284, January 1998.

[177] J. M. MacLaren, X.-G. Zhang, and W. H. Butler, "Validity of the Julliere model of spin-dependent tunneling", *Phys. Rev. B*, vol. 56, pp. 11827–11832, November 1997.

[178] Y. Qi, D. Y. Xing, and J. Dong, "Relation between Julliere and Slonczewski models of tunneling magnetoresistance", *Phys. Rev. B*, vol. 58, pp. 2783–2787, August 1998.

[179] J. Mathon, "Tight-binding theory of tunneling giant magnetoresistance", *Phys. Rev. B*, vol. 56, pp. 11810–11819, November 1997.

[180] J. M. MacLaren, X.-G. Zhang, W. H. Butler, and X. Wang, "Layer KKR approach to Bloch-wave transmission and reflection: Application to spin-dependent tunneling", *Phys. Rev. B*, vol. 59, pp. 5470–5478, February 1999.

[181] J. G. Simmons, "Generalized formula for the electrical tunnel effect between similar electrodes by a thin insulating films", *J. Appl. Phys.*, vol. 34, pp. 1793–1803, June 1963.

[182] L. S. Dorneles, D. M. Schaefer, M. Carara, and L. F. Schelp, "The use of Simmons' equation to quantify the insulating barrier parameters in Al/AlO$_x$/Al tunnel junctions", *Appl. Phys. Lett.*, vol. 82, pp. 2832–2834, April 2003.

[183] D. A. Rabson, B. J. Jönsson-Åkerman, A. H. Romero, R. Escudero, C. Leighton, S. Kim, and I. K. Schuller, "Pinholes may mimic tunneling", *J. Appl. Phys.*, vol. 89, pp. 2786–2790, March 2001.

[184] B. J. Jönsson-Åkerman, R. Escudero, C. Leighton, S. Kim, I. K. Schuller, and D. A. Rabson, "Reliability of normal-state current-voltage characteristics as an indicator of tunnel-junction barrier quality", *Appl. Phys. Lett.*, vol. 77, pp. 1870–1872, September 2000.

[185] J. J. Akerman, R. Escudero, C. Leighton, S. Kim, D. A. Rabson, R. W. Dave, J. M. Slaughter, and I. K. Schuller, "Criteria for ferromagnetic-insulator-ferromagnetic tunneling", *J. Magn. Magn. Mater.*, vol. 240, pp. 86–91, February 2002.

[186] Z. Zhang and D. A. Rabson, "Diagnosis and location of pinhole defects in tunnel junctions using only electrical measurements", *J. Appl. Phys.*, vol. 95, pp. 199–203, January 2004.

[187] W. F. Brinkman, R. C. Dynes, and J. M. Rowell, "Tunneling conductance of assymetric barriers", *J. Appl. Phys.*, vol. 41, pp. 1915–1921, April 1970.

[188] W. Oepts, M. F. Gillies, R. Coehoorn, R. J. M. van de Veerdonk, and W. J. M. de Jonge, "Asymmetric bias voltage dependence of the magnetoresistance of $Co/Al_2O_3/Co$ magnetic tunnel junctions: Variation with the barrier oxidation time", *J. Appl. Phys.*, vol. 89, pp. 8038–8045, June 2001.

[189] S. Zhang, P. M. Levy, A. C. Marley, and S. S. P. Parkin, "Quenching of Magnetoresistance by Hot Electrons in Magnetic Tunnel Junctions", *Phys. Rev. Lett.*, vol. 79, pp. 3744–3747, November 1997.

[190] Y. Ando, J. Murai, H. Kubota, and T. Miyazaki, "Magnon-assisted inelastic excitation spectra of a ferromagnetic tunnel junction", *J. Appl. Phys.*, vol. 87, pp. 5209–5211, May 2000.

[191] J. Klein, A. Léger, M. Belin, D. Défourneau, and M. J. Sangster, "Inelastic-Electron-Tunneling Spectroscopy of Metal-Insulator-Metal Junctions", *Phys. Rev. B*, vol. 7, pp. 2336–2348, March 1973.

[192] K. Hansen and M. Brandbyge, "Current-voltage relation for thin tunnel barriers: Parabolic barrier model", *J. Appl. Phys.*, vol. 95, pp. 3582–3586, April 2004.

[193] J. S. Moodera, J. Nowak, and R. J. M. van de Veerdonk, "Interface magnetism and spin wave scattering in ferromagnet-insulator-ferromagnet tunnel junctions", *Phys. Rev. Lett.*, vol. 80, pp. 2941–2944, March 1998.

[194] S. Colis, G. Gieres, T. Dimopoulos, L. Bar, and J. Wecker, "Large magnetoresistance at high bias voltage in double magnetic tunnel junctions", *IEEE Trans. Magn.*, vol. 40, pp. 2287–2289, July 2004.

[195] C. A. Dartora and G. G. Cabrera, "Ferromagnetic tunneling junctions at low voltages: Elastic versus inelastic scattering at T=0 K", *J. Appl. Phys.*, vol. 95, pp. 6058–6064, June 2004.

[196] G. G. Cabrera and N. Garcia, "Low voltage I-V characteristics in magnetic tunneling junctions", *Appl. Phys. Lett.*, vol. 80, pp. 1782–1784, March 2002.

[197] A. H. Davis and J. M. MacLaren, "Spin dependent tunneling at finite bias", *J. Appl. Phys.*, vol. 87, pp. 5224–5226, May 2000.

[198] X. H. Xiang, T. Zhu, J. Du, G. Landry, and J. Q. Xiao, "Effects of density of states on bias dependence in magnetic tunnel junctions", *Phys. Rev. B*, vol. 66, no. 17, pp. 174407, November 2002.

[199] P. LeClair, J. T. Kohlhepp, H. J. Swagten, and W. J. de Jonge, "Interfacial density of states in magnetic tunnel junctions", *Phys. Rev. Lett.*, vol. 86, pp. 1066–1069, February 2001.

[200] P. Leclair, J. T. Kohlhepp, C. H. van de Vin, H. Wieldraaijer, H. J. Swagten, W. J. de Jonge, A. H. Davis, J. M. MacLaren, J. S. Moodera, and R. Jansen, "Band structure and density of states effects in Co-based magnetic tunnel junctions", *Phys. Rev. Lett.*, vol. 88, no. 10, pp. 107201, March 2002.

[201] J. G. Simmons, "Generalized thermal J-V characteristics for the electrical tunnel effect", *J. Appl. Phys.*, vol. 35, pp. 2655–2658, September 1964.

[202] D. T. Pierce, R. J. Celotta, J. Unguris, and H. C. Siegmann, "Spin-dependent elastic scattering of electrons from a ferromagnetic glass, $Ni_{40}Fe_{40}B_{20}$", *Phys. Rev. B*, vol. 26, pp. 2566–2574, September 1982.

[203] C. H. Shang, J. Nowak, R. Jansen, and J. S. Moodera, "Temperature dependence of magnetoresistance and surface magnetization in ferromagnetic tunnel junctions", *Phys. Rev. B*, vol. 58, pp. R2917–R2920, August 1998.

[204] A. H. MacDonald, T. Jungwirth, and M. Kasner, "Temperature Dependence of Itinerant Electron Junction Magnetoresistance", *Phys. Rev. Lett.*, vol. 81, pp. 705–708, July 1998.

[205] Y. Xu, D. Ephron, and M. R. Beasley, "Direct inelastic hopping of electrons through metal-insulator-metal tunnel junctions", *Phys. Rev. B*, vol. 52, pp. 2843–2859, July 1995.

[206] X. Han, A. C. Yu, M. Oogane, J. Murai, T. Daibou, and T. Miyazaki, "Analyses of intrinsic magnetoelectric properties in spin-valve-type tunnel junctions with high magnetoresistance and low resistance", *Phys. Rev. B*, vol. 63, no. 22, pp. 224404, June 2001.

[207] A. M. Bratkovsky, "Assisted tunneling in ferromagnetic junctions and half-metallic oxides", *Appl. Phys. Lett.*, vol. 72, pp. 2334–2336, May 1998.

[208] B. Oliver, Q. He, X. Tang, and J. Nowak, "Tunneling criteria and breakdown for low resistive magnetic tunnel junctions", *J. Appl. Phys.*, vol. 94, pp. 1783–1786, August 2003.

[209] Yu. V. Sharvin, "A possible method for studying Fermi surfaces", *J. Exptl. Theoret. Phys.*, vol. 48, pp. 984–985, March 1965.

[210] J. Z. Wang, B. Z. Li, and Z. N. Hu, "Temperature dependence of magnetoresistance in the magnetic tunnel junction with an assymetric barrier", *Phys. Lett. A*, vol. 261, pp. 371–378, October 1999.

[211] J. S. Moodera, "Spin polarized tunneling", presented at the Joint European Magnetic Symposia, Dresden, Germany, 2004.

[212] B. Oliver, G. Tuttle, Q. He, X. Tang, and J. Nowak, "Two breakdown mechanisms in ultrathin alumina barrier magnetic tunnel junctions", *J. Appl. Phys.*, vol. 95, pp. 1315–1322, February 2004.

[213] B. Oliver, Q. He, X. Tang, and J. Nowak, "Dielectric breakdown in magnetic tunnel junctions having an ultrathin barrier", *J. Appl. Phys.*, vol. 91, pp. 4348–4352, April 2002.

[214] W. Oepts, H. J. Verhagen, R. Coehoorn, and W. J. M. de Jonge, "Analysis of breakdown in ferromagnetic tunnel junctions", *J. Appl. Phys.*, vol. 86, pp. 3863–3872, October 1999.

[215] E. Harari, "Dielectric-breakdown in electrically stressed thin-films of thermal SiO2", *J. Appl. Phys.*, vol. 49, pp. 2478–2489, April 1978.

[216] E. Rosenbaum, J. C. King, and C. M. Hu, "Accelerated testing of SiO2 reliability", *IEEE Trans. Electron. Devices*, vol. 43, pp. 70–80, January 1996.

[217] K. F. Schuegraf and C. M. Hu, "Effects of temperature and defects on breakdown lifetime of thin SiO2 at very-low voltages", *IEEE Trans. Electron. Devices*, vol. 41, pp. 1227–1232, July 1994.

[218] J. W. McPherson and H. C. Mogul, "Underlying physics of the thermochemical E model in describing low-field time-dependent dielectric breakdown in SiO_2 thin films", *J. Appl. Phys.*, vol. 84, pp. 1513–1523, August 1998.

[219] I.-C. Chen, S. E. Holland, and C. Hu, "Electrical breakdown in thin gate and tunneling oxides", *IEEE Trans. Electron. Devices*, vol. 32, pp. 413–422, February 1985.

[220] M. Kimura, "Field and temperature acceleration model for time dependent dielectric breakdown", *IEEE Trans. Electron. Devices*, vol. 46, pp. 220–229, January 1999.

[221] J. Das, R. Degraeve, P. Roussel, G. Groeseneken, G. Borghs, and J. D. Boeck, "Area scaling and voltage dependence of time-to-breakdown in magnetic tunnel junctions", *J. Appl. Phys.*, vol. 91, pp. 7712–7714, May 2002.

[222] D. Rao, K. Sin, M. Gibbons, S. Funada, M. Mao, C. Chien, and H.-C. Tong, "Voltage-induced barrier-layer damage in spin-dependent tunneling junctions", *J. Appl. Phys.*, vol. 89, pp. 7362–7364, June 2001.

[223] J. W. McPherson, R. B. Khamankar, and A. Shanware, "Complementary model for intrinsic time-dependent dielectric breakdown in SiO_2 dielectrics", *J. Appl. Phys.*, vol. 88, pp. 5351–5359, November 2000.

[224] J. W. McPherson, J. Kim, H. Mogul, and Rodriguez J., "Trends in the ultimate breakdown strength of high dielectric-constant materials", *IEEE Trans. Magn.*, vol. 50, pp. 1771–1778, August 2003.

[225] J. C. Slonczewski, "Current-driven excitation of magnetic multilayers", *J. Magn. Magn. Mater.*, vol. 159, pp. L1–L7, June 1996.

[226] J. C. Slonczewski, "Currents and torques in metallic magnetic multilayers", *J. Magn. Magn. Mater.*, vol. 247, pp. 324–338, June 2002.

[227] L. Berger, "Emission of spin waves by a magnetic multilayer traversed by a current", *Phys. Rev. B*, vol. 54, pp. 9353–9358, October 1996.

[228] J. A. Katine, F. J. Albert, R. A. Buhrman, E. B. Myers, and D. C. Ralph, "Current-Driven Magnetization Reversal and Spin-Wave Excitations in Co/Cu/Co Pillars", *Phys. Rev. Lett.*, vol. 84, pp. 3149–3152, April 2000.

[229] Y. Jiang, S. Abe, T. Ochiai, T. Nozaki, A. Hirohata, N. Tezuka, and K. Inomata, "Effective reduction of critical current for current-induced magnetization switching by a Ru lLayer insertion in an exchange-biased spin valve", *Phys. Rev. Lett.*, vol. 92, no. 16, pp. 167204, April 2004.

[230] Y. Huai, F. Albert, P. Nguyen, M. Pakala, and T. Valet, "Observation of spin-transfer switching in deep submicron-sized and low-resistance magnetic tunnel junctions", *Appl. Phys. Lett.*, vol. 84, pp. 3118–3120, April 2004.

[231] G. D. Fuchs, N. C. Emley, I. N. Krivorotov, P. M. Braganca, E. M. Ryan, S. I. Kiselev, J. C. Sankey, D. C. Ralph, R. A. Buhrman, and J. A. Katine, "Spin-transfer effects in nanoscale magnetic tunnel junctions", *Appl. Phys. Lett.*, vol. 85, pp. 1205–1207, August 2004.

[232] M. D. Stiles and A. Zangwill, "Anatomy of spin-transfer torque", *Phys. Rev. B*, vol. 66, no. 1, pp. 014407, June 2002.

[233] S. Zhang, P. M. Levy, and A. Fert, "Mechanisms of spin-polarized current-driven magnetization switching", *Phys. Rev. Lett.*, vol. 88, no. 23, pp. 236601, June 2002.

[234] Y. B. Bazaliy, B. A. Jones, and S. Zhang, "Modification of the Landau-Lifshitz equation in the presence of a spin-polarized current in colossal- and giant-magnetoresistive materials", *Phys. Rev. B*, vol. 57, pp. R3213–R3216, February 1998.

[235] X. Waintal, E. B. Myers, P. W. Brouwer, and D. C. Ralph, "Role of spin-dependent interface scattering in generating current-induced torques in magnetic multilayers", *Phys. Rev. B*, vol. 62, pp. 12317–12327, November 2000.

[236] E. B. Myers, F. J. Albert, J. C. Sankey, E. Bonet, R. A. Buhrman, and D. C. Ralph, "Thermally activated magnetic reversal induced by a spin-polarized current", *Phys. Rev. Lett.*, vol. 89, no. 19, pp. 196801, October 2002.

[237] J. Grollier, V. Cros, H. Jaffrès, A. Hamzic, J. M. George, G. Faini, J. Ben Youssef, H. Le Gall, and A. Fert, "Field dependence of magnetization reversal by spin transfer", *Phys. Rev. B*, vol. 67, no. 17, pp. 174402, May 2003.

[238] M. Alhajdarwish, H. Kurt, S. Urazhdin, A. Fert, R. Loloee, W. P. Pratt, and J. Bass, "Controlled normal and inverse current-induced magnetization switching and magnetoresistance in magnetic nanopillars", *Phys. Rev. Lett.*, vol. 93, no. 15, pp. 157203, October 2004.

[239] A. Fert, V. Cros, J.-M. George, J. Grollier, H. Jaffrès, A. Hamzic, A. Vaurès, G. Faini, J. Ben Youssef, and H. Le Gall, "Magnetization reversal by injection and transfer of spin: experiments and theory", *J. Magn. Magn. Mater.*, vol. 272, pp. 1706–1711, May 2004.

[240] J. Z. Sun, "Spin-current interaction with a monodomain magnetic body: A model study", *Phys. Rev. B*, vol. 62, pp. 570–578, July 2000.

[241] J. Bass, S. Urazhdin, N. O. Birge, and W. P. Pratt Jr., "Current-driven excitations in magnetic multilayers: a brief review", *Phys. Stat. Sol. (a)*, vol. 201, pp. 1379–1385, May 2004.

[242] M. Tsoi, J. Z. Sun, M. J. Rooks, R. H. Koch, and S. S. Parkin, "Current-driven excitations in magnetic multilayer nanopillars from 4.2 K to 300 K", *Phys. Rev. B*, vol. 69, no. 10, pp. 100406, March 2004.

[243] S. Urazhdin, N. O. Birge, W. P. Pratt, and J. Bass, "Current-driven switching in magnetic multilayer nanopillars (invited)", *J. Appl. Phys.*, vol. 95, pp. 7429–7434, June 2004.

[244] R. S. Sorbello, "Theory of electromigration", in *Solid State Physics*, H. Ehrenreich and F. Spaepen, Eds., vol. 51, pp. 159–231. Springer-Verlag, New York, 1998.

[245] E. T. Ogawa, K. D. Lee, V. A. Blaschke, and P. S. Ho, "Electromigration reliability in dual-damascene Cu interconnections", *IEEE Trans. Rel.*, vol. 51, pp. 403–419, December 2002.

[246] C.-L. Liu, X.-Y. Liu, and L. J. Borucki, "Defect generation and diffusion mechanisms in Al and Al-Cu", *Appl. Phys. Lett.*, vol. 74, pp. 34–36, January 1999.

[247] C. L. Gan, C. V. Thompson, K. L. Pey, W. K. Choi, H. L. Tay, B. Yu, and M. K. Radhakrishnan, "Effect of current direction on the lifetime of different levels of Cu dual-damascene metallization", *Appl. Phys. Lett.*, vol. 79, pp. 4592–4594, December 2001.

[248] K. N. Tu, "Recent advances on electromigration in very-large-scale-integration of interconnects", *J. Appl. Phys.*, vol. 94, pp. 5451–5473, November 2003.

[249] C.-L. Liu, X.-Y. Liu, and L. J. Borucki, "Defect generation and diffusion mechanisms in Al and Al-Cu", *Appl. Phys. Lett.*, vol. 74, pp. 34–36, January 1999.

[250] S. Bae, I. F. Tsu, M. Davis, E. S. Murdock, and J. H. Judy, "Electromigration study of magnetic thin films for the electrical reliability of spin valves read heads", *IEEE Trans. Magn.*, vol. 38, pp. 2655–2657, September 2002.

[251] K. S. Ralls, D. C. Ralph, and R. A. Buhrman, "Individual-defect electromigration in metal nanobridges", *Phys. Rev. B*, vol. 40, pp. 11561–11570, December 1989.

[252] O. Céspedes, G. Jan, M. Viret, M. Bari, and J. M. D. Coey, "Random telegraph noise in a nickel nanoconstriction", *J. Appl. Phys.*, vol. 93, pp. 8433–8435, May 2003.

[253] A. Deac, O. Redon, R. C. Sousa, B. Dieny, J. P. Nozières, Z. Zhang, Y. Liu, and P. P. Freitas, "Current driven resistance changes in low resistance x area magnetic tunnel junctions with ultra-thin Al-O_x barriers", *J. Appl. Phys.*, vol. 95, pp. 6792–6794, June 2004.

[254] J. R. Manning, *Diffusion kinetics for atoms in crystals*, New Jersey: D. van Nostrand Company, inc., 1968, 1968.

[255] L. A. Girifalco, *Statistical physics of materials*, New York: John Wiley & Sons, 1973, 1973.

[256] J. R. Manning, "Correlation correction to the activation energy for diffusion in crystalline solids", *Phys. Rev. Lett.*, vol. 1, pp. 365–367, November 1958.

[257] R. Ghez, *A primer of diffusion problems*, New York: John Wiley & Sons, 1988, 1988.

[258] E. J. S. Lage, *Fisica estatistica*, Lisbon: Fundacao Calouste Gulbenkian, 1995, 1995.

[259] C. K. Hu, K. P. Rodbell, T. D. Sullivan, K. Y. Lee, and D. P. Bouldlin, "Electromigration and stress induced voiding in fine Al and Al-alloy thin film lines", *IBM J. Res. Develop.*, vol. 39, no. 4, pp. 465–497, July 1995.

[260] N. W. Ashcroft and N. D. Mermin, *Solid state physics*, New York: Harcourt College Publishing, 1976, 5th ed., 1976.

[261] R. S. Sorbello, "Electromigration and the local transport field in mesoscopic systems", *Phys. Rev. B*, vol. 39, pp. 4984–4996, March 1989.

[262] E. Burstein and S. Lundqvist, *Tunneling Phenomena in Solids*, Plenum, New York, 1969.

[263] R. C. Sousa, I. L. Prejbeanu, D. Stanescu, B. Rodmacq, O. Redon, B. Dieny, J. Wang, and P. P. Freitas, "Tunneling hot spots and heating in magnetic tunnel junctions", *J. Appl. Phys.*, vol. 95, pp. 6783–6785, June 2004.

[264] Z. Chen and R. S. Sorbello, "Local heating in mesoscopic systems", *Phys. Rev. B*, vol. 47, pp. 13527–13534, May 1993.

[265] J. Wang, Y. Liu, P. P. Freitas, E. Snoeck, and J. L. Martins, "Continuous thin barriers for low-resistance spin-dependent tunnel junctions", *J. Appl. Phys.*, vol. **93**, pp. 8367–8369, May 2003.

[266] D. N. Bly and P. J. Rous, "Theoretical study of the electromigration wind force for adatom migration at metal surfaces", *Phys. Rev. B*, vol. 53, pp. 13909–13920, May 1996.

[267] P. A. M. Holweg, J. Caro, A. H. Verbruggen, and S. Radelaar, "Ballistic electron transport and two-level resistance fluctuations in noble-metal nanobridges", *Phys. Rev. B*, vol. 45, pp. 9311–9319, April 1992.

[268] H. Yasuda and A. Sakai, "Conductance of atomic-scale gold contacts under high-bias voltages", *Phys. Rev. B*, vol. 56, pp. 1069–1072, July 1997.

[269] E. B. Svedberg, K. J. Howard, M. C. Bønsager, B. B. Pant, A. G. Roy, and D. E. Laughlin, "Interdiffusion in CoFe/Cu multilayers and its application to spin-valve structures for data storage", *J. Appl. Phys.*, vol. 94, pp. 1001–1006, July 2003.

[270] J. V. Barth, "Transport of adsorbates at metal surfaces: from thermal migration to hot precursors", *Surf. Sci. Rep.*, vol. 40, pp. 75–149, October 2000.

[271] J. A. Rodriguez, J. Hrbek, Z. Chang, J. Dvorak, T. Jirsak, and A. Maiti, "Importance of O vacancies in the behavior of oxide surfaces: Adsorption of sulfur on $TiO_2(110)$", *Phys. Rev. B*, vol. 65, no. 23, pp. 235414, June 2002.

[272] N. Nilius, T. M. Wallis, and W. Ho, "Influence of a Heterogeneous Al_2O_3 Surface on the Electronic Properties of Single Pd Atoms", *Phys. Rev. Lett.*, vol. 90, no. 4, pp. 046808, January 2003.

[273] H. Li, P. P. Freitas, Z. Wang, J. B. Sousa, P. Gogol, and J. Chapman, "Exchange enhancement and thermal anneal in $Mn_{76}Ir_{24}$ bottom-pinned spin valves", *J. Appl. Phys.*, vol. 89, pp. 6904–6906, June 2001.

[274] J. Wang and P. P. Freitas, "Low-current blocking temperature writing of double barrier magnetic random access memory cells", *Appl. Phys. Lett.*, vol. 84, pp. 945–947, February 2004.

[275] A. M. Bratkovsky, A. P. Sutton, and T. N. Todorov, "Conditions for conductance quantization in realistic models of atomic-scale metallic contacts", *Phys. Rev. B*, vol. 52, pp. 5036–5051, August 1995.

[276] S. Kondo, K. Ogasawara, and K. Hinode, "Thermographic analysis of electromigration phenomena in aluminum metallization", *J. Appl. Phys.*, vol. 79, pp. 736–741, January 1996.

[277] I.L. Prejbeanu, W. Kula, K. Ounadjela, R.C. Sousa, O. Redon, B. Dieny, and J.-P. Nozieres, "Thermally assisted switching in exchange-biased storage layer magnetic tunnel junctions", *IEEE Trans. Magn.*, vol. 40, pp. 2625–2627, July 2004.

[278] P. LeClair, H. J. M. Swagten, J. T. Kohlhepp, R. J. M. van de Veerdonk, and W. J. M. de Jonge, "Apparent Spin Polarization Decay in Cu-Dusted Co/Al_2O_3/Co Tunnel Junctions", *Phys. Rev. Lett.*, vol. 84, pp. 2933–2936, March 2000.

[279] H. Kyung, C. S. Yoon, and C. K. Kim, "Microstructure and electrical properties of magnetic tunneling junction: NiFe/Co/Ta/Al-oxide/Co", *Mat. Sci. Eng. B*, vol. 90, pp. 13–15, November 2002.

[280] B. Chakraborty, W. E. Pickett, and P. B. Allen, "Density of states, optical mass, and dc electrical resistance of Ta, W, Nb, and Mo using Slater-Koster interpolation", *Phys. Rev. B*, vol. 14, pp. 3227–3230, October 1976.

[281] J. Ventura, J. B. Sousa, Y. Liu, Z. Zhang, and P. P. Freitas, "Electromigration in thin tunnel junctions with ferromagnetic/nonmagnetic electrodes: Nanoconstrictions, local heating, and direct and wind forces", *Phys. Rev. B*, vol. 72, pp. 094432, September 2005.

[282] I. K. Schuller, "private communication".

[283] S.-I. Ohfuji and M. Tsukada, "Recovery of electric resistance degraded by electromigration", *J. Appl. Phys.*, vol. 78, pp. 3769–3775, September 1995.

[284] K. S. Ralls and R. A. Buhrman, "Microscopic study of 1/f noise in metal nanobridges", *Phys. Rev. B*, vol. 44, pp. 5800–5817, September 1991.

[285] K. L. Merkle, L. J. Thompson, and F. Phillipp, "Collective Effects in Grain Boundary Migration", *Phys. Rev. Lett.*, vol. 88, no. 22, pp. 225501, June 2002.

[286] L. D. van Ee, B. J. Thijsse, and J. Sietsma, "Atomic two-level states and relaxations observed in a computer model of amorphous $Ni_{81}B_{19}$", *Phys. Rev. B*, vol. 57, pp. 906–913, January 1998.

[287] P. P. Freitas, S. Cardoso, R. Sousa, W. J. Ku, R. Ferreira, V. Chu, and J. P. Conde, "Spin dependent tunnel junctions for memory and read-head applications", *IEEE Trans. Magn.*, vol. 36, pp. 2796–2801, September 2000.

[288] M. Takagishi, K. Koi, M. Yoshikawa, M. Funayama, H. Iwasaki, and M. Sahashi, "The applicability of CPP-GMR heads for magnetic recording", *IEEE Trans. Magn.*, vol. 38, pp. 2277–2282, September 2002.

[289] R. Ferreira, P. P. Freitas, M. MacKenzie, and J. N. Chapman, "Low resistance magnetic tunnel junctions prepared by partial remote plasma oxidation of 0.9 nm Al barriers", *Appl. Phys. Lett.*, vol. 86, pp. 192502, July 2005.

[290] M. B. Weissman, "1/f noise and other slow, nonexponential kinetics in condensed matter", *Rev. Mod. Phys.*, vol. 60, pp. 537–571, April 1988.

[291] K. S. Ralls, W. J. Skocpol, L. D. Jackel, R. E. Howard, L. A. Fetter, R. W. Epworth, and D. M. Tennant, "Discrete Resistance Switching in Submicrometer Silicon Inversion Layers: Individual Interface Traps and Low-Frequency (1/f) Noise", *Phys. Rev. Lett.*, vol. 52, pp. 228–231, January 1984.

[292] X. Jiang, M. A. Dubson, and J. C. Garland, "Giant discrete resistance fluctuations observed in normal-metal tunnel junctions", *Phys. Rev. B*, vol. 42, pp. 5427–5432, September 1990.

[293] R. Ferreira, P. P. Freitas, M. MacKenzie, and J. N. Chapman, "Low resistance tunnel junctions with remote plasma underoxidized thick barriers", *J. Appl. Phys.*, vol. 97, pp. 10C903, May 2005.

[294] C. T. Rogers, *A study of individual electron trapping centers and 1/f noise in metal-insulator-metal tunnel junctions*, PhD thesis, Cornell University, 1987.

[295] F. W. Schmidlin, "Enhanced Tunneling through Dielectric Films due to Ionic Defects", *J. Appl. Phys.*, vol. 37, pp. 2823–2832, June 1966.

[296] N. Garcia, "Conducting ballistic magnetoresistance and tunneling magnetoresistance: Pinholes and tunnel barriers", *Appl. Phys. Lett.*, vol. 77, pp. 1351–1353, August 2000.

[297] Z. Yang, Y. Qi, and S. Zhang, "Magnetoresistance and resistance of magnetic nanoconstriction", *Phys. Rev. B*, vol. 70, no. 9, pp. 094404, September 2004.

[298] G. Wexler, "The size effect and the non-local Boltzmann transport equation in orifice and disk geometry", *Proc. Phys. Soc.*, vol. 89, pp. 927–941, June 1966.

[299] M. R. Sullivan, D. A. Boehm, D. A. Ateya, S. Z. Hua, and H. D. Chopra, "Ballistic magnetoresistance in nickel single-atom conductors without magnetostriction", *Phys. Rev. B*, vol. 71, no. 2, pp. 024412, January 2005.

[300] O. Ozatay, P. Chalsani, N. C. Emley, I. N. Krivorotov, and R. A. Buhrman, "Magnetoresistance and magnetostriction effects in ballistic ferromagnetic nanoconstrictions", *J. Appl. Phys.*, vol. 95, pp. 7315–7317, June 2004.

[301] N. Garcia, M. Munoz, and Y.-W. Zhao, "Magnetoresistance in excess of 200% in Ballistic Ni Nanocontacts at Room Temperature and 100 Oe", *Phys. Rev. Lett.*, vol. 82, pp. 2923–2926, April 1999.

[302] G. Tatara, Y.-W. Zhao, M. Munoz, and N. Garcia, "Domain Wall Scattering Explains 300% Ballistic Magnetoconductance of Nanocontacts", *Phys. Rev. Lett.*, vol. 83, pp. 2030–2033, September 1999.

[303] N. Garcia, M. Munoz, and Y.-W. Zhao, "Ballistic magnetoresistance in transition-metal nanocontacts: The case of iron", *Appl. Phys. Lett.*, vol. 76, pp. 2586–2587, May 2000.

93736

[304] H. D. Chopra and S. Z. Hua, "Ballistic magnetoresistance over 3000% in Ni nanocontacts at room temperature", *Phys. Rev. B*, vol. 66, no. 2, pp. 020403, June 2002.

[305] J. J. Mallett, E. B. Svedberg, H. Ettedgui, T. P. Moffat, and W. F. Egelhoff, "Absence of ballistic magnetoresistance in Ni contacts controlled by an electrochemical feedback system", *Phys. Rev. B*, vol. 70, no. 17, pp. 172406, November 2004.

[306] W. F. Egelhoff, L. Gan, H. Ettedgui, Y. Kadmon, C. J. Powell, P. J. Chen, A. J. Shapiro, R. D. McMichael, J. J. Mallett, T. P. Moffat, M. D. Stiles, and E. B. Svedberg, "Artifacts in ballistic magnetoresistance measurements (invited)", *J. Appl. Phys.*, vol. 95, pp. 7554–7559, June 2004.

[307] W. F. Egelhoff, L. Gan, H. Ettedgui, Y. Kadmon, C. J. Powell, P. J. Chen, A. J. Shapiro, R. D. McMichael, J. J. Mallett, T. P. Moffat, M. D. Stiles, and E. B. Svedberg, "Artifacts that mimic ballistic magnetoresistance", *J. Magn. Magn. Mater.*, vol. 287, pp. 496–500, February 2005.

[308] S. H. Chung, M. Munoz, N. García, W. F. Egelhoff, and R. D. Gomez, "Universal Scaling of Ballistic Magnetoresistance in Magnetic Nanocontacts", *Phys. Rev. Lett.*, vol. 89, pp. 287203, December 2002.

[309] S. H. Chung, M. Munoz, N. Garcia, W. F. Egelhoff, and R. D. Gomez, "Universal scaling of magnetoconductance in magnetic nanocontacts (invited)", *J. Appl. Phys.*, vol. 93, pp. 7939–7944, May 2003.

[310] L. R. Tagirov, B. P. Vodopyanov, and K. B. Efetov, "Ballistic versus diffusive magnetoresistance of a magnetic point contact", *Phys. Rev. B*, vol. 63, no. 10, pp. 104428, March 2001.

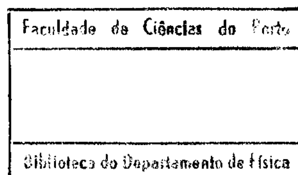
Faculdade de Ciências do Porto
Biblioteca do Departamento de Física